UNIVERSITY OF CALIFORNIA
SANTA CRUZ

# MICROPHYSICS OF PROTOPLANETARY DISKS AND EXOPLANET ATMOSPHERES

A dissertation submitted in partial satisfaction of the
requirements for the degree of

Doctor of Philosophy

in

ASTRONOMY AND ASTROPHYSICS

by

**Diana Powell**

June 2021

The Dissertation of Diana Powell is approved:

Ruth Murray-Clay, Chair

Xi Zhang

Jonathan Fortney

Hilke Schlichting

Quentin Williams
Interim Vice Provost and Dean of Graduate Studies

# Table of Contents

# List of Figures

# List of Tables

## Abstract

Microphysics of Protoplanetary Disks and Exoplanet Atmospheres

by

Diana Powell

An understanding of planetary histories and characteristics requires an empirical connection between planet formation and evolved planets—a long-sought goal of astrophysics and planetary science. This connection is now increasingly possible due to simultaneous revolutions in the observations of protoplanetary disks and exoplanet atmospheres. A crucial step towards relating these observations of different evolutionary stages is to characterize the fundamental properties of both disks and atmospheres.

The work presented in this dissertation uses microphysics—i.e., the physics that governs the evolution of small particles— to constrain the fundamental properties of both disks and atmospheres. This dissertation provides evidence that protoplanetary disks are more than an order of magnitude more massive than previously appreciated, that the detailed properties of clouds shape observations of exoplanet atmospheres, and that the physics of modeling clouds gives a new understanding of the solid content and composition in protoplanetary disks.

Clouds on extrasolar worlds are abundant and interfere with observations; however, little is known about their properties. Herein, cloud properties are predicted from first principles and are used to investigate and explain the novel observational properties of hot Jupiters—massive planets close to their host stars. This work describes

the use of clouds in tracing fundamental planetary properties and develops a method for probing non-uniform cloud properties using near-future observations.

The total mass available in protoplanetary disks is a critical initial condition for understanding planet formation, however, the surface densities of protoplanetary disks are largely unconstrained due to uncertainties in the dust-to-gas ratio and carbon monoxide (CO) abundance. In this dissertation, a new set of models (dust-line models) are developed that reconcile theory with observations of protoplanetary disks and create a new set of initial conditions for planet formation models. These models use recent, resolved, multiwavelength observations of disks in the millimeter to constrain the aerodynamic properties of dust grains and infer the total disk mass without an assumed dust surface density or tracer-to-total mass ratio. This work provides a picture of protoplanetary disks where they are significantly more massive than was previously appreciated. These qualitative changes to models of protoplanetary disks thus have significant implications for theories of planet formation; particularly for the important processes where the amount of gas determines the evolution of the solids.

The techniques used in modeling clouds in exoplanet atmospheres are then combined with the dust-line models of protoplanetary disks to show that the observed depletion of CO gas in well-studied disks is consistent with freeze-out processes in a moderately diffusive environment. This new model of ice formation and evolution in disks is able to use existing observations to constrain three crucial parameters that control planetary formation, namely: the solid and gaseous CO inventory at the disk midplane where planets form, the bulk disk diffusivities and mixing characteristics, and

the disk mass–through resolving inconsistencies in estimates of total mass using different tracers.

## Acknowledgments

First, I offer my thanks to my two advisors—Xi Zhang and Ruth Murray-Clay—for their unwavering support and guidance throughout the course of my career in graduate school. When I committed to graduate school at UC Santa Cruz, neither of my advisors were yet hired as professors. I consider the serendipitous events that led to us working together as a great gift from the universe.

Second, I offer my gratitude to my informal mentors and advisors who helped me succeed in a myriad of ways. I would particularly like to thank Peter Gao, Enrico Ramirez-Ruiz, Jonathan Fortney, Vivien Parmentier, Hilke Schilichting, Caroline Morley, Morgan MacLeod, Alexa Villaume, Mickey Rosenthal, Maggie Thompson, Emily Martin, and Maria Hamilton.

To my family and loved ones across the globe, your love and support is a continual source of strength and inspiration. From Singapore to Waco—I love you all!

Finally, my sincerest thanks to Jamie Alexander Powell Law-Smith, without whom I would be lost.

## Published Material

The text of this dissertation includes reprints of the following previously published material, led by myself, with the permission of the listed co-authors and the Astrophysical Journal.

Chapter 2 was published in the literature as Powell et al. (2018). This research was supervised by co-author Xi Zhang. Chapter 3 was published in the literature as Powell et al. (2019a). This research was supervised by co-author Xi Zhang. Chapter 4

was published in the literature as Powell et al. (2017). This research was supervised by co-author Ruth Murray-Clay. Chapter 5 was published in the literature as Powell et al. (2019b). This research was supervised by co-author Ruth Murray-Clay. Chapter 6 is currently submitted and is under review for publication. All of the figures and texts are my own, with feedback and edits from the listed co-authors, except for Section 3.7 which was written by Thomas Louden.

## Scientific Acknowledgments

This dissertation is based on work supported by the National Science Foundation Graduate Research Fellowship under grant DGE1339067, the Ford Foundation under a dissertation year fellowship, and the UC Santa Cruz Regents' Fellowship.

To Jamie.

*oh my God! – it's full of stars!*

*—2001: A Space Odyssey*

# Chapter 1

# Introduction

More than four thousand diverse exoplanets have been detected outside of our solar system, demonstrating that planet formation is a natural manifestation of baryonic matter. An understanding of planet formation and evolution requires an empirical connection between active planet formation and evolved planets. This connection is increasingly possible due to simultaneous revolutions in the observations of protoplanetary disks and exoplanet atmospheres. Protoplanetary disks, the birthplaces of planets, can now be observed with unprecedented angular resolution using facilities like *ALMA*. The atmospheres of several young, giant (directly imaged) planets have been observed using instruments like *GPI* and *VLT Gravity* and the atmospheres of evolved giant planets near their host stars (hot Jupiters) have been probed with high resolution spectroscopy and space-based facilities like *HST*, *TESS*, and *Kepler*. The advent of *JWST* and the extremely large telescopes like the *GMT* will further revolutionize the observational information available in both contexts.

Relating protoplanetary disks to planetary atmospheres is a major goal of astrophysics and planetary science. A crucial step towards relating observations of planetary evolution at different stages is to characterize the fundamental properties of both disks and atmospheres. Determining empirical constraints of the fundamental properties of both protoplanetary disks and exoplanet atmospheres, however, requires the use of sufficiently detailed theoretical models that can meaningfully interpret observations. Constraining the properties of protoplanetary disks has been hindered by a lack of direct observational probes of the total disk mass and the properties of material in the region of the disk where planet formation occurs. In particular, mass estimates based on different tracers often vary significantly, observations of trace gas species typically probe the disk surface layers that do not represent bulk disk properties, and the properties of solid material are largely inaccessible to observations (e.g., Andrews 2020). Constraining the properties of exoplanet atmospheres is often foiled by a lack of understanding of the nature of clouds or other aerosols. Clouds are the dominant source of opacity in most planetary atmospheres where they often obfuscate signatures of planetary properties (e.g., Kreidberg et al. 2014a; Sing et al. 2016).

The work presented in this dissertation uses microphysics—i.e., the physics that governs the evolution of small particles— to constrain the fundamental properties of both disks and atmospheres. This dissertation provides evidence that protoplanetary disks are more than an order of magnitude more massive than previously appreciated, that the detailed properties of clouds shape observations of exoplanet atmospheres, and that the physics of modeling clouds gives a new understanding of the solid content and

composition in protoplanetary disks.

## 1.1 Clouds on Exoplanet Atmospheres

The past decade of exoplanet studies has revealed a great diversity of planets, many with no solar system analogs. For the majority of exoplanets, the most promising avenue to determine their properties is by studying their atmospheres which are accessible to observations. To understand atmospheres, it is essential that we understand clouds, which obfuscate our interpretation of planetary properties by strongly shaping observations of exoplanet atmospheres in transmission, emission, and reflection (Skemer et al. 2014; Sing et al. 2016; Crossfield & Kreidberg 2017). While clouds on extrasolar worlds are abundant and interfere with observations, little is known about their properties. In particular, the microphysical properties of clouds, such as their size distribution (Chapters 2–3), vertical extent (Chapter 2), and composition (Chapter 3), significantly impact interpretations of atmospheric properties.

Herein, cloud properties are predicted from first principles and are used to investigate and explain the novel observational properties of hot Jupiters—massive planets close to their host stars. Hot Jupiters have atmospheres that are often dominated by clouds (e.g., Sing et al. 2016). Retrievals of these atmospheres are significantly impacted by assumed cloud properties such that interpretations of their atmospheric properties and composition are often imprecise (e.g., Taylor et al. 2020). This dissertation contains the development of the first microphysical vertical transport model of cloud formation capable of calculating the size distribution of cloud particles in the atmospheres of hot

Jupiters from first principles (Chapters 2–3). This model has revealed a great richness of information available from the perspective of cloud microphysics and has been used to demonstrate that the cloud particle size distribution is both difficult to predict and dramatically impacts the cloud opacity and observed atmospheric spectra (Chapters 2–3). Importantly, this dissertation shows that the specific microphysical properties of clouds are both highly sensitive to planetary properties and significantly influence atmospheric observables (Chapters 2–3). Excitingly, a consideration of these properties has enabled successful explanations of the observed cloudiness and temperature trends in the well-studied population of hot Jupiters (Gao et al. 2020; Gao & Powell 2021). This work describes the use of clouds in tracing fundamental planetary properties and develops a method for probing non-uniform cloud properties using near-future observations—thus laying the groundwork for detailed characterizations of exoplanet atmospheres.

## 1.2 Ice and Dust in Protoplanetary Disks

One of the strongest constraints on models of planet formation and evolution are the properties of protoplanetary disks, including their total mass (Chapters 4-5), radial composition (Chapter 6), turbulent transport properties (Chapter 6), and the partitioning between the solid and gas phase (Chapter 6).

Traditional methods of determining disk properties rely on significant assumptions, particularly regarding the abundance ratios of tracers of the primary mass constituent, $H_2$ gas, which is not readily observable. The research in this dissertation has shown that typically assumed tracer-to-$H_2$ ratios are often unphysical (Chapters 4,5,6)

and, due to these uncertainties, observations of disk properties using different tracers are often inconsistent or largely unconstrained (Bergin et al. 2013). At the same time, the composition of solids and gas in protoplanetary disks in the planet-forming regions is largely inaccessible to direct observational probes (e.g., Andrews 2020). By primarily focusing on describing the evolution of ice and dust in protoplanetary disks, the research in this dissertation places strong constraints on fundamental disk properties that control planet formation and evolution.

Herein, multiwavelength observations of protoplanetary disks are used to trace the aerodynamic properties of solid particles. These properties are in turn used to infer fundamental protoplanetary disk properties, including their total mass, without assuming an abundance ratio (Chapters 4–5). This work provides a picture of protoplanetary disks where they are significantly more massive than was previously appreciated. These qualitative changes to models of protoplanetary disks thus have significant implications for theories of planet formation; particularly for the important processes where the amount of gas determines the evolution of the solids. This new picture of protoplanetary disks—the dust line model—provides the ideal observationally-validated basis to study the evolution of volatile material in disks.

This dissertation then combines the dust-line models of protoplanetary disks with the microphysical models used to understand clouds in exoplanet atmospheres (Chapters 2–3) to show that the observed severe depletion of carbon monoxide (CO) gas in well-studied disks is consistent with freeze-out processes in a moderately diffusive environment. Together, this modeling constitutes a new global disk model of

non-equilibrium volatile freeze-out and radial transport and successfully explains the observed severe carbon monoxide (CO) gas depletion and the radial distribution of CO gas in the upper layers of the four most well-studied protoplanetary disks. The power of this new model of ice formation and evolution lies in its ability to use existing observations to constrain three crucial disk parameters that control planetary formation, namely: the solid and gaseous CO inventory at the disk midplane where planets form, the bulk disk diffusivities and mixing characteristics, and the disk mass–through resolving inconsistencies in estimates of total mass using different tracers.

## 1.3 Microphysics in Disks and Atmospheres

This dissertation uses four key microphysical processes to characterize large-scale properties of protoplanetary disks and exoplanet atmospheres: particle transport, coagulation, nucleation, and condensation.

In disks, particles are transported inwards towards their host stars over time, known as particle drift, due to aerodynamic drag. In Chapters 4–5, the process of particle drift is used to infer the total mass in disks as well as other key disk properties with minimal *a priori* assumptions. Particles grow via coagulation when collisions in disks occur at low relative velocities. Growth via coagulation is often limited by drift in the outer regions of protoplantary disks and can thus be used to infer properties of the solid particles in disks such as the solid surface density (Chapters 4–5). The processes of nucleation and condensational growth regulate the formation and growth of ice in disks. These processes are used in Chapter 6 to constrain the radial and temporal

compositional distribution of mass in disks.

In atmospheres, particles are transported due to vertical mixing. This transport of particles can dominate observations by determining the size distribution in the upper regions of exoplanet atmospheres as shown in Chapter 3. In Chapters 2–3, the processes of nucleation and condensation are used to create observational strategies that use clouds to uncover fundamental properties of exoplanet atmospheres.

# Chapter 2

# Formation of Silicate and Titanium Clouds on Hot Jupiters

## 2.1 Abstract

We present the first application of a bin-scheme microphysical and vertical transport model to determine the size distribution of titanium and silicate cloud particles in the atmospheres of hot Jupiters. We predict particle size distributions from first principles for a grid of planets at four representative equatorial longitudes, and investigate how observed cloud properties depend on the atmospheric thermal structure and vertical mixing. The predicted size distributions are frequently bimodal and irregular in shape. There is a negative correlation between total cloud mass and equilibrium temperature as well as a positive correlation between total cloud mass and atmospheric mixing. The cloud properties on the east and west limbs show distinct differences that

increase with increasing equilibrium temperature. Cloud opacities are roughly constant across a broad wavelength range with the exception of features in the mid-infrared. Forward scattering is found to be important across the same wavelength range. Using the fully resolved size distribution of cloud particles as opposed to a mean particle size has a distinct impact on the resultant cloud opacities. The particle size that contributes the most to the cloud opacity depends strongly on the cloud particle size distribution. We predict that it is unlikely that silicate or titanium clouds are responsible for the optical Rayleigh scattering slope seen in many hot Jupiters. We suggest that cloud opacities in emission may serve as sensitive tracers of the thermal state of a planet's deep interior through the existence or lack of a cold trap in the deep atmosphere.

## 2.2 Introduction

Observations of exoplanet atmospheres have revealed damped spectral features in transmission—indicating the presence of an optically thick absorber of stellar photons (e.g., Gibson et al. 2012, 2013; Deming et al. 2013; Jordán et al. 2013; Line et al. 2013; Mandell et al. 2013; Sing et al. 2011, 2013; Schlawin et al. 2014; Fukui et al. 2014; Mallonn & Strassmeier 2016; Mallonn et al. 2016; Louden et al. 2017). This damping of spectral features has been attributed to the presence of clouds and hazes and is observed in a variety of exoplanets with well-characterized atmospheres (e.g., Crossfield et al. 2013; Kreidberg et al. 2014b; Knutson et al. 2014b,a; Fraine et al. 2013; Sing et al. 2016; Iyer et al. 2016). Further studies of infrared phase curves reveal nightside emission that can be readily explained by the presence of clouds (e.g., Wong et al. 2016;

Stevenson et al. 2017).

While clouds appear to be pervasive on exoplanets, the properties of these clouds can vary substantially for planets that are seemingly quite similar (e.g., Sing et al. 2016; Mendonça et al. 2018). An understanding of cloud properties, such as particle size distribution and composition is necessary to correctly interpret current and future observations. Hot Jupiters in particular have a comparative wealth of atmospheric data as they are relatively good targets for transmission spectroscopy. However, a thorough understanding of these planets requires a theoretical understanding of the clouds present in their atmospheres. Theoretical techniques will be particularly necessary in furthering our understanding of exoplanetary atmospheres with the advent of exquisite observational datasets from JWST (Greene et al. 2016). It will be invaluable for observational programs to have a detailed theoretical framework able to give insight into an atmosphere's cloud properties before observation. The framework presented in this work is necessary for such theoretical insights.

### 2.2.1 Previous Studies

Previous studies have shown that condensational cloud and photochemical haze properties are strongly dependent on detailed planetary properties such as atmospheric irradiation, chemical composition, and dynamics (e.g., Kreidberg et al. 2014b). The properties of clouds and hazes can further vary with composition and first order formation mechanisms, for instance, clouds that nucleate homogeneously, clouds that form efficiently only in the presence of seed particles, and hazes that form via photochem-

istry. Each of these factors influences the particle size distribution, which in turn has an influence on the inferences made from observations (e.g., Han et al. 2005; Ebert & Curry 1992; Zhang et al. 1999).

Solar system observations, especially in-situ measurements on Earth, have further shown that there are multiple modes in the cloud particle size distribution and that these modes vary throughout the atmosphere (e.g., Korolev 1994; Carbary et al. 2004). Recently, simple bimodal particle size distributions have been proposed to interpret certain exoplanet observations as well (e.g., Pont et al. 2013). Multi-modal particle distributions tend to form due to differences in particle composition and formation process. Thus, while there are some indications of trends in cloud properties with equilibrium temperature/stellar irradiation (Stevenson 2016; Heng 2016; Parmentier et al. 2016; Barstow et al. 2017), this remains a complex problem that requires a detailed understanding of cloud formation and related processes.

There are several different forward and retrieval modeling techniques that are currently used to understand atmospheric properties despite the observational limitations imposed by the presence of clouds (Morley et al. 2013; Lee et al. 2015a, 2016; Marley et al. 2012; Parmentier et al. 2013; Helling et al. 2008a,b; Lavvas & Koskinen 2017). Each of these previous works rely on one of three ways of understanding and parameterizing cloud properties: equilibrium cloud condensation modeling, grain chemistry (a subset of the larger field of cloud microphysics), or microphysical modeling of the coagulation of photochemical hazes.

Equilibrium cloud condensation models use thermochemical equilibrium argu-

ments to determine a planet's atmospheric composition and whether or not a certain species will energetically favor condensation and cloud formation. The vertical distribution of the resultant cloud particles can then be determined through a consideration of parameterized cloud particle sedimentation balanced by lofting due to vertical mixing (Ackerman & Marley 2001). This technique has been applied extensively to interpret observations of brown dwarfs and exoplanets (e.g., Saumon et al. 2012; Morley et al. 2012, 2013, 2015) and has been applied to hot Jupiters in 3D by Parmentier et al. (2013) to investigate the potential for a day-night cold trap to deplete TiO on the dayside of HD 209458b. A simplified version of this model was further used in Parmentier et al. (2016) to show that transitions in cloud composition as a function of effective temperature can explain the observed variations in Kepler exoplanet light curves. Simplified work in this vein has shown that the chosen size distribution has a distinct effect on the resulting spectra and that, for log-normal distributions, the largest particles in the distribution dominate the cloud's spectral contribution (Wakeford & Sing 2015). By assuming that clouds are responsible for the Rayleigh scattering slope observed in the optical spectra of hot Jupiters, Wakeford & Sing (2015) further predict the presence of a distinct silicate feature in the infrared that may be observable using JWST.

Grain chemistry microphysical cloud models treat cloud formation from a kinetics approach where both the growth and diminishment of cloud particles proceed via heterogeneous chemical reactions on the surface of grains. Recent work has additionally considered the impact of plasma physics on dust evolution in substellar atmospheres (Stark & Diver 2017). This framework was originally developed in great detail for

brown dwarf atmospheres (Helling et al. 2001, 2004, 2008a,b; Woitke & Helling 2003, 2004; Helling & Woitke 2006; Witte et al. 2009, 2011) and has since been applied to hot Jupiter atmospheres and extended to 3D (Lee et al. 2015a, 2016; Helling et al. 2016). In this approach the cloud formation process is typically assumed to begin with the formation of $TiO_2$ seed particles in the upper atmosphere that settle downwards and act as sites of cloud formation for species such as $MgSiO_3$, $Mg_2SiO_4$, $SiO_2$, $Al_2O_3$, and Fe. These models have been used to study brown dwarf emission spectra (Witte et al. 2011), and have shown that a vertical gradient in cloud composition likely exists in brown dwarf atmospheres and in the atmospheres of comparable hot exoplanets. Recent work in 3D for hot Jupiters has further shown that two well studied and representative planets, HD 189733b and HD 209458b, could possess clouds in their atmospheres comprised of the same species thought to exist on brown dwarfs (Lee et al. 2015a, 2016). This recent work also uncovers vertical and latitudinal variations in cloud composition due to atmospheric dynamics and global temperature differences. The model of HD 189733b was shown to have a deeper cloud deck in comparison to HD 209458b, consistent with the presence of more pronounced molecular features in its transmission spectra.

An initial study of the coagulation of photochemical hazes in the upper atmospheres of hot Jupiters has shown that a consideration of these small lofted particles can reproduce the observed transmission spectra of HD 189733b (Lavvas & Koskinen 2017). In this model, haze particles are injected into the top of the atmosphere and are allowed to coagulate. In particular, this work has successfully reproduced the Rayleigh slope at short wavelengths.

Each of these three methods of modeling clouds in extrasolar atmospheres has advantages and disadvantages. Equilibrium cloud condensation models are not computationally intensive and can therefore be easily coupled with other atmospheric models. This technique, however, does not include the physical processes that govern cloud formation—namely the processes of nucleation, condensational growth, and evaporation, each with distinctive timescales and dependancies on planetary properties. The lack of detailed microphysics therefore limits the predictive power of this approach. Furthermore, these models require an assumed size distribution of cloud particles, which may skew inferences from observations.

Grain chemistry models are highly detailed and have built-in chemistry calculations. However, these models can be difficult to generalize due to their reliance on specific nucleation pathways for cloud formation. These models adopt the moment method in numerics that requires a prescribed shape of the particle size distribution. In other words, these models are not able to predict the particle size distribution from first principles. Furthermore, this approach does not consider the influence of saturation vapor pressure over the particle surface due to particle curvature (the Kelvin effect) and particle mixture (the Raoult effect) (Seinfeld & Pandis 2006), both of which can alter the resultant cloud properties.

Modeling of photochemical haze properties via coagulation can be used to determine the fully resolved haze particle size distribution. However, current work in this approach does not consider interaction with background gases via nucleation, condensational growth and evaporation. Once considered, these processes may have a

substantial impact on the predicted size distributions.

### 2.2.2 A New Modeling Framework

In order to resolve the cloud particle size distribution from first principles we need a model that relies on bin-scheme microphysics. In this work we present the first model of cloud formation on hot Jupiters from the perspective of bin-scheme cloud microphysics. This approach was pioneered on Earth where water clouds form primarily via heterogeneous nucleation and then evaporate or grow through condensation or coagulation (e.g., Pruppacher & Klett 1978). The microphysical processes of nucleation, growth, evaporation, and coagulation have been applied to every planetary body in the solar system with a substantial atmosphere. In particular, bin-scheme microphysics has been used to reproduce and understand observations of sulfuric acid clouds on Venus (e.g., Gao et al. 2014), $CO_2$ and water clouds on Mars (e.g., Michelangeli et al. 1993; Colaprete et al. 1999), hydrocarbon clouds and hazes on Titan (e.g., Barth & Toon 2003, 2004, 2006; Lavvas et al. 2010, 2011), and hydrocarbon hazes on Pluto (e.g., Gao et al. 2017).

In the bin scheme approach, the particle size distribution is discretized into multiple bins according to size. Each bin of particles evolves freely and interacts with other bins. Therefore, there is no a-priori assumption of the particle size distribution. Bin-scheme microphysics is widely used in cloud formation models of Earth's atmosphere and is able to reproduce the multi-modal distributions of cloud particles.

We use the one dimensional Community Aerosol and Radiation Model for Atmospheres (CARMA; Turco et al. 1979a; Toon et al. 1988) to conduct a detailed

parameter space study of titanium and silicate clouds on hot Jupiters taking into account cloud microphysics. CARMA models the processes that govern cloud formation from first principles and therefore allows us to not only determine cloud properties for a wide range of parameters but also to test the assumptions used in other cloud modeling efforts. CARMA, like grain chemistry modeling, treats cloud formation as a kinetics process. Thus particle formation and growth in CARMA also depends on how long it takes for the condensate molecule, or some rate limiting precurser (e.g., SiO in MgSiO3), to diffuse to the particle. In this work we calculate cloud properties for four representative locations along the equator of hot Jupiters (the substellar point, east limb, antistellar point, and west limb) as these planets are three-dimensional with atmospheric thermal profiles that vary with location.

Our approach can be applied to the wealth of condensates that have been hypothesized to exist in hot Jupiter atmospheres by chemical equilibrium modeling (Burrows & Sharp 1999; Lodders 2002). We choose $MgSiO_3$ and $TiO_2$ as our cloud species for this initial survey because silicate clouds are one of the more optically thick condensates (Wakeford & Sing 2015) and titanium is thought to often condense in hot Jupiter atmospheres with equilibrium temperatures less than $\sim$ 2000 K (Fortney et al. 2008; Parmentier et al. 2016; Wakeford et al. 2017) which is supported by a dearth of observed atmospheric TiO features (e.g., Sing et al. 2016). Titanium clouds may also nucleate more easily than silicate clouds and could thus be a condensation nuclei for the growth of other cloud species.

In Section 2.3, we give an overview of the theory used in our cloud model. In

Section 2.4, we discuss our model and computational setup in detail. In Section 2.2, we introduce characteristic timescales of relevant processes in our model. In Section 2.6, we discuss the results of our model grid and place these results in context. In Section 5.1, we discuss observational implications. We provide several conclusions and summarize our work in Section 2.8.

## 2.3 Theory

The universality of the microphysical processes handled by CARMA makes it a powerful tool that can simulate virtually any condensate in any atmosphere, provided certain physical properties are known. While the processes of microphysics are well studied, this work constitutes one of the first instances in which they have been applied to exoplanet atmospheres. We therefore provide a brief overview of the relevant processes and how they impact the formation of clouds in our model. For the specific equations that govern all of these processes in CARMA please see Gao et al. (2018) Appendix A.

### 2.3.1 Overview of Cloud Microphysics

Essential microphysical processes of cloud formation include nucleation, condensation, evaporation and coagulation. Nucleation refers to the initial phase change of a gaseous species to a solid or liquid state that starts the cloud formation process. Nucleation can occur either homogeneously or heterogeneously depending on the energy barrier associated with the process and the availability of seeds or cloud condensation

nuclei (CCN). CCN may take many forms, such as meteorite dust, photochemical hazes, or other cloud species (e.g., Lee et al. 2018). The associated energy barrier depends on the atmospheric conditions as well as the specific properties of a species—in particular its surface tension and molecular weight. It is easier for species with low surface tension and molecular weight to form homogeneously than species with high surface tension and molecular weight. Heterogeneous nucleation—the nucleation of one species onto a different species in either a solid or liquid state—tends to occur more efficiently than homogeneous nucleation when there are abundant seeds and if these seeds are favorable surfaces for the condensing species to nucleate on which further depends on the contact angle between the two species. In this work we treat the contact angle parameter as a nucleation efficiency parameter, similar to sticking efficiency in growth calculations, as it is otherwise not well known. In particular, we assume a low contact angle ($\sim 0.1°$), therefore providing an upper limit on cloud formation.

Heterogeneous nucleation is the favored pathway for cloud formation in the case of water clouds on Earth (e.g., Pruppacher & Klett 1978), $CO_2$ clouds on Mars (Michelangeli et al. 1993; Colaprete et al. 1999), ethane clouds on Titan (Barth & Toon 2003, 2004, 2006), and sulfuric acid clouds on Venus (e.g., Gao et al. 2014). Homogeneous nucleation, while less common in the solar system, is the favored pathway for the formation of high altitude water ice clouds on Earth (e.g., Jensen & Ackerman 2006).

Once nucleation has occurred, the processes of condensational growth or evaporation can occur. Condensational growth allows a cloud particle to grow larger by many

orders of magnitude. The pressure difference between the ambient gas pressure and the saturation pressure over the particle surface the driving force of both condensation and evaporation. Thus, many factors (such as temperature, curvature, and composition) could complicate the condensation and evaporation processes that fundamentally influence the final particle size distribution (e.g., Zhang et al. 2012).

Cloud particles are also free to undergo coagulation, commonly modeled as Brownian coagulation on small scales and controlled by the random collisions among particles (see **?**, for the implementation used in CARMA). We note that coagulation has been shown to play an important role in the evolution of photochemical hazes on Titan (e.g., Lavvas et al. 2010) and may be important in the evolution of high altitude photochemical hazes on hot Jupiters if haze is produced with an efficiency similar to that for Jupiter or Titan (Lavvas & Koskinen 2017). However, given the relatively low number densities of large particles produced in our modeling, coagulation does not significantly change the resultant particle size distributions when fully included in our modeling procedure. The effect of coagulation has been tested in all simulations presented in this work. We therefore focus on the three dominant processes of nucleation, condensation, and evaporation throughout this work.

### 2.3.2 Governing Equations for Nucleation and Growth

We apply classical theories of homogenous and heterogeneous nucleation to compute the rates of cloud particle generation (Pruppacher & Klett 1978; Lavvas et al. 2011). For homogenous nucleation the rate, in units of new particles per volume per

unit time is,

$$J_{\text{hom}} = 4\pi a_c^2 \Phi Z n \exp(-F/kT), \tag{2.1}$$

where $n$ is the number density of condensible vapor molecules, $k$ is the Boltzmann constant, and $T$ is temperature. The critical particle radius, $a_c$, is given by

$$a_c = \frac{2M\sigma_s}{\rho_p RT \ln S} \tag{2.2}$$

where $M$, $\sigma_s$, $\rho_p$, and $S$ are the molecular weight, surface tension, mass density, and saturation ratio of the condensible species. $R$ is the universal gas constant. The energy of formation, $F$, is defined as

$$F = \frac{4}{3}\pi\sigma_s a_c^2. \tag{2.3}$$

The rate of diffusion of vapor molecules to the forming particle, $\Phi$, in units of g cm$^{-2}$ s$^{-1}$ is given by

$$\Phi = \frac{p}{\sqrt{2\pi mkT}}, \tag{2.4}$$

where $p$ is the the partial pressure of the condensate vapor and $m$ is the mass of the vapor molecule. The inverse dependence on mass means that more massive molecules diffuse more slowly through the background gases. The Zeldovich factor, $Z$, takes into account non-equilibrium effects (such as the evaporation of newly formed particles) and is given by

$$Z = \sqrt{\frac{F}{3\pi kT g_m^2}}, \tag{2.5}$$

where $g_m$ is the number of molecules in particles of radius $a_c$.

The rate of heterogeneous nucleation, in units of critical germs per condensation nucleus, is given by,

$$J_{\rm het} = 4\pi^2 r_{\rm CN}^2 a_c^2 \Phi c_{\rm surf} Z \exp(-Ff/kT), \tag{2.6}$$

where $r_{\rm CN}$ is the radius of the condensation nuclei. The shape factor, $f$, is defined as

$$2f = 1 + \left(\frac{1-\mu x}{\phi}\right)^3 + x^3(2 - 3f_0 + f_0^3) + 3\mu x^2(f_0 - 1), \tag{2.7}$$

where $\mu$ is the cosine of the contact angle between the condensible species and the nucleation surface, $x = r/a_c$, $\phi = \sqrt{1 - 2\mu x + x^2}$, and $f_0 = (x - \mu)/\phi$. The number density of condensate molecules on the nucleating surface, $c_{\rm surf}$, is given by

$$c_{\rm surf} = \frac{\Phi}{\nu} \exp(F_{\rm des}/kT), \tag{2.8}$$

where $\nu$ is the oscillation frequency of the absorbed molecules on the nucleation surface, and $F_{\rm des}$ is the desorption energy of that molecule. **?** gives a brief overview of typical $\nu$ and $F_{\rm des}$ for different materials, however, the values for silicate clouds on titanium is not known. We therefore choose values typically chosen for water ($\nu = 10^{13}$ Hz, $F_{\rm des} = 0.18$ eV), which Lavvas et al. (2011) also used for hydrocarbons on tholin. To convert $J_{\rm het}$ to units of newly nucleated particles per volume per time this quantity needs to be

multiplied by the number of condensation nuclei.

The growth calculation in CARMA takes into account the diffusion of condensate particles to and away from the cloud particle, latent heat release, and several additional effects (see **?** and Jacobson et al. (1994) for a full derivation of this process). The complete growth equation is defined as

$$\frac{dm_p}{dt} = \frac{4\pi r D' p_s (S - A_k)}{\frac{RT}{MF_v} + \frac{D' M L^2 p_s}{k'_a R T^2 F_t}}, \tag{2.9}$$

where $r$ is the size of the cloud particle, $p_s$ is the saturation vapor pressure of the condensate, $M$ is the condensate mean molecular weight, and $L$ is the latent heat of evaporation of the condensate. The ventilation factors, $F_v$ and $F_t$, account for the air density variations around a particle as it sediments in an atmosphere (Toon et al. 1989; Lavvas et al. 2011). Note that the growth rate is directly proportional to particle size.

The Kelvin factor, $A_k$, takes into account the curvature of a particle's surface and is given by

$$A_k = \exp\left(\frac{2M\sigma_s}{\rho_p RTr}\right). \tag{2.10}$$

The molecular diffusion coefficient of the condensate vapor through the atmosphere, $D'$, and the thermal conductivity of the atmosphere, $k'_a$, are modified to account for gas kinetics near the particle surface and are defined as

$$D' = \frac{D}{1 + \lambda K n^c} \tag{2.11}$$

$$k'_a = \frac{k_a}{1 + \lambda_t K n_t^c}, \tag{2.12}$$

where $\lambda$ and $\lambda_t$ are defined as

$$\lambda = \frac{1.33 K n^c + 0.71}{K n^c + 1} + \frac{4(1 - \alpha_s)}{3\alpha_s} \tag{2.13}$$

$$\lambda_t = \frac{1.33 K n_t^c + 0.71}{K n_t^c + 1} + \frac{4(1 - \alpha_t)}{3\alpha_t} \tag{2.14}$$

where $\alpha_s$ is the sticking coefficient and $\alpha_t$ is the thermal accommodation coefficient, which are both assumed to be order unity. The Knudsen numbers of the condensing gas with respect to the particle, $Kn^c$ and $Kn_t^c$, are given by

$$K n^c = \frac{3D}{r}\sqrt{\frac{\pi M}{8RT}} \tag{2.15}$$

$$K n_t^c = \frac{K n^c k_a}{r D \rho_a (C_p - \frac{R}{2\mu_a})} \tag{2.16}$$

where $C_p$ is the heat capacity of the particle, $\rho_a$ is the atmospheric mass density, and $\mu_a$ is the atmospheric mean molecular weight.

### 2.3.3 Condensible Species

For the purposes of this study, we consider the condensation of two species: $MgSiO_3$ and $TiO_2$. We note that many species are thought to condense at temperatures

of $\sim$ 1000 - 2000 K. In particular, chemical equilibrium calculations show that other condensates such as $Ti_2O_3$, $Ti_3O_5$, $MgAl_2O_4$, $Mg_2SiO_4$, and $CaTiO_3$, among many others, may exist (Burrows & Sharp 1999; Lodders 2002). We leave the investigation of other relevant cloud species to future work and instead focus on the wealth of information that can be understood more intuitively through the modeling of two species.

We choose $MgSiO_3$ because it is one of the most abundant cloud species in equilibrium cloud condensation modeling (Wakeford et al. 2017), evidence of silicate grain absorption has been observed on brown dwarfs (e.g., Cushing et al. 2006; Burgasser et al. 2008; Looper et al. 2008), and has a signature that could be seen with JWST/MIRI (Wakeford & Sing 2015). $MgSiO_3$ has been proposed as a candidate for the Rayleigh scattering slope observed in transmission spectra due to its strong scattering properties (see Section 2.7.3; Lecavelier Des Etangs et al. 2008) though recent modeling of silicate clouds has called such assertions into question (Lee et al. 2017). We further use $MgSiO_3$ as a proxy for both $Mg_2SiO_4$ and $MgSiO_3$ as their optical properties are very similar, making them observationally difficult to distinguish (Wakeford & Sing 2015), and because the reduced stoichiometry of $MgSiO_3$ makes its modeling more straightforward.

We further consider the condensation of titanium in the form of $TiO_2$. We primarily consider $TiO_2$ due to its low surface tension, as explained in Section 2.3.5. Titanium clouds are also appropriate candidate species because thermal inversions caused by TiO absorption (Burrows et al. 2007b; Fortney et al. 2008) have not been observed in the majority of hot Jupiter atmospheres, suggesting that the titanium may have con-

densed out (Spiegel et al. 2009; Parmentier et al. 2013; Sing et al. 2016). Indeed, TiO has only been observed for hot Jupiters with $T_{eq} > 2100$ K (Haynes et al. 2015; Evans et al. 2016; Sedaghati et al. 2017), in line with theoretical predictions from Fortney et al. (2008). As such, we only consider cooler planets in this work.

### 2.3.4 Assumptions Regarding Cloud Formation and Evolution

Titanium and silicate clouds likely form via two different pathways. Titanium clouds are thought to commonly form via the following reaction:

$$TiO_2 = TiO_2(s), \tag{R1}$$

(Helling & Woitke 2006). This reaction is a Type I reaction following the reasoning in Helling & Woitke (2006) which is analogous to a gaseous molecule directly nucleating onto a grain. The seemingly direct nucleation and condensation of $TiO_2$ gas into solid $TiO_2$ cloud particles is well suited to modeling using classical nucleation and condensation theories without further assumptions. In our modeling we simply assume that all atmospheric Ti is located in condensible gaseous $TiO_2$.

Modeling the formation and evolution of silicate clouds requires additional assumptions due to uncertainties regarding their formation mechanism. We therefore adopt a simplified model for silicate clouds following classical formation theories. $MgSiO_3$ clouds are thought to form via the following reaction:

$$Mg + 2H_2O + SiO = MgSiO_3(s,l) + 2H_2, \tag{R2}$$

(Visscher et al. 2010). In reality, it is likely that the three gases (Mg, $H_2O$, and SiO) will diffuse to the surface of a particle where they will undergo a reaction leading to nucleation or condensational growth. This is a Type III reaction in Helling & Woitke (2006), in which multiple gaseous species are involved. Following Helling & Woitke (2006) Appendix B, we specify a key species (or educt) in the reaction, typically the least abundant species among the reactant molecules, that drives the surface reaction and growth (Helling & Woitke 2006). For Equation R2, we choose SiO, as it is both the least abundant species assuming a solar composition gas (Lodders 2003) among the three molecules, and the heaviest, meaning that it takes the longest time to diffuse to the growing cloud particles. We then assume that the cloud formation process is driven by the key species, SiO, such that $MgSiO_3$ cloud formation occurs when the partial pressure of SiO exceeds its equilibrium vapor pressure over $MgSiO_3$. Additionally, the formation of $MgSiO_3$ does not occur until an SiO molecule diffuses to the grain.

Assuming a key species allows us to determine a reaction supersaturation ratio for silicate cloud formation that approximates formation via grain chemistry, defined as

$$S_r = S^{1/v_r^{\text{key}}}, \tag{2.17}$$

where $S_r$ is the reaction supersaturation ratio which gives the ratio of the growth and evaporation rates, $S$ is the standard supersaturation ratio, and $v_r^{\text{key}}$ is the stoichiometric factor of the key species in the reaction (Helling & Woitke 2006). As our key species has a stoichiometric factor of unity, the reaction supersaturation ratio is the same as the standard supersaturation ratio. Finally, we assume that all atmospheric Si is present

in the form of SiO. As this assumption tends to be roughly correct compared to actual elemental abundances to within an order of magnitude (Visscher et al. 2010) we leave changes in abundance with temperature and additional cloud species to future work. Under these assumptions, classical nucleation and condensation theory can be used to approximate the microphysics of silicate cloud formation.

These assumptions and our general modeling scheme are not only similar to the scheme detailed in Helling & Woitke (2006), but are also analogous to earlier modeling of the formation of silicate dust in supernova remnants and stellar outflows (e.g., Todini & Ferrara 2001). More recent and detailed quantum chemistry calculations in the kinetic (as opposed to diffusive) regime have shown that actual nucleation rates may be suppressed at some temperatures and pressures and enhanced at high pressures compared to classical nucleation theory (Mauney & Lazzati 2018). However, modeling at this level of detail is computationally expensive and outside of the scope of this work. We therefore adopt the above assumptions as a first step in understanding the formation of these complex clouds.

Finally, we do not consider radiative feedback of the clouds on the background atmospheric temperature structure and instead leave these calculations for future work.

### 2.3.5 Surface Tension and the Kelvin Effect

Our CARMA setup relies on the assumption that molecules react kinetically to form a species that can then nucleate or condense onto a cloud. This cloud microphysics approach, in which a condensible species forms and then nucleates or condenses onto a cloud, depends on the surface tension of each specific condensible species.

In particular, the nucleation and condensation rates scale exponentially with surface tension to the third power (see Section 2.3.2) such that species with larger surface tensions rarely nucleate homogeneously when CCN are present.

The surface tension of a species also governs its behavior with regard to heterogeneous nucleation and growth through the Kelvin effect, as described by the Kelvin equation

$$\ln \frac{p}{P_{\text{sat}}} = \frac{2\sigma V_{\text{m}}}{rRT}, \tag{2.18}$$

where $p$ is the vapor pressure over the particle surface, $P_{\text{sat}}$ is the saturation vapor pressure over a flat surface, $\sigma$ is the surface tension, $V_{\text{m}}$ is the molar volume, $r$ is the particle radius, $R$ is the universal gas constant, and $T$ is the temperature.

Due to the Kelvin effect, the vapor pressure over the particle surface is larger than that on a flat surface and the effect depends on both surface tension and particle radius. For species with low surface tension the Kelvin effect is small, while for species with large surface tensions the Kelvin effect plays a role in the species's behavior with regards to growth and nucleation. The Kelvin effect causes species with large surface tensions to only heterogeneously nucleate or condense efficiently onto relatively large CCN or cloud particles with less curved surfaces. Furthermore, the Kelvin effect causes small particles to evaporate and large particles to grow with relative ease.

$TiO_2$ has a surface tension of 480 erg $cm^{-2}$ (Lee et al. 2015b) which is low enough for homogeneous nucleation to occur efficiently in our modeling. The low surface tension value also means that $TiO_2$ clouds are less susceptible to the Kelvin effect such

that small cloud particles are less likely to evaporate once formed. $TiO_2$ can therefore produce both cloud particles and CCN that act as nucleation sites for other cloud species.

The surface tension of magnesium silicate clouds is roughly 1280 erg $cm^{-2}$, measured in its solid state (de Leeuw et al. 2000, for $Mg_2SiO_4$, where we assume the same value for $MgSiO_3$). In our simulations of hot Jupiters we find that the supersaturation required for these clouds to homogeneously nucleate is extremely large. Therefore, if these clouds are abundant in hot Jupiter atmospheres, as suggested by equilibrium cloud condensation modeling, then their preferred method of formation must rely on heterogenous nucleation. We are thus forced to assume some form of CCN upon which heterogeneous nucleation can occur. For the purposes of this study, $TiO_2$ cloud particles act as the CCN. We note, however, that for $MgSiO_3$ cloud particles, growth is very efficient such that the Kelvin effect plays an insignificant role in determining the resultant cloud properties in our current modeling other than requiring silicate clouds to nucleate heterogeneously. This is because, regardless of the size of the initial CCN and evaporation of newly formed small cloud particles, silicate clouds will grow to roughly the same end size.

### 2.3.6 Transport Processes

Cloud particles are transported vertically in an atmosphere through the processes of gravitational settling and vertical mixing. Gravitational settling transports particles that form in the upper atmosphere to the lower atmosphere where they evaporate. Gravitational settling is modeled as Stokes fall velocity with a modifying Cun-

ningham slip correction factor (e.g., Seinfeld & Pandis 2006).

Turbulent vertical mixing in an atmosphere tends to decrease vertical gradients and smooth out inhomogeneities. Vertical mixing transports both gas and particles upward or downward depending on their relative mixing ratios. On hot Jupiters, the vertical mixing due to global circulation that consists of both upwellings and downwellings acts like a vertical diffusion process when globally averaged in a one-dimensional context (Parmentier et al. 2013; Zhang & Showman 2018b). Vertical mixing in atmospheres is therefore often parameterized using a diffusion coefficient, $K_{zz}$, which encapsulates all vertical transport processes in an atmosphere such as vertical advection and vertical wave mixing. As recently demonstrated in Zhang & Showman (2018b), the global-mean eddy mixing on hot Jupiters should depend on the large-scale circulation strength, horizontal mixing and local cloud tracer sources and sinks due to microphysics. When $K_{zz}$ is large, an atmosphere is well mixed and diffusive transport is of increased importance.

A $K_{zz}$ profile cannot be directly derived from vertical velocities from 3D general circulation models without careful consideration of tracer transport as doing so results in an overestimated diffusivity (Parmentier et al. 2013). Zhang & Showman (2018b) use a 3D GCM for hot Jupiters to show that different gaseous chemical species might have different eddy diffusion profiles, however, previous work in 3D from Parmentier et al. (2013) has demonstrated that the $K_{zz}$ parameter operates similarly for cloud particles of a broad range of sizes.

### 2.3.7 Atmospheric Cold Traps

An atmospheric "cold trap" can occur where the process of gravitational settling dominates the upward vertical mixing such that cloud particles rapidly settle after formation. In an atmosphere with a strong cold trap we expect to see the majority of cloud particles at the cloud base. This occurs because any cloud particles that form at higher altitudes will eventually settle downwards. At the same time, any gas that is vertically mixed upwards will first become supersaturated near the cloud base and will form clouds before reaching the upper atmosphere.

If a species can become supersaturated at two points (i.e., the pressure and temperature profile crosses the condensation curve for a species at two points) in the atmosphere then it is possible for two cold traps to form. In this case, the lower cold trap is referred to as a "deep cold trap". The deep cold trap may limit cloud formation in the upper atmosphere, therefore altering several atmospheric observables (e.g., Parmentier et al. 2013, 2016). Thus, the properties of clouds in the upper atmosphere can give insight into both the atmospheric vertical mixing and the deep thermal structure of a planet.

In this paper we will determine the presence or lack of deep cold traps in an atmosphere as a way to understand how atmospheric observables may give insight into underlying planetary properties.

## 2.4 Modeling Approach

We adapt the Community Aerosol and Radiation Model for Atmospheres (CARMA; Turco et al. 1979a; Toon et al. 1988) version 3.0 (Bardeen et al. 2008, 2010) for the study of titanium and silicate clouds on hot Jupiters. We describe our model setup and adjustments to the base model in Section 2.4.1. For a more comprehensive discussion of the microphysics and history of CARMA see Gao et al. (2018) or Turco et al. (1979a), Toon et al. (1988) and Jacobson et al. (1994).

### 2.4.1 Model Setup

CARMA determines the quantitative effects of physical processes on cloud particle concentrations by solving a particle continuity equation. The processes included in our calculations are nucleation (both homogenous and heterogeneous), condensation and evaporation, sedimentation, and diffusion. The following continuity equation corresponds to these processes:

$$\frac{\partial n}{\partial t} = \left.\frac{\partial n}{\partial t}\right|_{\text{nuc.}} + \left.\frac{\partial n}{\partial t}\right|_{\substack{\text{growth} \\ \text{or evap.}}} + \left.\frac{\partial n}{\partial t}\right|_{\text{sed.}} + \left.\frac{\partial n}{\partial t}\right|_{\text{diff.}}, \tag{2.19}$$

where $n$ is the cloud particle concentration, defined as $n(r, z, t)$ where $ndr$ is the number of cloud particles per volume of atmosphere at height $z$ with radii that range from $r$ to $r + dr$ at time $t$. The units of $n$ are particles cm$^{-3}$ $\mu$m$^{-1}$. A detailed discussion of each of these terms can be found in the appendix of (Gao et al. 2018) and is briefly discussed in Section 2.3.

Table 2.1: Model Parameters

| | Nominal Model | Other Values Used |
|---|---|---|
| Surface Gravity | 1000 cm $s^{-2}$ | |
| Atmospheric Mole. Wt. | 2.2 g $mol^{-1}$ (H/He) | |
| Condensable Mole. Wt. | 79.866 g $mol^{-1}$ ($TiO_2$) | |
| | 100.3887 g $mol^{-1}$ ($MgSiO_3$) | |
| $TiO_2$ Surface Tension | 480 erg $cm^{-2}$ (Lee et al. 2015b) | |
| $MgSiO_3$ Surface Tension | 1280 erg $cm^{-2}$ (de Leeuw et al. 2000) | |
| T-P Profiles | Figure 2.1 (top panel) | Figure 2.1 (bottom panel) |
| Diffusion Coefficient ($K_{zz}$) | $5\times10^8/\sqrt{P_{bar}}$ $cm^2$ $s^{-1}$ | $5\times10^7/\sqrt{P_{bar}}$ |
| | | $5\times10^9/\sqrt{P_{bar}}$ $cm^2$ $s^{-1}$, |
| | $5\times10^8$ below 1 bar | $5\times10^7$ and $5\times10^9$ below 1 bar |
| Time Step | 100 s | |
| Total Simulation Time | $10^9$ s | |
| Mass Ratio Between Bins | 2 | |
| Number of Bins | 75 | |
| Smallest Bin Size | 1 nm | |
| Largest Bin Size | 264 $\mu$m | |
| **Boundary Conditions** | | |
| Clouds (Top) | Zero Flux | |
| Condensation Nuclei (Top) | Zero Flux | |
| $MgSiO_3$ 'Gas' (Top) | Zero Flux | |

Table 2.1 (cont'd): Model Parameters

| | Nominal Model | Other Values Used |
|---|---|---|
| Clouds (Bottom) | 0 $cm^{-3}$ | |
| Condensation Nuclei (Bottom) | 0 $cm^{-3}$ | |
| $TiO_2$ Gas (Bottom) | Solar Abundance of Ti<br>$10^{-7.08}$ $n_H$ (Lodders 2003) | |
| SiO Gas (Bottom) | Solar Abundance of Si<br>$10^{-4.46}$ $n_H$ (Lodders 2003) | |

As noted before, CARMA operates using a bin scheme for particle microphysics where particle size is discretized into multiple bins that evolve freely and interact with other bins; this means that there is no a-priori assumption regarding the particle size distribution.

We discuss our adaptation of CARMA to hot Jupiters in Sections 2.4.1 - 2.4.2. A summary of the relevant model parameters can be found in Table 3.1.

**Saturation Vapor Pressures of Condensible Species**

For $TiO_2$, which exists in the gas phase, we use the saturation vapor pressure formula from Woitke & Helling (2004). In Equation 2.20 we rewrite this formula in approximate form with pressure units of bar and temperature in Kelvin assuming solar metallicity of Ti which is contained in gaseous $TiO_2$.

$$P_{\rm sat} = 10^{(9.5489-(32450.8451/T))} \tag{2.20}$$

The condensation curves for each species are shown in comparison to the planetary pressure and temperature profiles in Figure 2.1 for the high and low entropy cases (described below).

For $MgSiO_3$ we derive a condensation curve from Visscher et al. (2010) to calculate the saturation vapor pressure assuming that the limiting species for cloud formation is SiO. Condensation will occur when the partial pressure of SiO exceeds its equilibrium vapor pressure over $MgSiO_3$ (cf. Table 3 in Visscher et al. 2010). We assume that all of the silicate in the atmosphere is locked up in SiO and use this to derive a partial pressure. The calculated condensation curve is given in Equation 2.21, where [Fe/H] is the metallicity (which we take to be solar), and the saturation vapor pressure is given in Equation 2.22. In both equations pressure is in units of bar and temperature is in Kelvin.

$$T(P_{\rm total}) = \frac{10^4}{6.24 - 0.35\log_{10}(P_{\rm total}) - 0.7[{\rm Fe/H}]} \tag{2.21}$$

$$P_{\rm sat} = 10^{(13.37 - 28571.43/T - [{\rm Fe/H}])} \tag{2.22}$$

This formulation assumes that only $MgSiO_3$ clouds form and neglects the formation of $Mg_2SiO_4$.

In our modeling we neglect changes in equilibrium elemental abundance with equilibrium temperature and instead assume a solar abundance in all cases. We can therefore expect the resultant cloud populations to represent an upper limit in mass.

### 2.4.2 Planet Parameters and Grid

We adapted CARMA for hot Jupiters through an adjustment of the surface gravity, atmospheric composition, the parameterized vertical mixing, and the pressure

and temperature profile.

### Pressure and Temperature Profiles

We use solar composition pressure and temperature profiles from Parmentier et al. (2016) without TiO/VO absorption for a Jupiter-size planet tidally locked around a solar-type star with gravity of 10 m $s^{-2}$ calculated using the SPARC/MITgcm (Showman et al. 2009), a 3D general circulation model that uses the plane-parallel radiative transfer code of Marley & McKay (1999). We run a grid of models with different equilibrium temperatures ($T_{eq}$). Each planet in the grid has a unique $T_{eq}$, semi-major axis, and planetary rotation rate accordingly. We consider 9 different $T_{eq}$ (1300, 1400, 1500, 1600, 1700, 1800, 1900, 2000, and 2100 K) at 4 characteristic points in the atmosphere of a hot Jupiter along the equator: the west limb, east limb, antistellar point, and substellar point.

A variety of internal structures are needed to explain the diversity of radii observed for hot Jupiters of similar masses (e.g., Guillot & Gautier 2014; Komacek & Youdin 2017). All mechanisms that aim to explain the radius inflation in hot Jupiters invoke a higher entropy interior (Guillot & Showman 2002), including: ohmic dissipation (e.g., Batygin & Stevenson 2010), downward energy flux via circulation (e.g., Ginzburg & Sari 2015) or gravity waves (e.g., Arras & Socrates 2010), tidal heating (e.g., Miller et al. 2009), increased IR opacities (e.g., Burrows et al. 2007a), inefficient heat transport in the interior (e.g., Chabrier & Baraffe 2007), and downward entropy mixing (Tremblin et al. 2017). We therefore consider two extreme cases for the interior of a given planet: the case of a high entropy interior, illustrated by the mechanism from Tremblin et al.

(2017), and a low entropy interior with $T_{int} \sim 100$ K.

The mechanism from Tremblin et al. (2017) relies on the advection of potential temperature to the interior of a planet triggered by non-uniform atmospheric heating. This allows us to use the temperature profile from the upper atmosphere to constrain the temperature at depth. Given this understanding, these two extreme cases correspond to two different efficiencies of entropy mixing in hot Jupiter atmospheres. In the high entropy case entropy mixing is efficient and the planet is inflated, with a hot interior; the opposite is true for the low entropy case.

To create our full pressure and temperature profile for the high entropy case we therefore utilize the GCM profiles to roughly 3 bar of pressure—a point where the profiles at all representative locations converge. At this point the atmosphere is optically thick, such that assumptions made about the deep atmosphere will not change the resulting spectra. Below 3 bar, we assume that the planet has fully advected its potential temperature to the interior. The pressure and temperature profile of the planet can therefore be described by an adiabat below this point. Here we assume an adiabatic gradient of

$$\nabla_{ad} = 0.33 - 0.1(T/3000 \text{ K}) \tag{2.23}$$

for molecular hydrogen (Parmentier et al. 2015, Equation 13). The resulting temperature profiles for the high entropy case are shown in the top panel of Figure 2.1.

We take the high entropy interior as the default case. Furthermore, we consider the complimentary case of a low entropy interior to investigate the physics of cold traps

and to understand how differences in planet interiors can impact cloud properties.

For the low entropy interior case, we use the full pressure and temperature profiles from the GCM. For P>3 bar, this solution is close to the initial condition; a 1D planet averaged model with $T_{int}$ = 100 K (see Parmentier et al. 2015). We assume an adiabat below 100 bar, where the GCM profile ends. The resulting pressure and temperature profiles are shown in the bottom panel of Figure 2.1.

A notable feature of these profiles is the presence of an approximately isothermal region at roughly 10 bar in all profiles. As discussed in Section 2.3, the presence of an isothermal region can cause a supersaturation at two distinct points in the atmosphere. This region can therefore have an effect on the cloud properties and on the presence of a deep cold trap. Varying our choice of vertical resolution for both cases did not change the resultant cloud population.

**Vertical Mixing**

The strength of vertical mixing in a planet plays an important role in determining the properties of the planetary atmosphere and its constituents, as discussed in Section 2.3.6. For simplicity, we adopt the one-dimensional parameterized $K_{zz}$ from (Parmentier et al. 2013) for a canonical HD 209458b. This $K_{zz}$ takes the following form:

$$K_{zz} = \frac{5 \times 10^8}{\sqrt{P}} \text{ cm}^2 \text{ s}^{-1}, \tag{2.24}$$

where $P$ is pressure in bar.

This parameterization of $K_{zz}$ is derived from GCM modeling and is valid in the

upper regions of a hot Jupiter atmosphere where the GCM pressure and temperature profile is used. In order to investigate the cloud properties in the deep atmosphere we set our $K_{zz}$ equal to a constant value of $5 \times 10^8$ cm$^2$ s$^{-1}$ below 3 bar.

To test the sensitivity of our results to $K_{zz}$ we further vary the coefficient in the numerator as well as the constant value below 3 bar. We therefore additionally consider a $K_{zz}$ coefficient of $5 \times 10^7$ and $5 \times 10^9$ cm$^2$ s$^{-1}$.

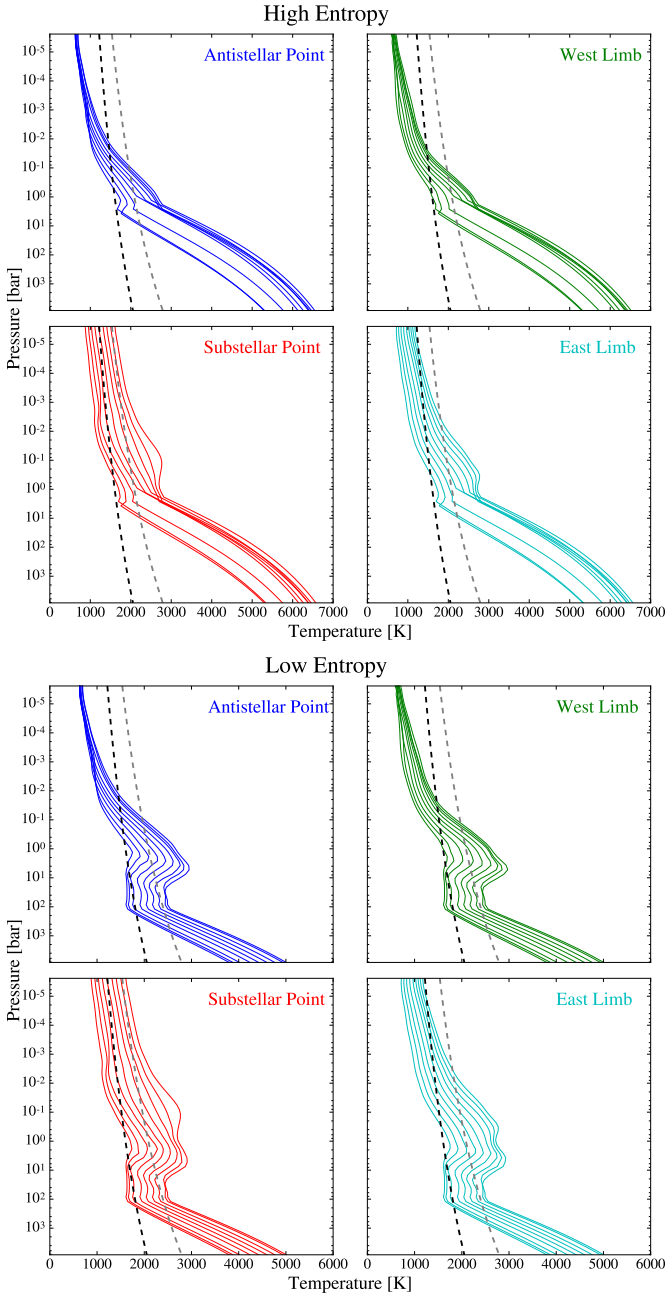


Figure 2.1: Top Panel: High entropy interior pressure and temperature profiles for four representative locations in a hot Jupiter atmosphere. These profiles were created by combining a constant adiabat to the GCM output pressure and temperature profile below $\sim$ 3 bar. In each, the profile with the coolest equilibrium temperature (1300 K) is the leftmost line and profiles increase in equilibrium temperature in 100 K steps. The dashed lines shown correspond to the condensation curves of $TiO_2$ (gray) and $MgSiO_3$ (black). Bottom Panel: The same but for low entropy interior pressure and temperature profiles. These profiles were created by combining a constant adiabat to the base of the GCM output pressure and temperature profile at $\sim$ 100 bar.

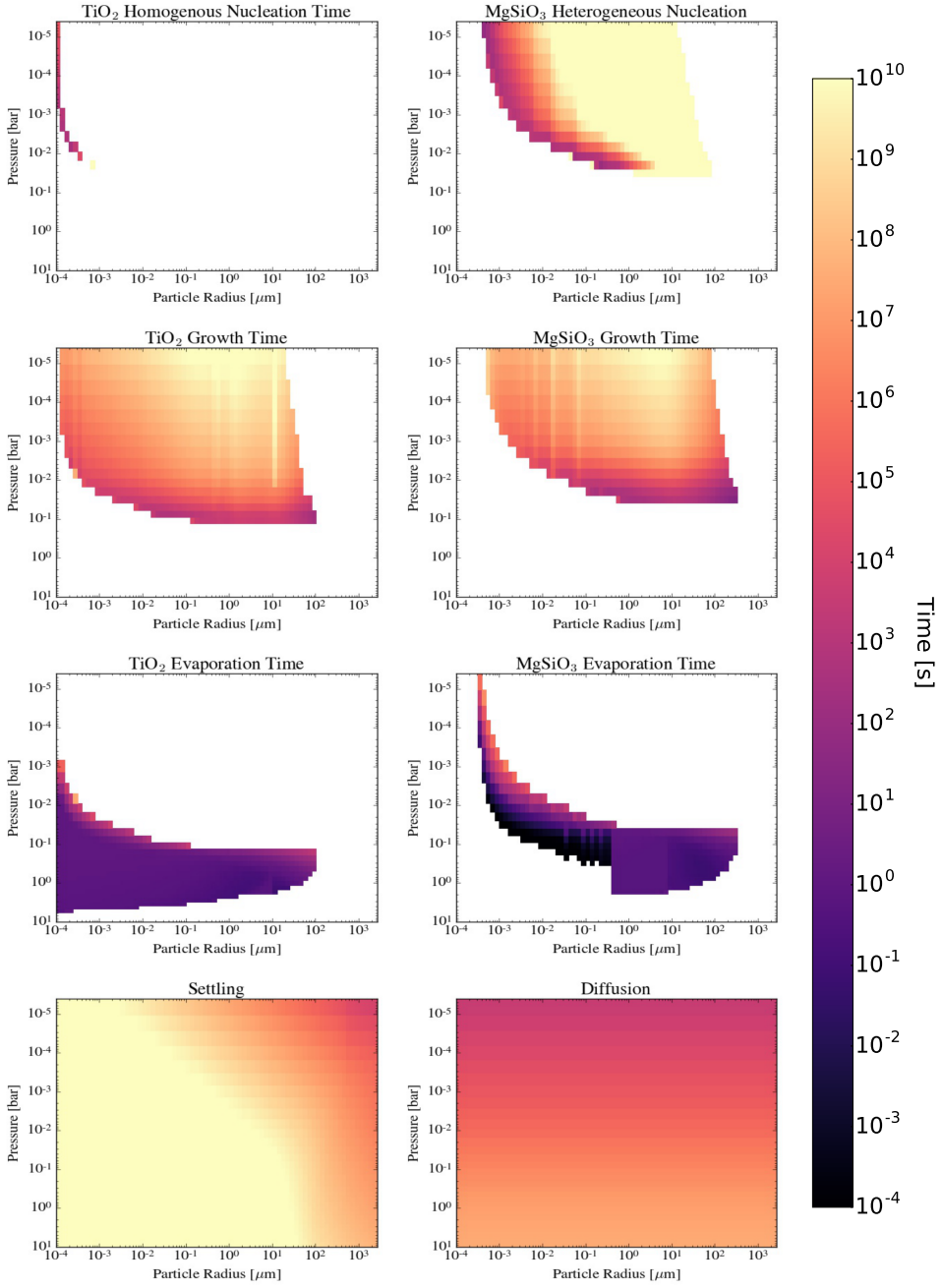


Figure 2.2: The timescales of relevant microphysical and atmospheric dynamic processes. All processes are plotted as a function of the CARMA model grid in terms of particle radius and pressure. The white spaces are points in the atmosphere where either cloud particles are not present or they are not undergoing that process. The growth of $TiO_2$ and $MgSiO_3$ clouds, the heterogeneous nucleation of $MgSiO_3$, and the settling of particles occur relatively slowly. The homogeneous nucleation of $TiO_2$ and the diffusive vertical mixing occur more quickly. The evaporation of both species occurs rapidly when favorable.

## 2.5 Timescales of Relevant Microphysical Processes

The processes of cloud microphysics depend sufficiently on the atmospheric parameters such that the timescales of these processes vary significantly with planetary properties. However, an understanding of the timescales of these processes can provide substantial insight into the resultant distribution of cloud particles. Before we present the detailed simulation results, we analyze the timescales of microphysical processes for a fiducial run of our hot Jupiter model: a high entropy interior hot Jupiter with an equilibrium temperature of 1700 K at the antistellar point. The processes that play an active role in governing the size distribution of cloud particles in our modeling are: the homogenous nucleation of $TiO_2$, the heterogeneous nucleation of $MgSiO_3$ on top of the $TiO_2$ CCN, the growth and evaporation of both $MgSiO_3$ and $TiO_2$, the settling of particles, and the diffusion of both gas and cloud particles. The timescales of these processes are shown in Figure 2.2 for our fiducial case.

The nucleation, growth, and evaporation timescales are calculated using flux outputs from the CARMA model. Once the run reaches a steady state (for more details see Section 2.6) we determine the flux into (or out) of a given bin, time averaged over three months in model time, in units of $cm^{-3}$ $s^{-1}$. The number density in a given bin is then divided by these flux values to arrive at our estimated timescales.

In all of our cases, cloud formation occurs above the point where the saturation vapor pressure is equal to the partial pressure of the species in the atmosphere (the point where the condensation curve crosses the pressure and temperature profile), known as the lifted condensation level (LCL) which can be a rough estimate of the cloud base

level. This location varies in our modeling with the thermal structure of a given planet, with $TiO_2$ having a lower cloud base than $MgSiO_3$. For this fiducial case, the cloud base for $TiO_2$ is located at $3.4 \times 10^{-1}$ bar and the cloud base for $MgSiO_3$ is located at $7.2 \times 10^{-2}$ bar.

In our model, gas diffuses from a well mixed interior into the upper atmosphere through vertical mixing. The timescale of this process can be approximated as the time that it takes to diffuse across an atmospheric scale height, i.e., $\tau_{\rm diff} = H^2/{\rm K_{zz}}$ where $H$ is the scale height. For the upper atmosphere above the cloud base it takes $10^3 - 10^5$ seconds for the gas to diffuse to an equilibrium state. When the model is at equilibrium, the partial pressure of a given gas species closely follows its saturation vapor pressure curve. This is because the microphysical processes that deplete the gas are faster than gaseous diffusion.

Once the gas has diffused above the cloud base, homogenous nucleation of $TiO_2$ cloud particles occurs. This nucleation takes roughly $10^3$ seconds, making it a moderately paced process.

After small $TiO_2$ particles form via homogenous nucleation, these particles are able to grow by condensation or be heterogeneously nucleated upon by $MgSiO_3$. These particles can also evaporate, sediment, or be diffusionally lofted. When $TiO_2$ cloud particles evaporate, $TiO_2$ gas is released. The condensational growth of $TiO_2$ occurs slowly for most of the upper atmosphere ($\sim 10^8$ seconds), but is significantly faster near the cloud base ($\sim 10^3$ seconds). The evaporation of $TiO_2$ primarily occurs below the cloud base and for very small particles. This evaporation occurs relatively quickly, on

timescales of $\sim 1$ second.

The heterogeneous nucleation of $MgSiO_3$ onto $TiO_2$ occurs relatively slowly, particularly for particles larger than one micron. While heterogeneous nucleation happens the quickest for the smallest particles, these particles are also susceptible to evaporation, which occurs quickly for small particles throughout the cloud forming region (see Section 2.3.5). The larger $MgSiO_3$ particles that form only evaporate below the $MgSiO_3$ cloud base where evaporation is rapid for particles of all sizes. When $MgSiO_3$ cloud particles evaporate, the component gases (e.g., Mg, SiO, $H_2O$) are released. The $TiO_2$ core is then able to evaporate into gaseous $TiO_2$ or survive as its own particle. $TiO_2$ particles are able to grow unimpeded unless they are nucleated on by $MgSiO_3$. Once a mantle of $MgSiO_3$ has formed only silicate condensation can occur.

Once $MgSiO_3$ has nucleated on a $TiO_2$ CCN, these clouds are also free to undergo microphysical and vertical transport processes. The condensational growth of $MgSiO_3$ occurs at roughly the same pace as the growth of $TiO_2$ and is again fastest at the cloud base.

Gravitational settling further acts on all cloud particles. We approximate the settling timescale as the time that it takes for a particle to settle through an atmospheric scale height, i.e., $\tau_{\rm settle} = H/v_{\rm fall}$ where $H$ is the scale height and $v_{\rm fall}$ is the settling velocity of the particle calculated in CARMA (see Gao et al. 2018, Appendix A). Particle settling happens at a relatively slow pace, particularly for particles smaller than $\sim$ 10 microns, for which settling across a scale height takes $10^9 - 10^{10}$ seconds. This timescale gradually transitions to faster times, however, and is noticeably more efficient

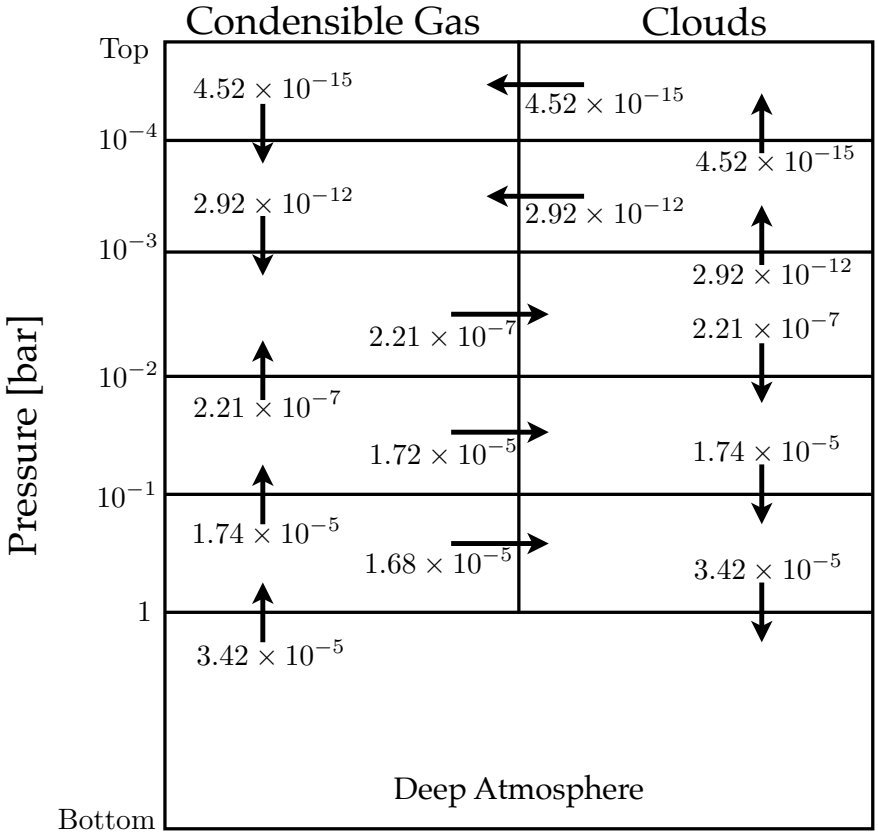


Figure 2.3: Condensible species flux flow (in units of g $cm^{-2}$ $s^{-1}$) for a hot Jupiter with $T_{eq} = 1700$ K at the antistellar point.

for particles larger than 10 microns, which can settle in $\sim 10^5$ seconds. Given our fiducial diffusivity profile, diffusive transport dominates settling for nearly all relevant particle sizes.

While these timescales vary with atmospheric location and particle size, they are roughly ordered in magnitude as described in Equation 2.25.

$$\tau_{\text{evap, MgSiO}_3} \sim \tau_{\text{evap, TiO}_2} << \tau_{\text{nuc, TiO}_2} \sim \tau_{\text{diff}} < \tau_{\text{gr, MgSiO}_3} \sim \tau_{\text{gr, TiO}_2} \sim \tau_{\text{setl}} \sim \tau_{\text{nuc, MgSiO}_3} \quad (2.25)$$

These timescales change throughout the atmosphere such that just above the cloud base, cloud particles are dominated by condensational growth, whereas higher in the atmosphere they are dominated by nucleation and vertical transport.

A picture of the mass balance in the atmosphere for this fiducial case is shown in Figure 2.3. Most of the cloud formation processes occur near the cloud base and at pressures higher than $10^{-3}$ bar. Below $\sim 10^{-3}$ bar particles preferentially experience settling, while above this point particles are more likely to be lofted upwards via vertical mixing.

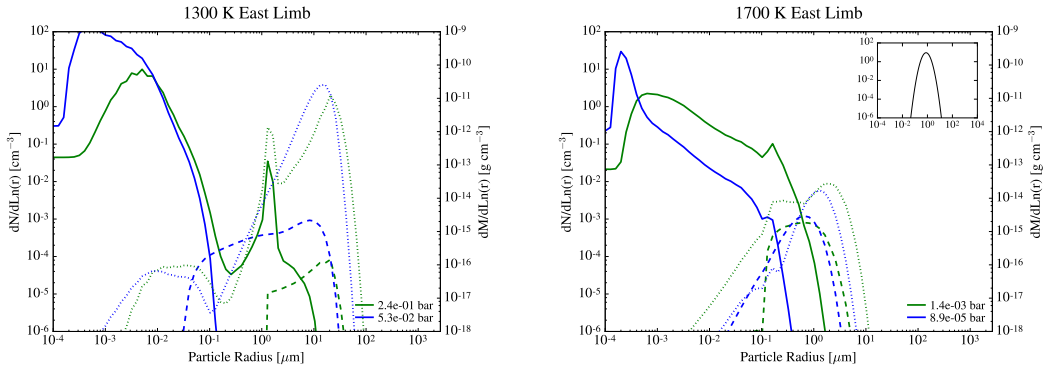


Figure 2.4: Cloud particle size distributions in terms of number density (solid lines for titanium clouds and dashed lines for silicate clouds) and mass density (dotted lines for titanium and silicate clouds added together) for two representative hot Jupiters. Size distributions are plotted for a specific pressure in the atmosphere as indicated in the legend. For the 1700 K case the inset plot depicts a standard log-normal size distribution. In all cases the cloud particle size distribution does not follow a smooth log-normal profile.

## 2.6 Simulation Results

We calculate the cloud particle size distributions, the total cloud mass, and the vertical distribution of cloud particles for a grid of 9 Jupiter-size tidally locked planets orbiting a solar-type star with equilibrium temperatures ranging from 1300 K to 2100 K. We sample the atmosphere at four representative locations along the equator: the antistellar point, substellar point, east limb, and west limb. We further consider two representative cases for these planets' interiors: high entropy and low entropy. A comprehensive discussion of our model grid can be found in Section 2.4.2.

In the following sections we discuss trends that are apparent in our results when time averaged over the last three Earth years of a thirty year run in model time. Our models arrive at a steady state solution rather than a true equilibrium (see **?**) where we define our steady state as stable oscillations around a mean value as is seen

in many 1D cloud formation models (Barth & Toon 2003). These oscillations occur on roughly Earth year timescales. This is suggestive of some intrinsic variability, though we leave further discussion for future work. In the following, we will mainly adopt the high entropy simulations as the nominal cases to discuss our findings, while the low entropy cases are merely used to test the effects of a deep cold trap.

### 2.6.1 Cloud Particle Size Distributions

The resultant cloud particle size distributions in our grid are not log-normal and are instead bimodal, broad, or irregular in shape. Figure 2.5 shows typical distributions for two representative equilibrium temperatures at two representative pressures in the atmosphere. It is important to note that the particle size distributions can vary significantly with altitude.

The silicate clouds are typically distributed broadly, sometimes without a distinct peak. The distribution of silicate cloud particles has a distinct peak closer to the cloud base where growth is efficient until it is limited by particle settling. The distribution has an indistinct peak when growth is less efficient and particles of nearly all sizes in the distribution can persist until they are limited by settling. Furthermore, the silicate clouds are frequently distributed asymmetrically such that the distribution skews towards smaller particles.

The titanium clouds frequently follow a bimodal distribution with a peak at small radii (the nucleation mode) and another peak at intermediate radii corresponding to the particles that are able to overcome the Kelvin effect and grow to a larger size (the growth mode). The first peak at smaller radii is typically broad while the second

peak at larger radii is narrow. At altitudes sufficiently above the cloud base only the nucleation mode is present in a broad distribution.

The CCN size on which silicate clouds can efficiently heterogeneously nucleate is approximately indicated by the size at which $TiO_2$ particle number densities drop below those of the silicate cloud particles. The existence of an optimal CCN size is due to the Kelvin effect, as smaller CCN are difficult to nucleate on without quickly undergoing evaporation while larger CCN are not as numerous.

For the case of the high entropy planetary interior, the cloud particle distributions in terms of mass density ($dM/dLn(r)$) are shown in Figure 2.6. Note that clouds are only present in the upper atmosphere in these cases. Here both the titanium and silicate cloud particles are plotted using the same colormap. The population of titanium cloud particles ranges in radius from $10^{-1}$ to 1 $\mu$m and is typically smaller than the population of silicate cloud particles, which range in radius from 10 to 50 $\mu$m.

When silicate clouds form in abundance, the titanium clouds form in two populations: below the silicate cloud base and above it. The titanium clouds that form below the silicate cloud base tend to grow larger in size than those that form above it as their growth is not limited by the heterogeneous nucleation of silicate clouds.

Titanium cloud particles, if they form, are typically abundant throughout the upper regions of the atmosphere, while silicate cloud particles are confined closer to their cloud base. This is shown in Figure 2.6.2 for the 1300 K hot Jupiter at the antistellar point. In Figure 2.6.2 the titanium cloud particles are abundant from above $10^{-1}$ bar to the top of the atmosphere while the silicate cloud particles are abundant closer to

their cloud base and extend to roughly $10^{-3}$ bar. This general trend is found for all cases where both clouds form.

### 2.6.2 The Effects of Local Temperature and Equilibrium Temperature

The formation of clouds occurs at all four representative locations along the equator for planets with $T_{eq} < 1800$ K. Planets with equilibrium temperatures greater than or equal to 1800 K have clear atmospheres (in terms of titanium and silicate clouds) at the substellar point, as the local temperature profile becomes too hot for cloud formation to occur. With increasing equilibrium temperature, the cloud base moves towards the upper atmosphere and the cloud cover becomes increasingly inhomogeneous as a function of longitude with the west limb and antistellar point being preferentially cloudy. Cloud particles located on hotter regions of the planet (the east limb and substellar point) tend to be smaller than the cloud particles present at cooler locations. This effect is due to the increase in temperature at the east limb and substellar point. The temperature increase changes the saturation vapor pressure leading to lower supersaturations. The lower supersaturations lead to limited growth and smaller mean particle sizes. This effect is particularly strong for planets with high equilibrium temperatures where the east limb and substellar points have particularly high temperatures.

In some locations there exists only a relatively small population of titanium cloud particles, with no silicate clouds, while both clouds are abundant in other locations. For example, for equilibrium temperatures greater than or equal to 1900 K, the east limbs only have a significant population of titanium clouds. The antistellar

points and west limbs, however, have both titanium and silicate clouds for all equilibrium temperatures in our grid. This is a temperature effect as there are specific regions of temperature space for which $TiO_2$ reaches a supersaturation and can form clouds while it is too hot for $MgSiO_3$ cloud particles to form. Furthermore, the east limb and substellar points experience more dramatic increases in temperature with increased equilibrium temperature as compared to the west limb and antistellar point.

The presence of a small local thermal inversion in the 1300 and 1400 K case (see Figure 2.1) has an impact on the vertical locations of the cloud populations, such that there are two small and distinct cloud layers. This occurs because there are two locations in the atmosphere that reach a supersaturation, separated by a small region of pressure space that is too hot for a supersaturation to be achieved. However, this primarily affects the deep population of titanium clouds without strongly affecting the overall cloud distribution.

There is a decrease in cloud mass density with increasing equilibrium temperature across all sampled regions of the planet, shown in Figure 2.6.2. This is because an increase in temperature reduces the supersaturation for a given condensate partial pressure, resulting in less gas condensing. For nearly all cases, the west limb and the antistellar point form the same density of cloud particles to within an order of magnitude as their temperature profiles are also quite similar. The cloud particle size distribution in these locations differs subtly, however, with the west limb preferentially forming larger cloud particles in a slightly narrower distribution. This subtle change is due to the west limb having slightly cooler temperatures in the cloud forming region of the at-

mosphere, leading to an increased supersaturation and supply of condensible gas which causes increased particle growth.

The hotter regions of a hot Jupiter's atmosphere (the east limb and substellar point) show a more dramatic dependence on equilibrium temperature, as shown by the steeper slope in Figure 2.6.2. At equilibrium temperatures lower than 1500 K, the east limb and substellar point also form roughly equal densities of cloud particles. The relatively flat slope for the antistellar point and west limb in Figure 2.6.2 indicates that cloud properties in the cooler regions of hot Jupiters may be relatively unaffected by increasing equilibrium temperatures, while hotter regions see much more dramatic changes leading to limited particle growth.

### 2.6.3 The Influence of Vertical Mixing on Cloud Properties

We choose the 1700 K hot Jupiter at the antistellar point as a fiducial case to determine the effect of atmospheric mixing on the cloud particle size distribution. To understand the effect that vertical mixing has on the distribution of cloud particles, we vary our input $K_{zz}$ by an order of magnitude—both smaller and larger. The distributions are shown in Figure 2.6.2, where we plot the titanium and silicate clouds separately.

When the atmospheric vertical mixing is reduced, the total cloud mass and vertical extent of both cloud particle populations are significantly smaller than in our nominal case. In particular, there is a decreased number of small titanium cloud particles. As atmospheric vertical mixing is increased, there is an increased population of both titanium and silicate clouds. With increased vertical mixing, the vertical extent of the cloud particle populations increases slightly while the mean particle size decreases

slightly compared to our fiducial case. This is due to an increased production of particles leading to greater number of particles vying for the gas with which to grow, leading to on-average smaller particles. This effect is subtle, however, as the increased vertical mixing also increases the available supply of condensible gas.

The enhanced vertical extent of the cloud population is primarily due to this increased supply of condensible gas to the cloud forming region of the atmosphere. The increased supply of gas leads to more growth and extends the region of rapid growth further above the cloud base. This leads to both an increase in cloud mass and vertical extent. There is also the secondary effect that particles are lofted higher in the atmosphere further extending the region of abundant cloud particles.

The total mass density of titanium and silicate clouds is strongly correlated with the amount of vertical mixing in the atmosphere. This is shown in Figure 2.6.3, where the total cloud mass density increases substantially with increased mixing.

### 2.6.4 Low Entropy Temperature Profile and the Presence of a Deep Cold Trap

We focus on the resulting cloud particle distributions for the low entropy cases in which a deep cold trap is present in the lower atmosphere—resulting in marked differences from the high entropy interior cases. This is true in our grid for hot Jupiters with equilibrium temperatures lower than 1800 K. For planets with equilibrium temperatures of 1800 K or higher the cloud particle distributions are very similar to those shown in the high entropy case in Section 2.6.2. The cloud particle distributions in terms of mass density are shown in Figure 2.6.3. Again, both the titanium and silicate cloud particles

are plotted using the same colormap.

The presence of an isothermal region in the pressure and temperature profile leads to the formation of two cloud populations that are spatially separated in the atmospheres of hot Jupiters (see bottom panel of Figure 2.1) for one or both of our cloud species for planets with temperatures below 1800 K. These populations exist because the isothermal layer reduces the temperature at depth, leading to the existence of two regions in the atmosphere where supersaturation can be achieved, separated by a region that is too hot for clouds to form (see Section 2.3.7). The one exception is the 1300 K case, where the temperatures are low enough to allow the two cloud populations to merge.

The first population of clouds is present in the deep atmosphere, at around 100 bar. This lower cloud deck is comprised of large cloud particles, with both titanium and silicate cloud particles growing to tens or hundreds of microns in size due to a large supply of gas at depth. This population of clouds varies in vertical extent with equilibrium temperature. At cooler temperatures cloud particles extend throughout most of the atmosphere while at hotter temperatures the lower cloud deck is confined to the deep atmosphere. This is because the layer of the atmosphere in which it is too hot for clouds to form becomes larger with increased equilibrium temperature (see Figure 2.1).

We refer to the lower population of clouds in this atmosphere as a deep cold trap (see Section 2.3.7). This deep cold trap theoretically limits cloud formation in the upper atmosphere; however, for all of the planets in our grid with a deep cold trap,

cloud formation in the upper atmosphere appears only subtly affected. This is because atmospheric mixing is strong enough to supply the upper atmosphere with sufficient gas for abundant cloud formation. We further discuss the efficiency of the deep cold trap in altering atmospheric observables in Section 5.1.

Increasing the equilibrium temperature of a planet decreases the total amount of cloud mass, as shown in Figure 2.6.2, following the same reasoning as for the high entropy case. In contrast to those cases, however, there is a much larger cloud particle mass density for atmospheres with a deep cold trap ($T_{eq} < 1800$ K) because this deep reservoir adds mass without substantially limiting supply to the upper atmosphere. Planets with equilibrium temperatures less than 1800 K form a nearly homogenous layer of clouds in the deep atmosphere such that the total condensed mass density is the same across all four planetary locations.

For equilibrium temperatures greater than 1800 K, where no deep cold trap is present and supersaturation is only achieved in the the upper atmosphere, the four locations again differ in cloud particle mass density. In particular, the west limb and antistellar point have very similar cloud particle mass densities while the east limb and substellar point show a stronger dependence on equilibrium temperature as seen in the high entropy case.

### 2.6.5 Comparison to Other Modeling Approaches

Our modeling framework differs considerably from models that rely on equilibrium cloud condensation or on grain chemistry. Here we summarize the similarities and differences between our study and previously published work. We note, however, that

any differences in assumed temperature profile could also result in differences between the studies, in addition to the differences caused by different modeling frameworks.

The modeling framework described in Ackerman & Marley (2001) assumed that clouds are not present below the cloud base. Indeed, none of our simulations produce abundant cloud particles below the cloud base, as evaporation occurs quickly. This finding indicates that this assumption is likely valid to first order and that the cloud base is thermodynamically controlled.

Previous modeling work done by Lee et al. (2015a) for HD 189733b found that silicate clouds are the main component of the total condensible inventory. While we do not consider a comprehensive list of condensible species, our simulations find that silicate clouds do dominate titanium clouds in terms of mass in most cases when both species are present.

Follow-up work for HD 189733b by Lee et al. (2016) found that the hottest regions of the atmosphere along the equator are populated by the smallest cloud particle grains. Our modeling also uncovers this trend, although the effect is sometimes subtle. Furthermore, the mean particle sizes of our clouds, particularly near the cloud base, are very similar to those derived in Lee et al. (2016). Unlike the modeling done in Lee et al. (2016), we do not consider horizontal mixing which could work to smooth inhomogeneities in cloud coverage with longitudinal location.

Our ability to predict fully resolved size distributions allows us to test common assumptions. Ackerman & Marley (2001) assume a log-normal distribution of cloud particles, and grain chemistry modeling as used in Lee et al. (2015a, 2016) uses the mo-

ment method to derive four governing parameters of a smooth particle size distribution. Our results do not support these assumptions; we instead find a varying cloud particle size distribution that is frequently bimodal or irregular in shape due to both cloud composition and formation mechanisms.

In contrast to some of the results in Lavvas & Koskinen (2017), we do not find that considering coagulation in our modeling has a significant effect on our derived cloud particle distribution. This result is unsurprising, however, as our work focuses on condensational clouds with much lower number densities than the photochemical hazes considered in their work. The maximum particle number densities we encounter in our results are $\sim 10^2$ cm$^{-3}$ for the high entropy interior cases, while Lavvas & Koskinen (2017) consider number densities greater than $10^4$ cm$^{-3}$.

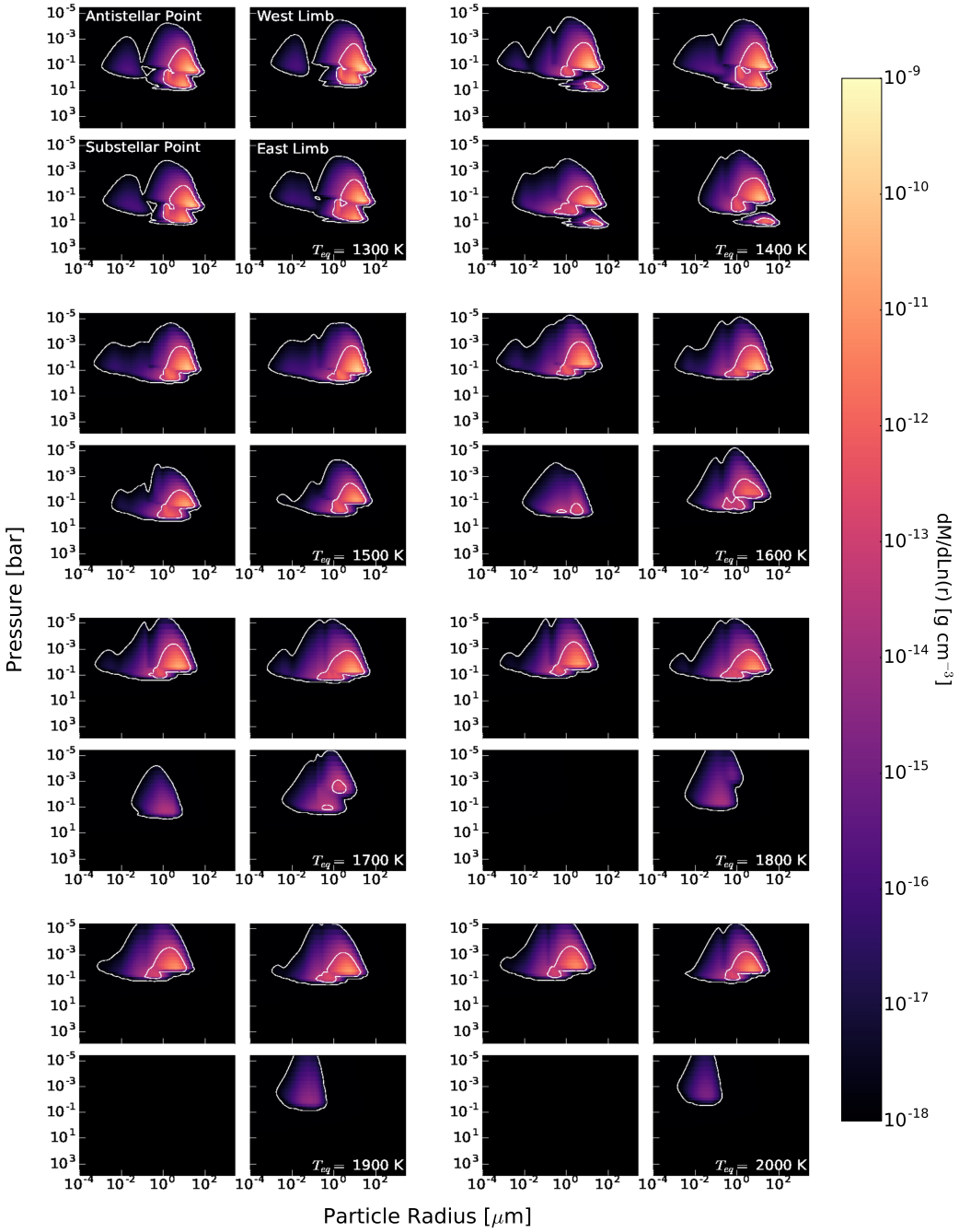


Figure 2.5: Vertical cloud particle size distributions for the high entropy interior case in terms of mass density ($dM/dLn(r)$). Both $TiO_2$ clouds and $MgSiO_3$ clouds are plotted using the same colormap. All plots are made using a log-scale. The clouds appear vertically extended while the majority of the mass is close to the base of the cloud deck. The contours correspond to the range in the colorbar divided into 3 even sections in log-space. There are distinct trends in cloud properties with equilibrium temperature and planet location. The 2100 K equilibrium temperature case is excluded from this plot as the resultant size distributions are very similar to those from the 2000 K case.

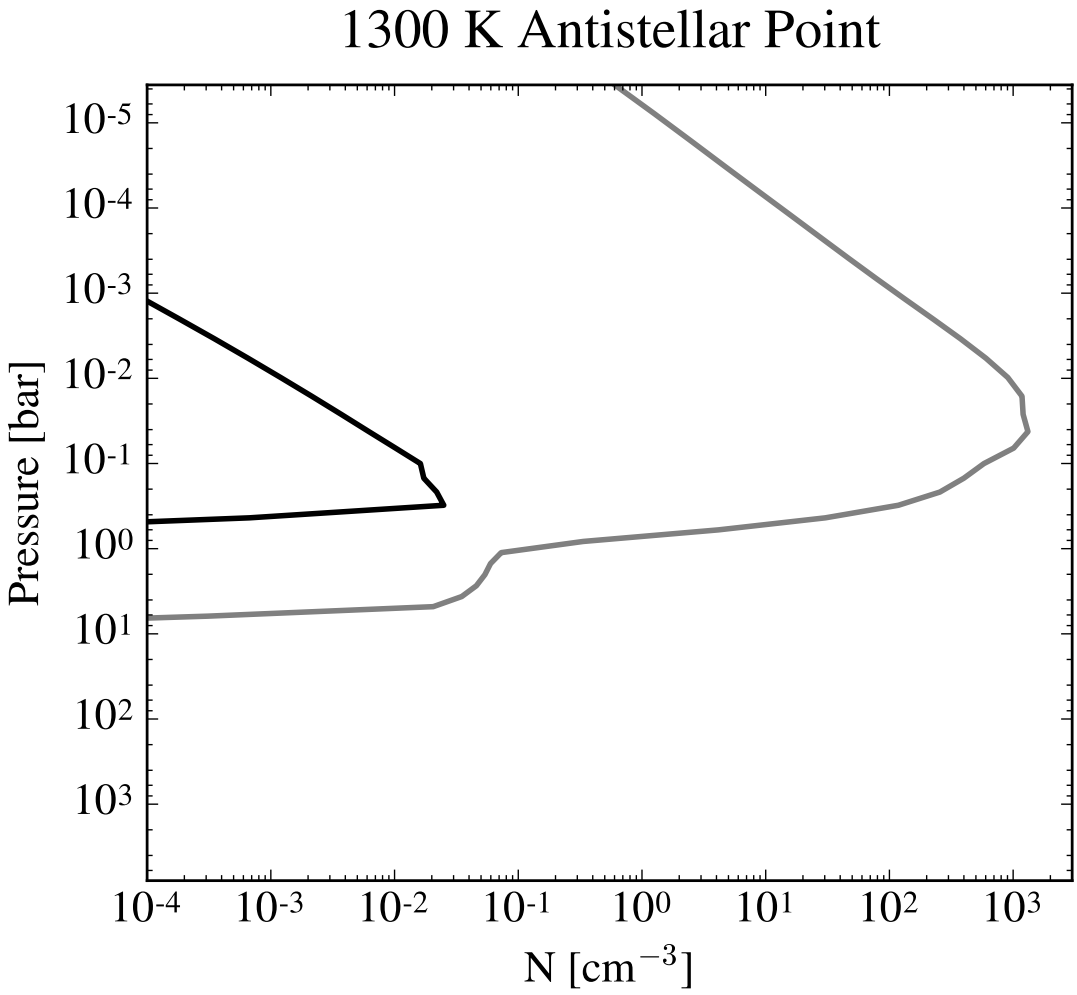


Figure 2.6: Total number densities as a function of pressure in the atmosphere of a 1300 K hot Jupiter at its antistellar point for titanium (gray) and silicate (black) cloud particles. The titanium cloud particles are abundant from above $10^{-1}$ bar to the top of the atmosphere. The silicate cloud particles are abundant closer to their cloud base and extend to roughly $10^{-3}$ bar.

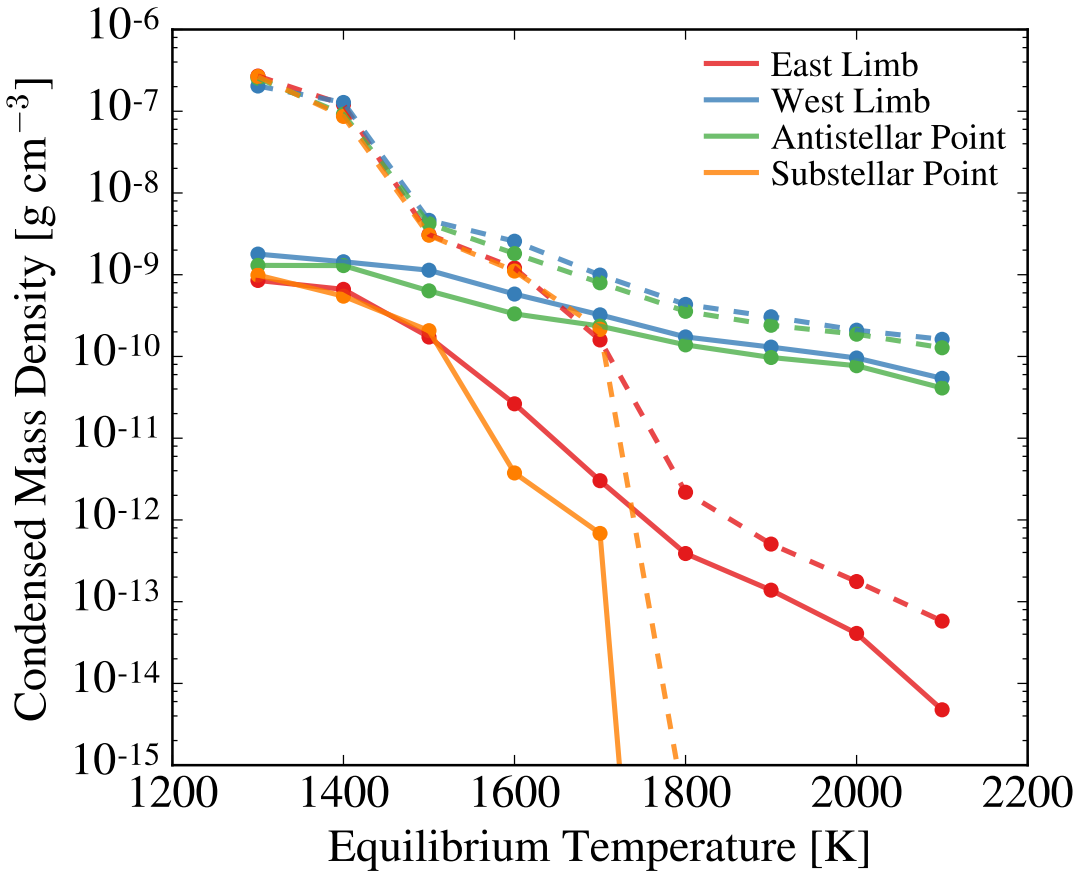


Figure 2.7: Total condensed mass density as a function of equilibrium temperature for four representative planetary locations for the case of a high entropy interior (solid lines) and low entropy interior (dashed lines, see Section 2.6.4). All locations show a marked decrease in condensed mass density as a function of equilibrium temperature, with the trend being more pronounced for the east limb and substellar point.

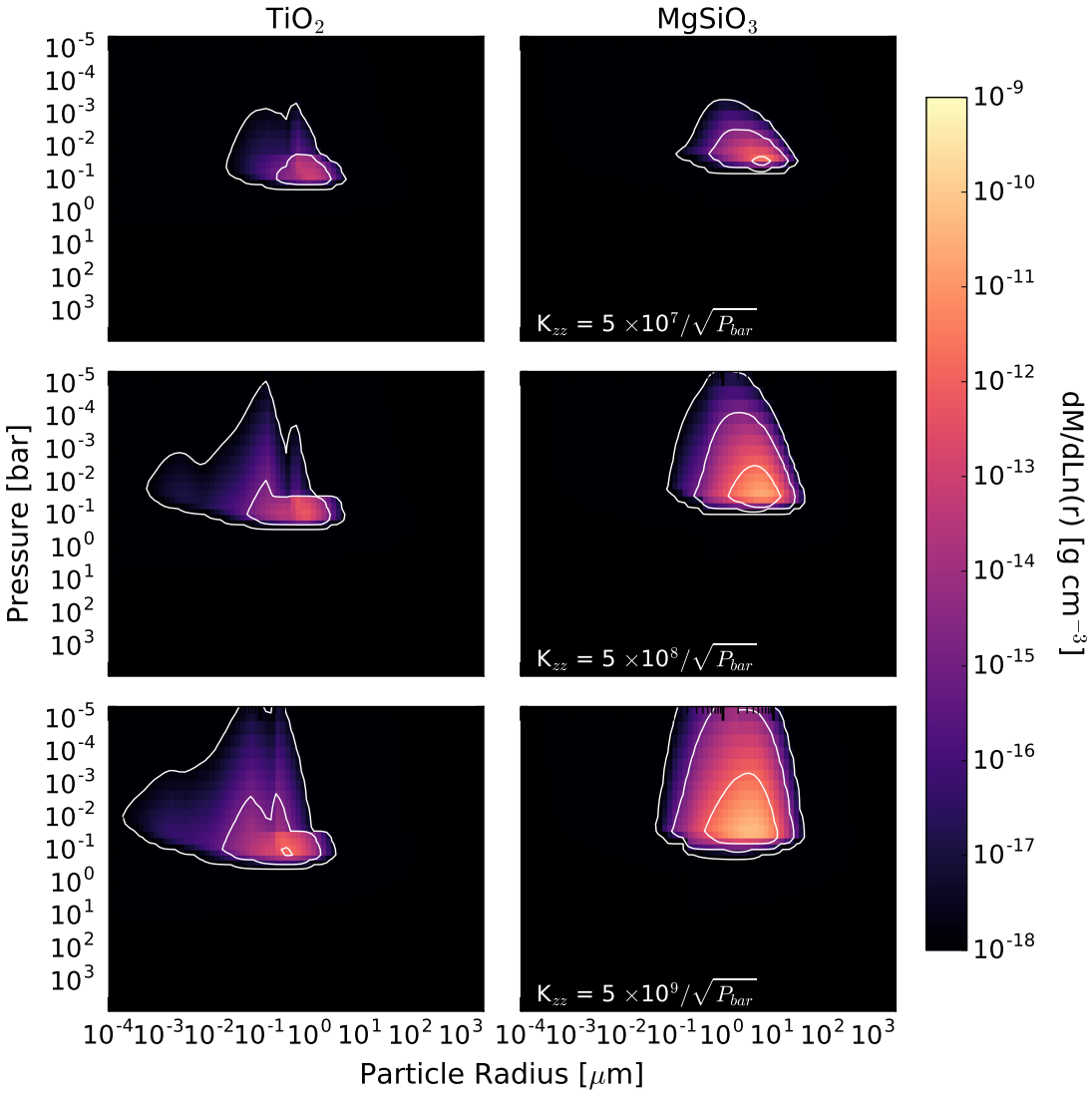


Figure 2.8: Vertical cloud particle size distributions for a 1700 K hot Jupiter at the antistellar point for the case of a high entropy interior as a function of atmospheric vertical mixing: low (top), fiducial (middle), and high (bottom). $TiO_2$ clouds (left) and $MgSiO_3$ clouds (right) are plotted separately. There is an increase in total cloud mass and differences in the properties of the cloud particle size distribution with increased vertical mixing.

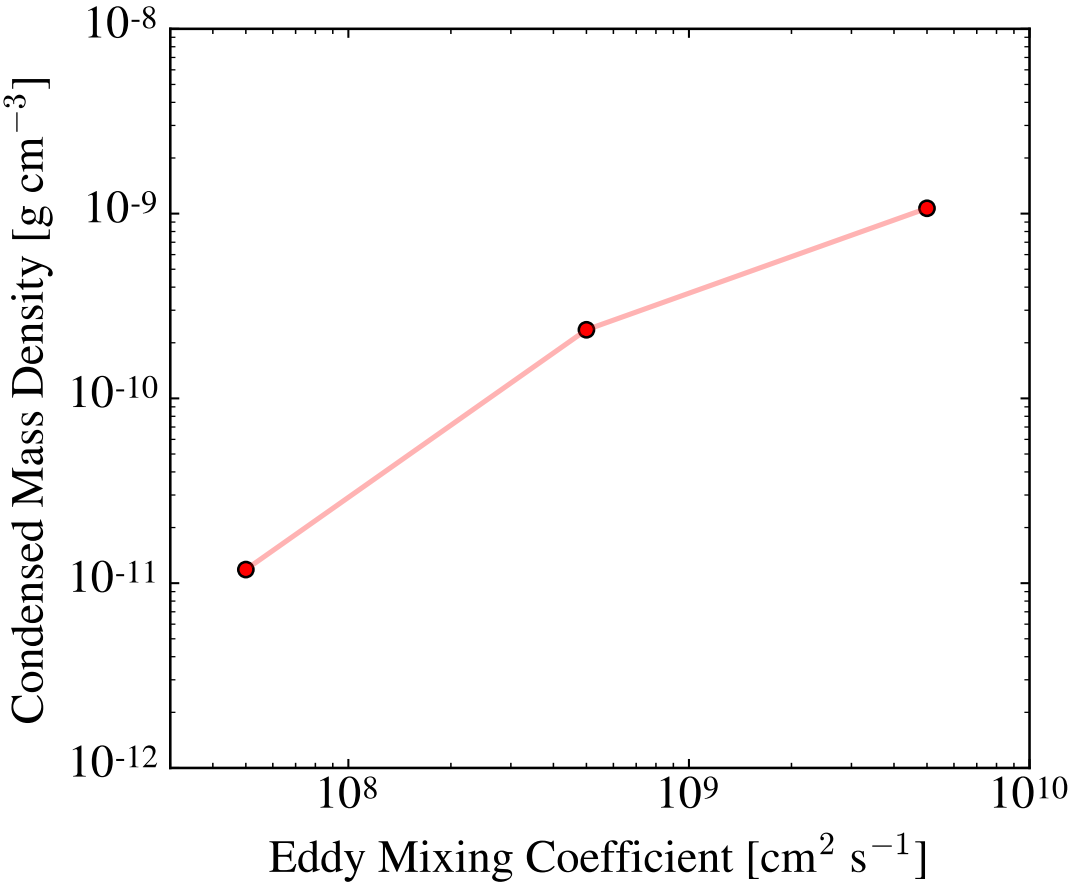


Figure 2.9: Total condensed mass density as a function of vertical mixing for a 1700 K hot Jupiter at the antistellar point for the case of a high entropy interior. There is a marked increase in total condensed cloud mass with increased vertical mixing.

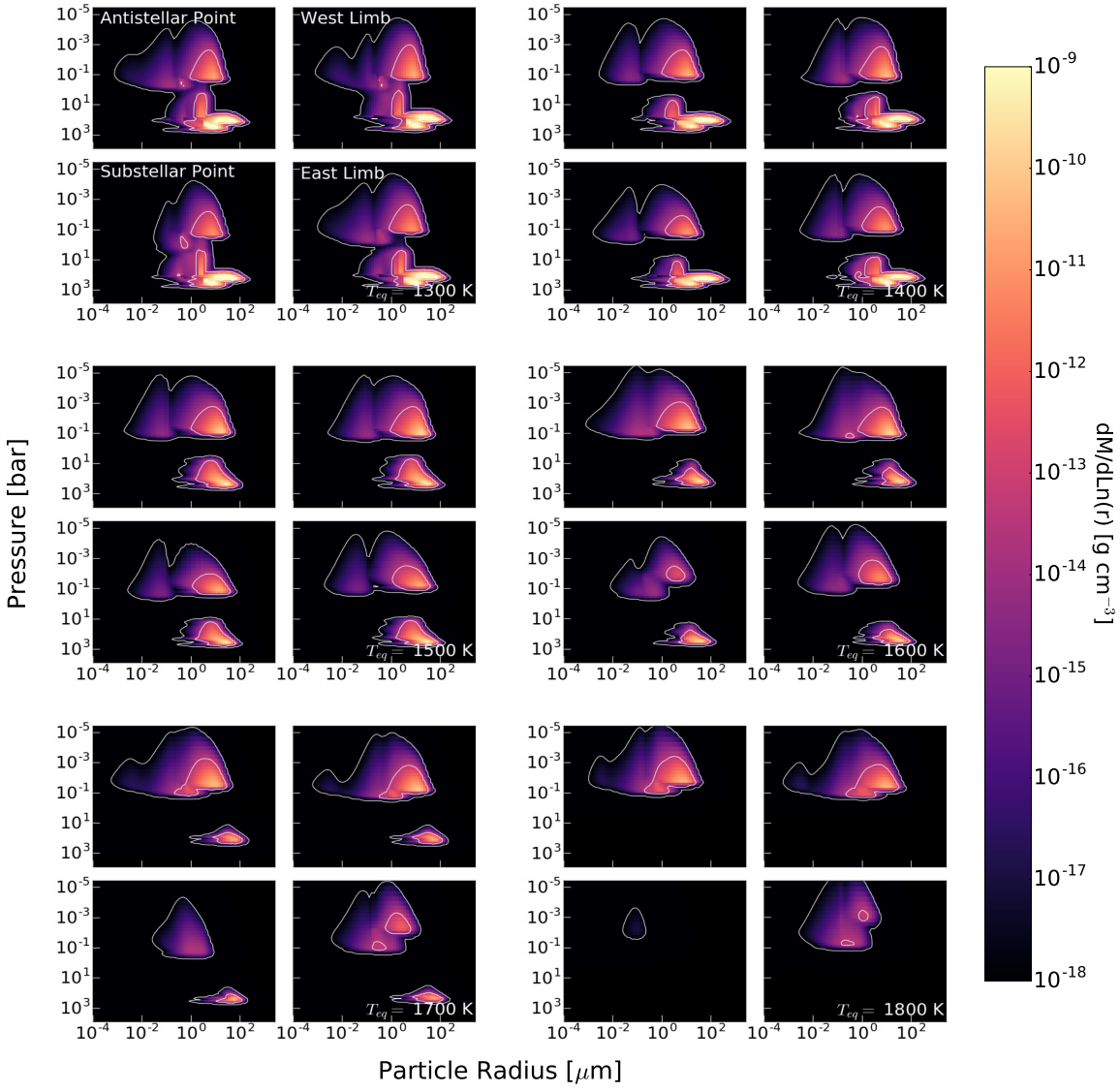


Figure 2.10: Same as Figure 2.6, but for the low entropy interior case with an emphasis on equilibrium temperatures that have a deep cold trap.

## 2.7 Observational Implications

We now discuss the observational implications of our derived cloud particle size distributions in detail. In the following sections we only discuss radiative properties of the cloud particles themselves given our derived cloud particle size distributions and do not consider the opacities of the background gases. We do so as a means to clearly understand how the radiative properties of clouds depend on planetary properties and their underlying size distribution.

First, we calculate cloud opacities and scattering properties in transmission and emission observational viewing geometries. We focus our discussion in part on the differences in cloud radiative properties between the high and low entropy cases as well as longitudinal differences in a planet's atmosphere. We also discuss trends in cloud opacity with equilibrium temperature. Second, we investigate the impact of using a full cloud particle size distribution in opacity calculations. In the following sections we focus solely on cloud opacities and other specific properties of our derived cloud populations.

To derive the cloud particles' opacity we use complex refractive indices for $MgSiO_3$ from Egan & Hilgeman (1975) and Dorschner et al. (1995). For $TiO_2$ we use complex refractive indices from Kangarloo (2010a,b). Data for both clouds were compiled by Wakeford & Sing (2015). Our $MgSiO_3$ cloud particles are not homogenous since they have a core ($TiO_2$) and mantle ($MgSiO_3$) of different compositions. It is possible that these mixed cloud particles have different optical properties than those of pure $MgSiO_3$, however, any adjustments to their optical properties requires detailed modeling and/or laboratory experiments outside the scope of this work. Generally, as

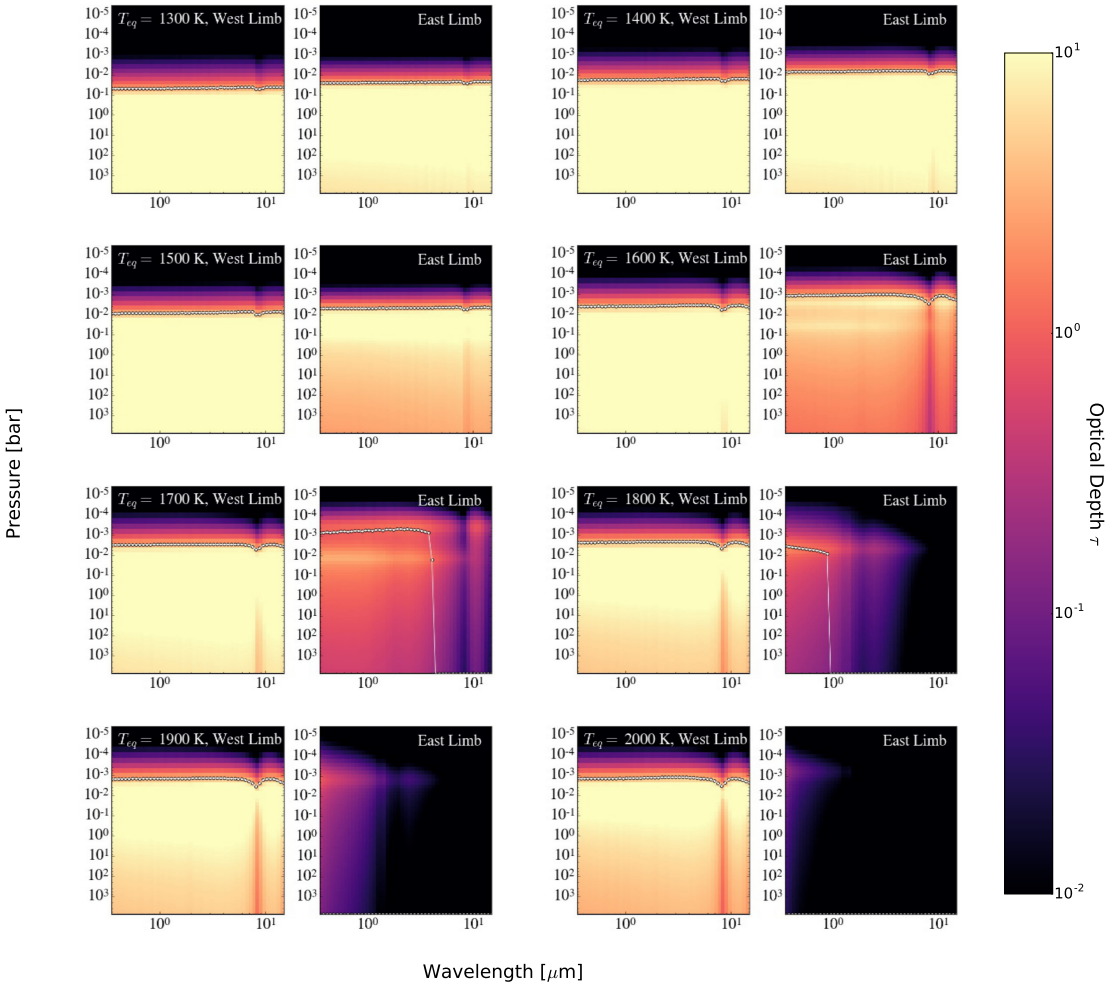


Figure 2.11: Cloud transmission opacities for the case of the high entropy interior. The white dotted line represents the point in the atmosphere where the clouds become opaque—the "opaque cloud level". There are noticeable hemispheric differences between the east and west limbs for hotter planets. The opaque cloud level is at roughly the same location for a range of wavelengths and equilibrium temperatures.

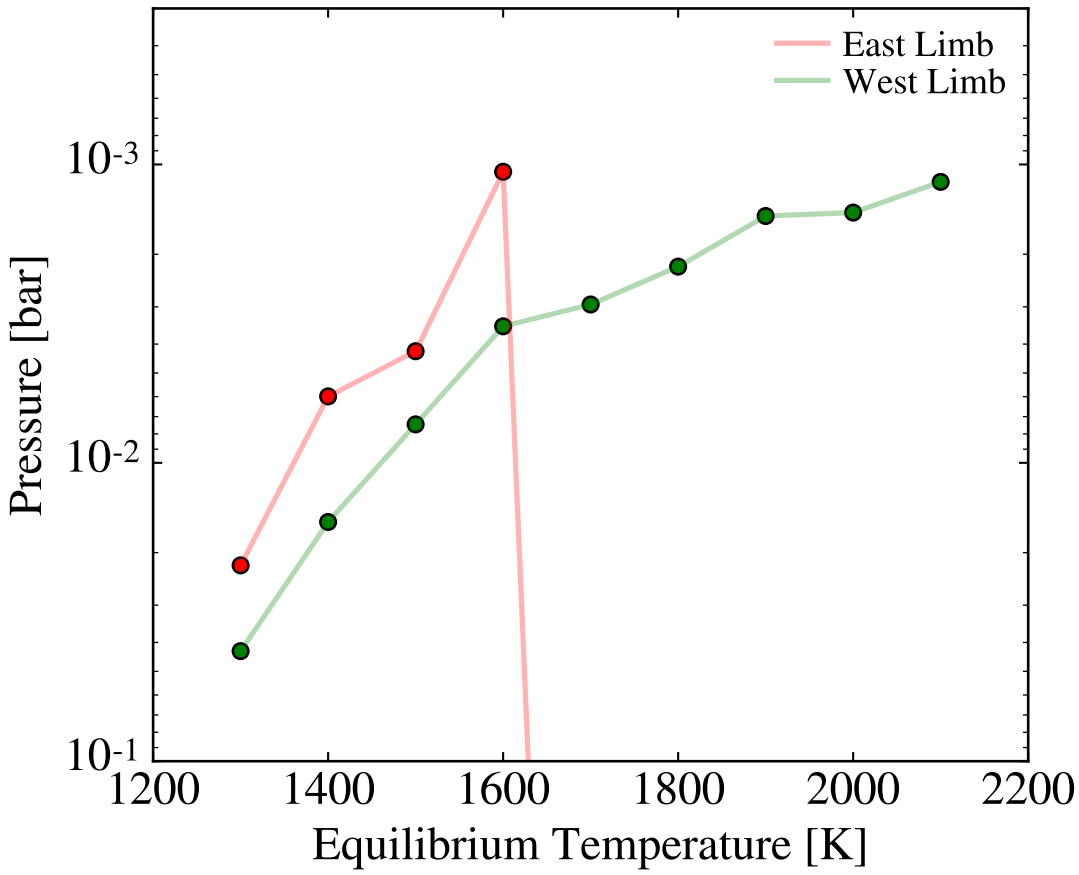


Figure 2.12: The opaque cloud level at 3 $\mu$m for the east and west limbs as a function of equilibrium temperature. For $T_{eq} \leq 1700$ K, the opaque cloud level at the east limb is higher in the atmosphere than at the west limb, despite there being a lower total cloud mass.

the size of the $TiO_2$ seed ($\sim 10^{-1}$ $\mu$m) is much smaller than the mantle of $MgSiO_3$ ($\sim 10$ $\mu$m), the optical properties should be similar to those of a pure $MgSiO_3$ particle. We therefore assume that the optical properties of the $MgSiO_3$ cloud particles with $TiO_2$ cores are roughly equivalent to those of pure $MgSiO_3$.

Given a wavelength and a complex refractive index, we can determine the extinction cross section ($\sigma_{ext}$) which in turn allows us to calculate the optical depth, ($\tau$). To compute $\sigma_{ext}$ we use *bhmie*, a routine that uses Bohren-Huffman Mie scattering for a homogenous isotropic sphere to calculate scattering and absorption (Bohren & Huffman 1983). This routine directly calculates the efficiency factor for extinction, efficiency factor for scattering, and the efficiency for backscattering. We use the extinction efficiency ($Q_{ext}$) to calculate $\sigma_{ext}$ via Equation 2.26 where $a$ is the grain radius.

$$Q_{ext} = \frac{\sigma_{ext}}{\pi a^2} \tag{2.26}$$

Given $\sigma_{ext}$ we calculate the optical depth for each particle size bin:

$$d\tau = n(l, r)\sigma_{ext}(r)dl, \tag{2.27}$$

where $n(l, r)$ is the number density of cloud particles as a function of the path length of light ($l$) and particle radius ($r$).

We then either take a cumulative sum of all of the vertical levels to find the emission optical depth (Nadir view) or we calculate the optical depth assuming transmission geometry along the line of sight. In the following sections we present the combined

opacities of both the pure $TiO_2$ clouds and the $MgSiO_3$ clouds.

### 2.7.1 Transmission Opacity

We calculate the cloud particle contribution to the total atmospheric opacity in transmission at both the east and west limbs for each planet in our grid. The full transmission cloud opacities are shown in Figure 2.7, where the white dotted line indicates the point in the atmosphere where the clouds become opaque ($\tau = 1$), which we refer to as the "opaque cloud level".

Of particular interest are observed differences between the two limbs as patchy cloud coverage has been shown to distinctly impact planetary transmission spectra (Line & Parmentier 2016). The clouds are optically thick at nearly all wavelengths for every equilibrium temperature at the west limb. The east limb, however, shows a clear progression from optically thick at lower equilibrium temperatures to optically thin at all wavelengths for equilibrium temperatures greater than 1800 K.

While the east limb has less total cloud mass than the west limb, the opaque cloud level is located higher in the atmosphere for $T_{eq} \leq 1700$ K. This trend is shown in Figure 2.7. The east limb, therefore, appears more cloudy with increasing equilibrium temperature until the planet becomes too hot for clouds to form ($T_{eq} > 1700$ K). This is because the cloud base is higher in the atmosphere at locations with hotter temperature profiles. Therefore, if enough clouds can form such that the clouds become opaque they do so at higher levels, causing the cloud top to be located higher in the atmosphere.

For all planets at the west limb and for planets with $T_{eq} \leq 1700$ K at the east limb, the cloud opacities are characteristically flat and featureless across a large

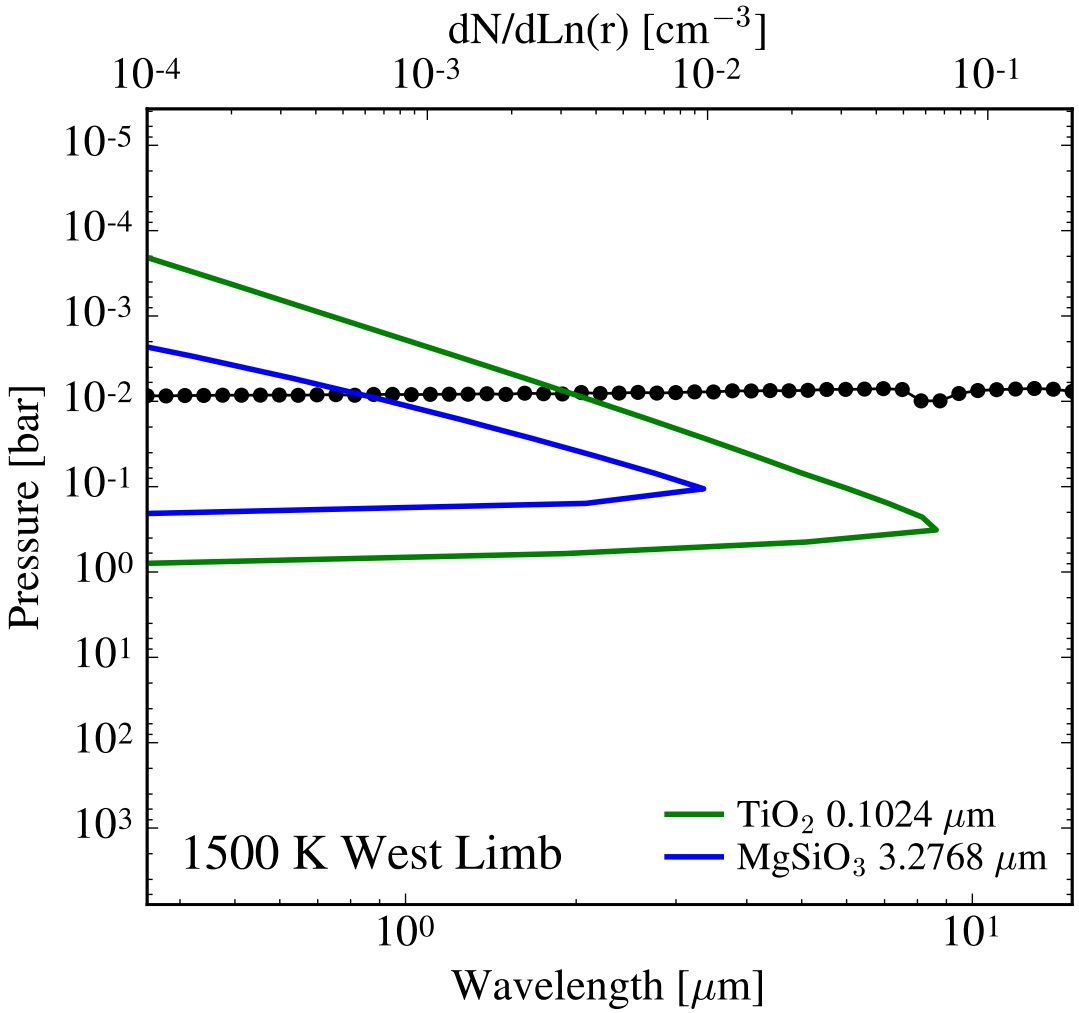


Figure 2.13: The opaque cloud level across the full wavelength range (black, dotted) as compared to the total distribution of cloud particles in terms of number density ($dN/dLn(r)$) for the particle size bins (see legend) that contribute the most to the cloud opacity. Shown is the case of a 1500 K hot Jupiter at the west limb. The distribution of titanium clouds is shown in green and the distribution of silicate clouds is shown in blue. There is not an increase in particle density near the cloud top.

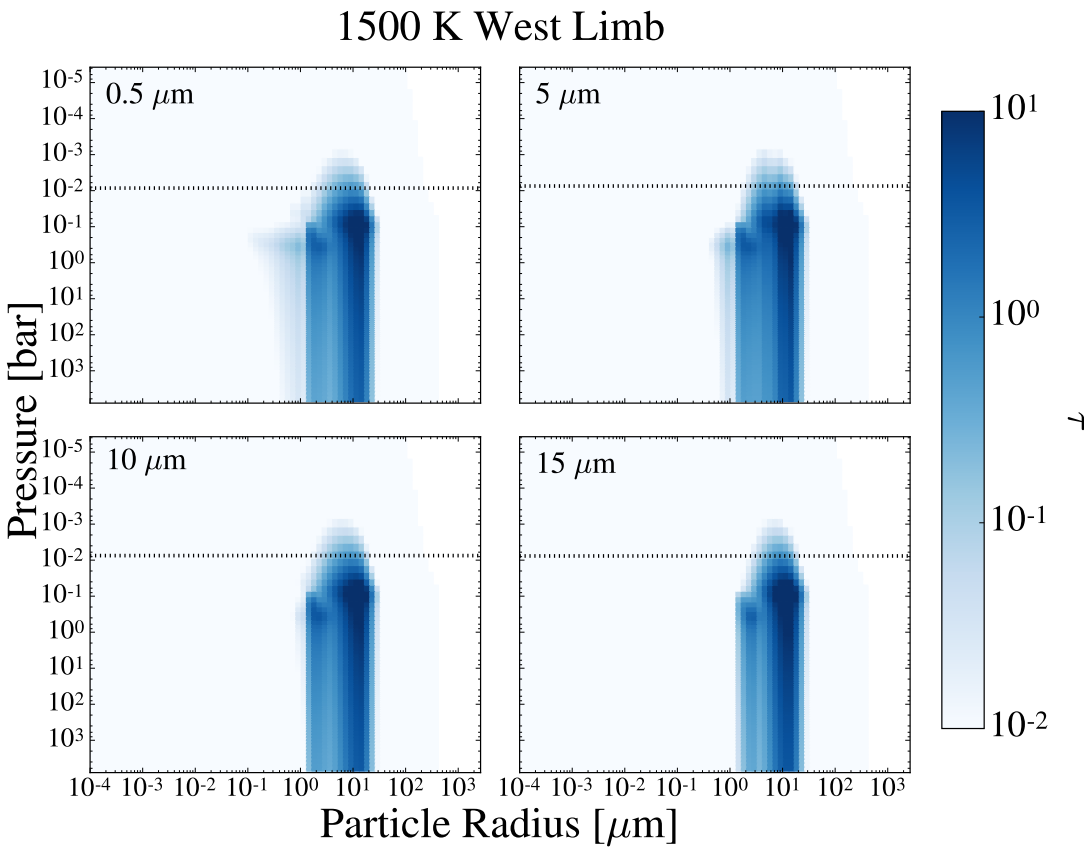


Figure 2.14: The contribution to the total cloud transmission opacity from each cloud particle size bin as a function of atmospheric pressure for 4 representative wavelengths. Shown is the case of a 1500 K hot Jupiter at the west limb. The black dashed line indicates the opaque cloud level at a given wavelength. The large cloud particle sizes cause the cloud opacities to be flat across a broad wavelength range.

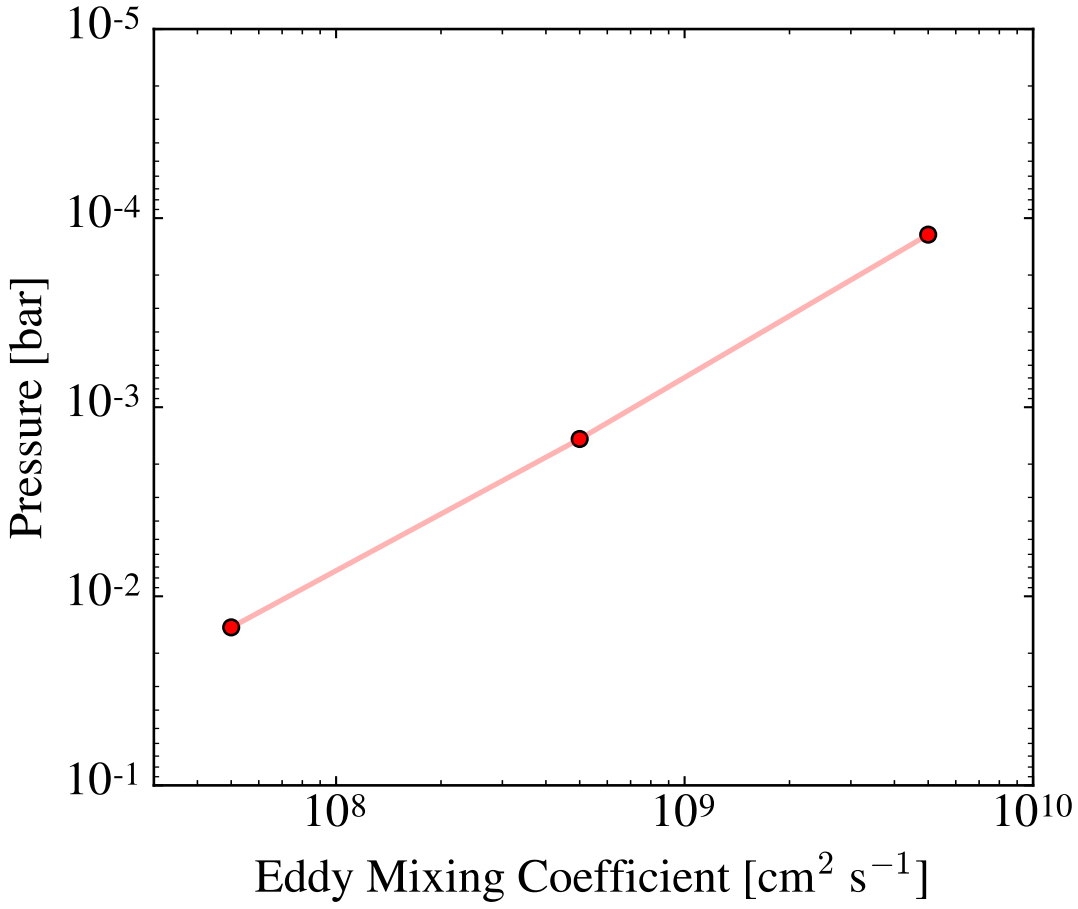


Figure 2.15: The opaque cloud level at 3 $\mu$m for a 1700 K hot Jupiter as a function of atmospheric vertical mixing. Increasing the vertical mixing coefficient by an order of magnitude correspondingly raises the location of the opaque cloud level by roughly an order of magnitude in pressure.

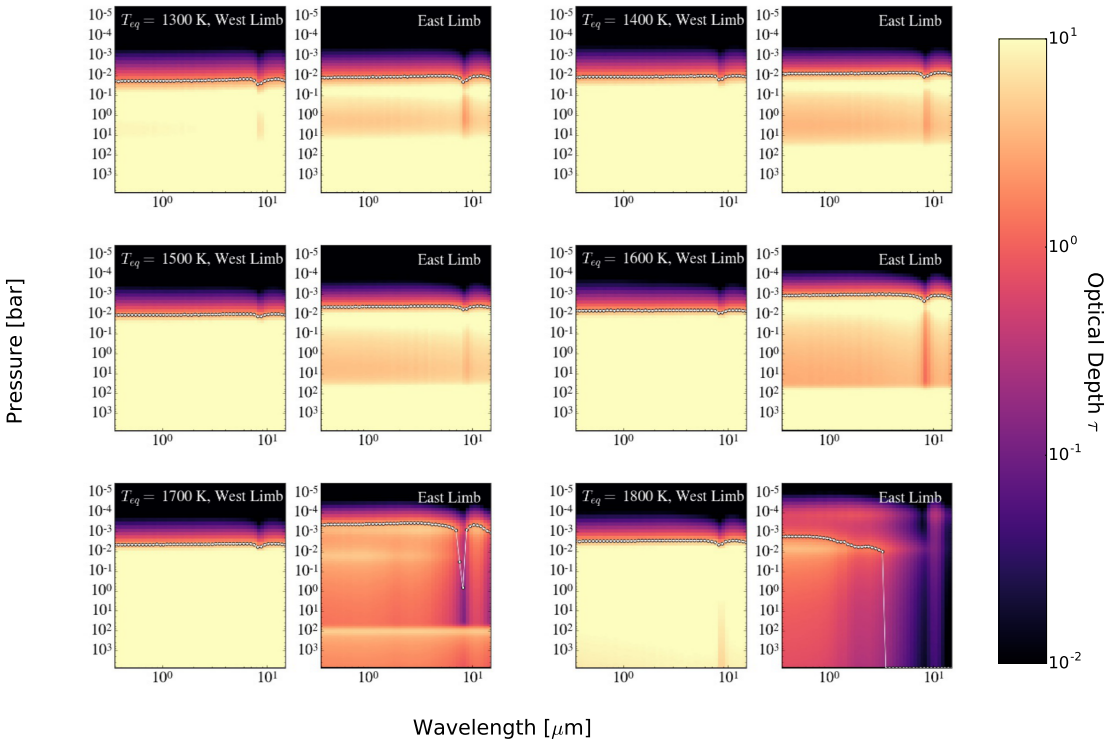


Figure 2.16: Cloud transmission opacities for the case of the low entropy interior. The white dotted line represents the opaque cloud level. There are noticeable hemispheric differences between the east and west limb for planets with equilibrium temperatures of 1700 and 1800 K.

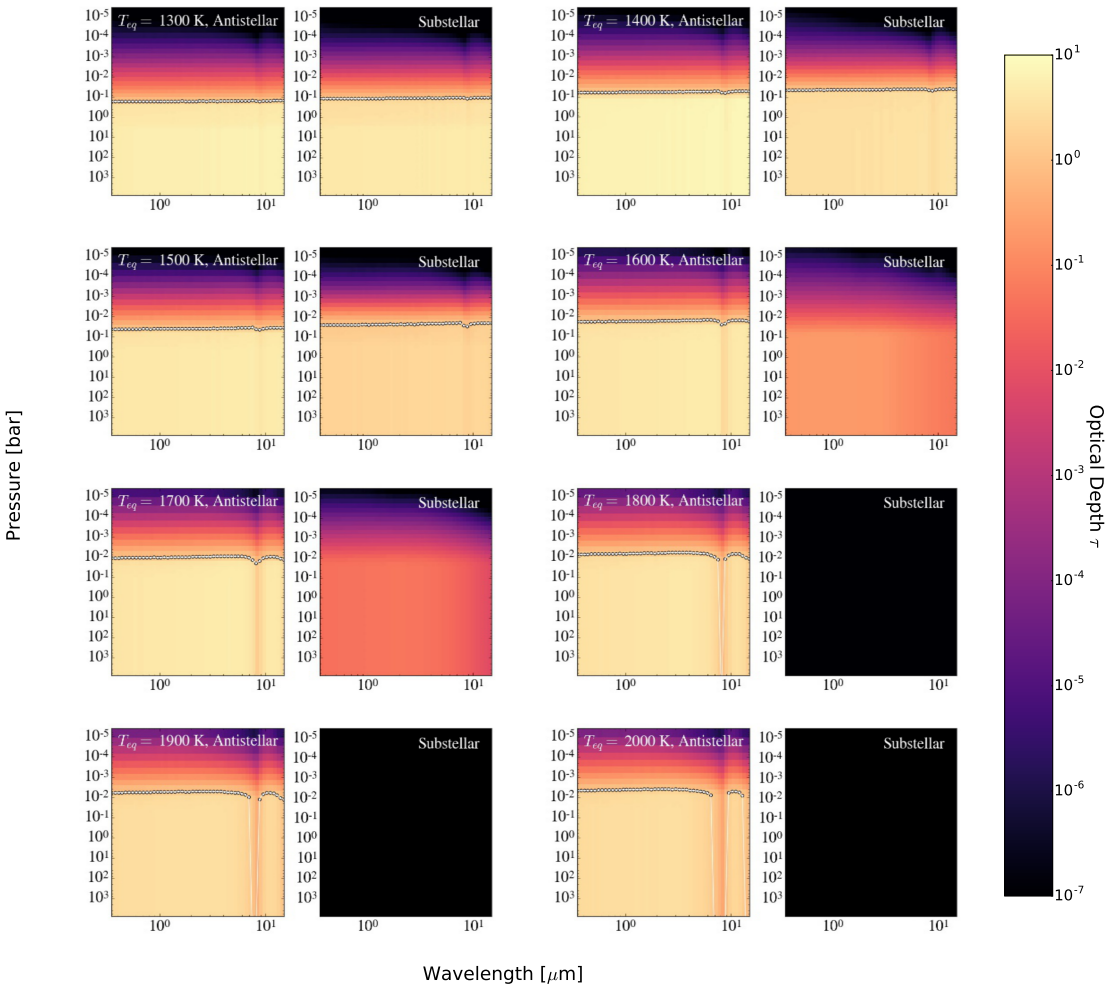


Figure 2.17: Cloud nadir view (emission) opacities for the case of the high entropy interior. The white dotted line represents the opaque cloud level. The clouds are optically thick along the antistellar point and optically thin for planets with temperatures greater than 1500 K at the substellar point.

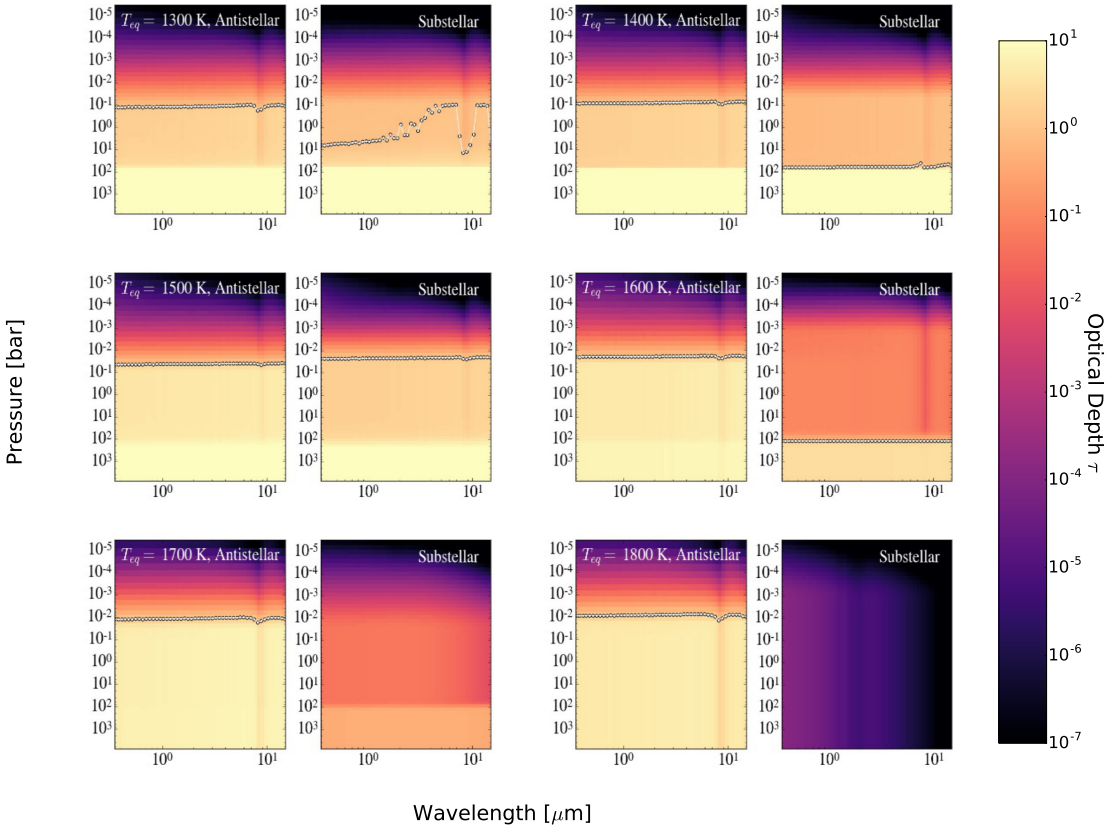


Figure 2.18: Cloud nadir view (emission) opacities for the case of the low entropy interior. The white dotted line represents the opaque cloud level. The clouds are optically thick in the deep atmosphere for equilibrium temperatures less than 1700 K due to the presence of a deep cold trap. These emission opacities significantly differ from the high entropy interior case.

wavelength range. One exception to this is a silicate absorption feature at 10 $\mu$m and a relatively clear region of the atmosphere at $\sim 8 - 9$ $\mu$m. These features in the infrared mirror the features in the refractive index of $MgSiO_3$ (see Wakeford & Sing 2015). Another exception is the east limb of the 1800 K planet, where only smaller $TiO_2$ cloud particles are abundant. The opacity profile in this case is reminiscent of the observed slope in transmission spectra at short wavelengths (e.g., Sing et al. 2016; Kirk et al. 2017).

Our calculated cloud opacities are gray across a large wavelength range due to the presence of relatively large cloud particles. Clouds can appear gray either due to having large sized particles or to a sharp increase in the number density of small particles near the cloud top (Benneke 2015). As shown in Figure 2.7.1, where we plot the cloud particle number density for the size bin that contributes the most to the opacity above the opaque cloud level, there is no such increase in cloud particles near the cloud top. The cloud particles instead appear opaque due to their large size, as indicated by Figure 2.7.1, where we plot each size bin's contribution to the total opacity for 4 representative wavelengths. While the opacity of each particle size bin varies with wavelength, the presence of relatively large particles causes the clouds to be gray across our full wavelength range.

We therefore conclude that it is unlikely that $MgSiO_3$ or $TiO_2$ clouds are responsible for the observed Rayleigh scattering slope in the optical confirming the result found using a different framework in Lee et al. (2017). For $MgSiO_3$ this is due to the inefficient rate of homogenous nucleation at small sizes as well as this species's

efficient growth. These two effects skew the particle distribution towards larger radii. While $TiO_2$ does nucleate homogeneously at small sizes, the number density of small cloud particles in the upper atmosphere is insufficient to produce the observed Rayleigh slope. The Rayleigh-like slope requires the presence of many small cloud particles in the upper atmosphere which may still occur for these cloud species if there is an enhanced presence of CCN (such as photochemical hazes) such that the gas supply is preferentially used for nucleation and growth is starved.

$MgSiO_3$ cloud particles contribute to silicate dust features at $\sim$ 10 $\mu$m that may be observable with JWST. However, these features are not as large as predicted by previous work (e.g., Wakeford & Sing 2015) due to the presence of large cloud particles. Furthermore, the cloud particles in our modeling are sufficiently opaque that we do not expect that signatures of a cloud base will be observable, as proposed by Vahidinia et al. (2014). The possible exception to this may be for clouds along the east limb for $T_{eq} > 1800K$ (see Figure 2.7), however, this would depend on the magnitude of the gas opacity which we do not take into account.

The strength of vertical mixing in an atmosphere will determine the location of the opaque cloud level. This is shown in Figure 2.7.1, where we plot the opaque cloud level pressure at 3 $\mu$m as a function of vertical mixing for a 1700 K hot Jupiter. Increasing the vertical mixing coefficient by an order of magnitude correspondingly raises the opaque cloud level by roughly an order of magnitude in pressure.

We now examine the cloud transmission opacities for the low entropy interior cases to understand the efficiency of the deep cold trap. The deep cold trap is inefficient

at most locations and equilibrium temperatures at limiting cloud formation in the upper atmosphere, such that the upper level clouds are optically thin in transmission. These opacities are shown in Figure 2.7.1. This is particularly true for the west limb, where the cloud particles high in the atmosphere are nearly as opaque as the cloud particles in the deep atmosphere. The cold trap is more efficient along the east limb. However, this effect is not typically large enough to significantly impact the location of the opaque cloud level as compared to the case of the high entropy interior.

The presence of a deep cold trap will likely be of increased importance in atmospheres with inefficient vertical mixing. This is because gas will be comparatively slow to diffuse to the upper atmosphere and replenish the supply of condensible material. Limiting the supply of cloud forming material in the upper atmosphere thus strengthens the effect of the deep cold trap. Furthermore, for planets with temperature profiles similar to those of the low entropy interior case, the presence of two cloud decks could complicate observational determinations of total cloud mass or atmospheric metallicity, as the deep clouds do not contribute to the observed opacity.

### 2.7.2 Nadir View Opacity

We calculate the cumulative optical depth of the clouds in a nadir viewing geometry for the antistellar and substellar points. This geometry is equivalent to a planet viewed in emission.

All planets in our high entropy grid are opaque in emission at the antistellar point with an opaque cloud level that ranges from $10^{-1}$ – $10^{-2}$ bar as shown in Figure 2.7.1. Planets with equilibrium temperatures greater than 1500 K are clear at the

substellar point across all wavelengths. For planets with temperatures less than 1500 K, the opaque cloud level at the substellar point is at roughly the same location as it is at the antistellar point.

The opacity profile in emission for these clouds is again flat and featureless across a broad wavelength range with the exception of a 10 $\mu$m absorption feature for planets with equilibrium temperatures greater than 1600 K. This absorption feature is accompanied by a narrow wavelength range for which the clouds are relatively clear, from roughly 8 – 9 $\mu$m, again mirroring features in the refractive index for $MgSiO_3$.

There is a difference between the high and low entropy cases in emission, as shown in Figure 2.7.1. The deep cold trap causes the opaque cloud level to be located lower in the atmosphere for the low entropy interior at the substellar point for equilibrium temperatures less than 1700 K. For these planets, the clouds in the upper atmosphere are clear across a broad wavelength range. There are also distinctive infrared features at the antistellar point in the 1300 and 1400 K planets and at the substellar point in the 1500 K planet that are not present in the case of the high entropy interior.

This difference in emission opacities demonstrates that observable cloud properties can be an indicator of the internal thermal structure of a planet and can even distinguish between different planetary inflation mechanisms. We therefore predict that differences in the internal structure of a hot Jupiter should be most readily observable in emission, particularly as this viewing geometry is a more sensitive probe of cloud mass (Fortney 2005a).

Interestingly, the nadir view cloud opacity at the substellar point for a low

entropy 1500 K planet are opaque slightly higher in the atmosphere than at the anti-stellar point. This location and equilibrium temperature represents a special case in which the atmosphere is hot enough such that only titanium clouds will form while the upper atmosphere is cool enough such that both silicate and titanium clouds are able to form (see Figure 2.1). This means that a supply of SiO gas is able to reach the upper atmosphere and form enough large clouds such that the upper cloud deck becomes opaque. This, along with the 1600 K case, are the only substellar cases in our modeling where both cloud species form while only one species is cold trapped. This differs from the substellar point of the 1400 K planet where both cloud species are cold trapped and both are also able to form in the upper atmosphere. The lower cold trap in this case limits cloud formation in the upper atmosphere such that the population of high clouds is optically thin in a nadir viewing geometry. The 1500 K planet also differs from the substellar point of the 1600 K planet where the supersaturation of silicate clouds in the upper atmosphere is significantly lower, resulting in the formation of only optically thin clouds high in the atmosphere. For the 1700 K planet at the substellar point only titanium clouds are cold trapped and only an optically thin layer of titanium clouds form in the upper atmosphere.

### 2.7.3 Single Scattering Albedo

Here we determine whether scattering plays an important radiative role for titanium and silicate clouds. We do this through calculating the single scattering albedo (SSA) of our cloud particle size distributions for both the nadir and transmission viewing geometry. The SSA is the ratio of the scattering efficiency to the total extinction

efficiency. When the SSA is close to unity the particles are strong scatterers and when the SSA is close to zero the particles are strong absorbers. This is particularly important as previous work by Heng et al. (2012) has shown that a consideration of scattering effects from clouds and hazes will modify the inferred temperature profile of a planet.

For all wavelengths and for all cases with appreciable clouds, scattering plays an important role in emission at wavelengths shorter than 10 $\mu$m. This is shown in the top panel of Figure 2.7.1 for the nadir viewing geometry for a 1500 K hot Jupiter at the antistellar point. While scattering is dominant at short wavelengths, it continues to play a significant role across the full wavelength range considered.

We also derive the single scattering albedo for our cloud particle distributions as viewed in transmission. While scattering effects are not typically calculated in modeling transmission spectroscopy, previous work has shown that scattering in transmission may be important in understanding spectra (Robinson 2017).

For all of our planet cases, scattering in transmission is significant. For example, the SSA for the representative case of a 1500 K hot Jupiter at the west limb for the high entropy interior case ranges from $\sim 1$ at shorter wavelengths to $\sim 0.5$ at wavelengths larger than 10 $\mu$m, as shown in the middle panel of Figure 2.7.1. This indicates that scattering is important in transmission calculations for silicate and titanium clouds.

This is further confirmed through a calculation of the asymmetry parameter, as shown in the bottom panel of Figure 2.7.1. The asymmetry factor indicates a particle's tendency to forward scatter, where particles with an asymmetry parameter of unity are

strongly forward scattering. Across all wavelengths and relevant pressures, titanium and silicate clouds are strong forward scatterers. This again indicates the importance of considering scattering effects in relevant transmission calculations.

### 2.7.4 The Impact of Using Realistic Particle Size Distributions

Using the fully resolved cloud particle size distribution has a distinct impact on derived atmospheric observables, indicating that detailed cloud modeling is essential for understanding the atmospheres of hot Jupiters. We confirm this by calculating the amount by which the full particle size distribution changes the opaque cloud level in transmission as compared to a calculation using the mean particle size alone.

For this comparison, we calculate three different mean particle sizes for each cloud species at each vertical level in the atmosphere. We calculate the mass weighted mean particle size, the area weighted mean particle size, and the cross section weighted mean particle size. We assume for each mean particle size that the total cloud mass is the same as for the full particle size distribution calculated using CARMA. We are then able to calculate transmission opacities for the resulting cloud particle distributions. A comparison of the opaque cloud level for these four methods is shown in Figure 2.7.1.

All methods that use a mean particle size underestimate the cloud opacity by a factor of $\sim 3 - 5$ or more. The reason for this is that all methods of deriving a mean particle size tend to skew towards a large mean value that neglects the substantial contributions to the opacity from smaller particles in the size distribution.

At higher equilibrium temperatures, the cross section weighted mean particle size nearly matches the opaque cloud level derived using the full size distribution at

short wavelengths. For lower equilibrium temperatures, all three mean particle size methods underestimate the opacity by roughly the same amount across all wavelengths. This shows that a consideration of the full cloud particle size distribution is essential for accurate spectral analysis.

A consideration of the full particle size distribution gives further insight into the process by which cloud particles impact atmospheric observables. For instance, the particle size that contributes the most to the cloud opacity depends on the cloud particle size distribution. Wakeford & Sing (2015) find that the largest particle size contributes the most to the opacity for a log-normal particle size distribution. However, we find that the largest particle size does not always contribute the most to the opacity for our fully resolved size distributions. This effect is shown in Figure 2.7.1, where we examine each particle size bin's contribution to the total cloud opacity in transmission at four representative wavelengths. In this case, the largest particles do not contribute the most to the opacity at the opaque cloud level.

In cases where there are significant populations of both large and small cloud particles, it is possible for large cloud particles to dominate the cloud opacity and effectively obscure cloud material in the deep atmosphere. This effect is wavelength dependent and can again be seen in Figure 2.7.1. In cases such as these, careful modeling of observations is necessary to accurately determine the total cloud mass and/or cloud dependent metallicity.

### 2.7.5 Comparison to Observational Inferences

We now provide a brief comparison of our more general results to several observed planets. The presence of a gray cloud deck is a necessary feature to understand the transmission spectra of most hot Jupiters. Our calculations confirm that the presence of a gray cloud deck should be ubiquitous across a range of planetary temperatures.

We are able to reproduce the opaque cloud deck for WASP 43b ($T_{eq}$ = 1440 K, Blecic et al. 2014) with a consistent location of the cloud top (opaque cloud level) of P = $10^{-1^{+1.1}_{-0.8}}$ bar as given in Kreidberg et al. (2014a). Recent retrievals in transmission for WASP 17b ($T_{eq}$ = 1740 K) and WASP 19b ($T_{eq}$ = 2050 K) indicate the presence of a cloud top at roughly $10^{-3}$ bar (Barstow et al. 2017), consistent with our derived cloud tops in transmission for similar equilibrium temperatures. Similarly, the presence of a gray cloud deck in the mid-atmosphere of HD 209458b ($T_{eq}$ = 1400 K) necessary to understand the transmission spectra (Benneke 2015) naturally arises from our calculations. Rough constraints on the cloud top of 200 mbar to 0.01 mbar from Benneke (2015) are roughly consistent with the cloud top inferred from our models for a hot Jupiter with a similar equilibrium temperature.

Additionally, WASP 2b ($T_{eq}$ = 1284 K), WASP 24b ($T_{eq}$ = 1583 K), and HAT-P 5b ($T_{eq}$ = 1713 K) have notably flat spectra across a broad wavelength range consistent with the presence of a gray cloud deck as derived in our calculations for planets of similar equilibrium temperatures (Turner et al. 2017). WASP 31b ($T_{eq}$ = 1580 K) also shows damped spectral features, again indicating the presence of a gray cloud deck (Sing et al. 2016).

Our derived titanium and silicate cloud populations do not produce the Rayleigh scattering slope at short wavelengths as observed in the transmission spectra of many hot Jupiters (Sing et al. 2016). This confirms the result from (Lee et al. 2017) where they are unable to fully reproduce observational slopes using condensational clouds. This slope might instead be due to the large abundance of small photochemical haze particles (Lavvas & Koskinen 2017) or the presence of a different cloud species. Or the Rayleigh slope could also be due in part to contaminating stellar activity (e.g., McCullough et al. 2014).

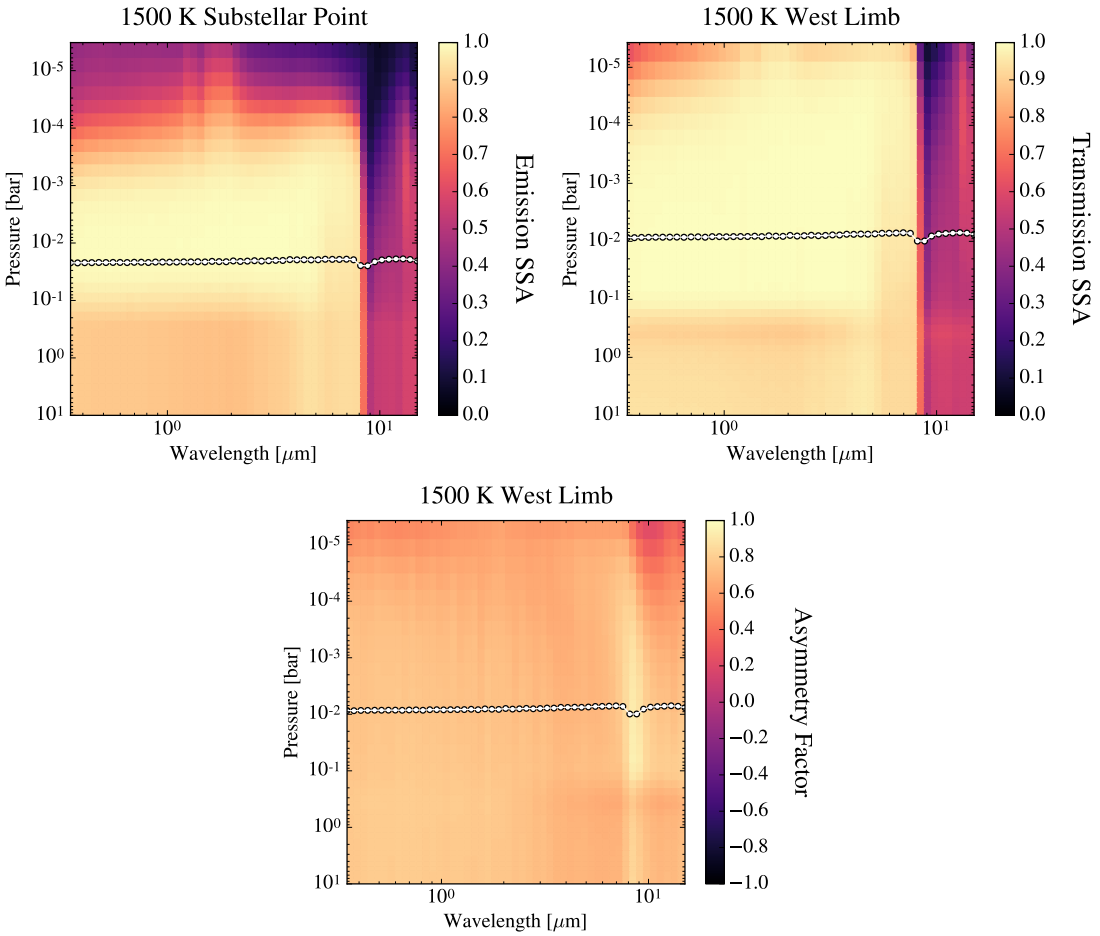


Figure 2.19: Scattering properties of titanium and silicate cloud particles in a 1500 K planet with a high entropy interior. The white dotted lines indicate the opaque cloud level at each wavelength. Across all sampled wavelengths and pressures, titanium and silicate clouds are strong forward scatterers. This is particularly true for wavelengths shorter than 10 $\mu$m. Top Panel: Cumulative single scattering albedo as a function of wavelength and pressure as observed in emission. Middle Panel: Single scattering albedo as observed in transmission. Bottom Panel: Asymmetry parameter as observed in transmission.

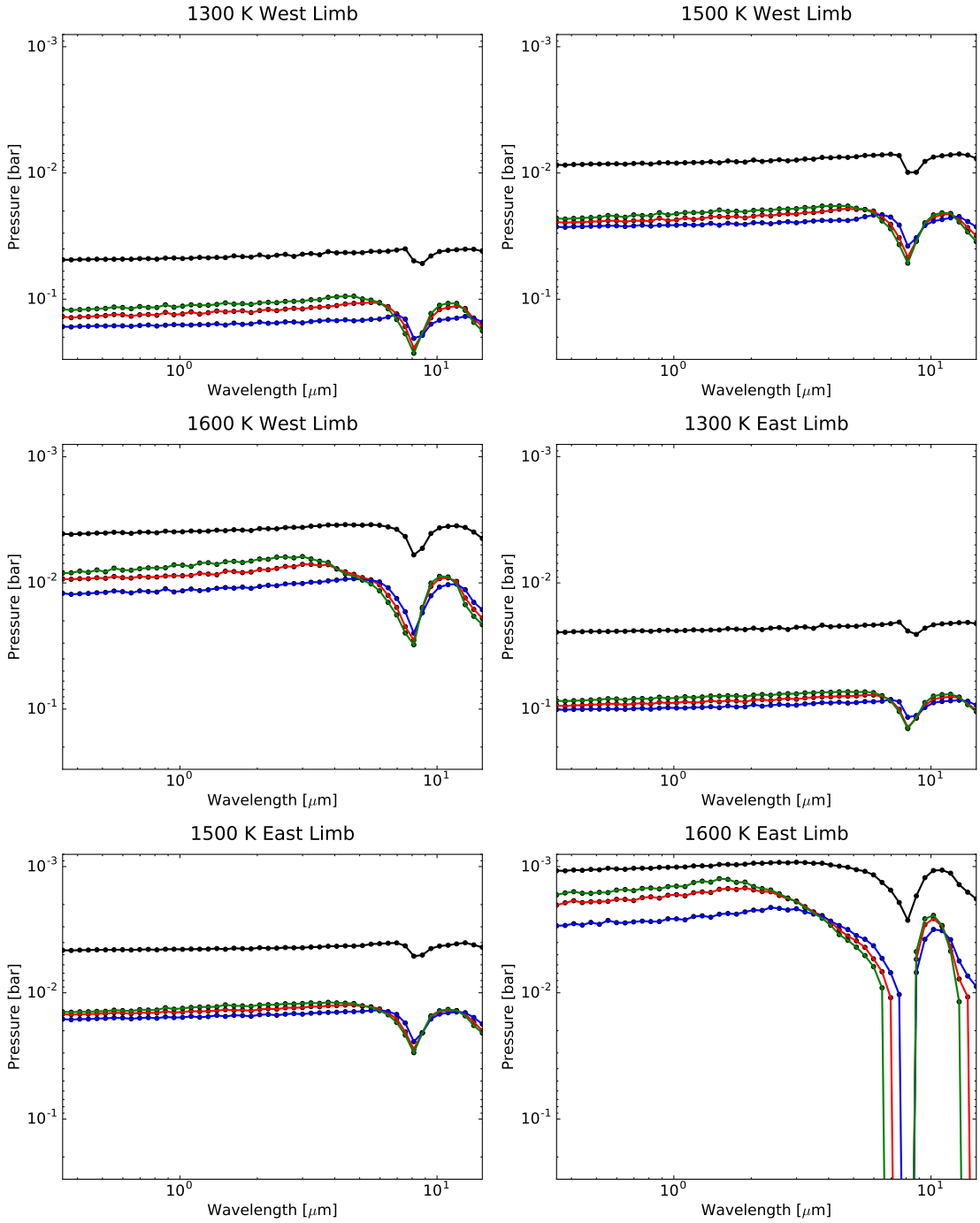


Figure 2.20: The opaque cloud level as a function of wavelength and pressure calculated using the full particle size distribution (black), a representative mass weighted mean particle size (red), a cross section weighted mean particle size (green), and an area weighted mean particle size (blue). Methods that use a mean particle size typically underestimate the cloud opacity by a factor of $\sim 3$ to 5 or more.

## 2.8 Summary and Conclusions

We present the first bin-scheme microphysical model of cloud formation on hot Jupiters. This framework can predict detailed cloud properties from first principles. In particular, this approach enables a derivation of the fully resolved cloud particle size distribution that will become increasingly important as atmospheric datasets continue to improve.

In this work we summarize the theory of cloud formation from the microphysical perspective, with a particular emphasis on the processes of nucleation, condensational growth, and evaporation. We then detail modifications made to the Community Aerosol and Radiation Model for Atmospheres to model cloud formation in the atmospheres of hot Jupiters. In our modeling, we consider a representative grid of planets that range in equilibrium temperature from 1300 - 2100 K with two different cases for their interior thermal structure. We also vary the amount of vertical mixing in the atmosphere and consider the impact this has on our derived cloud properties. We consider two cloud species thought to condense in this temperature range, $TiO_2$ and $MgSiO_3$. We introduce characteristic timescales of relevant processes in our model as a means to intuitively understand how the interplay between these processes influences cloud properties.

We derive fully resolved particle size distributions, total cloud masses, and vertical distributions of cloud particles for our full grid of hot Jupiters. We place these results in context by comparing the results from our modeling approach to those from other cloud models. We also calculate cloud opacities in both emission and transmission,

the single scattering albedo and the asymmetry parameter of the cloud particles, and the increased accuracy obtained using a full particle size distribution as opposed to a mean particle size. These calculations allow us to determine the observational implications of our models and we compare these results to published observational inferences. Our main conclusions are summarized below.

1. Cloud particle size distributions are not log-normal and are instead bimodal, broad, or irregular in shape. Silicate clouds tend to be distributed broadly with an indistinct peak. Titanium clouds often have a bimodal distribution with both nucleation and growth modes.

2. The population of titanium cloud particles is typically smaller in particle size than the population of silicate cloud particles. Titanium cloud particles are frequently abundant throughout the upper atmosphere while silicate clouds are abundant closer to their cloud base.

3. Cloud properties depend strongly on planetary properties—in particular the temperature profile of the planet and the vertical mixing in the atmosphere. We discover a strong negative correlation between total cloud mass density and equilibrium temperature. With increased planetary equilibrium temperature, the cloud base is higher in the atmosphere and the cloud cover becomes increasingly inhomogeneous. We find that increased vertical mixing increases both the total cloud mass and the vertical extent of the clouds in the atmosphere.

4. The presence of an isothermal-like layer in planets with a low entropy interior

gives rise to a deep cold trap at around 100 bar. Despite the presence of this deep cold trap, there is still significant cloud formation in the upper atmosphere.

5. The clouds are gray across a large wavelength range in transmission and emission due to the relatively large size of the cloud particles. In both emission and transmission, the cloud opacity profile is featureless across a broad wavelength range with the exception of small features in the infrared.

6. While the east limb has less total cloud mass than the west limb, the opaque cloud level is located higher in the atmosphere for $T_{eq} \leq 1700$ K. The east limb therefore appears observationally to become more cloudy with increasing equilibrium temperature until the planet becomes too hot for clouds to form. Clouds form on the west limb for all planets considered in our grid.

7. Titanium and silicate clouds have strong forward scattering properties across a broad wavelength range in both transmission and emission. This indicates that a consideration of cloud scattering effects will be important when making observational inferences.

8. A consideration of the full cloud particle size distribution leads to distinctly different cloud opacities as compared to a consideration of a mean particle size alone, often by a factor of $\sim$ 3 - 5.

9. When the full cloud particle size distribution is considered, the largest particles do not always dominate the opacity. The particle size that dominates the cloud opacity is instead dependent on the specific cloud particle size distribution. It is

also possible to have a large reservoir of "hidden" cloud mass that does not contribute to the observed cloud opacity as the cloud opacity alone is often sufficiently opaque enough to obscure the cloud base.

10. Due to the large size of our modeled silicate clouds it is unlikely that they are responsible for the Rayleigh scattering slope in the optical—we do not see this feature in our opacity modeling. Titanium clouds are also not able to reproduce the observed Rayleigh slope.

11. In emission, at the substellar point, the cloud opacity is highly sensitive to the presence of a deep cold trap. This indicates that cloud properties may serve as useful probes of the thermal state of a planet's interior.

This work reveals the richness and complexity involved in determining cloud properties from first principles. The results produced using bin-scheme microphysics have already changed our understanding of clouds on hot Jupiters.

We plan to study this richness in more detail. In particular, there are three notable caveats to our modeling that we plan to address in future publications: (1) we only consider two cloud species, although other species might condense, (2) we do not consider horizontal transport of particles, and (3) we do not consider radiative feedback from clouds on the background atmospheric temperature structure. We also plan to derive full transmission spectra capable of being directly compared to observations. We are currently working to expand CARMA to 2D and eventually 3D to study the interplay between microphysics and atmospheric circulation.

# Chapter 3

# Transit Signatures of Inhomogeneous Clouds on Hot Jupiters: Insights from Microphysical Cloud Modeling

## 3.1 Abstract

We determine the observability in transmission of inhomogeneous cloud cover on the limbs of hot Jupiters through post processing a general circulation model to include cloud distributions computed using a cloud microphysics model. We find that both the east and west limb often form clouds, but that the different properties of these clouds enhances the limb to limb differences compared to the clear case. Using *JWST*

it should be possible to detect the presence of cloud inhomogeneities by comparing the shape of the transit lightcurve at multiple wavelengths. This method is statistically robust even with limited wavelength coverage, uncertainty on limb darkening coefficients, and imprecise transit times. We predict that the short wavelength slope varies strongly with temperature. The hot limb of the hottest planets form higher altitude clouds composed of smaller particles leading to a strong rayleigh slope. The near infrared spectral features of clouds are almost always detectable, even when no spectral slope is visible in the optical. In some of our models a spectral window between 5 and 9 microns can be used to probe through the clouds and detect chemical spectral features. Our cloud particle size distributions are not log-normal and differ from species to species. Using the area or mass weighted particle size significantly alters the relative strength of the cloud spectral features compared to using the predicted size distribution. Finally, the cloud content of a given planet is sensitive to a species' desorption energy and contact angle, two parameters that could be constrained experimentally in the future.

## 3.2 Introduction

Clouds are ubiquitous in the atmospheres of solar system planets and are seemingly abundant in the atmospheres of exoplanets as well, where they affect the atmospheric dynamics, radiative energy distribution, and chemistry. The presence of clouds on exoplanets is commonly inferred through damped spectral features and enhanced Rayleigh-like slopes in the optical (e.g., Crossfield et al. 2013; Fraine et al. 2013; Knutson et al. 2014b,a; Kreidberg et al. 2014b; Iyer et al. 2016; Sing et al. 2016; Louden

et al. 2017) and these effects on the atmospheric spectra strongly inhibit our ability to constrain fundamental atmospheric properties for the majority of exoplanets (e.g., Ackerman & Marley 2001; Morley et al. 2013; Knutson et al. 2014b; Kreidberg et al. 2014b; Sing et al. 2016; Powell et al. 2018; Gao & Benneke 2018). An understanding of clouds on exoplanets and their effect on the observed atmospheric spectra is thus essential in interpreting observations.

Transmission spectroscopy is the leading technique for characterization of exoplanet atmospheres (e.g., Seager & Sasselov 2000; Brown et al. 2001; Hubbard et al. 2001), but its reliance on a slant light path makes it especially susceptible to high altitude clouds (Fortney 2005b). Most analysis of transmission spectra use 1D atmospheric models that assume temperature structures, chemical abundances, and cloud particle size distributions that are longitudinally and latitudinally homogeneous (e.g., Kreidberg et al. 2014b; Morley et al. 2015; Sing et al. 2016). However, exoplanets are inherently 3D with spectra that may be different at different locations due to differences in temperature structure (e.g., Feng et al. 2016; Caldas et al. 2019), atmospheric mixing (e.g., Dobbs-Dixon et al. 2012), cloud properties (e.g., Lee et al. 2015a, 2016; Powell et al. 2018; Lines et al. 2019), or a combination of the aforementioned - leading to a globally averaged spectra that is a combination of different spectra from different planetary locations.

### 3.2.1 Inhomogenous Cloud Cover on Hot Jupiters

Hot Jupiters have particularly inhomogeneous atmospheres because they are highly irradiated by their host stars and are likely tidally-locked which causes them

to have strong day-night temperature contrasts. The efficiency of heat redistribution in these atmospheres decreases for planets with higher equilibrium temperatures such that the day-night temperature contrast is particularly extreme for the hottest planets (Perez-Becker & Showman 2013; Komacek & Showman 2016).

Because cloud properties are highly sensitive to the local atmospheric thermal structure, we expect that these large temperature contrasts will lead to clouds with substantially different masses, vertical distributions, particle size distributions, and compositions (Powell et al. 2018). In particular, there are two identified mechanisms that could give rise to inhomogeneous cloud cover in the atmospheres of hot Jupiters (Line & Parmentier 2016). The first relies on the meridional transport of cloud particles from the equator to the poles (Parmentier et al. 2013; Charnay et al. 2015). The second relies on significant temperature gradients across the planet that alter the local cloud formation processes, leading to inhomogeneous cloud cover (e.g., Parmentier et al. 2016).

For many hot Jupiters, the temperature structure on the east limb is substantially hotter than the west limb such that the gaseous species that can condense and form clouds differ significantly (Powell et al. 2018). In particular, hot Jupiters with $T_{eq}$ in the range of 1800 – 2100 K may represent the most dramatic cases of inhomogeneous limb cloud cover. Cooler hot Jupiters may very well exhibit similar inhomogeneity as has been inferred from observations of HD 209458b ($T_{eq} \approx 1400$ K) (MacDonald & Madhusudhan 2017). However, previous work has proposed that atmospheric dynamics may reduce latitudinal and longitudinal inhomogeneities in the cloud properties of cooler hot Jupiters (Lee et al. 2017; Lines et al. 2018), complicating the general picture

of cloud inhomogeneity.

To date, there are roughly 25 hot Jupiters that have been observed in either transmission, emission, or reflection, within a range of equilibrium temperatures that may form significantly inhomogenous clouds (May et al. 2018; Fu et al. 2017; Tsiaras et al. 2018; Sing et al. 2016; Bixel et al. 2019; Zhang et al. 2018; Demory et al. 2013; Hu et al. 2015; Webber et al. 2015; Shporer & Hu 2015; Ranjan et al. 2014; Wong et al. 2015; Mackebrandt et al. 2017, etc.) and nearly all of these planets have spectral signatures that are interpreted as being due to the presence of clouds or hazes.

### 3.2.2 Finding a Transmission Signature of Inhomogenous Cloud Cover

Currently, the most robust measure of cloud inhomogeneity is optical phase curves which have offsets (the maximum of the phase curve compared to the secondary eclipse) that can probe longitudinal cloud cover (e.g., Parmentier et al. 2016). Using this method, signatures of inhomogenous cloud cover have been observed in the atmospheres of three hot Jupiters - Kepler-7b, Kepler-12b, and Kepler-41b - the only currently identified planets with optical phase curves that are dominated by atmospheric processes and can be modeled independently of approximations needed to simultaneously model orbital effects (Demory et al. 2013; Hu et al. 2015; Webber et al. 2015; Shporer & Hu 2015). The presence of inhomogeneous clouds is thus likely common because all of the planets with robust two dimensional atmospheric information have signatures of inhomogeneous clouds (Shporer & Hu 2015). In observations of optical phase curves, however, there can be substantial non-atmospheric processes, such as doppler boosting, tidal ellipsoidal distortion, and planetary obliquity, that require approximations for this

form of analysis (see review by Shporer 2017). This, coupled with the comparative difficulty of phase curve observations (Shporer 2017; Parmentier & Crossfield 2018) makes this method of probing inhomogeneous cloud cover difficult to generalize to the vast majority of hot Jupiters. It is therefore of great use to determine a robust observational signature of cloud inhomogenity in transmission alone which, in addition to aiding in planetary characterization, can also be used to constrain models of planetary phase curves.

Simplified atmospheric modeling has shown that inhomogeneous clouds on the east and west limbs can mimic an atmosphere with high mean molecular weight when observed in transmission (Line & Parmentier 2016). In addition, single-hemisphere clouds produce significant residuals in the shape of the transit light curve when fitted with a model assuming uniform limb radii (Line & Parmentier 2016; von Paris et al. 2016). It has also been suggested that inhomogeneous aerosol coverage could be a diagnostic for distinguishing between clouds and haze in hot Jupiters with $T_{eq} \gtrsim 2000$ K (Kempton et al. 2017a). However, specific transmission signatures of inhomogeneous cloud cover have not been well constrained.

In this work we present transmission signatures of inhomogeneous cloud cover that should be observable using the *James Webb Space Telescope* (*JWST*). In Section 3.3 we describe our non-equilibrium cloud model in which we determine cloud properties from first principles and discuss our model planet parameters and choice of model grid. In Section 3.5, we present our derived cloud properties at the relevant locations in the planetary atmosphere for our grid of model hot Jupiters. We calculate transmission

spectra using the cloud properties derived from our microphysical model for different planetary locations in our grid in Section 3.6 and discuss specific transmission signatures of condensible clouds and their effect on the transmission spectra as a whole. We then present forward and inverse modeling of the light curves of these modeled planets in Section 3.7 and present statistically robust transmission metrics of inhomogeneous clouds using *JWST*. We discuss our results in Section 5.7 and present our conclusions in Section 3.9.

## 3.3 Cloud Model

Clouds form via complex microphysical processes that depend strongly on planetary properties, notably a planet's thermal structure, chemical composition, and the strength of mixing in the atmosphere (e.g., Lee et al. 2015a, 2016; Powell et al. 2018; Gao & Benneke 2018). To model condensible clouds in the atmospheres of hot Jupiters we use the non-equilibrium one dimensional Community Aerosol and Radiation Model for Atmospheres (CARMA) (Turco et al. 1979b; Toon et al. 1988) version 3.0 (Bardeen et al. 2010, 2008). CARMA is a well tested code that was developed to study clouds on Earth and has since been applied to reproduce and understand observations of clouds on Mars (Michelangeli et al. 1993; Colaprete et al. 1999), Venus (Gao et al. 2014), Titan (Barth & Toon 2003, 2004, 2006), and Pluto (Gao et al. 2017). For a comprehensive discussion of the microphysics and history of CARMA see Gao et al. (2018); Turco et al. (1979b); Toon et al. (1988); Jacobson et al. (1994). We adapted CARMA to simulate titanium and silicate clouds on hot Jupiters in our previous work (Powell et al. 2018),

and in this paper we use an updated version of the model that includes additional cloud species (Gao et al. 2020, also see Appendix A.1). We present a brief description of our model setup and refer readers to Powell et al. (2018) and Gao et al. (2020) for a more detailed discussion.

CARMA treats the microphysical processes of homogenous nucleation, heterogenous nucleation, condensational growth, evaporation, and coagulation as well as vertical transport of cloud particles due to atmospheric mixing and gravitational settling. For a comprehensive discussion of these processes and the role they play in atmospheres of hot Jupiters see Powell et al. (2018). CARMA resolves the cloud particle size distribution using bin-scheme microphysics. In the bin-scheme approach, the size distribution is discretized into multiple bins according to size and the particles in each bin evolve freely and interact with other bins in an Eulerian framework. There is no a priori assumption of the particle size distribution. Bin-scheme microphysics is widely used in cloud formation models of Earth's atmosphere and is able to reproduce the multimodal and broad distributions of cloud particles (e.g., Fan et al. 2007; Duan et al. 2019). Furthermore, CARMA is a non-equilibrium cloud model such that it simulates the time-dependent formation and evolution of cloud particles. This model can therefore capture subtleties of cloud variability due to microphysical processes. Due to the inherent difference in magnitude between the timescale of atmospheric mixing and the timescales of microphysical processes (Barth & Toon 2003; Powell et al. 2018), our model does indeed predict cloud variability that may be real. However, in this work we present results that are time averaged over this steady state microphysical variability.

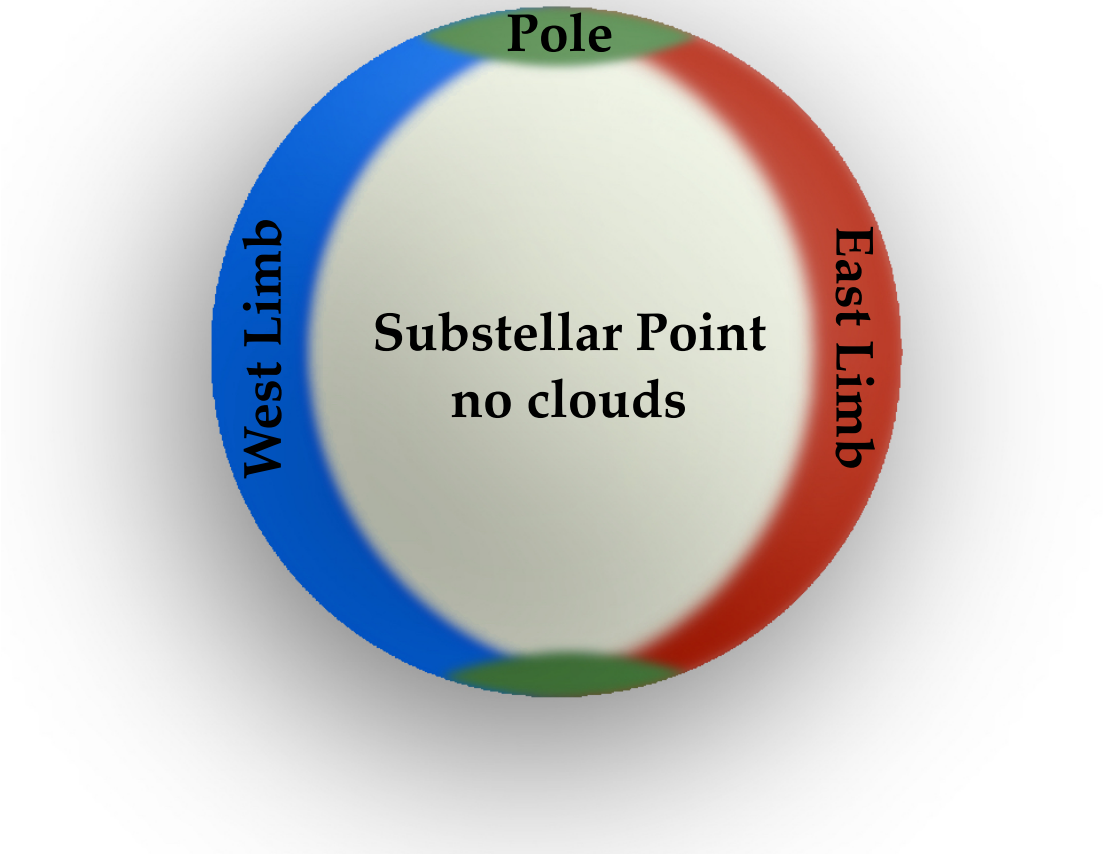


Figure 3.1: A schematic of the atmospheric regions along the terminator of a hot Jupiter that we sample in our modeling: the poles (green), east limb (red), and west limb (blue). For the temperature ranges probed in our modeling we do not expect cloud formation on the dayside (Powell et al. 2018), such that the clouds from the west limb cannot be transported to the east limb along a superrotating equatorial jet.

Table 3.1: Model Parameters

| | Values |
|---|---|
| Surface Gravity | 1000 cm $s^{-2}$ |
| Atmospheric Mole. Wt. | 2.2 g $mol^{-1}$ (H/He) |
| T-P Profiles | Figure 3.3 |
| Vertical Mixing | Section 3.4.2 |
| Time Step | 100 s |
| Total Simulation Time | $10^9$ s |
| Mass Ratio Between Bins | 2 |
| Number of Bins | 80 |
| Smallest Bin Size | 1 nm |
| **Boundary Conditions** | |
| Clouds (Top) | Zero Flux |
| Condensation Nuclei (Top) | Zero Flux |
| Condensible gases (Top) | Zero Flux |
| Condensible gases (Bottom) | Solar abundance |
| Clouds (Bottom) | 0 $cm^{-3}$ |
| Condensation Nuclei (Bottom) | 0 $cm^{-3}$ |

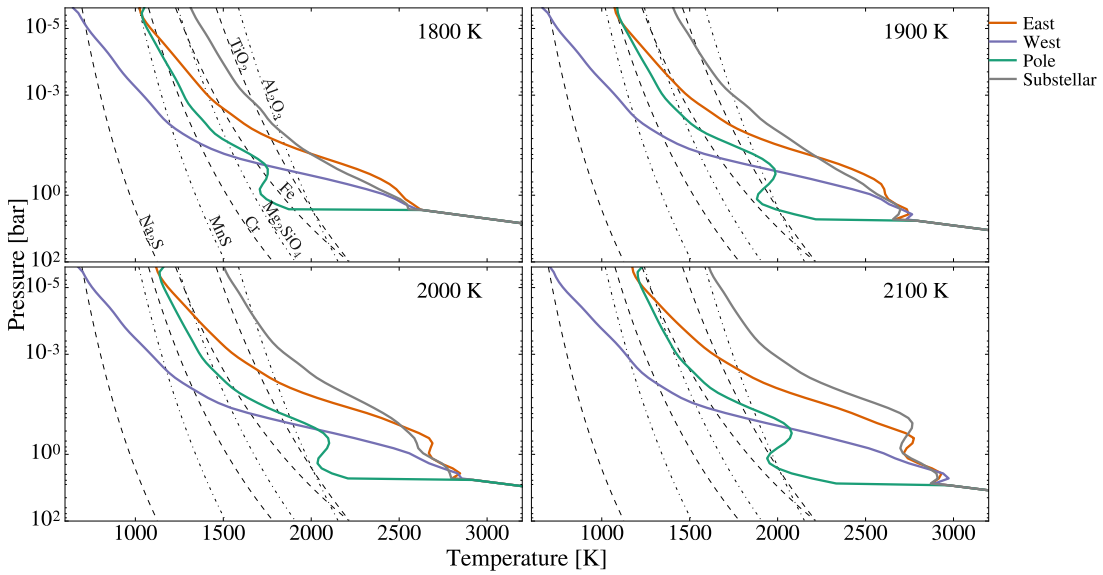


Figure 3.2: Pressure temperature profiles at the east limb, west limb, and poles for four planets with equilibrium temperatures ranging from 1800 - 2100 K. These temperature profiles all converge to an internal adiabat at a few bar. The dashed black lines indicate the condensation curves for the different species that we consider in our modeling.

In our model setup, gaseous species initially diffuse from the lower atmosphere until they reach a point in the atmosphere where the gas becomes supersaturated and cloud formation occurs via nucleation. In this model, the cloud species with the lowest surface tension ($TiO_2$) homogeneously nucleates and forms clouds. Once these cloud particles grow to a large enough size such that curvature effects no longer prevent heterogeneous nucleation, they become cloud condensation nuclei for other cloud species which are treated separately after nucleation occurs. These species will continue to grow through either condensation or coagulation. This growth is inhibited primarily by gravitational settling which causes cloud particles to fall to hotter regions of the atmosphere and quickly evaporate. For specific values used in our model setup see Table 3.1.

## 3.4 Simulation Cases

Ideally, we would fully couple our microphysical cloud model to a 3D general circulation model (GCM) (e.g., Lines et al. 2018). However, these simulations are currently computationally expensive, such that running a large grid of models is not yet feasible, and dependent on initial conditions. As a first approximation, we use output from a GCM to determine the temperature structure of the atmosphere and then compute cloud properties with our 1D model at specific locations along the terminator, namely the east limb, west limb, and poles. A schematic of our model setup is shown in Figure 3.3. This approach is similar to that in Helling et al. (2019a,b), however, we model a grid of planets instead of a detailed study of an individual planet and we

particularly focus on the cloud properties along the atmospheric limbs accessible to transmission observations.

### 3.4.1 Pressure/Temperature Profiles

We consider a grid of four hot Jupiters that range in equilibrium temperature from 1800 - 2100 K derived from the SPARC/MITgcm as presented in Parmentier et al. (2016). We utilize the GCM derived temperature profiles down to a pressure where interior models indicate that the temperature structure becomes adiabatic (Thorngren et al. 2019; Gao et al. 2020) - typically around the few bar level for planets with such high equilibrium temperatures. At this point the atmosphere is optically thick such that assumptions about the deep atmosphere will not change the resulting gas opacities, though they may alter the inferred cloud properties through the presence (or lack) of a deep cold trap (see Powell et al. 2018). The temperature structure of hot Jupiter interiors is highly uncertain, however, and a variety of internal structures are likely necessary to explain the observed diversity in radii (e.g., Guillot & Gautier 2014; Komacek & Youdin 2017). The temporally averaged limb temperature profiles are taken from the GCM at longitudes of -90° (west limb) and 90° (east limb) and are latitudinally averaged. The temporally averaged polar profile is sampled at a latitude of 90°. These temperature profiles thus differ from those presented in Powell et al. (2018). The resulting temperature profiles for each planet in our grid are shown in Figure 3.3.

We sample each atmosphere at the east limb, west limb, and polar region and calculate cloud properties. We sample the limbs and poles in particular as we are interested in the planetary properties as viewed in a transmission viewing geometry. Every

model planet in our sample has an east limb temperature structure that is significantly hotter than the west limb and the pole at all pressures lower than 1 bar (see Figure 3.3). While all of the planets in our grid are relatively hot such that the efficiency of their heat redistribution is low, they are not uncommon in the known sample of hot Jupiters (e.g., May et al. 2018; Fu et al. 2017; Tsiaras et al. 2018; Sing et al. 2016; Bixel et al. 2019; Zhang et al. 2018; Demory et al. 2013; Hu et al. 2015; Webber et al. 2015; Shporer & Hu 2015; Ranjan et al. 2014; Wong et al. 2015; Mackebrandt et al. 2017).

### 3.4.2 Atmospheric Vertical Mixing

The amount of vertical mixing in an atmosphere regulates the cloud formation process through delivering a fresh supply of condensible volatiles to the upper atmosphere where cloud formation can occur. In the supply-limited regime of cloud formation modeled in this work, the higher the vertical mixing in the atmosphere, the more cloud formation occurs (Powell et al. 2018).

We use globally averaged vertical mixing profiles for each planet derived from general circulation models that include tracer transport. We parameterize all vertical motions in the planetary atmosphere using eddy diffusion, controlled by a diffusive term known as $K_{zz}$. These profiles are calculated using time-averaged SPARC/MITgcm simulations for a highly irradiated Jupiter-sized planet (Parmentier et al. 2016; Parmentier et al. 2019). The method used to derive these $K_{zz}$ profiles follows Parmentier et al. (2013) (see their eq. 23) and Zhang & Showman (2018a,b) and depends on the tracer gradient, which can be both positive or negative. For each planet, we fit a power-law to the tracer derived $K_{zz}$ values, as shown in Figure 3.4.2, and assume a constant value

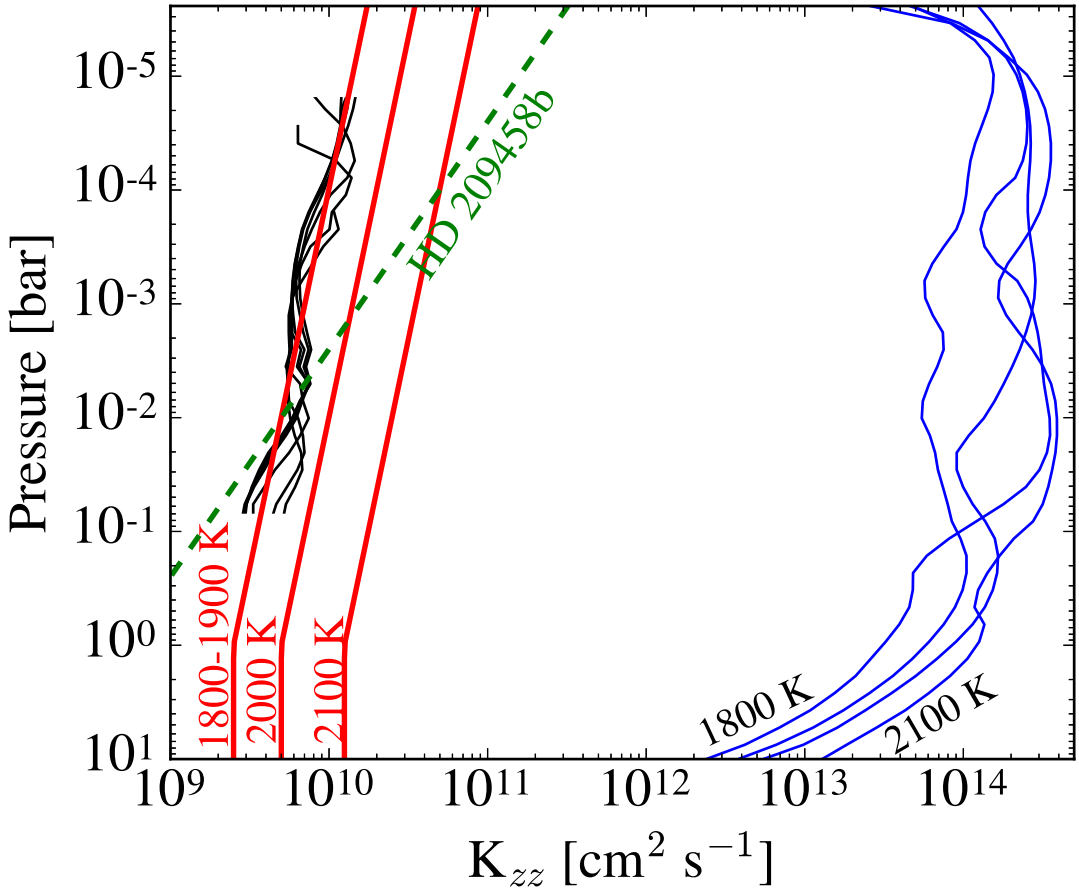


Figure 3.3: Globally averaged $K_{zz}$ profiles used in this work (red lines) fit to the transport of tracers with sizes 0.1-100 $\mu$m (black lines, for the 1800 K case) with a power-law in the upper atmosphere and a constant value below 1 bar. The previous tracer derived $K_{zz}$ profile for the cooler hot Jupiter, HD 209458b, is also shown (green line) as well as the roughly approximated $K_{zz}$ values derived for each planet (blue lines) as a global area-weighted root mean square of the vertical velocity times the vertical scale height. For every planet, the tracer-derived vertical mixing profile is roughly three orders-of-magnitude less than the approximate profile derived from the vertical wind speed.

below 1 bar as the GCM derived $K_{zz}$ is inaccurate at lower pressures due to integration time.

For all of the planets in our sample, the vertical mixing operates roughly the same for particles that range in size from 0.1-100 $\mu$m. There is also less of a dependence of mixing strength on atmospheric pressure in the upper atmosphere as was derived for the cooler hot jupiter, HD 209458b (Parmentier et al. 2013). Furthermore, the value of the vertical mixing is smaller by roughly 3 orders-of-magnitude compared to the global root mean square of the vertical velocity multiplied by the vertical scale height as shown in Figure 3.4.2, a common estimate of $K_{zz}$ in the literature.

The $K_{zz}$ profile that best describes the planets in our sample with $T_{eq}$ of 1800 and 1900 K is:

$$K_{zz} = \begin{cases} 2.5 \times 10^9 \mathrm{cm^2 s^{-1}} / P_{\mathrm{bar}}^{0.15} & P < 1 \text{ bar}, \\ 2.5 \times 10^9 \mathrm{cm^2 s^{-1}} & P > 1 \text{ bar}. \end{cases} \tag{3.1}$$

For planets with $T_{eq}$ = 2000 and 2100 K, the Kzz profiles are factors of 2 and 5 larger than that in Equation (3.1). The globally averaged vertical mixing in our modeling thus slightly increases with increased equilibrium temperature in this model range as predicted in Komacek et al. (2019).

### 3.4.3 Choice of Temperature Range

Our grid has a temperature range of 1800 - 2100 K. We chose this range as this regime may correspond to a maximum in limb cloud inhomogeneity. While most hot

Jupiters have significant temperature gradients from east to west that could very well lead to inhomogeneous cloudiness, cloud cover may be able to homogenize between the two limbs if both the atmospheric circulation from west to east is efficient and clouds are able to survive crossing the dayside of the planet or clouds are able to form efficiently on the dayside itself.

There are two possible circulation patterns on hot Jupiters that work to equilibriate insolation gradients (Showman et al. 2013). The first circulation pattern is jet dominated and is characterized by an efficient superrotating wind across the planetary equator from west to east where the efficiency with which this flow structure equilibriates the planetary temperature decreases with increasing equilibrium temperature (e.g., Komacek & Showman 2016). The second pattern is eddy dominated and is characterized by large scale flows from the dayside to both the nightside and the two limbs. The GCM models presented in this work are do not contain additional drag to the numerical one (Koll & Komacek 2018) such that they are in the jet-dominated regime. At these temperatures, however, magnetic effects or others might drag the winds and drive the flow towards the eddy dominated regime which may homogenize the temperature structure at the limbs (Showman et al. 2013). The strength of the drag in these atmospheres depends on planetary properties, such as the magnetic field strength, such that there may be planets with drag and planets without. We thus assume that the planets presented in this work have flows that are dominated by west to east advection such that the west limb can only directly advect material to the east limb via the superrotating equatorial wind.

For hot Jupiters with equilibrium temperatures larger than 1800 K, it is possible that no species of cloud forms on the dayside as it is too hot for titanium clouds, the most likely cloud condensation nuclei (Lee et al. 2018), to form and serve as nucleation sites for cloud species with higher condensation temperatures. If planets in this temperature range do still form superrotating equatorial jets, the clouds that form on the west limb will rapidly evaporate when advected across the dayside as the timescale for evaporation is very short, on the order of seconds or less when thermodynamically favorable (Powell et al. 2018) while the time to cross the dayside is $\sim R_p/v_{\rm advect} \sim 10^5$ seconds. Thus the cloud distribution on the east limb is likely isolated from the other more efficient cloud forming regions. Thus, for hot Jupiters with $T_{eq} > 1800$ K, the east and west limbs on hot Jupiters might represent the most extreme case of inhomogeneous cloud cover. We further choose a maximum equilbrium temperature in our model grid of $T_{eq}$ of 2100 K as hotter planets may reside in a different regime due to increased magnetohydrodynamic effects.

### 3.4.4 Choice of Microphysical Parameters

There are two key microphysical parameters that regulate heterogeneous nucleation that are not currently well-constrained: the contact angle and the desorption energy (See Appendix A.2). We discuss the sensitivity of our results to these microphysical parameters in Section 3.6.5.

In this work, we approximate each species' desorption energy as half of its calculated latent heat of vaporization. This approximation has previously been used to estimate the desorption energy of water and other condensible species and may thus be

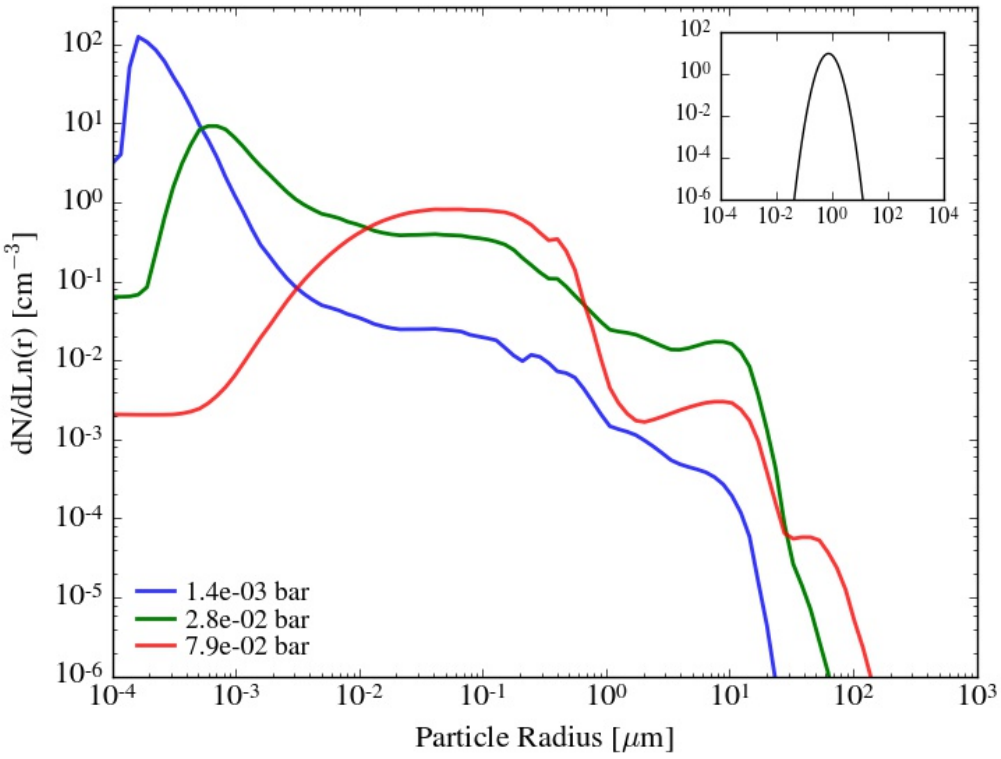


Figure 3.4: Combined particle size distributions for all cloud species at various atmospheric pressure levels for an 1800 K hot jupiter at the west limb. These size distributions are not log-normal and exhibit distinct bumps due to the different formation modes (i.e. nucleation mode vs. growth mode) of different cloud species. A log-normal size distribution is shown for reference.

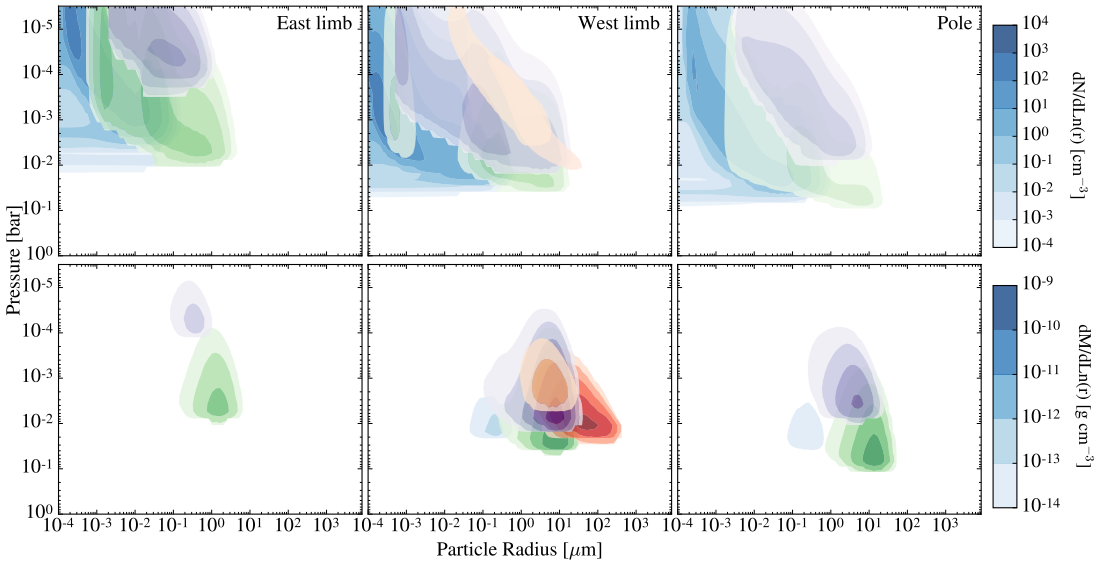


Figure 3.5: Particle number (top) and mass density (bottom) distributions at the east limb (left) west limb (middle) and pole (right) for a hot jupiter with an equilibrium temperature of 2000 K considering the maximum cloudy case. The cloud species shown are $TiO_2$ (blue), $Mg_2SiO_4$ (purple), $Al_2O_3$ (green), Fe (red), and Cr (orange).

the closest estimate we have for these values without detailed laboratory experiments (e.g., Greenwood et al. 2003; Bolis 2013; Kim et al. 2016). These values are given in the appendix in Table A.1. For the contact angle we choose the minimum theoretically motivated value, leading to a maximum in cloud formation, such that $\cos\theta_c = \sigma_C/\sigma_x$, where $\theta_c$ is the contact angle, $\sigma_C$ is the surface energy of the cloud condensation nuclei and $\sigma_x$ is the surface energy of the condensible species.

## 3.5 Cloud Properties and Particle Size Distributions

For each location on the planet we calculate cloud particle size distributions from first principles as a function of atmospheric depth. These particle size distributions change with cloud composition and atmospheric pressure level (Figure 3.4.4) and are

typically broad and irregular in shape. The shape of these particle size distributions gives rise to atmospheric features and changes the shape of the transmission spectra as described in Section 3.6.

The full two-dimensional cloud particle size distributions are shown for a nominal case of $T_{eq} = 2000$ K in Figure 3.4.4 for the three locations sampled in our grid. The cloud base of the different cloud species considered are often distinct from each other as they become supersaturated at different pressure levels in the atmosphere. This is particularly true at the east limb. Only the polar region of the $T_{eq} = 1800$ K exhibits a deep cold trap (see Powell et al. 2018). This cold trap is inefficient, however, as there is significant cloud formation in the upper atmosphere that contributes to the observed atmospheric opacity.

Interestingly, MnS clouds do not form. This is due to the relatively high surface energy of MnS which exponentially regulates nucleation efficiency and is roughly 10% larger than Fe, the species with the next largest surface energy. The degree of MnS supersaturation is also low compared to the nucleation barrier stemming from its high surface energy (see Figure 3.3) such that cloud formation does not occur. Iron, however, is able to form despite its high surface energy but is only able to do so at the west limb where it is significantly supersaturated. This illustrates that the condensation curve alone does not definitively describe when cloud formation will occur and detailed non-equilibrium microphysical studies are important when interpreting observations.

In all of the simulated cases, the west limb has over an order of magnitude higher condensed mass density than the east limb as shown in Figure 3.5. Furthermore,

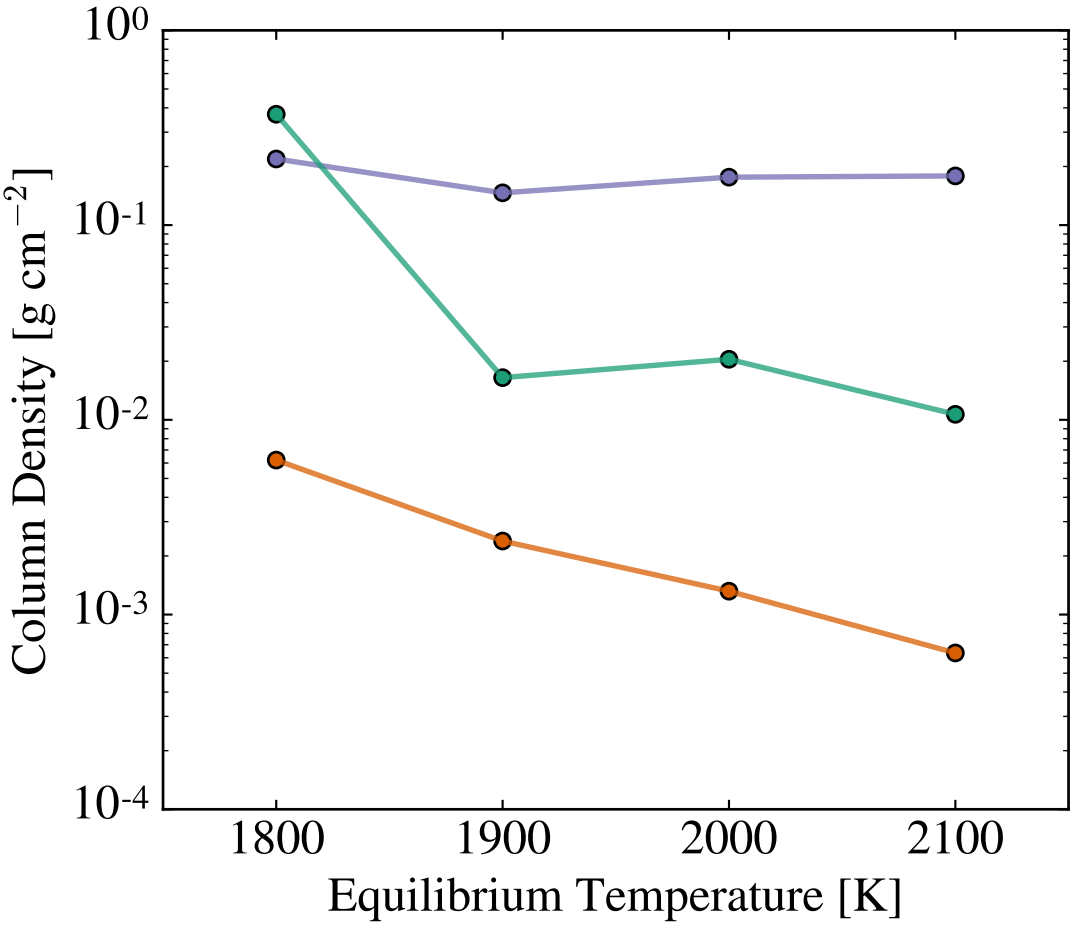


Figure 3.6: The column-integrated condensed mass density at the west limb (purple) exceeds that at the east limb (orange) for all equilibrium temperatures, and those at the pole (green) for all but the coolest equilibrium temperature. The planet with $T_{eq} = 1800$ K has a more mass at the pole than the west limb, though the majority of the mass is present in the deep atmosphere and does not contribute to the observed spectra.

the polar region of each planet has lower cloud mass density than the west limb in the upper regions of the atmosphere that contribute to the observed spectra.

## 3.6 Transmission Spectra

We modify Exo-Transmit (Kempton et al. 2017b) to consider the opacity from the fully resolved cloud particle size distributions calculated for these model atmospheres. We treat the cloud particles as Mie spheres and calculate the particle extinction cross sections using MIEX (Voshchinnikov 2004). Complex indices of refraction for Cr are taken from the compilation of Morley et al. (2012), those of $TiO_2$ are compiled in Posch et al. (2003); Zeidler et al. (2011) and those of Fe, $Mg_2SiO_4$ (crystalline), and $Al_2O_3$ are taken from the compilation in Wakeford & Sing (2015). In these calculations, we treat each cloud independently. While all cloud species other than $TiO_2$ are inhomogeneous in composition (with a $TiO_2$ core and a mantle of the primary condensible species) the optical properties are treated as that of the primary condensible species, an approximation that does not change the resultant spectral features in our results[1]. We calculate the abundance of the gaseous species assuming equilibrium chemistry with solar abundances including the rainout of condensible species. We do not include gaseous TiO or VO, consistent with the pressure/temperature profiles presented in this work, as the presence of these strong atmospheric absorbers in this range of equilibrium temperatures is uncertain. While TiO may well be present on the cloud-free daysides of these planets, we expect that much of the atmospheric TiO on the limbs of planets in this

[1] An test analysis of the spectra using PYMIECOATED, which calculates the optical properties of layered mie spheres, produces the same results.

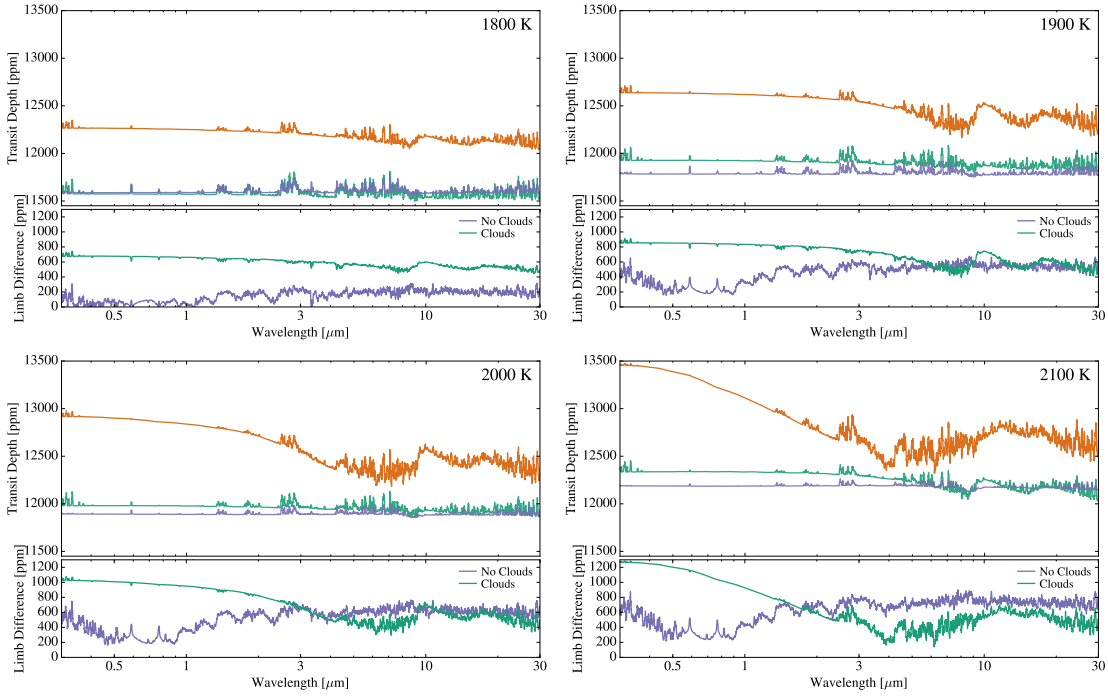


Figure 3.7: Transmission spectra (top half of each plot) for the east limbs (orange), west limbs (purple), and poles (green) at different equilibrium temperatures, and the difference between the limbs in the cloudy (green) and clear (purple) cases.

regime may be located in condensible species. All of the presented transmission spectra in this work have a binned resolution of R = $10^2$.

For every planet in our grid, the transmission spectra at the east and west limbs are significantly different (Figure 3.6). In particular, the transmission spectra of the east limb appear more clear and have noticeable molecular features at longer wavelengths. The west limb, however, appears significantly more cloudy with much more subdued molecular features. There is also a significant continuum difference between the two limbs such that the difference in spectra between the limbs can be as much as 1000 parts per million for a broad range of wavelengths. The transmission spectra for the polar region is similar to the west limb, though there are typically more spectral features

observable at longer wavelengths at the polar regions.

The difference in transmission spectra between different limb locations arises from differences in the atmospheric thermal structure which significantly alters both the cloud opacity and the total gaseous opacity. In particular, the local cloud properties are different at atmospheric locations with different temperature structures such that clouds form at different heights in the atmosphere with potentially different compositions as shown in Section 3.5. We discuss the specific effects of cloud properties on the transmission spectra in the following sections.

### 3.6.1 Observed Cloud Height

While the west limbs appear more cloudy when observed across a broad wavelength range due to significantly flattened spectral features (see Figure 3.6), the east limb can appear more cloudy than the west limb, particularly at wavelengths shorter than $\sim 2$ $\mu$m. This occurs because, while there is less total cloud mass on the east limb, the altitude where the relevant cloud species are supersaturated (the cloud base) is higher in the atmosphere (see Figure 3.3). Cloud formation is typically the most efficient near the cloud base (Powell et al. 2018). Thus, the higher cloud base can give rise to clouds that are opaque higher in the atmosphere with relatively low total cloud mass.

The pressure level where clouds become opaque in transmission (the cloud height) at 1.2 $\mu$m is shown in Figure 3.6.1 where, for both cloudiness cases at all equilibrium temperatures cooler than 2100 K, the cloud height is higher in the atmosphere along the east limb. Thus, while the east limb transmission spectra appear relatively

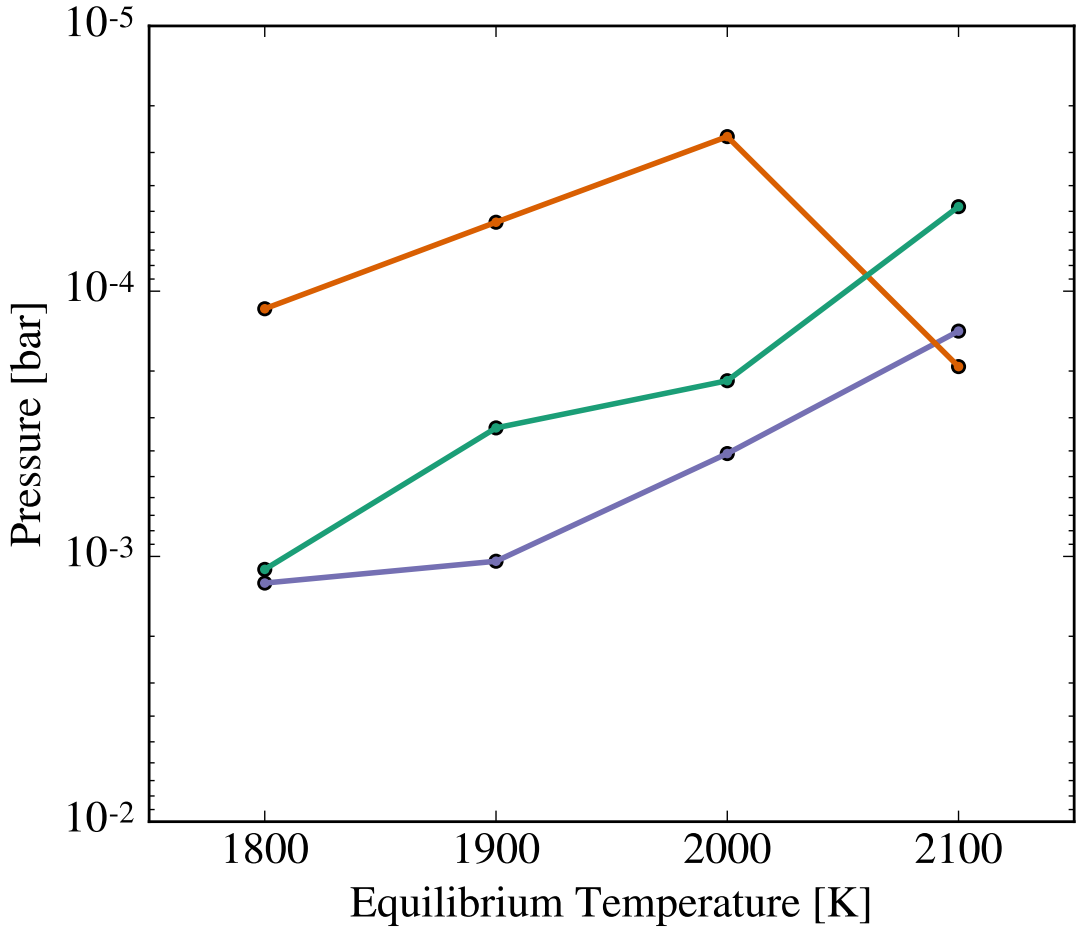


Figure 3.8: The opaque cloud layer at 1.2 $\mu$m at the west limb (purple), east limb (orange), and pole (green).

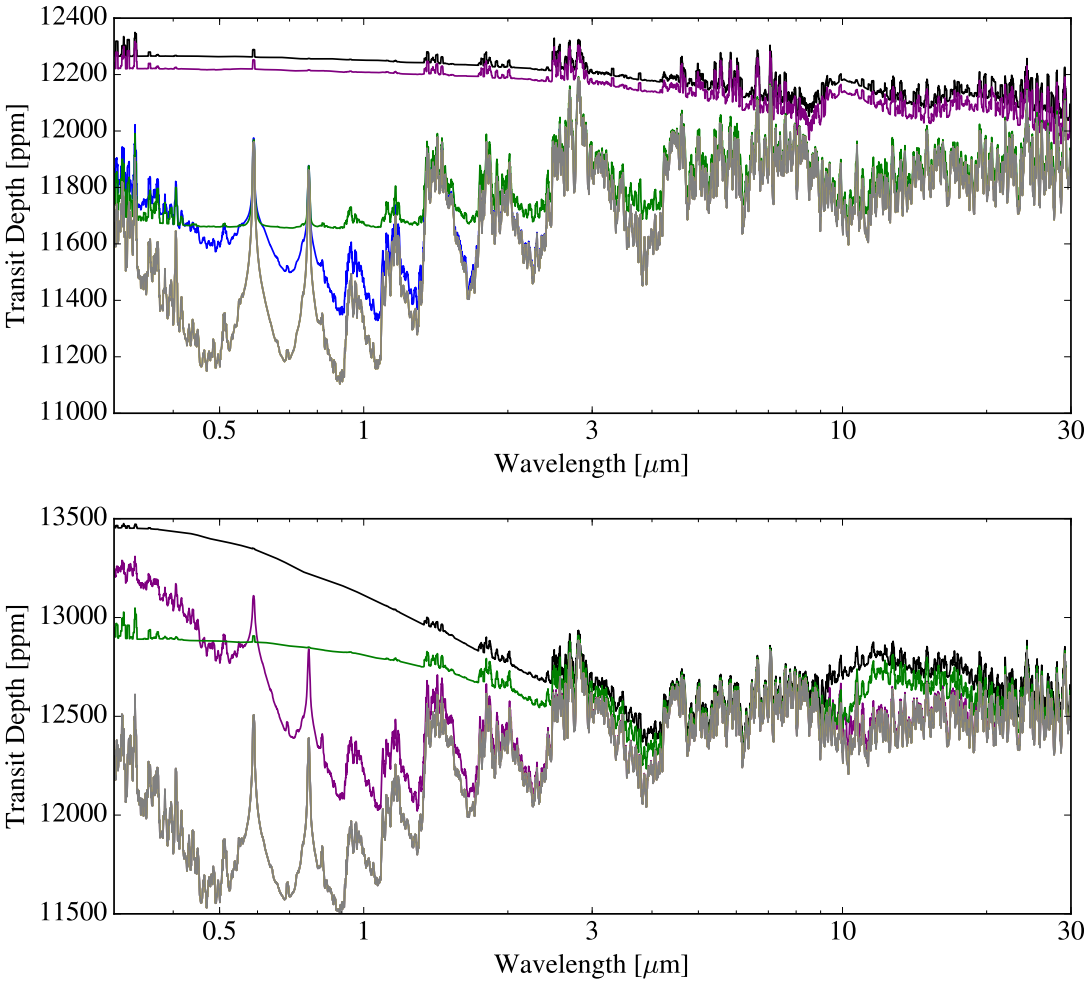


Figure 3.9: The contribution to the transmission spectra (black lines) from each cloud species for the 1800 K east limb (top) and the 2100 K east limb (bottom). Clear spectra for these planets are shown in gray. The cloud opacity is primarily dominated by silicate clouds (purple line) at all wavelengths except for the hottest regions of the hottest planets where aluminum clouds (green lines) play an increasingly significant role in shaping the spectrum. Titanium clouds (blue lines) primarily contribute to the total cloud opacity at short wavelengths.

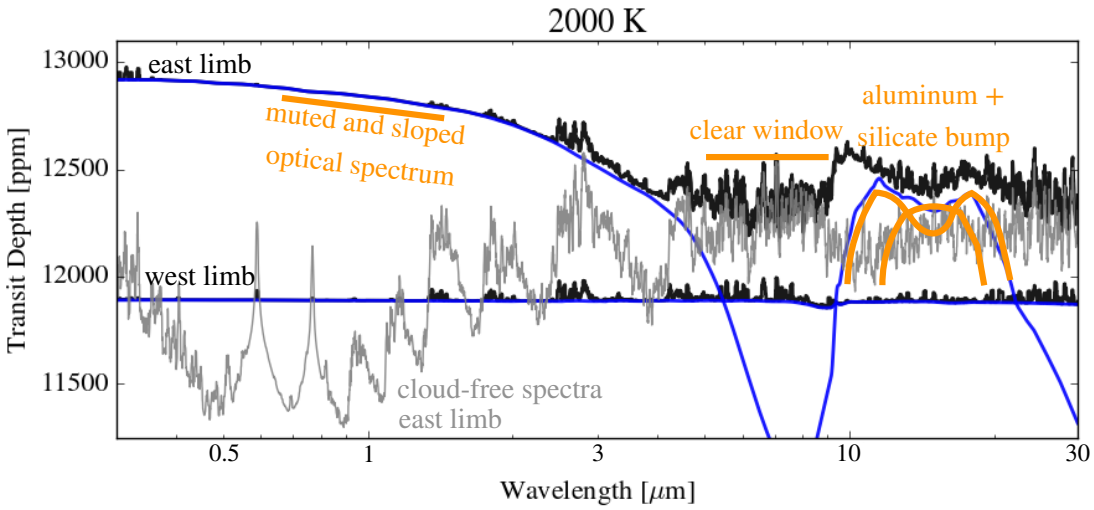


Figure 3.10: Transmission spectra (black lines) for a hot jupiter with an equilibrium temperature of 2000 K at the east and west limbs. The blue lines are the opacity continuum from clouds. The cloud-free transmission spectrum at the east limb is shown in gray. At the west limbs, clouds dominate the spectra at all wavelengths. At the east limb, clouds contribute to muted transmission features at short wavelengths and a sloped optical spectrum. There is a relatively clear window at 5-9 microns and enhanced silicate and aluminum cloud opacity from 10-20 microns.

clear at longer wavelengths where the clouds are less opaque, the features in transmission at short wavelength are often more damped in the hotter regions of the atmosphere with lower cloud mass.

### 3.6.2 The Dominant Cloud Species

We analyze each cloud species' contribution to the total opacity. As found in Gao et al. (2020), in nearly all cases the cloud opacity is dominated by silicate clouds with only small contributions to the total opacity from titanium and/or aluminum clouds. For the hottest planets in our sample at the east limb, where silicate cloud formation becomes less efficient, however, aluminum clouds tend to increasingly dominate the observed spectra. This is particularly true for the hottest planet in our grid at

the east limb, where aluminum clouds dominate the total cloud opacity and contribute to the Rayleigh-like slope in the optical. This is shown for two representative cases in Figure 3.6.1.

Both chromium and iron clouds, which form on the west limbs of all of the planets in our grid, do not significantly impact the transmission spectra due to their relatively low number densities as shown in Figure 3.4.4. While both of these species are able to grow to large, massive sizes once heterogeneous nucleation onto titanium seeds has occurred (the first step in the cloud formation process for Cr and Fe clouds), the rate of heterogeneous nucleation is suppressed due to the relatively high surface tensions of these species. Thus, while both cloud species can form particles that grow to large sizes, the total number of cloud particles is small in comparison with the more abundant aluminum, titanium, and silicate clouds. It is possible, therefore that significant constituents of the total cloud mass on the west limbs, such as Fe and Cr clouds, can have no significant impact on the observed spectra.

### 3.6.3 Significant Cloud Transmission Features

Our model spectra are strongly modulated by clouds as shown by muted spectral features, broad absorption features in the infrared, and sloped optical spectra. While clouds can give rise to a sloped optical spectrum, this can also arise due to stellar contamination and other effects (e.g., Oshagh et al. 2014; McCullough et al. 2014; Apai et al. 2018). However, the broad absorption features in the infrared in particular are clear, direct signatures of clouds.

Along the west limb for all of the planets, clouds act like gray absorbers and

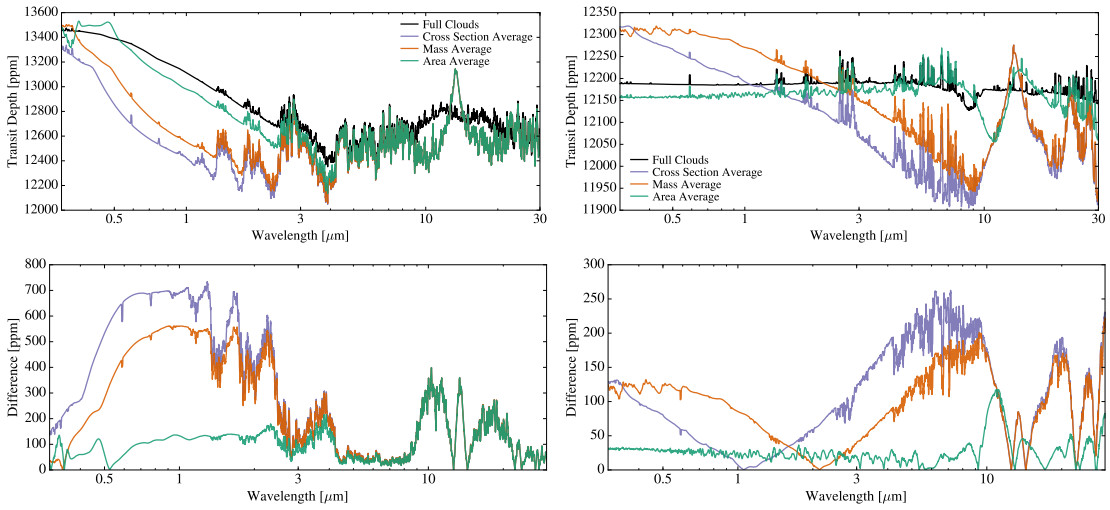


Figure 3.11: The absolute value of the difference between considering the fully resolved cloud particle size distribution (black spectrum) and assuming a mean particle size with the same cloud mass (blue, red, and green spectra) can be as large as 700 ppm. Here we show the 2100 K planet at the east (left) and west (right) limbs andthe difference between the full size distribution and a calculated mean size (left, bottom).

substantially damp the observed spectrum at all wavelengths as shown in Figure 3.6.1 (see also Figure 3.6). The damping of spectral features is a common outcome of the presence of clouds and occurs across a broad wavelength range when nucleation and condensation are efficient, as occurs on the west limbs. At the poles, we find similarly damped spectral features but begin to see a broad spectral signature of silicate clouds at $\sim$ 10 $\mu$m as predicted in Wakeford & Sing (2015) and $\sim$ 20 $\mu$m (i.e. 2100 K case in Figure 3.6. Also see Lee et al. 2019). These broad spectral features are clear signatures of the presence of clouds and often have amplitudes on the order of $\sim$100s of ppm which should be feasible for detection using *JWST* (Venot et al. 2019; Morley et al. 2017).

The east limbs show the most significant cloud features as demonstrated in Figure 3.6.1. At the east limb, the less massive populations of small cloud particles high in the atmosphere give rise to a muted and sloped optical spectrum, with slopes

that increase with increased temperature, as well as signatures of silicate (at $\sim$ 10 - 30 $\mu$m) and/or aluminum clouds (at $\sim$ 15 $\mu$m). Intriguingly, these hotter regions of the atmosphere have a cloud-free spectral window from $\sim$ 5 - 9 $\mu$m. These transmission features on the east limb are qualitatively similar to the mie slope and spectral window seen in the sub-neptune GJ 3470b (Benneke et al. 2019). Thus, the marginally super-saturated regions of a planetary atmosphere, despite forming fewer clouds, frequently provide a more clear signature of both the species and properties of the clouds present in the atmosphere.

### 3.6.4 Sensitivity to Cloud Particle Size Distributions

Considering the fully resolved cloud particle size distribution is essential when calculating observed transmission spectra and interpreting observations. To demonstrate this importance we compare the derived transmission spectra using calculated CARMA cloud opacities to a transmission spectra calculated using a single representative cloud particle size for each species at each atmospheric height. In particular, we consider the case in which the total condensed cloud mass is conserved. We calculate the average particle size through averaging the full CARMA cloud particle size distribution weighted by particle cross-section ($\pi r^2$), area ($\pi r^3$), or mass.

Transmission spectra calculated using a fully resolved particle size distribution differ distinctly from those calculated using a mean particle size for planets in our sample. Two examples of this effect are shown in Figure 3.6.3. While the area-averaged particle size is the closest to matching the opacity of the full particle size distribution, we find large differences in the transmission spectra across the entire broad wavelength

range for every mean particle size probed. The largest difference in calculated transmission spectra can be as much as 700 ppm and is typically on the order of several hundred ppm. This difference is quite typical for the planets probed in this sample [2]. In particular, the change in the optical slope and relative strength of the infrared cloud features demonstrate that these regions of the spectra are particularly sensitive to the distribution of cloud particles. For example, using a mean particle size gives rise to a sharp silicate feature, which is broadened when considering a distribution of particle sizes.

Using a representative particle size instead of a full particle size distribution will lead to an incorrect interpretation of cloud properties. Furthermore, reducing the cloud particle size distribution to a single representative size will likely skew retrieved planetary properties and abundances as a single representative particle size is not able to reproduce the spectra over a broad wavelength range, particularly the broad cloud features in the infrared. The difference in transmission spectra will also be significantly larger if other methods of calculating cloud properties do not estimate the correct total cloud mass, species, or the location of the cloud particles in the atmosphere. It is therefore essential to accurately model cloud properties when interpreting observations to characterize planetary atmospheres.

[2]In these cases, the difference between the limbs remains large and can be as much as 1000 ppm across a significant wavelength range (Figure 3.6.3).

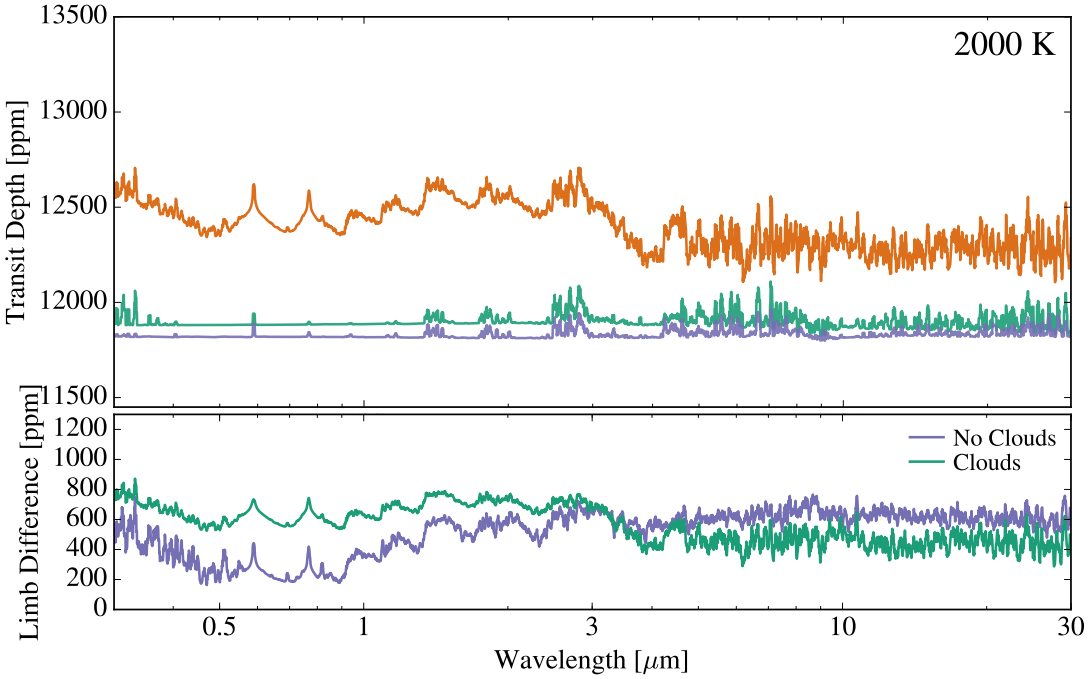


Figure 3.12: Same as Figure 3.6 for microphysical parameters that lead to less cloud formation for a hot Jupiter with $T_{eq}$ = 2000 K. The spectra at the east limb appears significantly less cloudy than the spectra for the same object with different microphysical parameters shown in Figure 3.6.

### 3.6.5 Sensitivity to Microphysical Parameters

To demonstrate the sensitivity of our results to the species' desorption energy and contact angle, we simulate cases where all modeled species have roughly the minimum desorption energy of 0.1 eV which is representative of the desorption energy of small molecules (such as $CH_4$) from silicate grains (Seki & Hasegawa 1983; Suhasaria et al. 2015, 2017). For the contact angle, we approximate the work of adhesion following the geometric mean method (Owens & Wendt 1969) assuming that the surface energy of a given species is made up entirely of either dispersive or polar contributions. The contact angle is therefore calculated as: $\cos\theta_c = W_{C,x}/(\sigma_x - 1)$ where $W_{C,x} = 2\sqrt{\sigma_x \sigma_C}$. This method of estimating the contact angle provides a value that is smaller than the true contact angle, if the surface tension of the cloud condensation nuclei and/or the condensing species is made up of both polar and dispersive contributions as is common for most species, though larger than the angle used in our nominal setup. These changes to the desorption energy and contact angle result in less efficient cloud formation, particularly for species that form on cloud condensation nuclei.

We find that our results are sensitive to these microphysical parameters, primarily because the efficiency of silicate and aluminum cloud formation is reduced. This effect can be most readily seen at the marginally supersaturated east limbs of the model atmospheres for the hotter planets in our grid where the molecular features are significantly less damped by clouds as shown in Figure 3.6.4. Furthermore, in this setup, chromium and iron clouds no longer form on the west limbs. As these species do not impact the resultant transmission spectra, however, this change does not result in spec-

tra on the west limbs and poles that are significantly different from the nominal cases shown in Figure 3.6.

To increase the accuracy of predictions from cloud microphysics in the future, the exact value of a species' contact angle and desorption energy needs to be determined from laboratory experiments.

## 3.7 Synthetic Light Curves and Observability of Light Curve Signatures

With the next generation of instruments on the horizon it is of interest to know whether, and with what certainty, the presence of inhomogenous clouds could be detected directly on exoplanets through the transit method. Not only will the final spectrum be imprinted with the signature of clouds, but a time variable signal will be present in the transit lightcurve, as different regions of the planet's atmosphere are preferentially weighted throughout the course of the transit, particularly during ingress and egress, when only one terminator of the atmosphere is transiting. This time varying transit signal has been used to detect the presence of high velocity equatorial jets on exoplanets (Louden & Wheatley 2015), and would also be sensitive to inhomogenous cloud coverage.

We simulated the time variable transit signal using the code TERMINATOR (Louden & Wheatley 2019), which uses the same framework as SPIDERMAN (Louden & Kreidberg 2018), but modified for use on transits rather than secondary eclipses. Both codes use a geometric algorithm for calculating analytically the area obscured

by the occulting object at each point in time during a transit/occultation. For this work, the algorithm was used to simulate the shape of a lightcurve when the opacity of the atmosphere varies around the limb. The planet is represented as a circle, with an additional half-annulus of variable width to represent the additional 'height' of the atmosphere, either due to absorbing species blocking light in lower pressure regions of the atmosphere, or locally higher temperatures increasing the scale height and leading to a locally more extended atmosphere. A schematic diagram of the model is shown in figure 3.7.

We first describe the simulated observations and the observational consequences of inhomogenous clouds through a simple forward model. We will then go on to show that the inference of inhomogenous clouds from these simulated observations is statistically robust in retrieval, even with limited wavelength coverage and in the presence of uncertainty on limb darkening coefficients and imprecise transit times.

### 3.7.1 Forward model

We simulated a hypothetical observation of a hot Jupiter with *JWST* using PandExo (Batalha et al. 2017), using NIRCAM and MIRI LRS to cover the wavelength range from 0.6 to 12 micron. Short exposure times of 10 seconds are used to capture the highest amount of information on the shape of the transit. As a test scenario, we assume a star-planet system similar to HD 209458 (G type star, J mag 6.6) with a planet orbiting with an inclination of 90 degrees for a realistic 'best case' observable target. The simulated observations with PandExo are used to calculate the signal to noise on each exposure in the lightcurves generated by TERMINATOR.

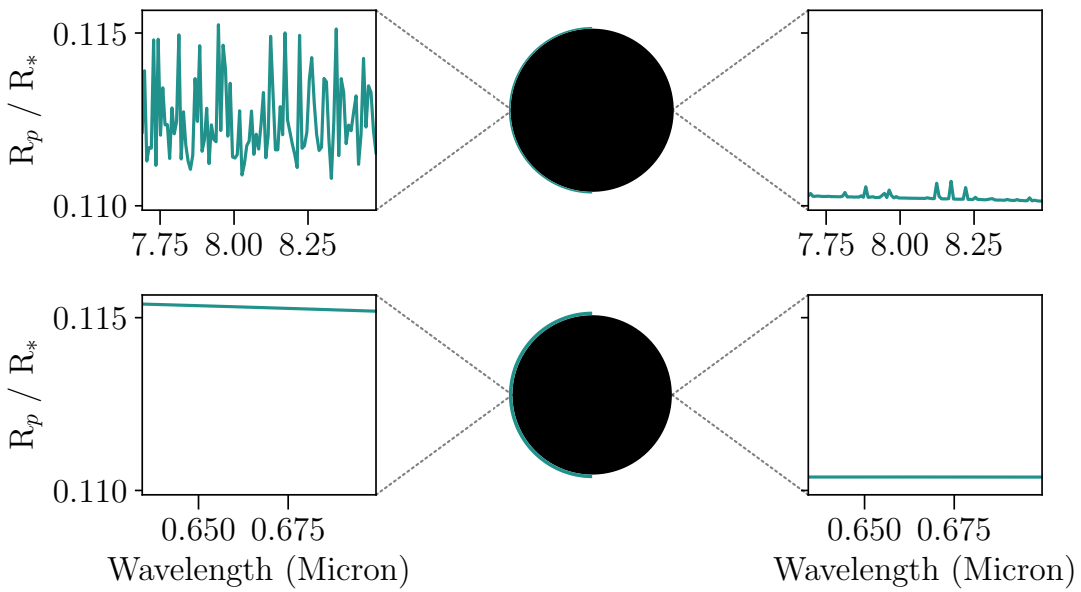


Figure 3.13: A comparison of the spectra on the eastern and western sides of the planet and a scale diagram showing the resulting difference in radius (highlighted in green). *Top:* The 2100 K planet with a clear atmosphere. *Bottom:* The same planet but with a cloudy atmosphere.

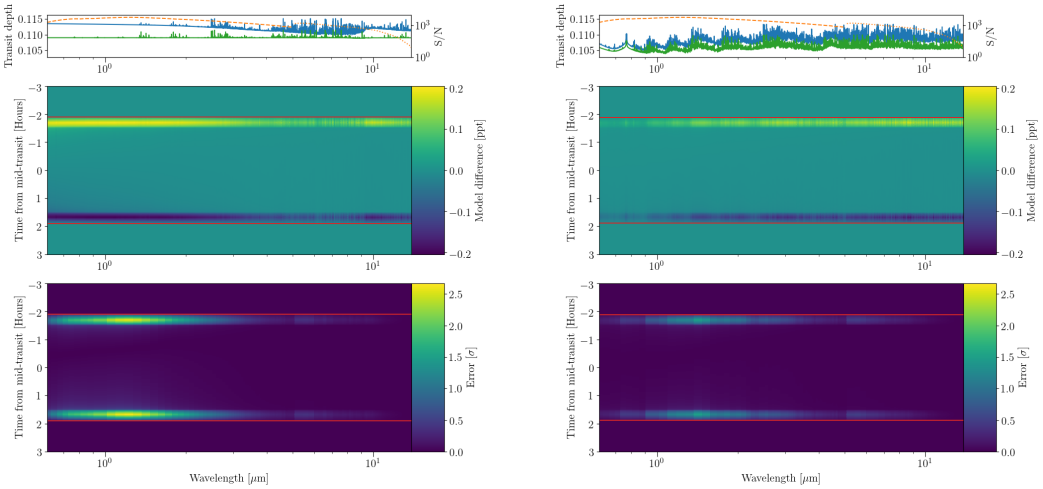


Figure 3.14: Simulated observations of asymmetric planets for a 2000 K planet, with a maximally cloudy case on the left and a model with no clouds on the right. *Top*: The transit depths for the eastern (blue) and western (green) terminators of the planet, plotted alongside the S/N of the simulated JWST observation, dashed for NIRCAM and dotted for MIRI LRS. *Middle*: The absolute difference between assuming a planet with an asymmetric atmosphere and a uniform one as a function of time and wavelength. *Bottom*: The detectability of the signal with JWST for a planet around a star with the same magnitude as HD 209458. The wavelength channels have been binned by a factor of 5 for clarity.

TERMINATOR requires a stellar model to implicitly account for the limb darkening at every wavelength. A limb-resolved model of the star was calculated using Spectroscopy Made Easy (Valenti & Piskunov 2012) with 99 limb angles sampled.

For each of the simulations described in section 3.4 we first calculated a transit model for a planet with a uniform atmosphere, which is constructed by averaging the east and west terminator models. The uniform model is compared to a lightcurve made using inhomogenous atmospheres. In all cases there is a very clear difference between the two resulting lightcurve models, which can easily be seen by subtracting one from the other, as shown in figure 3.7.1. As expected, the difference is largest at ingress and egress, where one terminator is much more heavily weighted than the other in the inhomogenous case. With the simulated signal to noise for a JWST observation the difference between the two models is statistically highly significant, with over $2\sigma$ of difference in some individual wavelength channels.

### 3.7.2 Retrievals

Figure 3.7.2 shows the difference in the shape of the lightcurve between the homogeneous and inhomogeneous models. The results are similar to those of von Paris, P. et al. (2016), who showed that the observational consequence of a planet with a different absorption radius on the eastern and western limbs is a distorted lightcurve, which to first order looks very similar to what one would expect if the ephemeris of the planet were not known accurately enough, presenting a slightly early or late transit. This time offset would typically be small, on the order of a few tens of seconds, so it would seem difficult to confidently assign this to the atmosphere of the planet instead

of an error in the calculated ephemeris of the planet. However, as can be clearly seen in figure 3.7.1 the effect is chromatic, in that it is largest at wavelengths where there is a large difference in the spectra, and smallest where the two sides are more similar.

It is therefore possible to confidently distinguish between uncertainty on the ephemeris and a true asymmetric atmosphere signal if a chromatically resolved signal is found where larger offsets correspond in wavelength to expected features in the planetary spectrum. This conclusion would be strengthened further if combined with optical phase curve observations of the planet that indicate inhomogenous cloud coverage, such as a westward offset bright spot in the optical (Dang et al. 2018), or a transmission spectra showing clear signatures of clouds in the atmosphere (see Section 3.6.3).

We ran a full Bayesian recovery test to check whether it was possible to infer differences in the two sides of the planet from a low resolution spectral lightcurve even in the presence of uncertainty on the true ephemeris of the planet, and to test whether this could be attributed to inhomogenous cloud cover. While an ideal retrieval would use the entire wavelength range, we use a minimal case of two small wavelength bands for clarity, in order to isolate the observational signal and potential confounding variables, therefore the significances we find in this section should be considered lower limits on what are possible.

The planet is observed for a full transit in the two wavelength regions, $\lambda 1$ and $\lambda 2$ - First with an instrumental setup optimized to observe the wavelength region with the largest expected distortion in the lightcurve, and a second instrumental setup optimized for the wavelength of the smallest effect to establish a baseline.

A simple metric is used to select $\lambda 1$, $\lambda 2$ and the optimum JWST instruments used in the retrieval. Using the model transit depths the difference between the eastern and western limbs is calculated for both the maximally cloudy and the cloud-free cases, $d1$ and $d2$. Since the purpose of this test is to discriminate between these two cases, we then take the difference between $d1$ and $d2$, and multiply it by the signal to noise of each JWST instrument available on pandexo, therefore the metric, $m$ for a JWST instrument i is

$$m_i = (d1 - d2) \cdot SNR_i \tag{3.2}$$

$m$ is then optimised over both instrument and wavelength. The second region, the baseline, is chosen similarly with metric $m2$. If $d1_{max}$ is the value of $d1$ where $m$ is optimized, then

$$m2_i = (d1 - d1_{max}) \cdot SNR_i \tag{3.3}$$

In all cases tested the greatest signal to noise was achieved with $\lambda 1$ having a short wavelength ( 1 micron) and being observed with NIRCAM, and $\lambda 2$ having a longer wavelength ( 6 micron) being observed with MIRI LRS. It is important to note that it is not a necessity to observe with two instruments, and the same results can be achieved with a single instrument, though with slightly lower significance.

When forward modelling we used a full stellar atmosphere model to account for limb darkening at all wavelengths. We wish to check that the uncertainty on the limb darkening parameters does not correlate with any measures of inhomogeneity during retrieval, and since it is computationally expensive to calculate atmosphere models we

instead use a quadratic limb darkening law. The limb darkening coefficients for the two wavelength regions are calculated using ldtk (Parviainen & Aigrain 2015). ldtk provides an uncertainty on the limb darkening parameters propagated from the uncertainty of the parameters on the star, which we conservatively increase by a factor of 10 and use as priors in our retrieval. We use a modified version of ldtk to work in the triangular sampling re-parametisation of Kipping (2013) for increased efficiency.

For each planet case we generate a simulated inhomogenous lightcurve for the two wavelength regions with the noise from pandexo, and then attempt to fit these lightcurves and recover the parameters used to initially generate the model. As part of the Bayesian analysis, we also fit a null hypothesis model, where the atmosphere of the planet is uniform, as would typically be assumed. Comparing the Bayesian evidences of these two scenarios gives the Bayes factor, which determines whether the more complex two-sided planet model is justified by the data. The retrieval is calculated through nested sampling with PyMultinest (Buchner 2016).

In our retrieval we assume the planet is spherical (i.e. we do not consider oblateness) and fix the planet's orbital parameters with the exception of the time of central transit t0, which we assume is known with an a-priori precision of $\pm$ 10 seconds. Of the remaining fit parameters, the radius of the planet before any additional atmosphere segments are added is denoted "$r_p$ core" 1 and 2 for $\lambda 1$ and $\lambda 2$. The additional absorbing area due to the atmosphere segment "atm" 1 and 2 in units of fractional stellar area, and is positive to denote it is on the eastern limb and negative to denote the western limb. A completely uniform atmosphere would have a value of zero for atm

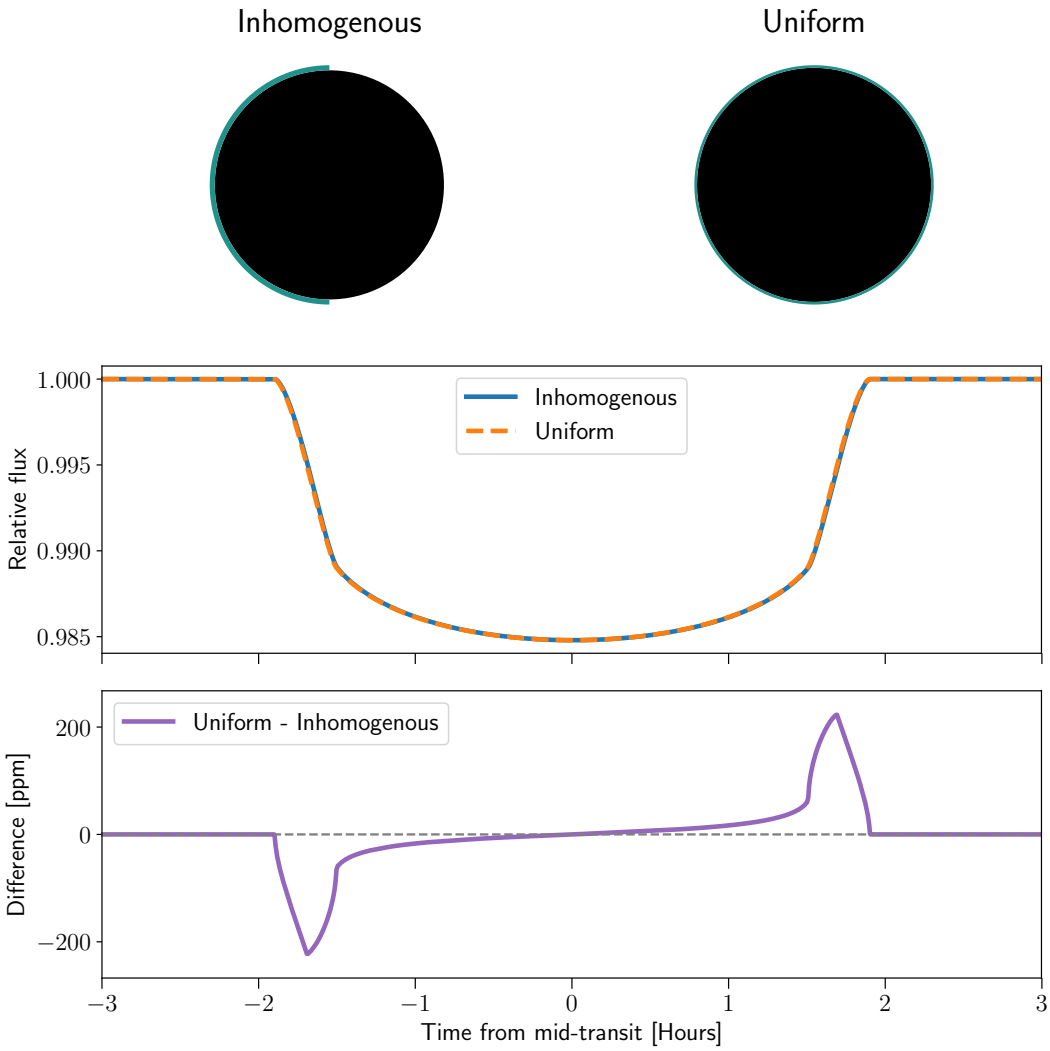


Figure 3.15: *Top:* Scale diagram of the planet models used for the 2100 K case, where the additional atmosphere height is highlighted in green. *Middle:* The lightcurves calculated by TERMINATOR for these planet geometries *Bottom:* The difference between the two lightcurves - the presence of an asymmetric atmosphere leads to a characteristic signature, similar to the residuals from an incorrect ephemeris.

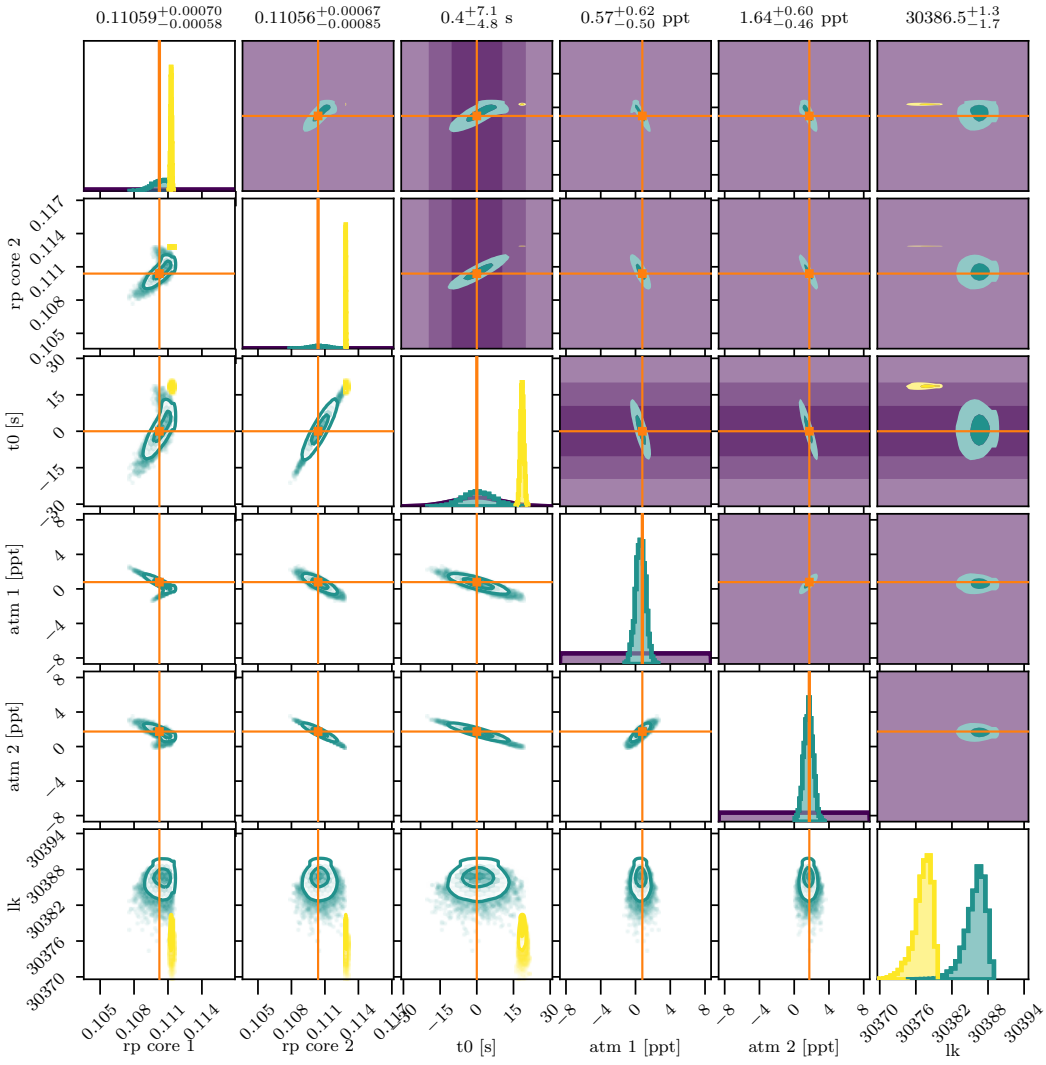


Figure 3.16: An example corner plot from Bayesian retrieval for the 2100 K models. Purple indicates prior distributions used, the model posteriors are in green and the posteriors for the null model are in yellow. The values used to generate the model are indicated with orange lines. "rp core" 1 and 2 are the radii of the planet in the two wavelength bands before additional segments are added, "t0" is the difference in time of central transit from the prior value, "lk" is the log likelihood of the model. The addition of the parameters atm 1 and 2, the asymmetric atmosphere area for the two wavelength regions, significantly increases the quality of the fit.

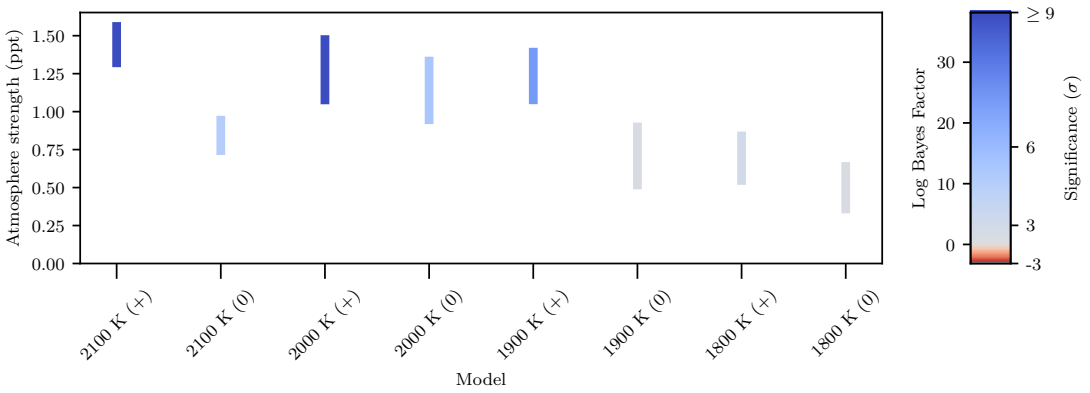


Figure 3.17: The detectability of the lightcurve asymmetry in the test system as a function of equilibrium temperature. Cases marked with a (+) are those where clouds are present at their maximal level , those marked with a (0) are where no clouds are calculated. Atmosphere strength is the modulus of the "atm" value for the wavelength with the strongest asymmetry effect, i.e., it is the additional fractional area of the star covered compared to a model with no additional atmosphere. The length of the bar is the 68% credible interval. The color code is a sigma-equivalent of the Bayes factor for how favoured the asymmetrical model is in each instance to the uniform one, a negative sigma value (red) would indicate that the simpler model is preferred.

1 and 2. The planet radius and atmosphere area for both wavelengths have uniform priors.

This model is compared to a 'null' model, which has identical priors but lacks the parameters for the additional atmosphere segments on top of the planet base, i.e., it is a standard transit model. The asymmetric atmosphere model has a total of nine fitted parameters, and the null therefore has seven.

The advantage of using Multinest over other methods such as MCMC is that it calculates the Bayesian evidence, allowing rigorous model selection rather than relying on approximations such as the Bayesian Information Criterion (BIC). The comparison of the Bayesian Evidences of the two scenarios gives the Bayes Factor, which gives an assessment of which model is best supported by the data, weighted by the model

complexity.

Inspecting an example corner plot, figure 3.7.2, for the case of a 2100 K atmosphere with clouds shows that as expected, the asymmetric atmosphere parameters correlate with the time of central transit for both wavelengths. However, since the central transit time is shared by the two wavelength regions the degeneracy is lifted - i.e. attempting to fit an observation of an asymmetric atmosphere with a model with zero asymmetry in the atmosphere would require a different value of t0 in the two wavelength regions, since this value must be shared the fit is poor. This same breaking of the degeneracy worked in every case tested.

The results are shown in figure 3.7.2, with both the strength of the detected atmosphere and the significance over the null model shown. We found that in all of our tested cases the preferred excess atmosphere depth was significantly greater than 0, and the Bayesian evidence with respect to the null hypothesis of a uniform atmosphere was greater than 3 $\sigma$ equivalent in all but 2 of the tested scenarios, both of which were cloud free model atmospheres, at 1800 and 1900 K.

The evidence for an inhomogeneous atmosphere and strength of the feature was in all cases significantly stronger when clouds were included in the atmosphere model, and increased in strength with the planetary equilibrium temperature. This technique is therefore capable of robustly detecting inhomogeneity in a planetary atmosphere with JWST, even in the presence of uncertainty on the time of central transit and limb darkening parameters. Inhomogenous cloud cover could be studied in detail by combining this technique with optical phase curves, providing strong constraints on

cloud formation models.

## 3.8 Discussion

### 3.8.1 Implications for Interpretation of Phase Curve Offsets

The signatures of inhomogeneous cloud cover discussed in Section 3.7 will help in both understanding limb averaged observations of inherently three dimensional planetary atmospheres and constraining interpretations of exoplanet phase curves.

Exoplanet phase curves are particularly powerful tools that can give insight into inhomogenous cloud cover, chemistry, and temperature structure, particularly when observed at multiple wavelengths (e.g., Parmentier & Crossfield 2018). However, these observations are intrinsically difficult to make as both the timescale ($\sim$ days instead of hours) and shape of a phase curve makes these observations more difficult than occultations (Shporer 2017; Parmentier & Crossfield 2018). In addition to the intrinsic observational difficulties of observing phase curves, there are significant interpretation difficulties such as the higher uncertainties in derived atmospheric properties (Shporer & Hu 2015).

The combination of the transit signatures of inhomogenous clouds presented in this work will aid in breaking the degeneracies between non-atmospheric and atmospheric contributions to the planetary phase curve as the presence of inhomogeneous clouds can be constrained by this complementary and cheaper method.

### 3.8.2 Tests for Mechanisms that Could Reduce Cloud Inhomogeneity

While inhomogeneous cloud cover on the limbs of hot Jupiters with $T_{eq} \sim 1800 - 2100$ K is a likely outcome, the models described in Section 3.3 and the observational metrics described in Section 3.7 will allow us to test for the following three mechanisms that could reduce inhomogeneities in limb cloudiness.

Firstly, it is possible that atmospheric circulation at the equilibrium temperatures probed in this study is strongly affected by atmospheric drag. In this case, the large scale atmospheric winds flow from day to night (Showman et al. 2013). Such a flow pattern may equilibriate the temperature structure at the limbs and lead to a homogenized cloud population. Thus, the metric presented in Section 3.7 could indirectly probe the flow pattern, and thus the strength of the atmospheric drag, if there is strong evidence for a homogeneous model for a hot Jupiter in this temperature regime.

Secondly, the metric presented in this work could test for the presence of a condensible species in the upper atmosphere of the west limbs, such as MnS, which may mimic the high-altitude silicate and aluminum clouds present on the east limbs at short wavelengths. Although MnS clouds are not thought to form abundantly (Section 3.6.2, Gao et al. 2020), this theory could be tested observationally using such a probe of inhomogeneity. This mechanism could be distinguished from the first mechanism with observations at longer wavelengths where the east limb appears more clear or if broad features due to MnS or other cloud species are present in the transmission spectrum.

Finally, this metric could test for the presence of homogeneous high level hazes that can be transported across the planet and can form and persist at high temperatures.

Though the formation pathway of hazes is an active area of research, this mechanism may be distinguishable from the first two mechanisms because the production of photochemical hazes may depend on the energetic flux from the host star and should thus vary for different planets as a function of this quantity. Indeed, many hot Jupiters do not show significant evidence of high level hazes that could produce a significant Rayleigh-like slope in the optical (e.g., Sing et al. 2016) suggesting that at least some hot Jupiters are not homogeneously covered in high temperature hazes.

## 3.9 Conclusions

We simulated clouds on hot Jupiters with 1800 K $< T_{eq} <$ 2100 K using a size distribution-resolving cloud microphysics model to assess the feasibility of observing inhomogenous clouds from transit observations alone. Cloud formation is efficient for all planets probed in the modeled grid. The model transmission spectra including microphysical clouds is different on each limb of the planet, often by as much as $\sim$1000 ppm. At short wavelengths, despite having lower total cloud mass, the east limb appears cloudier than the west limb for planets with equilibrium temperatures less than 2100 K. Silicate clouds typically dominate the cloud opacity for all planets in our model grid with the exception of the hottest planets at the east limbs where aluminum clouds also significantly contribute to the total cloud opacity.

There are three primary transmission spectrum signatures of condensational clouds. First, condensational clouds can substantially mute absorption features across a broad wavelength range. Second, clouds can also contribute to muted and sloped

spectra in the optical. The strength of this slope depends strongly on temperature with hotter planetary locations producing more distinct slopes. Third, both silicate and aluminum clouds can also give rise to broad features (Wakeford & Sing 2015) in the infrared between $\sim$ 10 - 20 $\mu$m that should be observable with *JWST* (Venot et al. 2019; Morley et al. 2017). Furthermore, for some locations in a planetary atmosphere we find a cloud-free spectral window from $\sim$ 5 - 9 $\mu$m where the opacity of silicate clouds is decreased.

The cloud paerticle size distributions in this work are not log-normal and differ for different condensible species. It is essential to use the full cloud particle size distribution when interpreting or creating model spectra, as considering a representative particle size leads to a spectra that is unpredictably and significantly different in both magnitude and shape - though even these cases produce spectra that are different between the east and west limbs. Furthermore, the cloud content of a given planet is sensitive to the material properties of a condensible species - namely its desorption energy and contact angle.

We use the fact that the observed difference in limb radii in the presence of clouds characteristically changes with observing wavelength to assess the feasibility of observing inhomogeneous clouds in transmission with *JWST*. We use the detailed TERMINATOR code to map the transits of the modeled planets including inhomogeneous limb radii. Using a forward model across a broad wavelength range, the errors in fitting a homogeneous model to observations of a planet with inhomogeneous clouds leads to chromatic errors that are distinct from the clear case - thus providing a clear

signature of inhomogeneous clouds. Using an inverse bayseian retrieval, we show that these synthetic JWST observations can be used to probe inhomogenous clouds in a way that is statistically robust, even with limited wavelength coverage and in the presence of uncertainty on limb darkening coefficients and imprecise transit times.

# Chapter 4

# Using Ice and Dust Lines to Constrain the Surface Densities of Protoplanetary Disks

## 4.1 Abstract

We present a novel method for determining the surface density of protoplanetary disks through consideration of disk 'dust lines' which indicate the observed disk radial scale at different observational wavelengths. This method relies on the assumption that the processes of particle growth and drift control the radial scale of the disk at late stages of disk evolution such that the lifetime of the disk is equal to both the drift timescale and growth timescale of the maximum particle size at a given dust line. We provide an initial proof of concept of our model through an application to the disk

TW Hya and are able to estimate the disk dust-to-gas ratio, CO abundance, and accretion rate in addition to the total disk surface density. We find that our derived surface density profile and dust-to-gas ratio are consistent with the lower limits found through measurements of HD gas. The CO ice line also depends on surface density through grain adsorption rates and drift and we find that our theoretical CO ice line estimates have clear observational analogues. We further apply our model to a large parameter space of theoretical disks and find three observational diagnostics that may be used to test its validity. First we predict that the dust lines of disks other than TW Hya will be consistent with the normalized CO surface density profile shape for those disks. Second, surface density profiles that we derive from disk ice lines should match those derived from disk dust lines. Finally, we predict that disk dust and ice lines will scale oppositely, as a function of surface density, across a large sample of disks.

## 4.2 Introduction

Extrasolar planetary systems display a large diversity in both orbital architecture and the physical characteristics of the planets. This diversity could be the result of late stage planetary collisions (e.g. Inamdar & Schlichting 2016), the properties and evolution of the initial gas disk (e.g. Ginzburg et al. 2016), different initial planetary formation locations in the disk (e.g. Inamdar & Schlichting 2015) or a combination of these factors. The immediate initial conditions of planet formation are encapsulated in the protoplanetary disks that surround young stars. However, many disk characteristics remain largely unconstrained. Recent telescopic advances, particularly the Atacama

Large Millimeter Array (ALMA), have enabled exploration of disks with unprecedented spatial resolution. These advances have already given us many insights into the spatial structure of disks (e.g. Nomura et al. 2016; Pérez et al. 2016; Tobin et al. 2016; Andrews et al. 2016; Williams & McPartland 2016). Here, we take advantage of this spatial resolution to propose new observational constraints on disk surface density, a property that is fundamental for understanding both disk evolution and planet formation.

Protoplanetary disk surface density cannot be measured directly because the majority of the disk mass resides in $H_2$ which is a symmetric particle that does not readily emit. Instead, densities have been inferred using observations of disk dust, CO, and HD. The reliability of each of these tracers has recently been called into question, leaving open the possibility that disk surface densities are entirely unconstrained (Mundy et al. 1996; Andrews et al. 2009, 2010; Isella et al. 2009, 2010; Guilloteau et al. 2011; Bergin et al. 2013; Williams & Best 2014; Schwarz et al. 2016).

The first and most commonly used tracer of the surface density is the disk dust mass which is typically derived from resolved continuum observations or spectral energy distribution fitting (Andrews & Williams 2005; Calvet et al. 2002; Guilloteau et al. 2011). Using dust as a tracer of total disk surface density is fallible, however, as it requires an assumed dust-to-gas ratio. This ratio is not well constrained and can be altered from the ISM value of $10^{-2}$ (**?**) through processes such as grain growth and particle drift (Andrews et al. 2012) and can further have a non-uniform value throughout a disk.

CO gas has also been used as a tracer of the total gas present in disks (e.g.

Rosenfeld et al. 2012). However, recent observations have called into question the typically assumed abundance of CO ($10^{-4}$ in warm molecular clouds; Lacy et al. 1994), suggesting that the existence of disk processes such as photodissociation may alter this value or that there may be a global depletion of gas phase carbon in disks such as TW Hya (van Zadelhoff et al. 2001; Dutrey et al. 2003; Chapillon et al. 2008; Schwarz et al. 2016). In addition to this unknown, many CO lines are optically thick and are therefore unreliable measures of mass. The use of CO observations thus further requires careful consideration of lower optical depth CO isotopologues to estimate the gas mass to within an order of magnitude (Williams & Best 2014; Ansdell et al. 2016).

More recently, observations of the HD $J = 1 - 0$ line have been used to probe the gas mass in disks (Bergin et al. 2013; McClure et al. 2016). HD is thought to be a good tracer of the total gas mass as the deuterium to hydrogen fraction is relatively well-known for objects near to the sun (Linsky 1998). However, because HD emits at temperatures above 20 K, HD emission will only trace the warm gas and thus provides a lower limit on the total gas mass present in a disk.

Given the uncertainties that accompany these observational tracers, in this paper we choose to adopt an agnostic point of view in regards to surface density. We develop a novel method to derive this quantity through asserting that the dust line locations are determined by the microphysical process of particle drift. We use physics that has been studied extensively in previous disk models. Our contribution is to suggest a new interpretation of disk observations in light of this physics.

Previous theoretical work indicates that, for the outer regions of evolved disks,

drift dominates the processes of growth and collisional fragmentation in determining the maximum particle size at a particular radial scale. Particle growth can be limited by either a lack of total time (disk age), by fragmentation, or by drift. For typically turbulent disks, the disk lifetime allows plenty of time for particles to grow. The particle size at a given radial scale is limited, however, as particles are removed from the outer disk due to particle drift at a smaller maximum size than could be removed by collisional fragmentation. The maximum particle size at a given radius is thus defined as the size for which the growth timescale ($t_{\rm grow}$) and the drift timescale ($t_{\rm drift}$) are equal (i.e. $t_{\rm drift} = t_{\rm grow}$). This is described both numerically and analytically in Birnstiel et al. (2012) and Birnstiel & Andrews (2014) as the "late phase" of disk evolution in which dust growth has progressed such that it is limited by the removal of larger grains via the process of radial drift for roughly sub-centimeter sized particles.

Thus, the maximum particle size at a given radial location is limited by particle drift which will remove all particles with a drift timescale less than the age of the system (i.e. $t_{\rm disk}$). This indicates that the equilibrium particle size at a particular disk location is limited by the time in which that particle has been able to interact dynamically with the disk gas. The maximum disk radius where we would therefore expect to see emission from a given particle size is defined as the location for which the drift timescale (and thus the growth timescale) is equal to the age of the system (i.e. $t_{\rm drift} = t_{\rm grow} = t_{\rm disk}$). These locations can be seen observationally as the point where emission drops off at an observed wavelength ($\lambda_{\rm obs}$) where we assume that the observed particle size is roughly equal to $\lambda_{\rm obs}$. Any particle larger than this size would result in a shorter drift and/or

growth timescale and would therefore reach an equilibrium location at a shorter radial scale. We note that we expect the equilibrium particle size at a particular radial location to decrease with increasing system age such that we expect larger disk radial scales at the same $\lambda_{\rm obs}$ for younger disks, limited only by the size of the gas disk itself.

In this paper we thus make the assumption that $t_{\rm drift} = t_{\rm grow} = t_{\rm disk}$ to derive fundamental disk properties. We demonstrate that, if validated, this assertion allows us to recover the surface density distribution for observed disks. To test this central premise of our modeling we use two sets of observations that give empirical information about disk *dust* and *ice* lines.

The first set of observations is a collection of recent observations, using ALMA, the Jansky Very Large Array (JVLA) and the sub-millimeter array (SMA), of TW Hya that demonstrate that the disk radial scale is distinctly smaller at longer wavelengths (Menu et al. 2014; Cleeves et al. 2015; Andrews et al. 2012). These observations provide information about the distribution of dust grains throughout the disk. We describe these observations in terms of disk *dust lines* which refer to the disk radial scale as it corresponds to a particular wavelength. We use these dust lines to derive disk surface densities through equating $t_{\rm disk}$ and $t_{\rm drift}$ as described in Section 4.4.1.

ALMA also provides direct observations of disk ice lines, either through direct measurements of CO gas line emission (Nomura et al. 2016; Schwarz et al. 2016) or through indirect measurements of $N_2H^+$, which is only present in large abundance when CO freezes out (Qi et al. 2013, 2015). For TW Hya, the observation of $N_2H^+$ yields an ice line location of $\sim 30$ AU (Qi et al. 2013) while the emission from the $C^{18}O$ $J = 3-2$

line indicates an ice line of $\sim$ 10 AU (Nomura et al. 2016). The direct observations of CO emission also give insight into the surface density contributed by CO (Cleeves et al. 2015; Rosenfeld et al. 2012). The CO ice line location depends on the CO surface density through grain adsorption rates and particle drift. These observations therefore provide a constraint on the disk surface density and CO fraction.

After discussing representative parameters for our fiducial disk, TW Hya (Section 4.3), we explain how we derive disk surface densities from dust lines (Section 4.4). In Section 4.5 we provide additional tests of our model through considering the disk ice lines. In Section 4.6 we present a description of three observational diagnostics of our model and an application to a larger range of disk parameter space. If these diagnostics confirm our interpretation, this will provide a new way to observationally measure disk masses and surface density profiles. We conclude with a paper summary and a discussion of the presented observational diagnostics in Section 4.7.

## 4.3 Parameters for Fiducial Disk TW Hya

We adopt TW Hya as our fiducial protoplanetary disk because it is the nearest observed disk ($d = 54 \pm 6$ pc) that is nearly exactly face-on ($i \sim 7°$; Qi et al. 2004) and hence boasts a wealth of observational data. TW Hya is a long-lived disk ($t_{\rm disk} = 3 - 10$ Myr; Barrado Y Navascués 2006; Vacca & Sandell 2011) that is likely an unusually massive representative of a class of evolved protoplanetary disks as the typical disk lifetime is thought to be a few million years (Mamajek 2009). We note that disks are typically assumed to have the same ages as their host stars and estimates of stellar

ages are subject to observational uncertainties. For our discussion of TW Hya we use an approximate age of 5 Myr, however, $t_{\rm disk}$ could be treated as a tunable quantity as appropriate.

We assume a temperature structure for TW Hya that is dominated by passive stellar irradiation. We expect that this model holds for the outer disk and note that TW Hya may be irradiation dominated at all but the very inner radii (Dullemond et al. (2007) Figure 3, based on models from D'Alessio et al. (2006)). Our parameterization of the disk midplane temperature follows Chiang & Goldreich (1997) where the canonical temperature profile is:

$$T(r) = T_0 \times \left(\frac{r}{r_0}\right)^{-3/7} \tag{4.1}$$

where the coefficient $T_0$ is a function of stellar luminosity and stellar mass, defined at $r_0 = 1$ AU, and is determined via:

$$T_0 = L_\star^{2/7} \left(\frac{1}{4\sigma_{SB}\pi}\right)^{2/7} \left(\frac{2}{7}\right)^{1/4} \left(\frac{k}{\mu G M_\star}\right)^{1/7}. \tag{4.2}$$

We adopt the following parameters for TW Hya: $L_\star = 0.28 L_\odot$, $M_\star = 0.8 M_\odot$, and $\mu = 2.3 \mathrm{m_H}$ assuming a hydrogen/helium disk composition (Qi et al. 2013; Rhee et al. 2007). Using Equation 4.3, we derive $T_0 \sim 82$ K. We note that our derived midplane temperature profile is in good agreement with the observationally constrained midplane temperature derived in Cleeves et al. (2015) as well as the upper limit on the

midplane temperature from Schwarz et al. (2016). We vary the normalization of this temperature profile in Section 4.6.2 and discuss the effect that this has on our ice line derivations. We also note that a factor of 2 change in temperature normalization ($T_0$) leads to a change of a factor of $\sim 0.7$ in our surface density profile derived in Section 4.4.1.

Spatially resolved CO observations of TW Hya have been well fit by the following surface density profile:

$$\Sigma(r) = \Sigma_c \left(\frac{r}{r_c}\right)^{-\gamma} \exp\left[-\left(\frac{r}{r_c}\right)^{2-\gamma}\right], \tag{4.3}$$

which follows from the self-similar solution to the viscous evolution equations as shown in Lynden-Bell & Pringle (1974) and Hartmann et al. (1998). This profile is a shallow power law at small radii and follows an exponential fall off at radii larger than the critical radius, $r_c$. Using an assumed CO abundance of $\sim 10^{-4}$ $n_H$ (the standard CO fraction in warm molecular clouds; Lacy et al. 1994), Rosenfeld et al. (2012) derive best fit parameters for TW Hya of $r_c = 30$ AU, $\gamma = 1$, and $\Sigma_c \sim 0.5$.

As we move forward with our discussion of TW Hya we accept the best fit parameters for all values mentioned above, except for $\Sigma_c$, which relies on an assumed CO abundance. Instead, we treat $\Sigma_c$ as a free parameter. This is motivated by discrepancies between assumed and derived CO abundances in disks. We further note that there is also a potential discrepancy between the measured and derived mass accretion rates for TW Hya.

TW Hya has an average measured accretion rate of $\sim 1.5 \times 10^{-9}$ $M_\odot$ $yr^{-1}$

(Brickhouse et al. 2012). As a consistency check, we can use the surface density profile from Equation 4.3 to derive an approximation of the mass accretion rate using the following expression (Jones et al. 2012):

$$\dot{M} = \frac{M_{\rm disk}}{t_{\rm disk}} \tag{4.4}$$

where $\dot{M}$ is the mass accretion rate, $t_{\rm disk}$ is the age of the disk, and $M_{\rm disk}$ is the disk mass which we take to be the mass of TW Hya interior to the critical radius of 30 AU. This estimate for $\dot{M}$ is a rough approximation for protoplanetary disks under the assumption that the primary mode of disk evolution is accretion. For instance, a rate that is higher than this derived $\dot{M}$ would quickly evolve the disk past the current state and a lower $\dot{M}$ would indicate that a process other than accretion drove the disk to evolve into its current state.

Thus, if the disk age is a proxy for evolution timescale, Equation 4.4 gives an accretion rate of $\sim 10^{-11}$ $M_\odot$ yr$^{-1}$ for TW Hya using the best fit parameters from Rosenfeld et al. (2012) – a value that is 2 orders of magnitude smaller than the observational value. This value is inconsistent with observations. However, it is important to note that the accretion rates onto pre-main sequences stars are likely variable or episodic in nature (e.g. Armitage et al. 2001; Salyk et al. 2013; Hein Bertelsen et al. 2016). For episodic accretion to explain this discrepancy, TW Hya would have to be currently undergoing an episode of high accretion – a result that is unlikely given the smooth, axisymmetric nature of the disk and its observed central cavity.

We further note that photoevaporation can also remove mass in the outer disk.

Since this process reduces a disk's accretion rate onto its star for a given disk mass, if important, it would make Equation 4.4 an upper limit for $\dot{M}$, making its agreement with observed accretion rates worse. The rate of photoevaporative mass loss for typical fluxes is $< 10^{-10}$ $M_\odot$ $yr^{-1}$ (Alexander et al. 2006), which is less than TW Hya's observed accretion rate, so it is likely subdominant. Thus, while the estimate of the mass accretion rate from Equation 4.4 is not necessarily conclusive, it nevertheless provides a reason to believe that mass in the disk may be higher than indicated by CO observations.

TW Hya also has an observational lower limit of total gas mass of 0.05 $M_\odot$ from HD measurements of the warm gas in the disk (Bergin et al. 2013). The mass estimate is inconsistent with the mass estimate from the CO observations and gives an accretion rate of $\sim 6 \times 10^{-9}$ $M_\odot$ $yr^{-1}$ which is more consistent with the observed rate.

We consider the discrepancy between the measurements of the CO emission, HD gas emission, and observed accretion rate to be additional motivation for treating $\Sigma_c$ as a free parameter.

## 4.4 Dust Lines

The observed extent of TW Hya is wavelength dependent, ranging from a radius of $r \approx 25$ AU at a wavelength of $\lambda = 9$ mm to $r \approx 130$ AU at a wavelength of 1.6 $\mu$m as shown in Figure 4.4. In particular, observations at 0.87 mm show a disk size of approximately 60 AU (Andrews et al. 2012, 2016), at 1.3 mm the disk size is around 50 AU (Cleeves et al. 2015), and at 9 mm the disk size is approximately 25 AU (Menu et al. 2014). We take the observed disk size of approximately 130 AU at 1.6 $\mu$m to

indicate the total radial extent of the disk as this distance matches the observed radial extent of the CO emission (Qi et al. 2013).

Recent observational work has found that the continuum emission at each wavelength exhibits a markedly sharp decrease over a very narrow radial range such that $\Delta r/r \lesssim 0.1$ (Andrews et al. 2012; de Gregorio-Monsalvo et al. 2013). Thus, while these are only approximate radial sizes for the TW Hya disk, they are adequate for our preliminary physical interpretation. In our further discussion of TW Hya we allow the radius error bars to vary by $\pm 10$ AU and find little change in our theoretical modeling. These error bars are slightly larger than those derived from treating the systematic uncertainty in distance to the TW Hya system alone ($d = 54 \pm 6$ pc or $d = 51 \pm 6$ pc van Leeuwen 2007; Mamajek 2005, which gives uncertainties that roughly range from $\pm$ 3 AU at $\lambda_{obs} = 9$ mm to $\pm$ 7 AU at $\lambda_{obs} = .87$mm). We inflate the error bars to account for error in measuring the disk radial scale without modeling the disk visibilities. We will improve on these error estimates in future work.

Models of disk emission from particles with a range of sizes indicate that $\lambda_{\rm obs}$ roughly corresponds to the primary particle size, $s$, contributing to the observed emission (Birnstiel & Andrews 2014). We therefore set the particle radius $s = \lambda_{\rm obs}$ for all that follows and leave a more detailed evaluation of the particle size distributions for future work. We call the cutoff distance for emission at $\lambda_{\rm obs} = s$ the "dust line" for particles of size $s$.

In Figure 4.4 we note that the observed locations of dust lines as a function of particle size (equivalent to the disk size as a function of $\lambda_{\rm obs}$) can be well fit by a

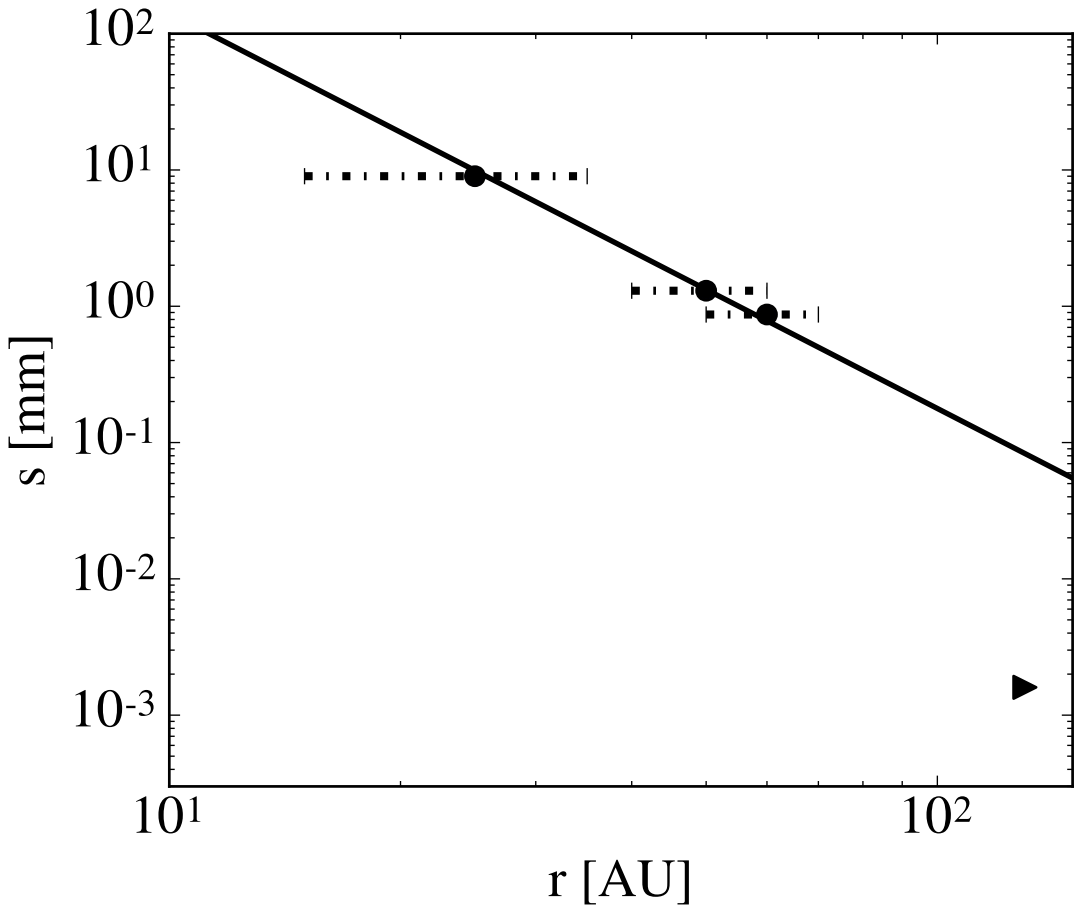


Figure 4.1: The dominant particle size in the disk as a function of radius which follows a power law relationship. The three black points represent disk sizes derived from observations by Menu et al. (2014), Cleeves et al. (2015), and Andrews et al. (2012, 2016). The upper limit arrow represents measurements of the radial extent of both the CO gas disk and the disk size of the smallest grains which we take to be indicative of the total radial extent of the disk (Debes et al. 2013). This is a theoretical lower limit as we expect that small dust sizes would have a larger radial extent if the gas disk was larger. The error bars shown correspond to our chosen nominal error for the disk radius of ±10 AU, consistent with the observationally sharp cut-off in disk emission (see text).

power law, with the exclusion of the disk size at the shortest $\lambda_{\rm obs} = 1.6$ $\mu$m. Because the radial extent of the 1.6 $\mu$m grains matches that of the CO gas, they are limited by the total disk size and not by the equilibrium that governs disk sizes at longer $\lambda_{\rm obs}$. We conclude that this point acts as a theoretical lower limit for the radius at which you would expect to find these grains (Rosenfeld et al. 2012; Debes et al. 2013). Given their present location, they have not yet had to time to grow or drift due to the long dynamical timescales for micron sized particles in the outer disk.

The presence of dust lines in TW Hya indicate that a physical process is removing particles larger than a set maximum size from the outer disk. Particle growth can be truncated by particle fragmentation, particle drift, or a lack of total dynamical time. If we consider the case of TW Hya, the age of the system ($t_{\rm disk}$) is sufficiently large that there is plenty of time for particle growth to occur.

Previous work has shown that for the outer regions of evolved disks, such as TW Hya, particle drift is significant for sub-centimeter sized bodies such that these particles are not able to grow to a size that can be disrupted due to collisional fragmentation (see Birnstiel et al. 2012; Birnstiel & Andrews 2014). This is physically intuitive as small particles in the outer disk drift faster as they grow larger (see Section 4.4.1).

This drift limited regime reaches an equilibrium such that the radial drift of particles imposes a size limit as large particles are removed faster than they can be replenished due to particle growth. Particles in the outer disk are also removed at a size that is smaller than the limit imposed by collisional fragmentation, for disks of standard turbulence, as the relative turbulent velocities between particles of these

sizes is not sufficiently large for efficient destruction (Birnstiel et al. 2012). Thus, the maximum particle size at a given radial location in the disk is given by the size for which the growth timescale is equal to the drift timescale (i.e. $t_{\rm grow} = t_{\rm drift}$).

Smaller particles have longer drift timescales (see Section 4.4.1) which means that the dust lines in a disk will evolve with disk age such that we expect the radial location of a dust line at a specific $\lambda_{\rm obs}$ to decrease with increasing disk age. This therefore indicates that the dust line of a disk is determined by the time in which particles are able to drift, which is necessarily the age of the system. We can thus expect the fall-off of emission from a given particle size to correspond to the location where a particle's drift timescale is equal to the lifetime of the disk ($t_{\rm drift} = t_{\rm disk}$). Therefore, the system can be described at any given time by an equilibrium state in which $t_{\rm drift} = t_{\rm grow} = t_{\rm disk}$. This new picture of disks is summarized in Figure 4.4.

Using the dust line observations of TW Hya in conjunction with our theoretical premises we can now consider the dominant physical processes of growth and drift and use these calculations to derive the total disk surface density for TW Hya as well as the dust-to-gas ratio in the outer disk. We do this through the use of our central modeling premise that $t_{\rm drift} = t_{\rm grow} = t_{\rm disk}$.

### 4.4.1 Radial Drift

As discussed above, we assume that the disk radial scale as a function of wavelength is set by the distance that a particle of radius, $s = \lambda_{\rm obs}$, can drift in the age of the system. We therefore set the drift timescale $t_{\rm drift}$ equal to the lifetime of the system $t_{\rm disk}$.

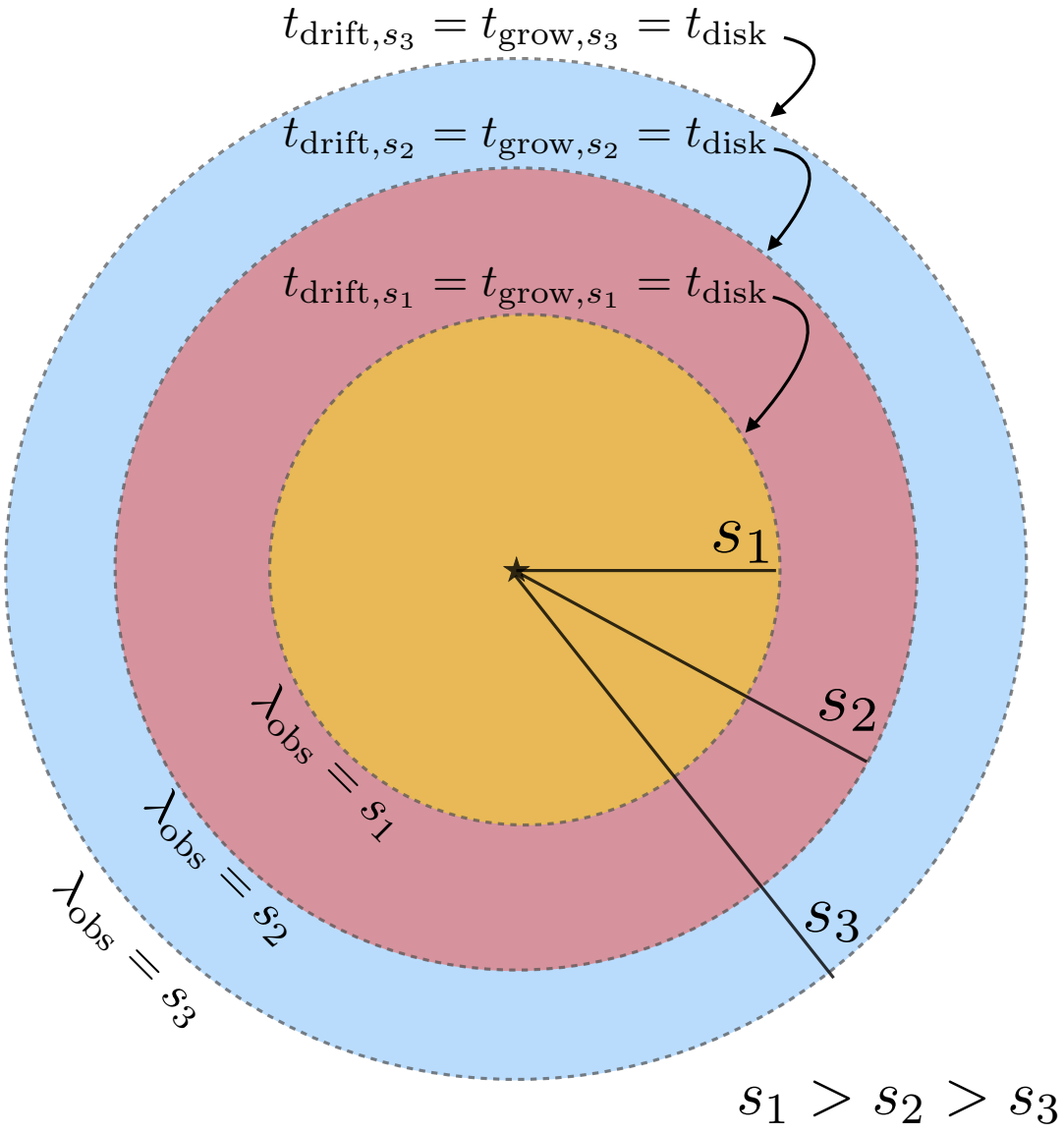


Figure 4.2: Cartoon of our model for disk dust lines (dashed lines). Particle sizes are denoted $s_1$, $s_2$, and $s_3$ where $s_1 > s_2 > s_3$. Particles of size $s_1$ are present in the disk throughout the yellow region. Particles of size $s_2$ extend throughout the yellow and red regions while particles of size $s_3$ are present throughout all depicted disk regions. At the dust lines for each particle size the growth and drift timescale are equal to the age of the system. When observed at $\lambda_{\mathrm{obs}} = s_1$ only the yellow region of the disk will be observed, while for $\lambda_{\mathrm{obs}} = s_2$ the disk extends radially to the end of the red region and for $\lambda_{\mathrm{obs}} = s_3$ the disk appears to extend to the end of the blue region.

In a protoplanetary disk particle drift occurs because the gas disk orbits at a sub-Keplerian velocity due to an outward pressure gradient (Weidenschilling 1977a). The particles in the disk continue to rotate at a Keplerian velocity ($v_k \equiv \Omega_k r$) and experience a headwind from the gas. This headwind causes the particles to loose angular momentum and drift radially inwards (Weidenschilling 1977a; Takeuchi & Lin 2002). The amount of drift that a particle experiences depends on how well-coupled the particle is to the gas, quantified by a dimensionless stopping time: $\tau_s \equiv \Omega_k t_s$ where $\Omega$ is the Keplerian frequency and

$$t_s = \begin{cases} \rho_s s / \rho c_s & s < 9\lambda/4, \text{ Epstein drag,} \\ 4\rho_s s^2 / 9\rho c_s \lambda & s > 9\lambda/4, \mathrm{Re} \lesssim 1 \text{ Stokes drag} \end{cases} \tag{4.5}$$

(summarized in Chiang & Youdin (2010)). Here $\rho$ is the gas midplane density, $\rho_s = 2$ g cm$^{-3}$ is the density of a solid particle, $s$ is the particle size, and $\lambda = \mu/\rho\sigma_{\mathrm{coll}}$ is the gas mean free path where $\sigma_{\mathrm{coll}} = 10^{-15}$ cm$^2$.

The radial particle drift velocity is:

$$\dot{r} \approx -2\eta\Omega r \left( \frac{\tau_s}{1+\tau_s^2} \right) \tag{4.6}$$

where $\eta \approx c_s^2/2v_k^2$, $c_s$ is the sound speed of the gas, and $v_k$ is the Keplerian velocity (see the review by Chiang & Youdin 2010).

We can now derive an equation for drift timescale ($t_{\mathrm{drift}} = |r/\dot{r}|$) that directly depends on the disk surface density, $r$, and $s$. We first note that the particle sizes we consider ($s < 1$ cm; see Section 4.4) typically interact with the disk gas via the

Epstein law for gas drag and have a dimensionless stopping time less than 1. Once our calculation is complete we verify that the Epstein regime applies for our reconstructed surface density profile and that $\tau_s < 1$.

We approximate a dimensionless stopping time in the Epstein regime as $\tau_s = \Omega\rho_s s/\rho c_s$. We can rewrite this quantity by noting that the disk's scale height $H = c_s/\Omega$ and its surface density in gas $\Sigma_g = H\rho$ to obtain $\tau_s = \rho_s s/\Sigma_g$. As found in Rosenfeld et al. (2013), increasing temperature with height can inflate the aspect ratio of an observed disk when layers several scale-heights above the midplane are probed. As most of the disk mass is contained within the scale height closest to the midplane, however, the temperature at the midplane sets the volumetric density in the disk to an order of magnitude as described above.

We reformulate the drift timescale through defining the parameter $v_0$ which physically corresponds to the maximum drift velocity. For a passively irradiated disk, $v_0 \equiv \eta v_k = c_s^2/2v_k$ varies very weakly with radius. We find that $c_s \propto r^{-3/14}$ where $c_s = \sqrt{kT/\mu}$ using Equation 4.1 for temperature as a function of radius. For the Keplerian velocity we find that $v_k \propto r^{-1/2}$ using Kepler's third law. This gives a parameter $v_0$ that is weakly dependent on radius: $v_0 \propto r^{1/14}$.

We can now write the drift timescale directly in terms of the surface density, radius, particle size, and the maximum drift velocity $v_0$:

$$t_{\text{drift}} = \left|\frac{r}{\dot{r}}\right| = \Omega^{-1}\left(\frac{r}{H}\right)^2 \tau_s^{-1} \approx \frac{\Sigma r}{v_0 \rho_s s} \tag{4.7}$$

We can now set the drift timescale equal to the age of the disk ($t_{\text{drift}} = t_{\text{disk}}$)

and solve for the gas surface density at a given dust line radius. We thus derive the following equation for disk surface density as a function of radius.

$$\Sigma(r) = \frac{t_{\rm disk} v_0 \rho_s s}{r} \tag{4.8}$$

From this equation we see that $\Sigma(r) \propto s/r$ with $s(r)$ plotted in Figure 4.4. This reformulation is thus particularly powerful as it gives a direct scaling between surface density and radius with only a very weak dependence on the temperature profile of the disk via the term $v_0$.

We now apply Equation 4.8 to TW Hya again assuming that the dominant particle size $s$ is given by the wavelength of the observation ($\lambda_{\rm obs}$). The resulting surface density points are well described by a steep power law function of approximately $r^{-4}$. Initially, this appears to be an unrealistically steep relation for the disk surface density as typical scalings for the minimum mass solar nebula are $\Sigma \propto r^{-1}$. However, as these points fall close to the observationally derived exponential fall-off range for the measurements of CO in Rosenfeld et al. (2012), the data match this profile quite well when we allow $\Sigma_c$ to be a floating normalization factor (see Section 4.3). We find that a surface density normalization of $\Sigma_c \approx 10^{2.5}$, approximately 3 orders of magnitude larger than $\Sigma_c$ from Rosenfeld et al., adequately matches our derived surface density points. The derived surface density profile with error estimates is shown in Figure 4.4.1. We find that the particle sizes we consider in the outer disk are indeed still well within the Epstein regime as was assumed in our derivation of the disk surface density profile.

We note that this surface density estimate depends on the age of the disk

which may be uncertain by as much as a factor of 2 (e.g. Pecaut et al. 2012). For TW Hydra the surface density normalization, $\Sigma_c$, ranges from $\sim$ 200 at 3 Myr to $\sim$ 800 at 10 Myr. We note that the upper end of this age range will lead to a derived disk surface density that is Toomre-Q unstable, however, due to the order of magnitude nature of this derivation those numbers could be revised through a more detailed calculation. This trend generally holds such that the derived disk surface density increases with an increase in estimated disk age.

We can now convert our surface density profile to a derived gas mass as well as a mass accretion rate for TW Hya. We find that our derived gas mass of approximately 0.05 $M_\odot$ is consistent with the observational lower limit of 0.05 $M_\odot$ as derived from HD measurements of the warm gas (Bergin et al. 2013). We remark that this agreement implies no low-density cool gas and note that there is room within the errors for there to be a comparable amount of cold and hot mass present within the disk, however, to avoid being Toomre-Q unstable the mass cannot increase by a substantial amount.

Following the discussion in Section 4.3, with the inclusion of rough radius error estimates, we find a mass accretion rate of $\dot{M} \sim 4\times10^{-9} - 2\times10^{-8}$ $M_\odot$ yr$^{-1}$. Compared to the measured value of $\sim 1.5 \times 10^{-9}$ $M_\odot$ yr$^{-1}$ (Brickhouse et al. 2012) our derived accretion rates give a larger value more in line with measured accretion rates for younger systems than the derived disk accretion rate using CO surface density observations as in Rosenfeld et al. (2012). We note that TW Hya has an inner disk gap at 1 AU (Andrews et al. 2016). It is possible that this gap was formed by the presence of an accreting protoplanet which could be allowing only $\sim$ 10% of the accretion flux onto the star

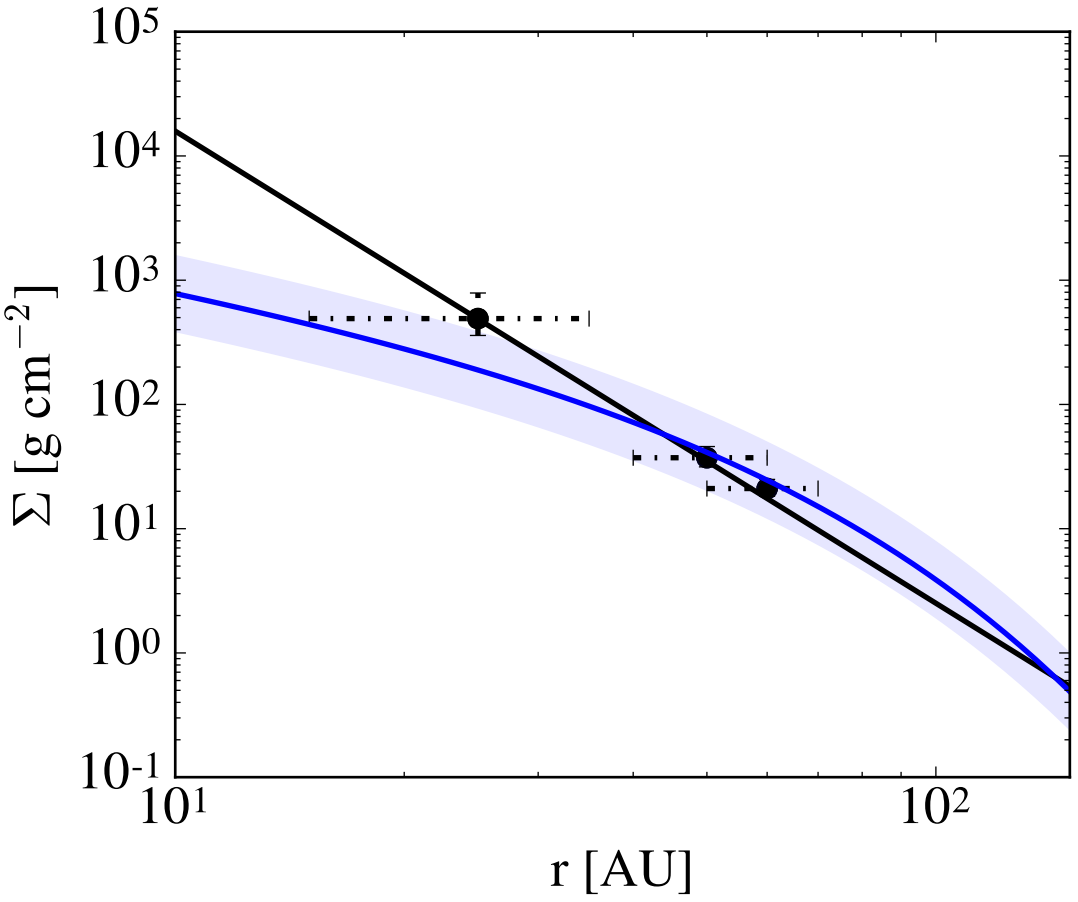


Figure 4.3: Surface density of TW Hya (points) derived from Equation 4.8 using the three observed disk sizes $r(s)$ with radius error bars of $\pm$ 10 AU and their corresponding errors in surface density. The surface density profile at these radii are well fit by an $r^{-4}$ power law shown by the solid black line. The normalized surface density profile is shown in blue with the corresponding shading region indicating the roughly normalized surface density profile with the inclusion of the radial error estimates. The normalized surface density profile is an $r^{-1}$ power law interior to the critical radius ($r_c$) of 30 AU and is then described by an exponential fall off at radii larger than $r_c$. We find that a surface density normalization of $\Sigma_c \approx 10^{2.5}$ adequately matches our derived surface density points.

(Papaloizou & Nelson 2005; Najita et al. 2007; Zhu 2015; Eisner 2015).

We also note that, given our estimated disk age, our derived surface density profile is Toomre-Q unstable for the higher region of our estimated errors. We note, however, that assuming a shorter age of the system ($\sim$ 3 Myr) gives a stable disk surface density profile for all estimated errors.

### 4.4.2 Particle Growth and the Dust-to-Gas Ratio

Given that TW Hya is an evolved disk in dynamical equilibrium, we can use an approximation of the growth timescale to determine the dust-to-gas ratio in the outer disk through allowing $t_{\rm grow} = t_{\rm disk}$ as discussed in Section 4.4. We derive our growth timescale by first considering the growth rate in terms of particle size ($s$):

$$\dot{m} = \rho_d \sigma \Delta v \tag{4.9}$$

where $\rho_p$ is the density of the particles which we take to be $\sim \rho_g f_d$ where $f_d$ is the dust-to-gas ratio and $\sigma = \pi s^2$ where $s$ is the size of the dominant particle at that radius $r$. In the outer disk we assume that the relative particle velocities $\Delta v$ are due to turbulence which we approximate as:

$$\Delta v = \alpha c_s^2 \frac{t_L}{t_\eta} (\tau_{s,1} - \tau_{s,2})^2 \tag{4.10}$$

(Ormel & Cuzzi 2007) where $t_L$ is the overturn time of the largest eddies which we take to be the orbital period, $t_\eta = Re^{-1/2} t_L$, $\tau_{s,1}$ is the stopping time of our dominant particle size, $\tau_{s,2}$ is the stopping time of the particle size that contributes to growth, and

$\alpha$ is the parameter of ignorance for turbulence in a disk which we take to be a standard value of $10^{-3}$ (e.g. Rafikov 2017). This $\Delta v$ is valid for particles that are tightly coupled to the gas. We note that direct observations of disk turbulence (Hughes et al. 2011a; Teague et al. 2016) do not yet probe the disk midplane.

We are now able to solve for the dust-to-gas ratio in the disk through setting the growth timescale ($t_{\rm grow}$) equal to the age of the system ($t_{\rm disk}$) and solving for $f_d$. We do this while assuming that the particles grow through perfectly efficient sticking with particles that are similar in size. We make this approximation as most of the dust surface density will be in the largest grains such that these particles dominate particle growth. Given this assumption, typical values of $\Delta v$ for our TW Hya calculation are $\sim 3 - 10$ cm s$^{-1}$. For TW Hya this exercise gives an average dust-to-gas ratio of $f_d \approx 10^{-3}$ in the outer disk where we observe the disk dust lines.

As a consistency check we can compare this derived dust-to-gas ratio with the observed dust surface density profile described in Andrews et al. (2012). We note that the total dust mass and the dust surface density profile are model dependent quantities with values that vary across the literature (Calvet et al. 2002; Andrews & Williams 2005; Hughes et al. 2008, 2011b; Kamp et al. 2013; Hogerheijde et al. 2016). We thus choose the Andrews et al. (2012) model as it is based off of 870 $\mu$m emission which is within the range of our dust line observations.

In their model, the dust surface density profile is well described by a shallow power law $\Sigma_d \propto r^{-0.75}$ until the emission falls off at roughly 60 AU. This profile is normalized such that $\Sigma_d = 0.39$ g cm$^{-2}$ at 10 AU. When we divide this dust surface

density profile by our derived total surface density profile we find an average dust-to-gas ratio of $\sim 10^{-2.5}$ which is roughly consistent with our derived dust-to-gas ratio above.

We further compare our dust surface density points at the three dust line locations using our derived dust-to-gas ratios with the best fit model from Andrews et al. (2012) in Figure 4.4.2. We find a dust surface density that is systematically lower than the best-fit model from the 870 $\mu$m emission, however, without error bars on this observationally derived model it is difficult to know if our results are discrepant. We determine an extremely rough estimate of the uncertainty of this model by propagating uncertainties on the mass opacity, flux calibration ($\sim$ 10 % systematic uncertainty), and distance (a few percent uncertainty). The largest source of uncertainty in the Andrews et al. (2012) model is the mass opacity. We adopt an uncertainty on this value of roughly $\sim$ 99 % as the range in assumed mass opacities for dust at $\sim$ 870 $\mu$m ranges from $\sim 10^{-2} - 10^{0}$ in the relevant literature (e.g. Hildebrand 1983; Pollack et al. 1994; Henning & Stognienko 1996; Andrews & Williams 2005; Andrews et al. 2012). The error on the mass opacity thus dominates the uncertainty in the dust measurement. We note that our points represent the dust surface density comprised of the large particles in some set size distribution and that including the contribution of smaller grains to the total surface density should increase our answer by a few tens of percent.

We also compare to dust depletion in a time evolving disk as shown in Birnstiel & Andrews (2014) (see their Figure 4a) where they find a solid depletion of up to two orders of magnitude in their fiducial model for the outer regions of late stage disks. We therefore find that our estimate of dust depletion is consistent with their model results

for evolved disks.

In conclusion, by considering particle drift we derive a total disk surface density for TW Hya that is roughly 3 orders of magnitude larger than the surface density derived from CO observations through considering particle drift. We further derive a dust-to-gas ratio of approximately $10^{-3}$ in the outer disk ($\sim 25 - 60$ AU).

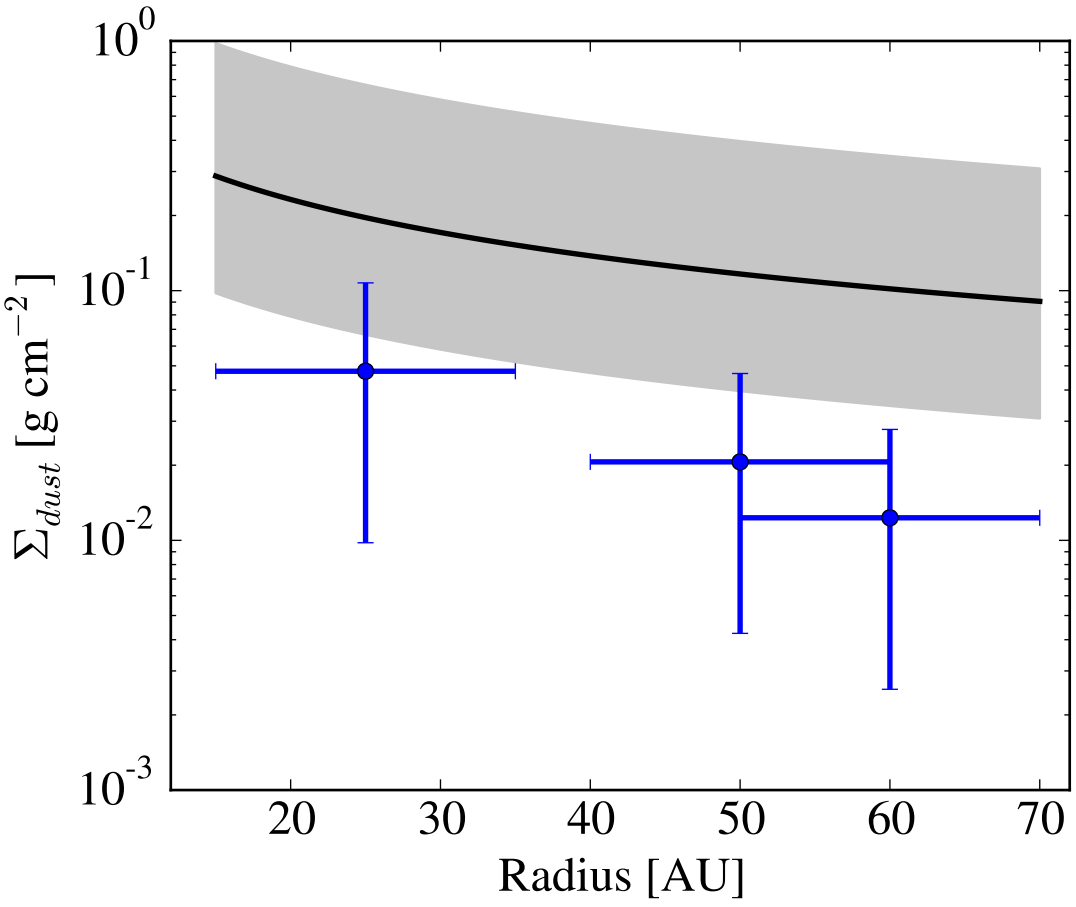


Figure 4.4: The dust surface density of TW Hya (points) determined from our derived dust-to-gas ratio in conjunction with our dust line derived total surface density profile. These points can be compared to the best-fit dust surface density profile (black line) from Andrews et al. (2012) for TW Hya derived using 870 $\mu$m emission. We find a dust surface density that is systematically lower than the best-fit model from the 870 $\mu$m emission. We provide a rough estimate of the uncertainty surrounding the dust surface density profile from Andrews et al. (2012) (gray shaded region, see text) and find that our results are not discrepant within the assumed error.

## 4.5 Ice Lines

We can now further our discussion of the disk surface density through a careful treatment of the molecular ice lines. The three ice lines that are most frequently calculated are $H_2O$, $CO_2$, and CO as these species are considered to be in relatively high abundance (Öberg et al. 2011). To date, the CO ice line is the most readily observed due to its large radial distance from the central star (Qi et al. 2013). We thus primarily focus on the CO ice line in our calculations. However, when we expand our discussion to consider a larger parameter space of disk parameters, we further extend our arguments to the other volatile species as well.

While we consider a passively heated disk (see Section 2), we note that the water ice line may be impacted by accretion heating. We include some plots of the $H_2O$ ice line for reference, but these should be viewed with caution.

Our discussion focuses on the *midplane* ice lines as opposed to the surface ice lines frequently discussed in the literature (Blevins et al. 2016; Schwarz et al. 2016). As a result we will compare our derived ice lines to observations that probe the midplane ice line directly (via the $C^{18}O$ line; Qi et al. 2015; Dartois et al. 2003) or indirectly (via the $N_2H^+$ ion; Qi et al. 2013, 2015).

There are three pieces of physics that we consider in our ice line calculations: particle adsorption, desorption, and drift.

### 4.5.1 Volatile Adsorption and Desorption

The classic ice line calculation balances adsorption and desorption flux onto a grain to determine the ice line radius (Hollenbach et al. 2009; Öberg et al. 2011). We refer to this ice line as the 'classical ice line'. Following Hollenbach et al. 2009, these two fluxes are quantified as:

$$F_{\rm adsorb} \sim n_i c_s \tag{4.11}$$

$$F_{\rm desorb} \sim N_{s,i} \nu_{\rm vib} {\rm e}^{-E_i/kT_{\rm grain}} f_{s,i} \tag{4.12}$$

where $n_i$ is the relevant gas density species, $c_s$ is the sound speed, $N_{s,i} \approx 10^{15}$ sites cm$^{-2}$ is the number of adsorption sites per volatile per cm$^2$, $\nu_{\rm vib} = 1.6 \times 10^{11} \sqrt{(E_i/\mu_i)}$ s$^{-1}$ is the molecules vibrational frequency in the surface potential well, $E_i$ is the adsorption binding energy in units of Kelvin, and $f_{s,i}$ is the fraction of the surface adsorption sites that are occupied by species $i$ (which we take to be unity). Finally, we assume that $T_{\rm grain} = T$, meaning that the dust and gas have the same temperature in the disk mid-plane.

Balancing Equations 4.11 and 4.12 allows for us to solve for the freezing temperature of a species as a function of radius for a given disk surface density profile. We then locate the classical ice line by finding the disk radius where the molecular freezing temperature is equal to the disk temperature. This self-consistent method allows us to determine how the ice line location changes as a function of both disk surface density

and temperature.

### 4.5.2 The Influence of Particle Drift

Particle drift, as described in Section 3, influences the location of the ice lines (Piso et al. 2015, 2016). This is because particles that drift faster can cross the ice line before desorbing, thus potentially moving the location of the ice line inwards. The drift ice line location can be calculated by setting the desorption timescale,

$$t_{\rm des} = \frac{\rho_s}{3\mu_i m_{\rm H}} \frac{s}{N_{s,i}\nu_{\rm vib} {\rm e}^{-E_i/kT_{\rm grain}}}, \tag{4.13}$$

(where $\mu_i$ is the molecular weight of the desorbing species) equal to the drift timescale (the radial location of a particle divided by Equation 4.6) and solving for the desorption distance, $r_{\rm des}$ (as verified by time evolving calculations in Piso et al. 2015). This is done analytically for the small stopping time approximation in the Appendix of Piso et al. (2015). We extend this calculation to the $\tau_s > 1$ regime through making no approximations in Equation 4.6 in regards to $\tau_s$. Instead, we use the two distinct stopping time expressions given both Stokes and Epstein regimes (Equation B.9). We use the SciPy subroutine fsolve (Jones et al. 2001) to solve for radius through balancing the drift timescale with the desoprtion timescale ($t_{\rm drift} = t_{\rm des}$) where these timescales are given by $t_{\rm drift} = |r/\dot{r}|$, where $\dot{r}$ is given by Equation 4.6, and Equation 4.13. We consider the radial dependence of each term without approximation, which allows us to derive a completely self-consistent estimate of $r_{\rm des}$ for any arbitrary surface density and/or temperature profile.

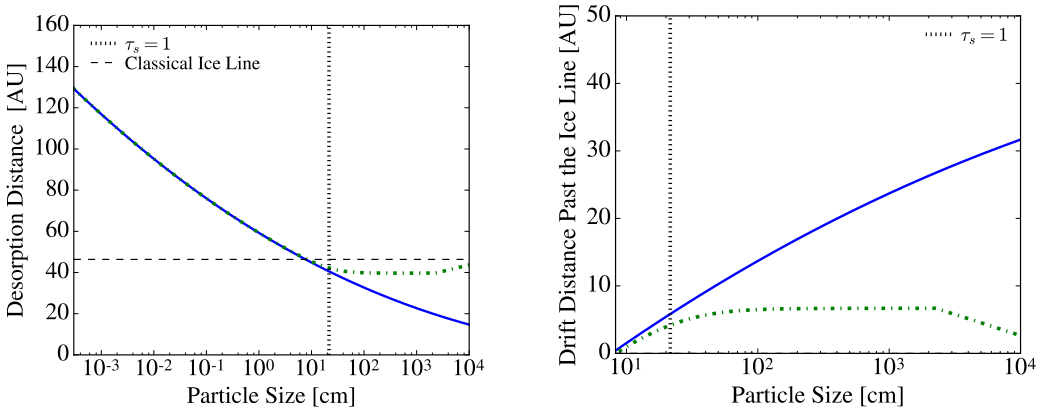


Figure 4.5: Left: The desorption distance, the location where the drift timescale equals the desorption timescale, calculated using the analytic method from Piso et al. (2015) (blue, solid) and our new extended solver (green, dashed). We find great agreement for particles with a stopping time less than unity. Right: The distance that a CO particle is able to drift past the classical CO ice line before desorbing using the analytic method from Piso et al. (2015) (blue, solid) and our new self-consistent solver (green, dashed). Using our extended solver we see that, for this comparison case, particles smaller than $\sim$ 10 cm do not drift past the ice line and are not shown. Particles larger than $\sim$ 8 cm do experience drift in this case, with the maximum drift reached at a particle size slightly larger than $\tau_s \approx 1$ that reaches a near constant value at larger stopping times.

We compare the difference between the drift ice line and the classical ice line for our new self-consistent solver and the analytic solver from Piso et al. (2015) in Figure 4.5.2. We use the disk temperature and surface density profiles from Piso et al. (2015) and find that particles smaller than $\sim 10$ cm ($\tau_s \sim 0.5$) do not drift past the CO ice line. Particles larger than $\sim 10$ cm do experience drift, with the maximum drift reached at a $\tau_s \approx 1$ that then reaches a near constant value at higher stopping time. We note that, while small particles do not drift to the same radial location as large particles, accretion of disk gas has been shown to pull smaller particles in past the ice line as shown in Piso et al. (2015).

The nearly constant drift distance at particle sizes with a stopping time greater than 1 occurs due to the interplay between two different pieces of physics. The first is that the larger the particle size the longer it takes for that particle to desorb and the further it can drift past the ice line. The second is that the maximum drift velocity occurs for particles with $\tau_s = 1$. The decrease in drift velocity past a stopping time of one is offset by the increase in particle size until the regime changes from Epstein to Stokes. The drift timescale for a particle in the Epstein with $\tau_s >> 1$ is $t_{\rm drift} = |r/\dot{r}| \sim \tau_s/\eta\Omega \sim \rho_s s/\rho c_s \eta$. The desorption timescale is simply proportional to the particle size ($t_{\rm des} \propto s$) with a desorption constant such that $t_{\rm des} \sim C_{\rm des} s$. When we equate these two timescales we find that the dependence on particle size cancels out and that the drift distance is therefore independent of this quantity. We find that this approximation is roughly accurate for particles in the Epstein regime with $\tau_s$ close to or greater than 1.

Due to this effect, we consider the "drift ice line" to be the location for which

a $\tau_s = 1$ particle starting at the classical ice line location drifts and then desorbs for situations in which we know the disk surface density. If we do not know the disk surface density we use a large sized particle such that it desorbs at the maximum drift radius for a range of disk parameters. We numerically solve for the drift distance without making any further approximations in all further discussions of drift. The existence of a maximum drift distance found in our self-consistent solution allows us to predict the circumstances in which drift affects the ice line locations.

We find that the radial location of the classical ice line strongly impacts the amount in which drift will play a role. In particular, we find that the process of drift becomes important when the classical ice line is located where larger particles have a stopping time close to 1 as $\tau_s = 1$ particles drift the fastest and larger particles take longer to desorb (see Figure 4.5.2). The size of the $\tau_s = 1$ particle depends on the overall surface density profile of the disk. Drift will therefore matter the most in determining the true ice line location at the disk radial location where the particles with $\tau_s = 1$ reach a maximum size. If the classical ice line of a particular molecule is located near this point then drift will affect the location of the ice line radius pushing it inwards. This is shown in Figure 4.5.2 through a consideration of our derived surface density profile for TW Hya and the standard profile used for the minimum mass solar nebula ($\Sigma \propto 1700$ g cm$^{-2} \times r^{-3/2}$) (Öberg et al. 2011; Chiang & Youdin 2010).

### 4.5.3 Application to TW Hya

Given our derived total surface density profile for TW Hya, the last parameter needed to derive the CO ice line location is the CO abundance. We use the measured

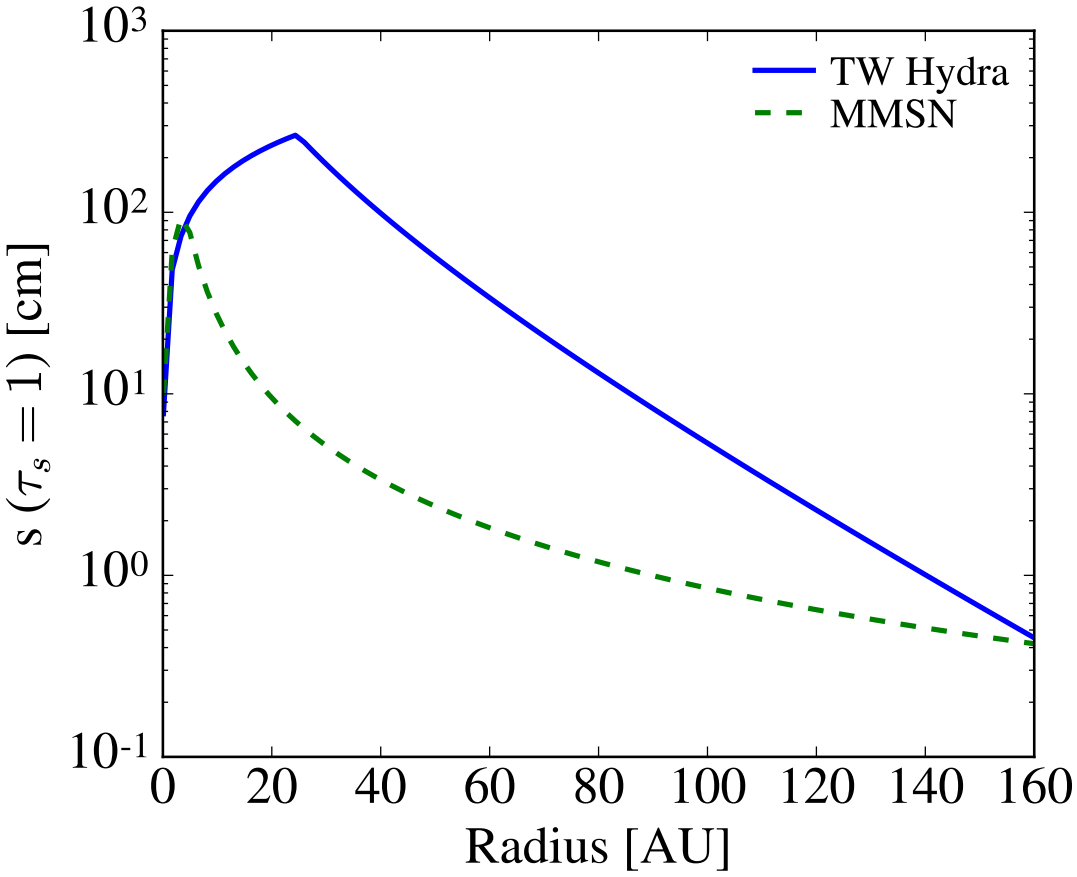


Figure 4.6: More massive disks reach a peak in the size of $\tau_s = 1$ particles at radii further from their central star as is the case for TW Hya as compared to the minimum mass solar nebula. Shown here is the size of $\tau_s = 1$ particles in the disk as a function of radius for two different surface density profiles: our TW Hya surface density profile (blue, solid) and the commonly used minimum mass solar nebula surface density profile (green, dashed). The $\tau_s = 1$ particles are the largest particles that are still well-coupled to the gas. Drift affects the ice line locations the most when the classical ice lines occur close to the peak in these plots.

CO surface density from Schwarz et al. 2016 in conjunction with our derived total surface density profile to uncover an approximate CO abundance of $10^{-7}$ $n_H$ from $\sim 10-60$ AU. This value is consistent with the average upper limit of $10^{-6}$ $n_H$ found in Schwarz et al. (2016) which was derived by comparing their CO surface density to the surface density profile derived from HD observations of the warm gas (Bergin et al. 2013).

This reduction of 3 orders of magnitude from the measured abundance in the ISM ($10^{-4}$ $n_H$) demonstrates that our model requires a global depletion of volatile carbon in TW Hya. Cleeves et al. (2015) infer a similar level of depletion using observations of CO and modeling by Du et al. (2015) supports this conclusion.

We can now calculate both the classical and maximum drift CO ice lines. For our calculations we use a binding energy of $E_i/k \sim 850$ K (Aikawa et al. 1996) [3]. For TW Hya, we derive a classical CO ice line of $\sim 30$ AU and a drift ice line of $\sim 15$ AU.

We find that our derived classical ice line is in agreement with the ice line determined observationally via the $N_2H^+$ ion of $\sim 30$ AU (Qi et al. 2013). We further find that our derived drift ice line is in good agreement with the CO ice line as derived through the $C^{18}O$ $J = 3-2$ line where a decrement of CO emission is observed until $\sim 10$ AU (Nomura et al. 2016). Given the discrepancy between the ice line as determined by $N_2H^+$ and $C^{18}O$ and the corresponding agreement we find with our theoretical model, we note that the $C^{18}O$ $J = 3-2$ line may be the most sensitive probe of a disk's midplane ice line, particularly when particle drift effectively smears the ice line out over

[3] We note that observations discussed in Schwarz et al. (2016) indicate a CO binding energy closer to $E_i/k \sim 960$ K for TW Hya. Using this binding energy we determine that the classical CO ice line is located at $\sim 23$ AU and the drift ice line is located at $\sim 10$ AU. These derived values are also reasonably consistent with the observed ice lines of TW Hya (see text).

a relatively large radial scale. This could be because the presence of $N_2H^+$ requires a lack of CO gas in the disk and may thus require that all particle sizes have frozen out (i.e. the classical ice line).

We can now put together our complete model for the dust and ice lines in TW Hya as shown in Figure 4.5.3.

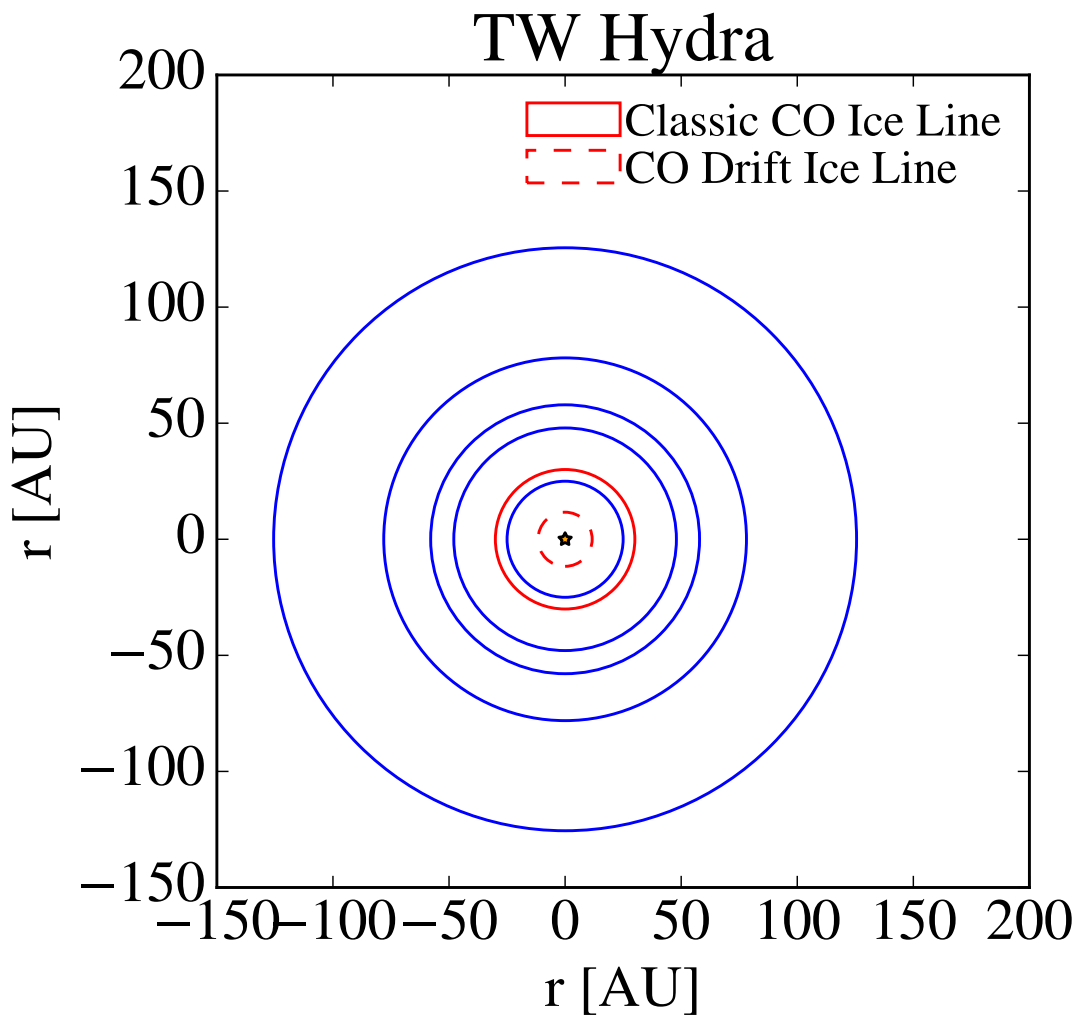


Figure 4.7: A model of the dust and ice lines in TW Hya. The blue lines are the dust lines solved by assuming that the drift timescale is equal to the age of the system. The blue lines adequately reproduce the observed disk radial scale of TW Hya at various wavelengths. The solid red line is the classical CO ice line solved by balancing the adsorption and desorption flux onto a grain. This line is in agreement with the observed CO ice line of $\sim$ 30 AU using $N_2H^+$ (Qi et al. 2013). The dashed red line is the CO drift ice line for a $\tau_s = 1$ particle at a radius of $\sim$ 15 AU which we find to be in close agreement with the ice line derived from $C^{18}O$ measurements in Nomura et al. (2016), suggesting that $C^{18}O$ is a sensitive probe of the CO drift ice line.

## 4.6 Observational Diagnostics

We now propose three different observational tests of our model framework beyond the application to TW Hya. The first test is whether or not other disks have dust lines that can be well fit by a normalized form of the physically motivated surface density profile in Equation 4.3 for disks where $r_c$ is constrained by CO observations. This is a particularly powerful test of concept if we find dust lines in other disks that are located in the power-law region of the surface density profile interior to the exponential fall-off. The second test is whether we can derive a surface density profile from the disk ice lines that is consistent with the surface density profile derived from disk dust lines. The third test is whether or not the dust and ice lines scale oppositely, as a function of surface density, across a large sample of disks.

Our second and third tests rely on an understanding of both classical (i.e. classical regime) and drift (i.e. drift dominated regime) ice lines as described in Section 4.5. The particular assumptions and/or prior knowledge of a disk will inform which of the two regimes is relevant as discussed in Section 4.6.2.

### 4.6.1 Test 1: Surface Density from Disk Dust Lines

The first test of our model is whether or not other disks have dust lines that can be well fit by a normalized form of the physically motivated surface density profile in Equation 4.3. In the era of ALMA, multiple disks will have high resolution data at several wavelengths – the ideal data set for this fundamental test. Following the technique described in Section 4.4 we can convert these dust lines into a surface den-

sity measurement and see if these measurements scale with the observationally derived surface density profiles.

In the case of TW Hya, the disk dust lines were near the exponential fall-off point, which unexpectedly (due to the steep slope of the derived power law) matched previous surface density models with the application of a normalization factor. For other disks there is no reason to think that the disk dust lines will necessarily fall in the same exponential fall-off region of the disk surface density profile. If a disk has a critical radius further from the star then it is increasingly likely that we will be able to detect dust lines interior to this point.

This test is thus a powerful test of concept that will allow us to see whether other disk sizes can be well fit through considering drift as the primary driver of disk dust lines and using these derived surface density values to normalize previous observationally fit disk surface density profiles.

- **Test 1 Observational Requirements:** This test can be best carried out on disks with CO observations, such that there is a derived critical radius, and observations of dust emission at several wavelengths such that the disk dust lines are known.

### 4.6.2 Ice Line Regimes

It is now helpful for us to distinguish between the drift and classical ice lines from observations of CO or other ice line tracers. Here we provide several rules of thumb to aid in the use of ice lines as useful diagnostics. However, we note that these aids should be used initially and then verified for self-consistent results.

Our proposed tests using these ice lines differ as the classical ice line depends on the CO abundance while the drift ice line does not. This makes the drift ice line particularly useful as it relies on fewer assumptions while the classical ice line retains its usefulness when considered across a sample of disks.

As mentioned in Section 4.6, there are two regimes that dictate when the drift or classical ice lines are relevant: the drift-dominated regime and the classical regime. In the drift-dominated regime the drift ice line is interior to the classical ice line and thus there should be only be CO freeze out exterior to this point with complete freeze-out occurring exterior to the classical ice line, making the drift ice line the most interior detectable ice line in the disk. In the classical regime particle drift does not happen quickly enough for particles to cross the ice line without desorbing and the classical ice line is observed.

To interpret the surface density from the disk ice line (see Section 4.6.3) we need a priori knowledge of the relevant ice line regime in the disk. Without knowledge of the disk surface density profile we can roughly determine the correct regime through an analysis of the ice line dependence on elemental abundance and disk temperature as well as a comparison of the ice line location with respect to the disk's critical radius.

One simple metric in determining the ice line regime is the knowledge that the ice line location is preferentially dominated by drift for disks that have large particles with a stopping time of unity near the ice line location. As seen in Section 4.5.2, particles can drift further without desorbing where the $\tau_s \approx 1$ particle size is large. This size increases at a given radius with increased disk critical radii and surface density

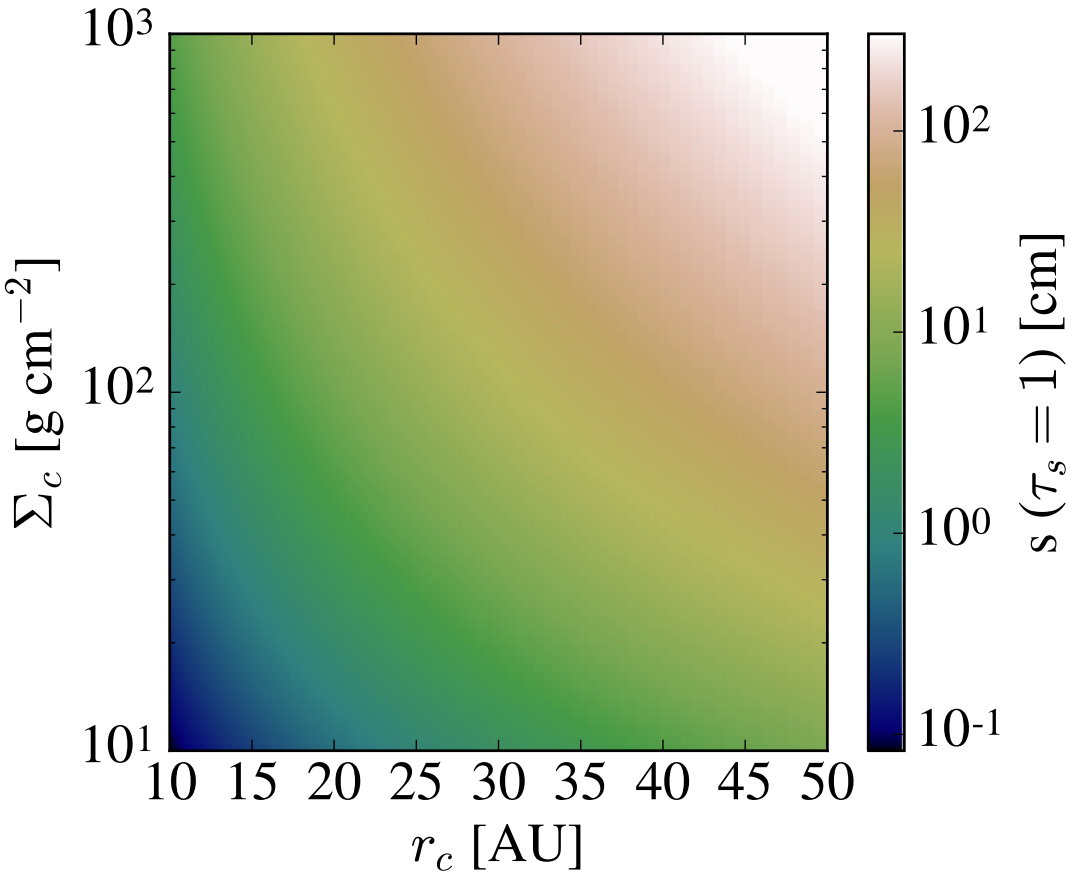


Figure 4.8: The $\tau_s = 1$ particle size for a disk using our derived temperature profile for TW Hya (see Equation 4.1 with $T_0 = 82$ K) at a radius of 30 AU (the observed classical ice line radius). We vary the disk critical radius and the surface density normalization and find that the ice line is likely to be dominated by drift for disks with large critical radius and high surface density normalization.

as demonstrated in Figure 4.6.2 where we calculate the $\tau_s = 1$ particle size at 30 AU for a disk with the same temperature profile as TW Hya for a range of surface density normalization factors and disk critical radii. We find that an ice line observed interior to the critical radius is likely dominated by drift for massive disks with large critical radii.

Another parameter that determines the ice line regime is the amount of radia-

tion that the disk receives from its host star (i.e. the stellar luminosity). The importance of this parameter is shown in Figure 4.6.2 for generally assumed molecular abundances ($n_{CO} = 1.5 \times 10^{-4}$ $n_H$, $n_{CO_2} = 0.3 \times 10^{-4}$ $n_H$, $n_{H_2O} = 0.9 \times 10^{-4}$ $n_H$; Pontoppidan 2006).

We find that we are in the drift dominated regime for disks with moderate densities and high temperatures across all three molecular species. At very high disk densities we find that the drift ice line is irrelevant and only the classical ice line can be observed, as a large increase in disk density moves the classical ice line inwards such that the disk temperature at the ice line is higher and the desorption timescale is shorter (i.e. the increased temperature near the star overwhelms the effect of the increase in disk density, see Equation 4.12). As the disk density is not known a priori we posit that the drift ice line is likely relevant for disks with high stellar irradiation.

We further find that, given a molecular depletion as in the case of our derived disk parameters for TW Hya and may be true for the majority of disks, drift sets the true ice line location across a wide range of parameter space as shown in Figure 4.6.2. Drift is more important when the CO abundance is smaller because the decrease in CO abundance moves the classical ice line further from the star while the drift ice line remains unchanged with the change in abundance. Therefore, we find that disks depleted in CO should have ice lines that are determined by drift. This is further demonstrated in Figure 4.6.2 where, across a wide range of molecular CO abundances, the drift ice line is constant and interior to the classical ice line given our derived disk parameters for TW Hya.

It is therefore a relatively safe assumption to consider the CO ice line location

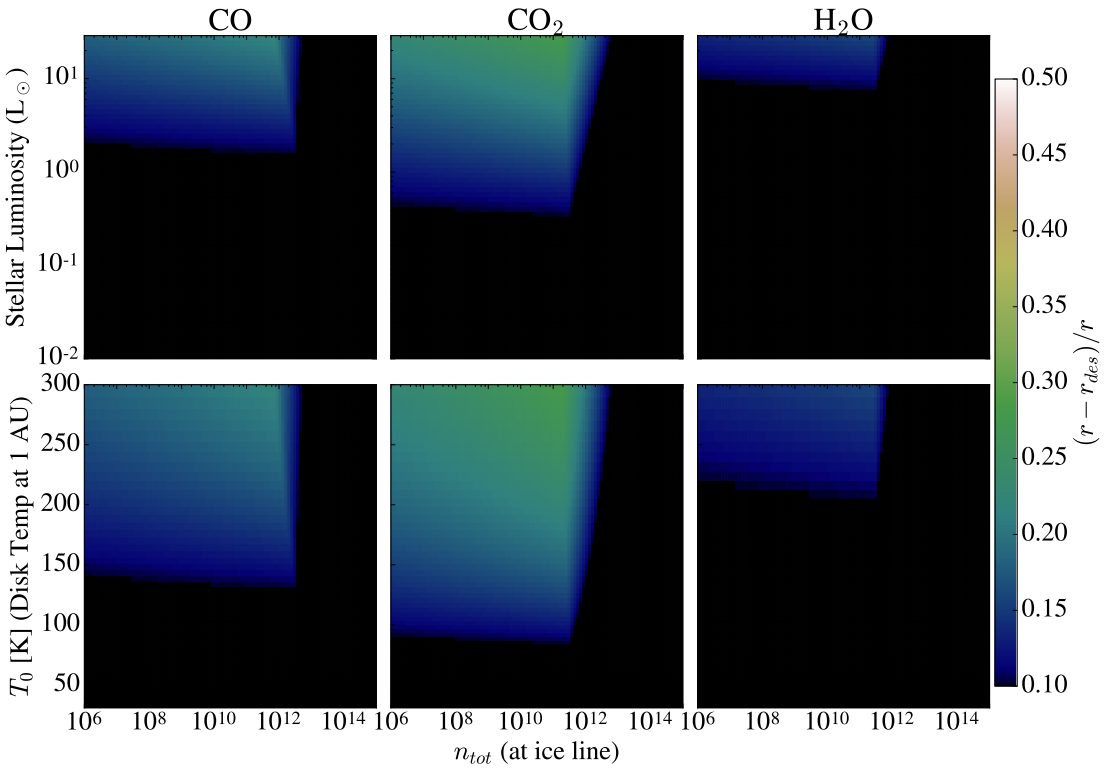


Figure 4.9: The fractional difference between the classically derived ice line $r$ and the drift ice line $r_{des}$ as a function of stellar luminosity and disk density (top) as well as disk density and temperature (bottom) for the following molecular abundances: $n_{CO} = 1.5 \times 10^{-4}$ $n_H$, $n_{CO_2} = 0.3 \times 10^{-4}$ $n_H$, $n_{H_2O} = 0.9 \times 10^{-4}$ $n_H$ (Pontoppidan 2006). Drift is most important for $CO_2$ and generally increases at moderate densities and high temperatures. The y-axis label $T_0$ refers to the temperature normalization for Equation 4.1 and we can convert from this temperature normalization to stellar luminosity using Equation 4.3. For stellar luminosities below $10^{-2}$ $L_\odot$ drift does not play a role in determining the ice line locations.

to be determined by drift for disks that are hot, depleted in CO, and/or have an observed ice line interior to a large critical radius and appear to be relatively massive. Disks for which the opposite is true are in the classical regime and their ice lines should be theoretically treated as classical ice lines.

### 4.6.3 Test 2: Surface Density from Disk Ice Lines

The second test of our model is whether or not the surface density profile derived from a consideration of the disk ice line matches the surface density profile derived from the disk dust lines. We now discuss how empirical knowledge of a disk's molecular ice line can be used to independently determine the total surface density profile of a disk. This can be done as both the drift and classical ice lines depend on the disk surface density.

#### Drift Ice Line Surface Density Determination

If the disk in question is in the drift dominated ice line regime (see Section 4.6.2), solving for the disk surface density profile simply involves setting Equation 4.6 for $\tau_s = 1$ (where particle drift reaches a maximum) equal to Equation 4.13 and solving for surface density given an assumed characteristic particle size. This surface density measurement can then be used to normalize the total disk surface density profile, thus giving us an independent estimate that can be compared to the profile derived via the disk dust lines.

While this method requires the assumption of a characteristic particle size, we note that a wide range of particle sizes will result in the same drift ice line location (see

Figure 4.5.2) and thus, the derived surface density profile will not be sensitively affected by this value. For computational purposes we use a particle size of 1 m such that its stopping time exceeds unity for a wide range of disk parameter space. As is the case for all particles close to or larger than a stopping time of unity, these particles should desorb after drifting to the maximum drift ice line.

Consideration of the drift ice line in determining disk surface density has the advantage of not needing a measure of the molecular abundance in the disk. Regardless of CO abundance this location will be constant as it is dependent on disk surface density and not the CO surface density. Thus, a sensitive probe of the CO ice line (i.e. the $C^{18}O$ $J = 3 - 2$ emission) should be able to detect the uptick in CO emission past this point and provide a probe of disk surface density from this measurement alone without further assumption.

**Classical Ice Line Surface Density Determination**

If the disk in question is in the classical ice line regime (see Section 4.6.2), the surface density can be derived by balancing Equation 4.11 and Equation 4.12. Unlike the drift dominated regime, this calculation requires an assumed molecular abundance. While these uncertainties may diminish the robustness of this test, we can make the simplifying assumption that molecular abundances are roughly constant across a single stellar type. This could be a reasonable assumption if molecular abundances are primarily shifted from ISM values via photochemical processes. If we accept this assumption as true, we can determine the disk surface density profile for disks of a stellar type for which one member has a relatively well determined molecular abundance. We

note that, for this method, a factor of 2 change in the ice line location will change the derived surface density by a factor of 3.

The relative behavior of the classical ice line across many disks will also improve this test and may indeed allow the potential for deriving the CO abundance in conjunction with Test 1.

- **Test 2 Observational Requirements:** This test can be carried out on disks with accurate ice line measurements (either via $C^{18}O$ or $N_2H^+$). To carry out this test more precisely it is also useful to have observationally derived CO surface density profiles for these disks.

### 4.6.4 Test 3: Disk Dust and Ice Line Scalings

The third test is whether or not the dust and ice lines scale oppositely across a large sample of disks. Our model predicts that this will happen as disks with dust lines at larger radial scales should have ice lines located at shorter radii across a particular disk temperature profile and molecular abundance. This arises as larger particles become well coupled to the gas as disk surface density increases, thus causing a given particle size to have a dust line located further out in the disk. Conversely, increased surface density increases the adsorption flux onto a grain such that the freezing temperature is hotter and the ice line is moved closer to the star.

To clearly see how the dust and ice lines in a disk scale as a function of surface density alone, we vary the disk surface density for a set disk temperature profile. Using the empirical evidence that the Earth is not formed of water ice, we consider the case

of a passively irradiated disk that is normalized such that the $H_2O$ ice line is outside of 1 AU as shown in Figure 4.6.4 as our fiducial temperature profile. We take this temperature profile to be roughly representative of a young sun like star. This profile follows Equation 4.1 with a derived $T_0 \approx 210$ K.

This profile is derived through the use of an assumed canonical $H_2O$ abundance of $0.9{\times}10^{-4}$ $n_H$ (Pontoppidan 2006). While this assumption is sufficient for our illustrative example, we again note that disk molecular abundances may be poorly constrained. However, let us naively assume that molecular abundances vary from ISM values as a function of photochemistry such that they are constant across a particular stellar type and thus a particular temperature profile. Thus, using this temperature profile we can derive the trends that we expect to see as we vary the disk surface density.

We find that for all three of our molecular species: CO, $CO_2$, and $H_2O$, the radial extent of the disk increases with increasing surface density while the ice line location decreases as expected (see Figure 4.6.4). For the CO and $H_2O$ ice lines, the drift distance past the classical ice line is negligible while for the $CO_2$ ice line drift plays a small role that decreases in importance with increasing surface density. We note that while the importance of the drift ice line will vary with disk parameters, the general trend should hold.

This trend remains true across a range of molecular abundances as long as they are held constant across a sample of disks. Here we have assumed the following abundance values for our molecular species: $n_{CO} = 1.5 \times 10^{-4}$ $n_H$, $n_{CO_2} = 0.3 \times 10^{-4}$ $n_H$, $n_{H_2O} = 0.9 \times 10^{-4}$ $n_H$ (Pontoppidan 2006). We note that lower molecular

abundances result in lower freezing temperatures (see Section 4.5.1) which, depending on the temperature profile of the disk, pushes the classical ice lines further from the star with the reverse being true for higher molecular abundances.

This trend is therefore a key observational diagnostic that will be confirmed if, across a constant molecular abundance, disks with dust lines at larger radii have ice lines closer to their star. We also note that, if drift determines the ice line location (see Section 4.6.2) we can observe these trends without the need for an assumed molecular abundance.

- **Test 3 Observational Requirements:** To best perform this test there needs to exist a significant sample of disks with observations of both the dust and ice lines.

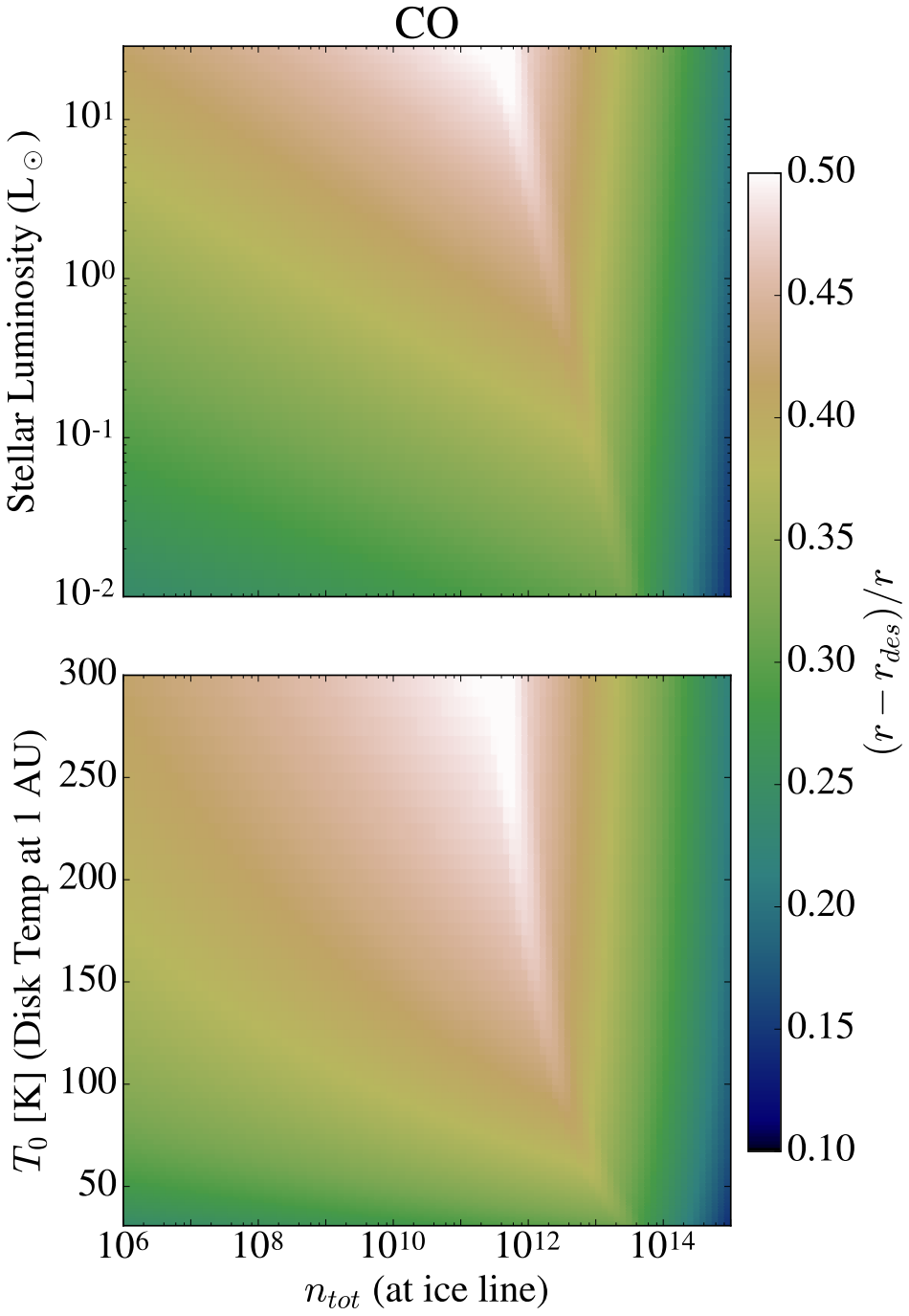


Figure 4.10: The fractional difference between the classically derived ice line $r$ and the drift ice line $r_{des}$ as a function of stellar luminosity and disk density for an $n_{CO}$ of $10^{-7}$ $n_H$. We find that drift plays a role in determining the extent of the ice line location across the full range of our parameter space.

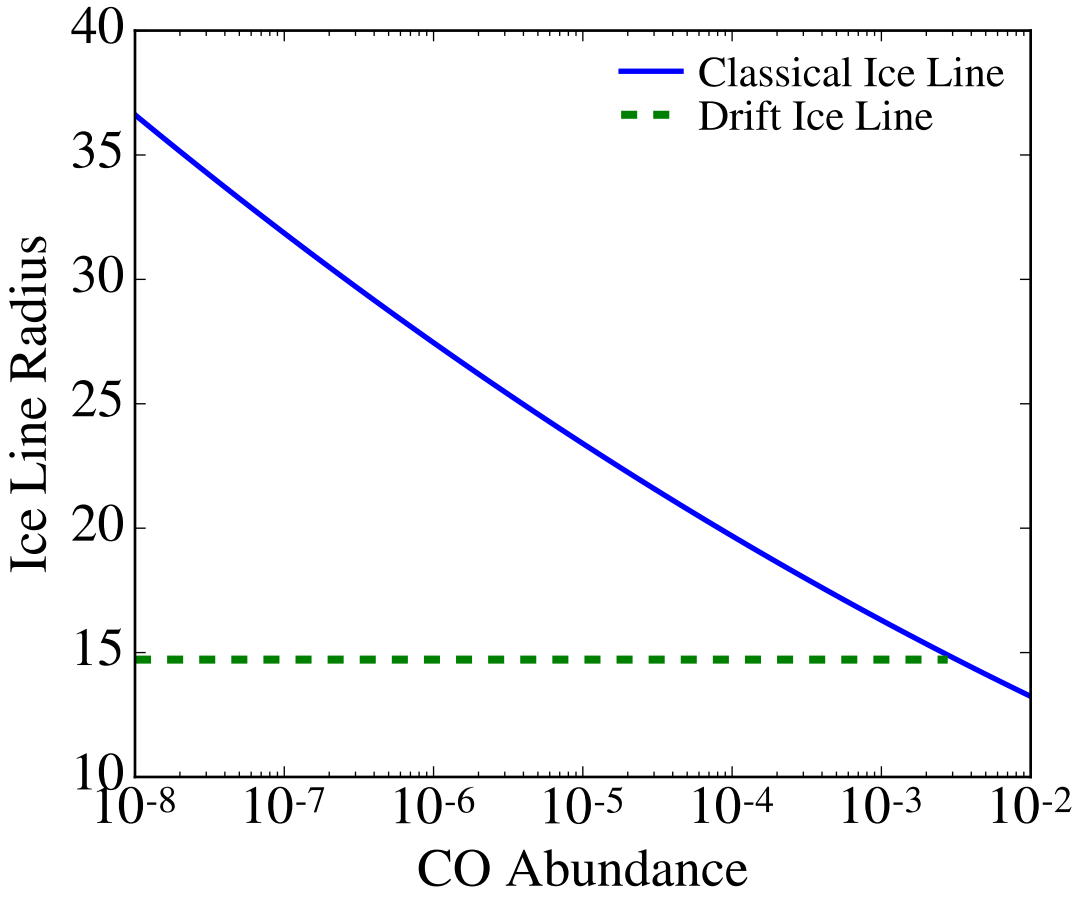


Figure 4.11: The classical ice line location (blue) and drift ice line location (green, dashed) as a function of CO abundance for our derived disk surface density and temperature profile for TW Hya. The drift ice line location is constant and interior to the classical ice line radius for a wide range of CO abundances.

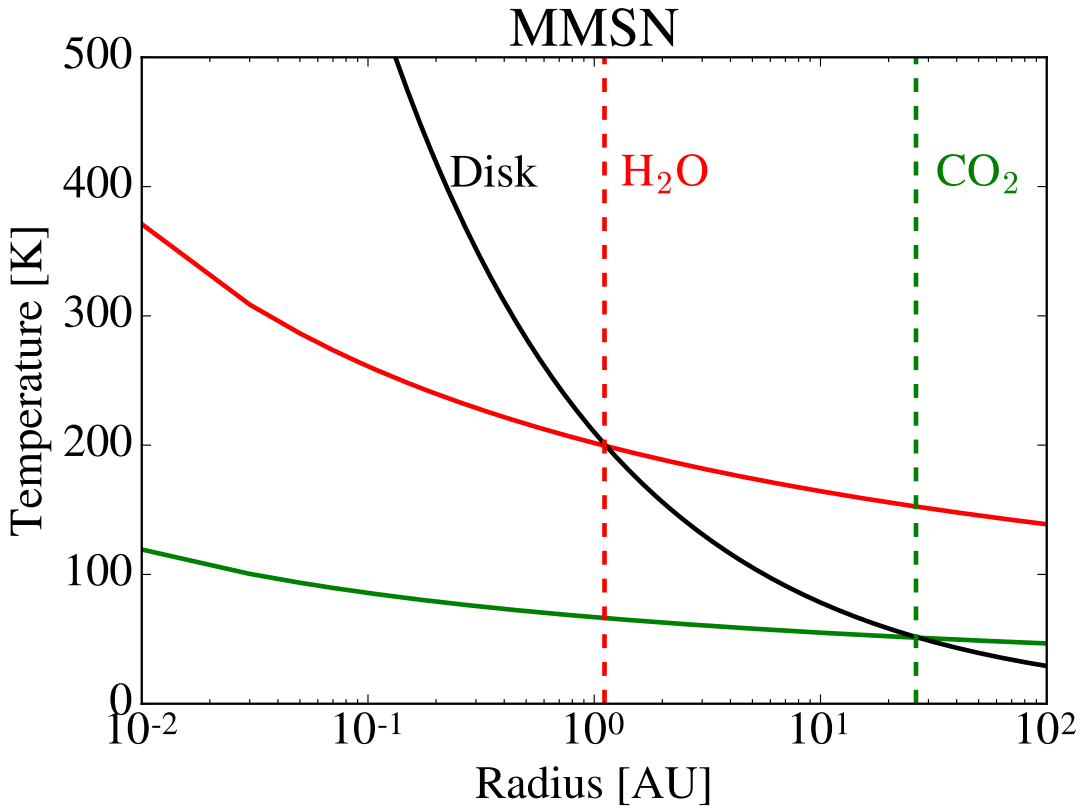


Figure 4.12: The $H_2O$ (red) and $CO_2$ (green) freezing temperature (calculated by self-consistently balancing Equations 4.11 and 4.12) as a function of radius for the minimum mass solar nebula (MMSN). The black line is the minimum temperature profile that places the $H_2O$ ice line outside of 1 AU. Classical snow lines occur where the freezing temperature and the disk temperature are equal (dashed lines).

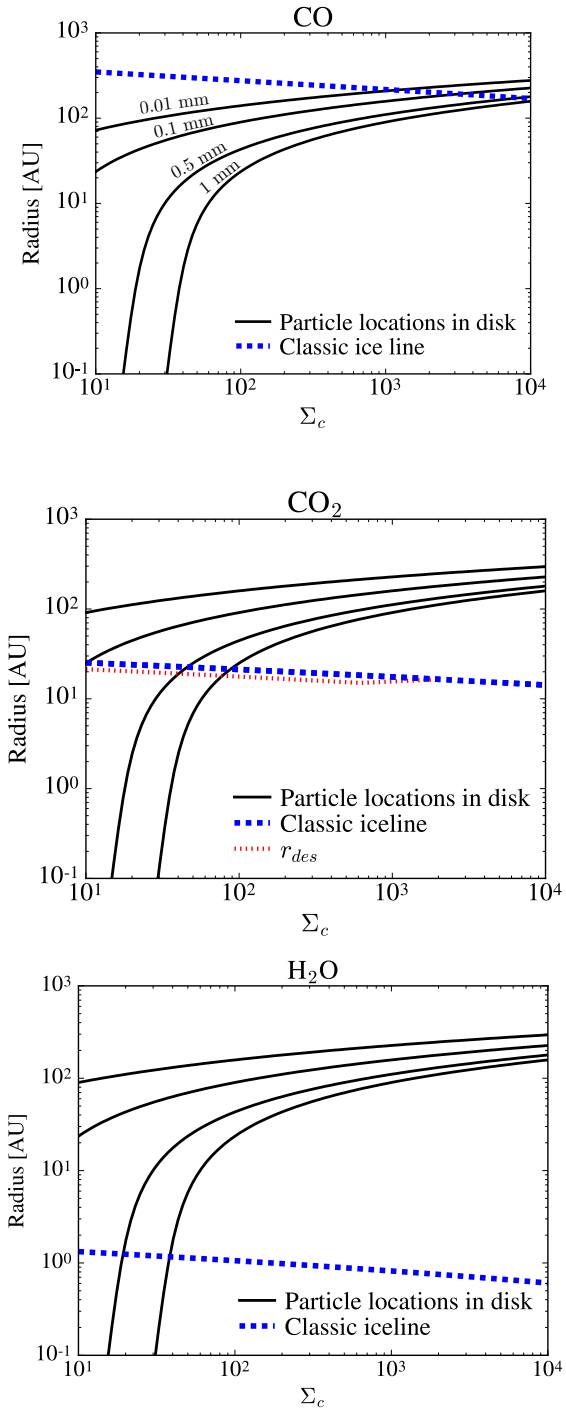


Figure 4.13: The disk radial scale for different particle sizes (black, solid), the classically derived ice line locations (blue, dashed) and the drift ice line (red, dotted) for CO (top; with particle sizes labeled), $CO_2$ (middle), and $H_2O$ (bottom) as a function of surface density. The dust line locations increase dramatically with increased surface density while the ice line location decreases.

## 4.7 Summary & Discussion

We propose a novel method to derive disk surface density through the consideration of disk dust and ice lines. To derive this method we adopt an agnostic point of view in regards to disk surface density which we do in particular response to the uncertainties that accompany typical observational tracers. This method relies on the assumption that, at late stages of evolution, the growth timescale, drift timescale, and the lifetime of the disk are all equal for the dominant particles at a dust line location ($s = \lambda_{\rm obs}$).

While other work finds that these timescales are equal they are often unable to match the disk surface density. We therefore make the assumption that these timescales are equal and use this to determine the surface density profile without evoking other observational tracers. These assumptions allow us to self-consistently derive a disk surface density profile as well as a dust-to-gas ratio in the outer disk without the further assumption of a given molecular abundance.

We apply our modeling technique to our fiducial disk TW Hya. We find that our derived surface density profile and dust-to-gas ratio are consistent with the lower limits found through measurements of the HD gas in the disk (Bergin et al. 2013; Schwarz et al. 2016). Using our derived surface density profile we uncover a theoretical estimate of the disk accretion rate that is more closely aligned with the measured accretion onto TW Hya. We further find that our theoretical classical and drift ice lines have clear observational analogues where the classical ice line is predictive of the ice line found via $N_2H^+$ emission (Qi et al. 2013) and the drift ice line is probed by the $C^{18}O$ emission

(Nomura et al. 2016). We conclude that the ice line derived through observations of $C^{18}O$ emission may be more sensitive to the extent of the drift ice line in the disk and thus may be the best observational method to test our model's assumptions. We note here that our method highlights the likelihood of detecting multiple ice lines for a given molecular species as there will be relatively large regions in the disk where some of the material has desorbed and some of the material has not.

Furthermore, if the banded structure in the ALMA images of HL Tau and TW Hydra reflect substantial variations in surface density then our model should still hold. However, ice lines may be preferentially found in less dense bands in the disk where drift slows.

We next consider a large range of theoretical disk parameter space and uncover three observational tests of our model. The first test is whether or not the dust lines of other disks, once converted to surface densities, can be matched with a previously derived normalized surface density profile for the disk. For TW Hya, the disk dust lines fall near the exponential cut off region of the disk but there is no reason that this needs to be true across many objects and thus provides a powerful test of the model. In the age of ALMA, dust lines can be determined observationally for a significant sample to protoplanetary disks which will provide the ideal observations necessary for this test.

The second test is whether we can derive a surface density profile from the disk ice lines that matches the surface density profile derived via disk dust lines. The third and final test is whether or not disk dust and ice lines scale oppositely, as a function of surface density, across a large sample of disks. Disk ice lines have been observed for an

increasing number of disks such that the last two tests could be carried out in the near future with the aid of facilities such as ALMA.

# Chapter 5

# New Constraints From Dust Lines on the Surface Densities of Protoplanetary Disks

## 5.1 Abstract

We present new determinations of disk surface density, independent of an assumed dust opacity, for a sample of 7 bright, diverse protoplanetary disks using measurements of disk dust lines. We develop a robust method for determining the location of dust lines by modeling disk interferometric visibilities at multiple wavelengths. The disks in our sample have newly derived masses that are 9-27% of their host stellar mass, substantially larger than the minimum mass solar nebula. All are stable to gravitational collapse except for one which approaches the limit of Toomre-Q stability. Our

mass estimates are 2-15 times larger than estimates from integrated optically thin dust emission. We derive depleted dust-to-gas ratios with typical values of $\sim 10^{-3}$ in the outer disk. Using coagulation models we derive dust surface density profiles that are consistent with millimeter dust observations. In these models, the disks formed with an initial dust mass that is a factor of $\sim$10 greater than is presently observed. Of the three disks in our sample with resolved CO line emission, the masses of HD 163296, AS 209, and TW Hya are roughly 3, 115, and 40 times more massive than estimates from CO respectively. This range indicates that CO depletion is not uniform across different disks and that dust is a more robust tracer of total disk mass. Our method of determining surface density using dust lines is robust even if particles form as aggregates and is useful even in the presence of dust substructure caused by pressure traps. The low Toomre-Q values observed in this sample indicate that at least some disks do not accrete efficiently.

## 5.2 Introduction

Protoplanetary disks are the likely initial conditions of planet formation. One of the most fundamental parameters in planet formation theory is the disk surface density – or the total disk mass inventory. The most common method of observationally determining disk surface densities is to infer the total mass through the use of a mass tracer that emits more readily than the main mass constituent – molecular hydrogen. The two most commonly used tracers of mass are dust and rotational lines of carbon monoxide gas, since both emit substantially in the millimeter. From dust observations,

the solid surface density is inferred from the dust's assumed optically thin thermal emission and is converted to a total surface density via an assumed dust-to-gas ratio. From observations of rotational lines of CO, the gaseous surface density is inferred from observations of one or more CO isotopologues that are thought to be optically thin and is converted to a total surface density via an assumed CO-to-$H_2$ ratio. Mass estimates derived from these methods, however are often inconsistent and can vary by orders of magnitude (e.g., Bergin et al. 2013). There are several reasons to question the accuracy of these methods.

When inferring solid surface densities, a dust grain opacity must be assumed. However, the opacity of dust grains in disks is highly uncertain (e.g., Wright 1987; Beckwith et al. 2000; Beckwith & Sargent 1991; Andrews & Williams 2005; Birnstiel et al. 2018) and dust continuum observations lose sensitivity to solids that are much larger than the observing wavelength (e.g., Williams & Cieza 2011). It is therefore possible that measurements from dust observations are missing a reservoir of mass. Furthermore, the dust-to-gas ratio in disks should differ from the ISM value of $10^{-2}$ due to processes such as grain growth and drift (e.g., Hughes & Armitage 2012). A differing dust-to-gas ratio will change the inferred total gas surface density even if it does not change the inferred solid surface density. These effects work to complicate extrapolations of disk mass from continuum dust observations as the total mass in dust is uncertain and the ratio used to convert to a total gaseous surface density may be incorrect by orders of magnitude (e.g., Birnstiel et al. 2012).

Recent observational work has also indicated that the typically assumed CO-

to-$H_2$ ratio of $10^{-4}$ (derived primarily from studies of the interstellar medium (ISM)) is likely over simplified. This is true not only in the context of protoplanetary disks but also in the context of star-forming molecular clouds where CO isotopologues have been shown to be weaker tracers of mass than dust and to be depleted in regions near B-stars as well as at the location of protostellar cores (e.g., Goodman et al. 2009; Imara 2015). In particular, there are several observational lines of evidence pointing to a depletion or lack of CO, and potentially all gas phase carbon compounds, in disks. Observations of HD gas, the most direct observational probe of disk mass as it is a hydrogen molecule line with a well defined ratio with respect to $H_2$, derive a disk mass for TW Hya that is significantly higher than observations of CO alone by $\sim$2 orders of magnitude (Bergin et al. 2013; Favre et al. 2013; Schwarz et al. 2016; Kama et al. 2016b). The HD derived masses for two other disks (GM Aur and DM Tau) are also significantly larger than those derived from CO isotopologues (McClure et al. 2016). Unfortunately, while HD gas is the most direct available tracer of total disk mass, observations were only made for a few disks by the Herschel Space Observatory before its decommissioning.

Furthermore, a recent survey of disks in the Lupus star-forming region by Ansdell et al. (2016) found that assuming an ISM CO-to-$H_2$ ratio leads to anomalously small derived disk masses (often less than 1 $M_{jup}$). These disk masses seem to be inconsistent with observations of accretion onto these stars which indicate the presence of abundant gas, indicating that CO is a poor tracer of the total mass in these systems. Indeed, for the same sample of disks the derived dust masses are correlated with the measured accretion rates as predicted by viscous accretion theory, while the gas mass derived from

CO observations has no correlation with measured accretion rates, suggesting that dust is a better tracer of disk mass (Manara et al. 2016; Miotello et al. 2017). An analogous CO survey of disks in the Chameleon star forming region also derives implausibly low gas masses for the objects with detected emission (Long et al. 2017). A separate large survey of disks done by Kama et al. (2016a) using carbon lines thought to be less affected by the photodissociation of CO also finds that many systems are either carbon-depleted or gas-poor disks.

Chemical modeling of observed disks around more massive stars suggest that the gaseous carbon abundance is depleted, suggesting low dust-to-gas ratios (Chapillon et al. 2008; Bruderer et al. 2012). Similar modeling of recent observations of $DCO^+$ in HD 169142 also require a CO depletion of a factor of 5 relative to the fiducial literature model to reproduce the observed $DCO^+$ radial intensity profile (Carney et al. 2018).

CO has been historically used as a tracer of total gas mass because it is believed to have stable chemistry and to remain in the gas phase for temperatures $> 20$ K in disks around sun-like stars (Öberg et al. 2011; Qi et al. 2013). However, the disk-averaged CO abundance can be much lower than the canonical ISM value due to freezeout and CO photodissociation (e.g., Thi et al. 2001; Dutrey et al. 2003; Chapillon et al. 2010). Newer theoretical studies have further found that CO chemistry in the disk environment is more complicated than previously assumed. Yu et al. (2016) use a chemical model that includes detailed photochemistry to propose that the CO abundance varies with distance in the planet forming regions of disks and that the CO-to-$H_2$ ratio drops to an order of magnitude below the interstellar value inside the CO freeze-out radius and is

also a function of time due in part to the formation of complex organic molecules. Recent work using this modeling technique further shows that CO depletion in the outer disk driven by ionization is a robust result for realistic T-Tauri star ionization rates (Dodson-Robinson et al. 2018). These factors may cause disk masses measured from standard CO observations to be under-predicted due to CO being chemically depleted in the outer disk where emission is optically thin (Yu et al. 2017).

The observational and theoretical evidence presented thus far points towards disks potentially having more mass, or a broader range in mass, than standard observational and theoretical assumptions derive. There are several other reasons to expect that disks may be more massive, or exhibit a broader range in mass, than typically assumed. For example, recent observations in the millimeter have uncovered a new class of disks with spiral arms. These disks have morphologies that potentially indicate that they are massive, gravitationally unstable objects (Pérez et al. 2016; Huang et al. 2018b). Furthermore, planet formation models for our solar system often require around an order of magnitude enhancement in density from the minimum mass solar nebula (MMSN) to form Jupiter and the other giant planets within a disk lifetime (e.g., Pollack et al. 1996; Hubickyj et al. 2005; Thommes et al. 2008; Lissauer et al. 2009; Matsumura et al. 2009; Dodson-Robinson & Bodenheimer 2010; D'Angelo et al. 2014). Schlichting (2014) show that if close-in Earth-to-Neptune-sized planets formed *in situ* as isolation masses, then the disk in which they formed would be gravitationally unstable assuming standard dust-to-gas ratios. If these planets instead formed at smaller isolation masses and then grew to their present size by giant impacts, then the surface density of the

disks in which they formed is at least a factor of 20 larger than the MMSN when giant impacts are considered, close to the limit of gravitational stability. A derivation of a standard minimum mass extrasolar nebula (MMEN) by Chiang & Laughlin (2013) further derives an average minimum disk mass that is a factor of 5 larger than the MMSN, while other work has indicated that there is no universal MMEN and extrasolar disks must have a variety of different properties (Raymond & Cossou 2014). In addition, the properties of a protoplanetary disk are set by the initial properties of the star forming cloud core, which vary from cloud to cloud (e.g., Kratter et al. 2010; Williams & Cieza 2011). Recent simulations of embedded disks derive masses that are greater than those typically inferred from observations of dust by at least a factor of 2-3 and that exceed the MMSN for objects with stellar masses as low as 0.05-0.1 $M_{\odot}$ (Vorobyov 2011).

Powell et al. (2017) suggest an alternative method for determining disk mass that does not rely on an assumed tracer-to-hydrogen mass ratio. They demonstrate that it may be possible to use dust to trace the total disk mass through a consideration of the aerodynamic properties of the grains. This can be achieved empirically through the consideration of spatially resolved multiwavelength observations of disks in the millimeter. These aerodynamic grain properties are thought to cause particle drift radially inward towards the star. Recent multiwavelength observations of disks appear to show signatures of particle drift as the radial extent of several disks becomes smaller at longer wavelengths (e.g., Isella et al. 2010; Tripathi et al. 2017; Guilloteau et al. 2011; Banzatti et al. 2011; Pérez et al. 2012, 2015; Tazzari et al. 2016). The radial extent of a disk at a particular wavelength is known as a disk dust line (Powell et al.

2017) as, in the millimeter, we can assume that emission at the observed wavelength is dominated by particles with a size comparable to that wavelength. As these particles are all in the Epstein drag regime, the surface density of a given disk can be readily determined given the maximum radius where particles of a given size are present. This model was successfully applied to the disk TW Hya, yielding a large total disk mass, consistent with measurements of HD gas and far in excess of measurements based on CO emission (Powell et al. 2017). In this work we further develop and test this model through applying it to six new disks.

The two input parameters of this model are the wavelength of observation and the radial extent of the disk. This model is thus independent of an assumed tracer-to-$H_2$ ratio or dust opacity model. The observational studies that find a decrease in disk radial extent as a function of wavelength also tend to find that the continuum emission at each wavelength exhibits a markedly sharp decrease over a very narrow radial range such that $\Delta r/r \lesssim 0.1$ (Andrews et al. 2012; de Gregorio-Monsalvo et al. 2013). This is encouraging, as models of radial drift predict such a cut-off. However, accurately determining the outer edge of disk emission empirically is not trivial (Tripathi et al. 2017).

In this work, after summarizing the Powell et al. (2017) model in Section 5.3, we introduce several model updates. In Section 5.4, we adapt the method derived in Tripathi et al. (2017) to accurately determine the outer edge of disk emission through modeling the interferometric visibilities. We describe the archival data used in this modeling work in Section 5.5. In Section 5.6, we apply this method to multiwavelength

observations of six new disks plus TW Hya. We compare our estimates of disk surface density and disk mass to previous observations and to limits from gravitational stability. We provide a validation of our analytic model using the semi-analytic model from Birnstiel et al. (2012). In Section 5.7, we comment on how to recognize whether the extent of dust emission at a given wavelength is set by drift or pressure bumps and provide a discussion of the effects of particle porosity. We provide a summary and conclusion of our results in Section 5.8.

## 5.3 Disk Surface Density Derivation

To determine the disk surface density without assuming a tracer-to-$H_2$ ratio we use recent resolved images of disks in the millimeter to infer the maximum radial location of different particle sizes in the disk. We then use reasonable assumptions about the aerodynamic properties of the grains to determine the total gaseous disk surface density profile. Through a consideration of particle growth, we further calculate the surface density profile in dust which provides a consistency check with observations of total integrated dust emission.

The location of the protoplanetary disk outer edge at a given millimeter wavelength is meaningful because it indicates that the particles that primarily contribute to the emission do not extend to larger radii. We refer to the empirically measured disk outer radius at a given millimeter wavelength as a disk "dust line" (Powell et al. 2017). A dust line could be set by particle trapping in a ring or be set by the inward radial drift rate of solid particles. Particle trapping in rings likely occurs (see Section 5.7.1),

but for many disks the fact that the dust lines are at different locations at different wavelengths suggests a differentiation of particle size with radial extent. As a significant particle trap should be efficient for particles across a range of sizes, this indicates that the dust line is not set by a strong particle trap for disks with an outer edge that varies with wavelength (see Section 5.7.1 for a more detailed discussion, including the effects of an inefficient particle trap in the outer disk). We therefore assume that in these cases the dust lines are set by particle drift.

There are several theoretical reasons to think that the disk radial extent is governed by particle drift. In evolved disks, particle growth is typically limited by fragmentation in the inner disk and drift in the outer disk (Birnstiel et al. 2012). Particles in the outer disk will therefore grow until they reach a size such that their motion is sufficiently decoupled from the motion of the gas and they begin to experience a significant headwind. This headwind will rob the particle of angular momentum and it will begin to drift radially inwards (Weidenschilling 1977a). In the outer disk, large particles will drift more quickly than smaller particles and will not be present at larger radii as they drift faster than they can be replenished due to particle growth (e.g., Birnstiel et al. 2012). This is known as the drift-limited regime because the local particle size is limited by drift. Observationally we would expect disks in this regime to look smaller at wavelengths that probe larger particle sizes and for there to be a sharp decrease in flux exterior to the disk dust line. There are several disks in the literature that show evidence of particle drift (e.g., Pérez et al. 2012, 2015; Andrews et al. 2012; de Gregorio-Monsalvo et al. 2013). Disks that demonstrate this behavior are good candidates for

this new method of determining disk surface density.

Following the method described in Powell et al. (2017), the disk surface density can be derived using dust lines that are set by radial drift. Assuming that we are in the drift-limited regime, we expect that the drift timescale of the maximally sized particle at a given dust line is equal to the age of the system, $t_{\rm drift} = t_{\rm disk}$. We further assume that the timescale at a dust line can be determined using the current disk surface density profile. This assumption is reasonable because, for particle sizes of interest in the outer regions of a disk, drift is faster at larger separations. The time that it takes for a particle to drift to its observed location is thus dominated by the local drift timescale. Furthermore, when the overall surface density was higher, which was likely true at earlier times, the overall drift rate was slower. Using the current surface density profile to determine the disk surface density is therefore a conservative assumption. Under these assumptions, the disk surface density can be determined by

$$\Sigma_g(r) \approx \frac{2.5 t_{\rm disk} v_0 \rho_s s}{r} \tag{5.1}$$

where $\Sigma_g$ is the disk surface density which varies with semi-major axis, $t_{\rm disk}$ is the current age of the system, $v_0$ approximately corresponds to the maximum drift velocity and is defined as $v_0 \equiv c_s^2/2v_k$ where $v_k$ is the Keplerian velocity, $\rho_s$ is the internal particle density, $s$ is the particle size, and $r$ is the maximum radius in which particles of size $s$ are present in the disk. By defining $v_0$ in this way, we implicitly set the power-law index of the gas pressure profile to unity as it is not known *a priori*.

This assumption about the power-law index is not entirely self-consistent.

However, one can self-consistently determine the surface density, including this factor, through iteratively fitting a surface density profile to the derived surface densities at the dust line locations. We have done this iteration for the disks in our sample (not shown). Given the small number of current observational data points, we fix the inner disk index and vary the critical radius and total surface density profile normalization (see Equation 5.12). Unsurprisingly, doing this iteration with current data results in an excellent fit because the number of data points is comparable to the number of fitting parameters. More importantly, this fitting procedure changes our derived critical radius and total disk mass by 20-30 %, well within the anticipated error of an order of magnitude model. As such, we move forward with the more simplified modeling described below with the note that when more data-points are available it may be appropriate to determine a surface density profile through iterative fitting of the data alone, without reference to previously inferred profiles.

To derive Equation (5.1) we use $t_{\rm stop} = m\Delta v/F_{\rm drag}$, where $F_{\rm drag} = 4/3\pi\rho_g\Delta v\bar{v}_{\rm th}s^2$, the volumetric gas density $\rho_g = \Sigma_g/2H$, $H$ is the scale height of the gas, $\Delta v$ is the relative velocity between a particle of mass $m$ and the gas, and $\bar{v}_{\rm th} = (8/\pi)^{1/2}c_s$ is the mean thermal velocity of the gas (assuming a Maxwellian velocity distribution). In this derivation we have assumed that particles are in the Epstein drag regime in the outer disk which we find to be true for all currently modeled disks.

Using Equation (5.1), the disk's total surface density can be derived as a function of radius given empirically determined dust lines. If the wavelength directly corresponds to the size of the emitting particle, as is typically assumed, then we can

associate each observed dust line with a particle size. The optical depth of dust grains $\tau \propto n(s)\sigma(s)$ where $n$ is the number density, $\sigma$ is the interaction cross section between particles and light, and $s$ is the particle radius. For particles larger than the observed wavelength, $\lambda_{\rm obs}$, $\sigma$ is the geometric cross section ($\pi s^2$). Particles somewhat smaller than $\lambda_{\rm obs}$ are in the Mie scattering regime such that $\sigma = \pi s^2 (2\pi s/\lambda_{\rm obs})$. Size distributions are typically expressed as $dN/ds \propto s^{-q}$ which gives $n(s) \propto s^{-q+1}$, so that

$$\tau \propto \begin{cases} s^{3-q} & \lambda_{\rm obs} < 2\pi s, \\ s^{4-q} & \lambda_{\rm obs} > 2\pi s. \end{cases} \tag{5.2}$$

We note that for values of $q$ less than 3, the largest particles in the disk should dominate the emission at all wavelengths and for $q$ values greater than 4 the smallest particles dominate the emission at all wavelengths. In either case, we would see the same disk dust line at all wavelengths, inconsistent with the observations. For example, we would expect relatively smaller disk sizes for $q < 3$ with the outer edge tracing large particles that have drifted inwards, and larger disk sizes for $q > 4$ with the outer edge tracing small particles that are present throughout the disk. We therefore assume that $3 < q < 4$, which implies that the particles dominating the observed emission at the disk outer edge have size $s = \lambda_{\rm obs}/2\pi$.

For the commonly invoked Dohnanyi size distribution, $q = 3.5$, which is in our preferred range (Dohnanyi 1969). There is no *a priori* reason that dust in the drift-limited regime will have a Dohnanyi size distribution because a collisional cascade is not expected. However, if $q$ instead had a value of 2.5 as has been suggested to explain

observations of objects where grain growth may be significant (e.g., D'Alessio et al. 2001; Natta & Testi 2004; Ricci et al. 2010,?), the largest grains would always dominate the emission and the dust line should be at the same location across all wavelengths. The observational fact that some disks have dust lines at different locations thus suggests that $q$ is indeed between 3 and 4.

Since, emission at an observed wavelength $\lambda_{\rm obs}$ is dominated by particles of size $s = \lambda_{\rm obs}/2\pi$, the dust line (maximum disk radius) observed at $\lambda_{\rm obs}$ gives the maximum radial extent of particles of this size. The radius $r$ of the disk dust line can therefore be used to determine the disk surface density at the dust line location following Equation (5.1). If the dust emission is optically thin, it is straightforward to associate the dust line with a drop off in dust density. If the dust emission is instead optically thick, one might worry that the dust line would be measured exterior to the location at which the density falls off. However, because the observed decrease in emission at a given wavelength is sharp (Andrews et al. 2012; de Gregorio-Monsalvo et al. 2013; Birnstiel & Andrews 2014, see schematic in Powell et al. (2017)), which we do not expect to result from a transition in optical depth in a disk with smoothly declining density, dust lines are likely associated with steep decreases in dust density even in the case of optically thick emission.

In our modeling we assume, and later verify, that the disks are dominated thermodynamically by passive stellar irradiation at the radii of interest. This assumption is valid for all but the innermost radii for disks with average accretion rates of $\sim 10^{-8}$ $M_\odot$ yr$^{-1}$ or less (Dullemond et al. 2007). We therefore parameterize the disk midplane

temperature following Chiang & Goldreich (1997), where the canonical temperature profile in the disk midplane is

$$T(r) = T_0 \times \left(\frac{r}{r_0}\right)^{-3/7} \tag{5.3}$$

where the temperature $T_0$, defined at $r_0 = 1$ au, is

$$T_0 = L_\star^{2/7} \left(\frac{1}{4\sigma_{\rm SB}\pi}\right)^{2/7} \left(\frac{2}{7}\right)^{1/4} \left(\frac{k}{\mu G M_\star}\right)^{1/7} r^{-3/7} \tag{5.4}$$

where $L_\star$ is the stellar luminosity, $\sigma_{\rm SB}$ is the Stefan-Boltzmann constant, $k$ is the Boltzmann constant, $\mu$ is the reduced mass taken to be $2.3{\rm m_H}$ assuming a hydrogen/helium disk composition, $G$ is Newton's gravitational constant, $M_\star$ is the stellar mass, and $r$ is the disk semi-major axis.

While CO may be depleted in disks, the shape of the surface density profile derived from resolved observations may still roughly correspond to the distribution of the underlying hydrogen and helium gas mass. Therefore, if this method is valid in determining surface density, we might expect that the derived surface density points will follow the shape of the CO emission although the normalization of the surface density profile is expected to differ. Alternatively, the surface density profiles derived from simultaneously modeling multiwavelength millimeter observations of dust might approximate the shape of the surface density profile. While it is not obvious that either profiles should necessarily match the distribution of the underlying gas disk completely, this comparison provides a useful initial method check.

### 5.3.1 Dust Surface Density

As described in the above model, knowing the dust surface density is not necessary to determine the gas surface density. We can, however, derive the dust surface density profile from our gas surface density profile using a drift and coagulation model without the need for an assumed dust opacity model. Comparing our derived dust surface density with the observed profile provides a consistency check for our model of total gaseous surface density.

In the drift-limited regime, the maximum particle size at a given radius is the particle whose growth timescale is equal to its drift timescale, as larger particles with higher drift velocities will be removed by drift before they are replenished by growth (Birnstiel et al. 2012; Birnstiel & Andrews 2014). We can therefore expand our assumptions regarding the drift-limited regime to include the growth timescale such that $t_{\rm drift} = t_{\rm grow} = t_{\rm disk}$. This differs from the method described in Lambrechts & Johansen (2014) as we do not prescribe a dust-to-gas ratio or dust surface density profile *a priori* and we further consider a constantly evolving disk at the outer edge instead of a disk in steady state. We assume that these disks are formed with an ISM dust-to-gas ratio; if our growth model finds a lower dust-to-gas ratio this implies that the additional solids inherited from the ISM have drifted into the interior of the disk.

Before particles reach the regime of drift-limited growth they must grow from very small, submicron grains to roughly millimeter size grains that are affected by gas drag. This initial stage of growth can potentially be significant. This timescale is approximately given by:

$$t_{\text{early growth}} \approx \frac{0.033\alpha^{-0.63}}{\Omega f_d} \ln\left(\frac{a_{\max}}{a_0}\right) \tag{5.5}$$

where $f_d = \Sigma_d/\Sigma_g$ is the dust-to-gas ratio, $\Sigma_d$ is the surface density in dust, $\Omega$ is the local Keplerian orbital angular velocity, $a_{\max}$ is the maximum particle size at a given location which in this case is set by particle drift, and $a_0$ is the initial particle size inherited from the ISM which we assume to be $\sim 0.1$ $\mu$m. The dimensionless value $\alpha$ is the standard Shakura-Sunyayev parameter describing disk viscosity (Shakura & Sunyaev 1973), which in this work we use only to parameterize the local eddy diffusivity of the gas and which may be a function of location in the disk. Equation (5.5) is based on the approximation for this timescale derived in Birnstiel et al. (2012) where particle growth is collisional and particles are assumed to grow by collisions with similarly sized grains. We modify the Birnstiel et al. (2012) expression, however, to account for the slower growth of very small particles that is affected by the amount of turbulence in the disk (see Appendix B.2). Our modification increases the growth timescale by a factor of two for $\alpha = 10^{-3}$ and by larger factors for smaller values of $\alpha$. Given an initial dust-to-gas ratio of $10^{-2}$, particles will have grown to the drift-regulated stage of growth in disks with ages roughly $\gtrsim$1 Myr as long as $\alpha \gtrsim 10^{-7}$. We include this early growth phase in our models, but it does not affect our results.

Once particles have undergone a phase of early growth, we model particle growth in more detail. Our growth timescale is derived by first considering the collisional growth rate of particles following:

$$\dot{m} = \rho_d \sigma \Delta v \tag{5.6}$$

where $\rho_d$ is the volumetric density of particles in the disk (not the particle internal density, $\rho_s$) and $\sigma = \pi s^2$ is the particle cross section where $s$ is the size of the largest particles at a given radius. We can convert this growth rate to a growth timescale such that:

$$\tau_{\rm grow} = \frac{m}{\dot{m}} \sim \frac{8 s \rho_s H_d}{3 \Sigma_d \Delta v f} \sim \frac{8 s \rho_s H_d}{3 f_d \Sigma_g \Delta v f} \tag{5.7}$$

where $H_d$ is the particle scale height and is given by $H_d = H\sqrt{\alpha/(\alpha + St)}$ (Ormel & Kobayashi 2012) and $\Delta v$ is the relative particle velocity. Particle relative velocities loosely fall into three regimes as discussed and derived in an order of magnitude scheme in Appendix B.1.1 to B.1.4. As this model can derive a range of disk masses, we do not prescribe a relative velocity *a priori*. We instead use the full expression from Ormel & Cuzzi (2007) (see their Equation 16) that encapsulates the three different regimes of particle growth. For ease of comparison we also introduce a coagulation efficiency parameter, $f$, to calibrate our coagulation estimates with detailed numerical simulations. We adopt a value of $f = 0.55$ following Birnstiel et al. (2012) which produces results in agreement with numerical models.

We assume a Dohnanyi particle size distribution, which has a value of $q = 3.5$ lying between 3 and 4 (see Section 5.3) and which is commonly used in disk modeling.

The Dohnanyi size distribution is dominated in mass by the largest sized particles (mass $\propto s^{0.5}$). In our calculations, this choice is roughly consistent with choosing any size distribution that is also dominated in mass by the largest particles such as the drift-limited size distribution defined in Birnstiel et al. (2015). For size distributions with this attribute, the growth of the large particles can be modeled through collisions with similarly sized grains. This is valid because the largest grains dominate both the density and cross section terms in Equation (5.6). For particle sizes probed by millimeter observations, the intermediate relative velocity regime is typically appropriate. In this regime, the relative velocity is roughly independent of the small body size. Thus, the growth rate is dominated by the largest particles.

Assuming that particles have taken time $t_{\text{early growth}}$ to grow to a size such that their growth timescale is given by $\tau_{\text{growth}}$, the growth timescale is given by $\tau_{\text{growth}} = t_{\text{disk}} - t_{\text{early growth}}$. With this known formulation for the particle growth timescale we are able to solve for the dust-to-gas ratio for the maximally sized particles at a given dust line such that

$$f_d \sim \frac{8 s \rho_s H_d}{3 \tau_{\text{grow}} \Sigma_g \Delta v f}. \tag{5.8}$$

This empirically derived dust-to-gas ratio, calculated at each dust line given the above assumptions, can then be used to convert the total surface density profile to a dust surface density profile following:

$$\Sigma_d(r) = \Sigma_g(r) f_d \tag{5.9}$$

where $\Sigma_d$ is the dust surface density and $\Sigma_g$ is the total surface density which is dominated by the gas mass. In a Dohnanyi size distribution, roughly 70 % of the mass is in grains whose radii are within an order of magnitude of the maximally sized particles. After deriving the dust surface density for the maximally sized grains we therefore add the additional surface density in smaller grains such that $\Sigma_{\rm d,tot}(r) \approx 1.3\Sigma_d$.

### 5.3.2 Main Sources of Uncertainty

In this modeling, there are several sources of uncertainty that may not be well constrained such as the age of the system and the distance to the system. The disk age is usually assumed to be the same as the stellar age. However, for young stars, stellar ages are subject to significant observational uncertainties. For example, literature age estimates for several disks in our sample span many millions of years. In this modeling it may therefore be appropriate to tune the disk age. The inferred disk surface density and therefore the disk mass is linearly proportional to disk age (see Equation 5.1). In this work, however, a single inferred age is used for each disk in this study as described in Section 5.6.

The distances to particular disks is another likely source of uncertainty in this work. For example, the disk HD 163296 is located at 100 pc (Gaia DR2, Gaia Collaboration et al. 2018) as opposed to the previously determined location of 122 pc (van den Ancker et al. 1998). This amount of uncertainty in distance introduces an uncertainty of $\sim 10\%$ when determining the dust line location. In this work we use the previously derived distance of 122 pc so as to easily compare with previous observations that use this distance. We do, however, calculate the dust line locations for this disk

given the updated distance and provide these values in Section 5.6.

Our modeling is not a complete model of all growth in protoplanetary disks as we model the small particles whose aerodynamic properties give rise to substantial particle drift. Larger particles may form following different processes or may form at earlier times in disk evolution and persist to later stages in the disk lifetime. As there are little observational constraints on larger planetesimal sized particles they are not included in our modeling. We note, however, that our model does not preclude their presence.

## 5.4 Determining the Disk Outer Edge and the Dust Line Locations

We increase the accuracy of this model by using a detailed method of empirically deriving the location of the disk dust lines. The most accurate determination of disk radial scale at a given wavelength can be derived through modeling of the interferometric visibilities using a Monte Carlo Markov Chain (MCMC) method. We model multi-wavelength millimeter observations following the fitting routine described below and derive radial distances of disk dust lines with characterized errors. In particular, the quantity of interest is the radius at which the flux falls off steeply. We expect such a radius to exist as previous work has indicated that the continuum emission at each wavelength exhibits a markedly sharp decrease over a very narrow radial range such that $\Delta r/r \leq 0.1$ (Andrews et al. 2012; de Gregorio-Monsalvo et al. 2013).

Previous work typically models disk continuum emission using either a power-

law brightness profile with a sharp cut-off (e.g., Andrews et al. 2008, 2012; Hogerheijde et al. 2016) or a similarity solution brightness profile that follows from models of viscous accretion disks (e.g., Hughes et al. 2010; Isella et al. 2010; Andrews et al. 2011). Tripathi et al. (2017) find that different disks are better described by one of these two options and therefore invokes a flexible surface brightness profile.

As we are most interested in the disk radial scale in which the flux drops off steeply, and not necessarily the shape of the disk brightness profile, we use two different models for the disk surface brightness profile and test their accuracy in finding the disk outer edge. In particular we test both the computationally less intensive power-law profile with a sharp cut-off and the more flexible Nuker surface brightness profile (Lauer et al. 1995) using a method adapted from Tripathi et al. (2017). From a given surface brightness profile we compute visibilities from the model's Fourier transform (for further details see Pinilla et al. 2017). The model visibilities are sampled at the same spatial frequencies as the simulated or real data. The modeled visibilities are also transformed to account for the disk position angle and inclination which we constrain from the literature (see Table 5.1).

For our initial tests of the method we simulate ALMA data and use an MCMC method to minimize the free parameters in the surface brightness profile which we fit to the data in visibility space. The advantages of fitting to data in visibility space are well described in the literature (e.g., MacGregor et al. 2013, 2015a,b). We employ the ensemble sampler proposed in Goodman & Weare (2010) and implemented it as described in Foreman-Mackey et al. (2013). To simulate ALMA observations we first

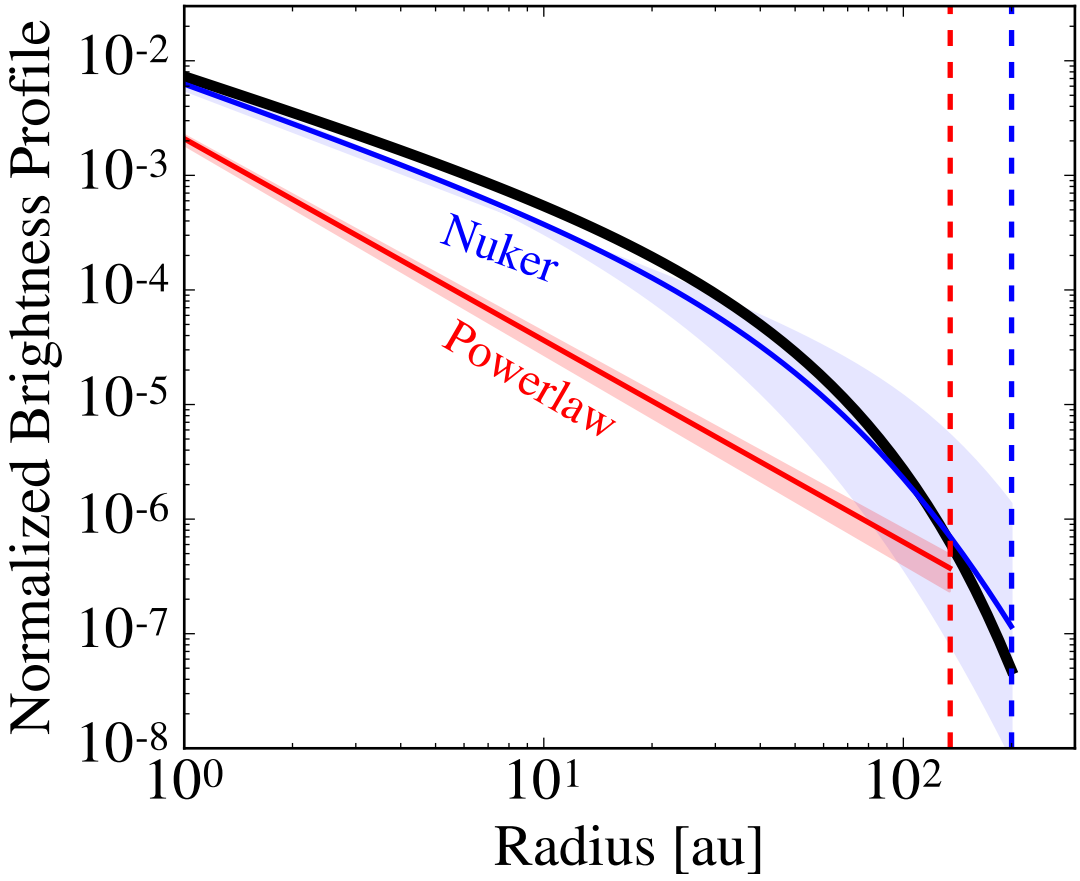


Figure 5.1: The Nuker brightness profile fit (blue, solid line) matches the model brightness profile used to generate simulated ALMA data (black line) well and also finds the correct disk outer edge (blue, dashed line). The power-law brightness profile (red, solid line) does not find the disk outer edge as accurately (red, dashed line). The shaded regions correspond to the one sigma errors for the different profile fitting parameters.

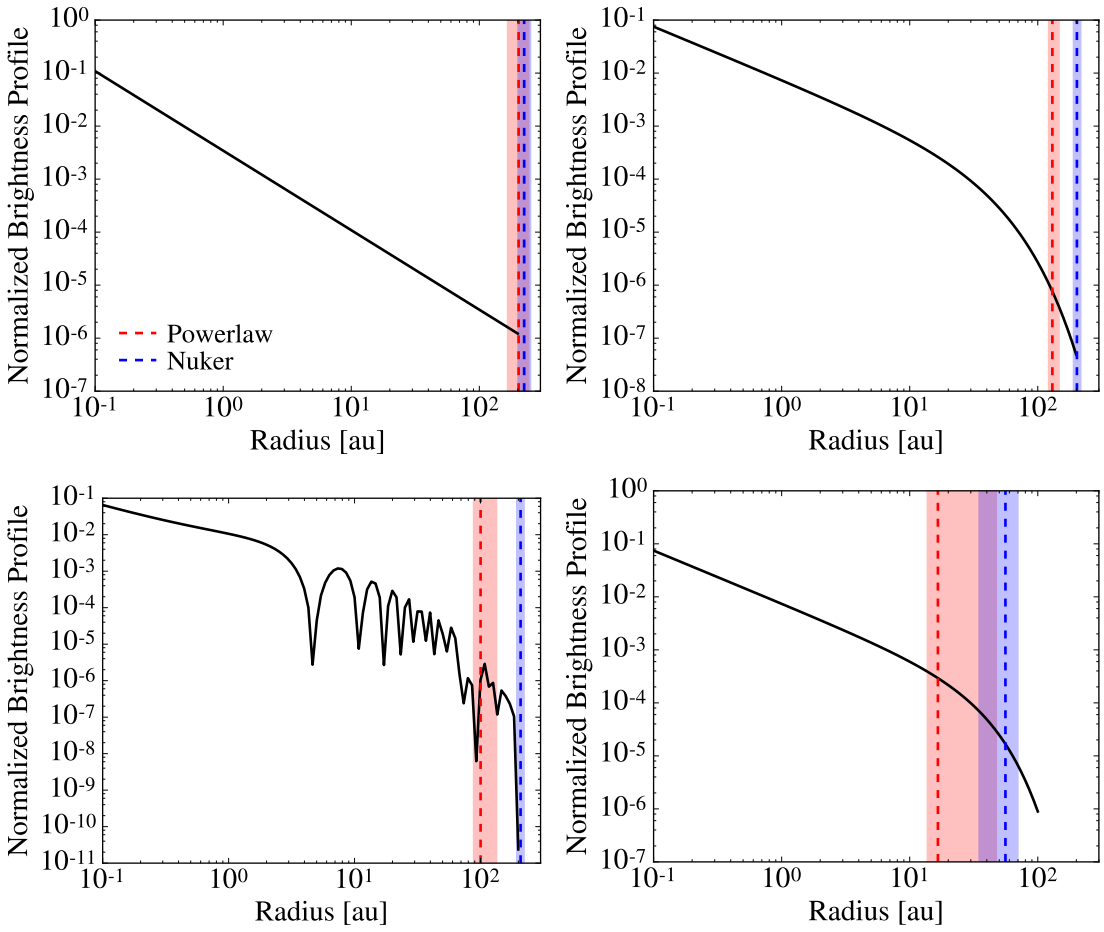


Figure 5.2: The Nuker profile finds the outer radius well (blue, dashed) for several different simulated surface brightness profiles (black) even when there are confounding dips in brightness (bottom left) or a significant taper in brightness (bottom right). The best fit for the outer radius using the power-law brightness profile only finds the outer edge of the disk (red, dashed) more accurately for a simple power law disk brightness profile (top left). The shaded regions corresponding to the colored dashed lines show the one sigma errors for the disk outer edge.

create model FITS images from a known surface brightness profile and then derive simulated noise-free interferometric visibilities using the CASA software package (McMullin et al. 2007)[4].

The power-law brightness profile with a sharp cut-off (see Figure 5.4) is the least computationally intensive of the two profiles as it only has three free parameters. The power-law visibility profile has the following form:

$$I_\nu(\varrho) \propto \left(\frac{\varrho}{\varrho_0}\right)^{-\gamma}, \tag{5.10}$$

where $\varrho$ is the radial coordinate projected on the sky, $\gamma$ is the disk index and $\varrho_0$ is a reference radial location which we set to 10 au. The power-law profile has three free parameters assuming that the position angle and inclination are well-constrained in the literature: the total flux $F_{\rm tot}$, $\gamma$, and $R_{\rm out}$. All three parameters have uniform priors in linear space such that: $p(F_\nu) = \mathcal{U}(0,\ 10\ {\rm Jy})$, $p(\gamma) = \mathcal{U}(\text{-}3,\ 3)$, and $p(R_{\rm out}) = \mathcal{U}(0,\ 300$ au).

The Nuker profile introduces several free parameters and is well suited for approximating the behavior of both a power-law disk with a sharp cut-off and a disk with an exponential fall-off (see Figure 5.4). We therefore additionally choose this model to test as it has a comparable number of free parameters as a similarity solution brightness profile but is more flexible and well-suited for modeling multiple disks with a range in profile shapes. This profile takes the following form:

[4]In the mock observations, we chose a configuration with baselines ranging from 50 m to 4 km. When fitting, we binned the visibilities in 40 k$\lambda$ sized bins, a common bin size for observations at 1.3 mm (e.g., Pérez et al. 2015). With inflated error bars we derive similar fits to the simulated data.

$$I_\nu(\varrho) \propto \left(\frac{\varrho}{\varrho_t}\right)^{-\gamma} \left[1 + \left(\frac{\varrho}{\varrho_t}\right)^{\alpha}\right]^{(\gamma-\beta)/\alpha}, \tag{5.11}$$

where $\varrho_t$ is the transition radius, $\gamma$ is the inner disk index, $\beta$ is the outer disk index, and $\alpha$ is the transition index. The Nuker profile is a flexible brightness profile such that when $\varrho \ll \varrho_t$ or $\varrho \gg \varrho_t$ the brightness profile scales as $\varrho^{-\gamma}$ or $\varrho^{-\beta}$ respectively. The index $\alpha$ controls the asymptotic behavior and when $\alpha$ is small the profile behaves like a similarity solution brightness profile. The behavior of this profile is discussed in more detail in Tripathi et al. (2017).

The Nuker profile has 6 free parameters: $F_{\rm tot}$, $\gamma$, $\beta$, $\alpha$, $\varrho_t$, and $R_{\rm out}$. The priors on these parameters are uniform in linear space except for $\alpha$ which has a log-uniform prior as most of the variation occurs in the first decade of prior space. The priors on these values are: $p(F_\nu) = \mathcal{U}(0,\ 10\ {\rm Jy})$, $p(\varrho_t) = \mathcal{U}(0,\ 300\ {\rm au})$, $p(R_{\rm out}) = \mathcal{U}(0,\ 300\ {\rm au})$, $p(\gamma) = \mathcal{U}(\text{-}3,\ 3)$, $p(\beta) = \mathcal{U}(2,\ 10)$, $p(\log_{10}\alpha) = \mathcal{U}(0,\ 2)$. These priors are set following Tripathi et al. (2017), however, we neglect for the time being the logistic tapers in the prior on $\gamma$ which we find to have a negligible effect on fitting the disks in our current sample. For both $\varrho_t$ and $R_{\rm out}$ we convert distances in au to the projected radial location on the sky.

Because we are interested in the outer edge of the disk where we assume that the emission falls of steeply, we prescribe an outer radius as a free parameter in our model brightness profiles that is defined as the location where disk emission is roughly zero. We therefore do not define an effective disk size metric as defined in Tripathi et al. (2017) where they prescribe an effective disk size that encompasses 68 % of the total

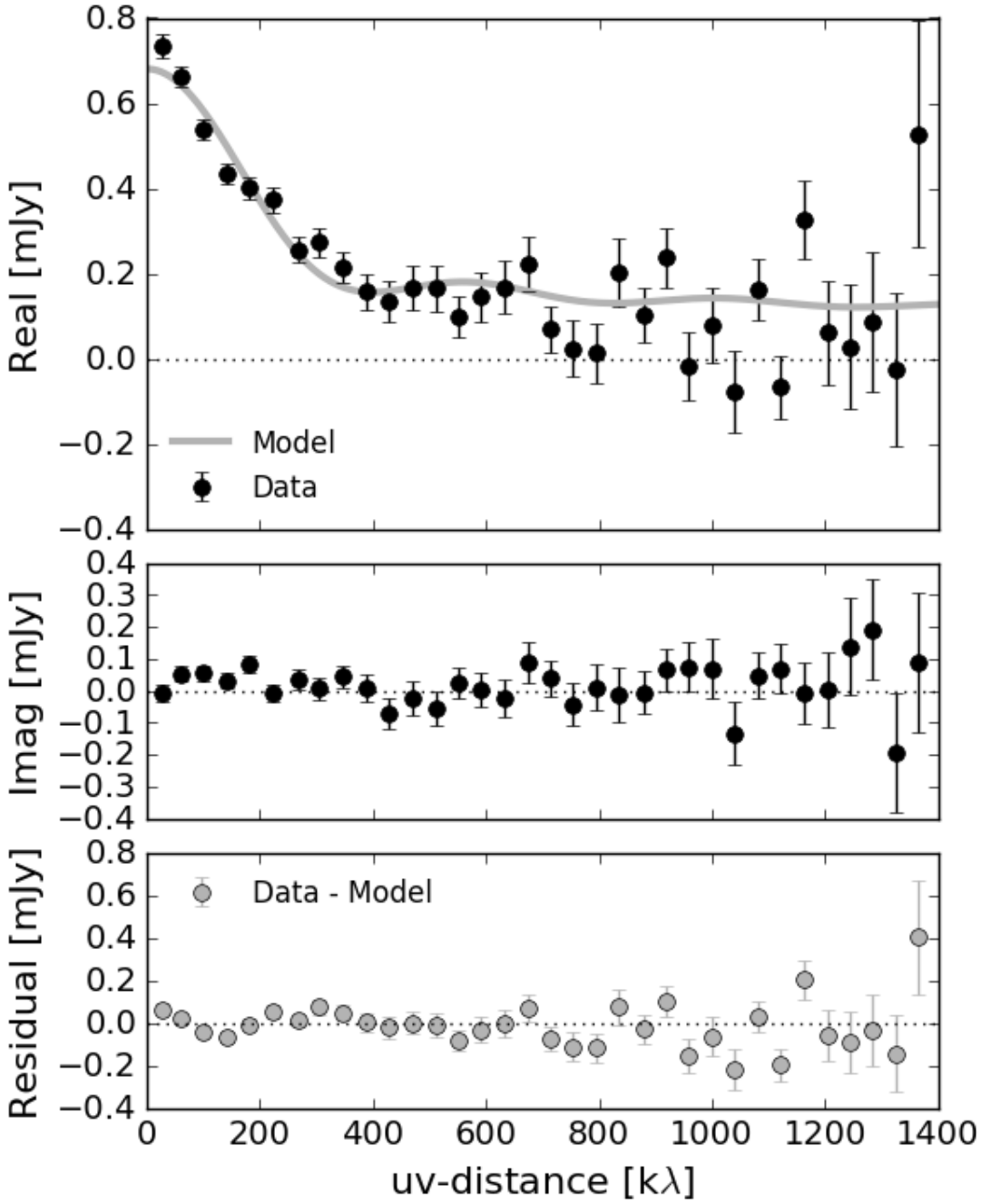


Figure 5.3: Modeled interferometric visibility data for the disk AS 209. The data was taken using the VLA at 10 mm and was originally presented in Pérez et al. (2012). The top panel shows the modeled real component of the visibilities, the middle panel shows the imaginary component of the visibilities which the model assumes to be zero, and the residuals of the real visibilities and the model are shown in the bottom panel.

flux. As an assumed effective radius depends strongly on the strength of the inner disk index (Tripathi et al. 2017) this metric will not likely determine the dust line location. For example, a disk that is very bright within a few AU of the star as compared to the outer disk will have a 95 % or 98 % flux threshold outer radius that is not the true outer disk radius of interest. By instead assuming that there is a true outer radius we introduce comparatively larger errors primarily because the observations have the poorest sensitivity at larger radial coordinates. A comparison between $R_{out}$ derived in this work and $R_{eff}$ described in Tripathi et al. (2017) is discussed in Section 5.6.

A comparison between the Nuker and power-law brightness profiles is shown for a simulated ALMA observation in Figure 5.4. The Nuker profile does a better job of constraining the shape of the surface brightness profile as well as the location of the disk outer edge. Furthermore, the Nuker brightness profile more consistently finds the outer edge of disk emission accurately even when there are confounding dips in brightness or when there is a width/taper to the emission cutoff. This is shown for several simulated disk brightness profiles in Figure 5.4 where the outer edge derived using the Nuker and power-law brightness profiles is shown. In each case the fit using the Nuker brightness profile accurately finds the location of the disk outer edge when the surface brightness falls off quickly and approximates the disk outer edge relatively well when there is a significant taper to the disk emission profile. This is encouraging as we expect the decrease in millimeter emission to be distinct, as indicated by observations.

We generally find that both brightness profiles used for fitting disk visibilities are sensitive to the initial guesses used for the parameters. In particular, the most

robust methodology for determining the disk outer radius in our tests is to first fit using a power-law surface brightness profile with a sharp cut-off and then use the best fit parameters as the initial guesses for a longer parameter space search using the Nuker brightness profile.

Our method for modeling the disk visibilities is able to describe real data well. An example of an observed visibility profile and best-fit model is shown in Figure 5.4 for the disk AS 209 where we find good agreement with the data from Pérez et al. (2012), even out to large radial coordinates. This fit is characteristic for the objects in our sample.

## 5.5 Archival Data

We analyze multi-wavelength millimeter observations of 6 disks: AS 209, HD 163296, FT Tau, DR Tau, DoAr 25, and CY Tau. These disks were chosen from the literature as they all have relatively recent resolved millimeter observations at more than two wavelengths (see Table 5.1). These objects also all have published reduced complete visibility profiles readily available for this modeling work. We also update our model analysis of the disk TW Hya. While TW Hya has an abundance of data, the completely reduced interferometric visibilities at the relevant wavelengths are not always provided in the literature. We therefore model this disk using the dust lines as derived in Powell et al. (2017). These are not the only disks that seem to have decreasing radial extent at longer wavelengths; however, we aim to provide the tools in this work such that the community at large will be able to reproduce our disk models with their own data.

The archival observations of these disks are detailed in Table 5.1. When available we compare our derived surface density profile to the profile derived from detailed modeling of both integrated dust emission and resolved CO emission. When surface density profiles from integrated dust emission are used for comparison we compare to a single surface density profile derived via multi-wavelength millimeter continuum observations. All disks besides DoAr 25 have a single surface density profile derived via multi-wavelength dust observations or resolved CO emission with which to compare.

Disks with surface density profiles from resolved CO emission are AS 209 (Huang et al. 2016), HD 163296 (Williams & McPartland 2016), and TW Hya (Rosenfeld et al. 2012). Disks with surface density profiles from multi-wavelength continuum observations are FT Tau (Tazzari et al. 2016), DR Tau (Tazzari et al. 2016), CY Tau (Guilloteau et al. 2011), AS 209 (Tazzari et al. 2016), and HD 163296 (Guidi et al. 2016). For DoAr 25 the only surface density profiles from integrated dust emission available are from individual observed millimeter wavelengths. We therefore primarily consider a surface density profile calculated by fitting a similarity solution, which comes from models of viscously evolving disks, to our derived surface density points (see Equation (5.12), parameters shown in Table 5.2). As shown in Section 5.6, this surface density profile fit happens to be nearly identical in shape to the dust surface density profile inferred for this disk from observations at 2.8 mm.

The parameters for the observationally derived surface density profiles used to model these disk are given in Table 5.2. Every surface density profile that we use in our modeling follows from the self-similar solution to the viscous equations as shown in

Table 5.1: Archival Observations

| Object | Millimeter Dust Observations | CO and Other Relevant Observations |
|---|---|---|
| AS 209 | Pérez et al. (2012) | Huang et al. (2016); Tazzari et al. (2016) |
| HD 163296 | Guidi et al. (2016) | Williams & McPartland (2016); Qi et al. (2011); Isella et al. (2007) |
| FT Tau | Tazzari et al. (2016) | Garufi et al. (2014) |
| CY Tau | Pérez et al. (2015) | Guilloteau et al. (2011) |
| DR Tau | Tazzari et al. (2016) | |
| DoAr 25 | Pérez et al. (2015) | Andrews et al. (2008) |
| TW Hya | Andrews et al. (2012, 2016); Cleeves et al. (2015); Menu et al. (2014) | Rosenfeld et al. (2012) |

Table 5.2: Disk Surface Density and Temperature Profile Parameters

| Object | $R_{crit}$ [au] | $\gamma$ | Reference |
|---|---|---|---|
| AS 209 | 98 | 0.91 | (1), integrated dust emission |
| | 100 | 1 | (2), CO emission (neglecting ring) |
| HD 163296 | 119 | 0.88 | (3), integrated dust emission |
| | 213 | 0.39 | (4), CO emission |
| FT Tau | 28 | 1.07 | (1), integrated dust emission |
| CY Tau | 65.6 | 0.28 | (5), integrated dust emission |
| DR Tau | 20 | 1.07 | (1), integrated dust emission |
| DoAr 25 | 105 | 0.36 | |
| TW Hya | 30 | 1 | (6), CO emission |

References. — (1) Tazzari et al. (2016), (2) Huang et al. (2016), (3) Guidi et al. (2016), (4) Williams & McPartland (2016), (5) Guilloteau et al. (2011), (6) Rosenfeld et al. (2012)

Lynden-Bell & Pringle (1974) and Hartmann et al. (1998). However, the exact functional form of this profile varies in the literature according to the author's preference. For readability, we convert all surface density profiles to our preferred form:

$$\Sigma_g(r) = \Sigma_0 \left(\frac{r}{r_c}\right)^{-\gamma} \exp\left[-\left(\frac{r}{r_c}\right)^{2-\gamma}\right] \tag{5.12}$$

where this similarity solution profile is a shallow power law at small radii and follows an exponential fall off, goverened by the parameter $\gamma$ at radii larger than the critical radius, $r_c$. For the disk DoAr 25, which does not have a similarity solution profile derived from simultaneous modeling of multiwavlength data or CO emission, we use $\chi^2$ minimization to derive a similarity solution profile that fits the derived surface densities at the disk dust lines well. In our modeling we derive new values of $\Sigma_0$, is the surface density profile normalization, which are given in Table 5.4.

## 5.6 Modeled Disks

We first use the method detailed in Section 5.4 to determine the location of the disk outer edge at each observed wavelength (the disk dust line) for the six disks that we consider. These radii are listed in Table 5.3 where the wavelengths quoted are from the original published archival data. The dust lines for the disk TW Hya are taken directly from Powell et al. (2017). The stellar luminosity, and stellar mass used in our modeling are also noted.

Using the information in Table 5.3 we derive total disk surface densities at the location of disk dust lines as shown in Figure 5.4. We then renormalize the disk surface

density profiles based on either multiwavelength dust emission or resolved CO emission, as described in Table 5.2, to derive the new disk surface density profile. The newly determined values of $\Sigma_0$ are given in Table 5.4 along with the constant that determines the disk temperature profile (see Equation 5.3).

For DoAr 25 we show both the derived fit to the new surface density values and the comparison to the dust surface density profile derived from modeling dust emission at the one wavelength that best matches the newly derived values. In each case we find good agreement in shape between the empirically derived surface density points and the surface density profiles derived from other observational methods. For disks with profiles derived from both CO emission and integrated dust observations, we typically choose the dust surface density profile as the canonical surface density profile in which to determine disk properties. This is because, as discussed below, the mass derived from dust is more consistent with our newly derived masses. However, for the disk TW Hya we primarily consider the renormalized profile derived from CO observations as there is not currently a published profile derived based on the simultaneous fitting of multiwavelength millimeter dust observations for this object.

Table 5.3: Dust Lines

| Object | Stellar Lum. | Stellar Mass | Observed Wavelength | Outer Radius/Dust Line |
|---|---|---|---|---|
| AS 209[a] | 1.5 $L_\odot$ | 0.9 $M_\odot$ | 0.85 mm | $154.7^{+17.5}_{-32.8}$ au |
| | | | 2.8 mm | $159^{+19.3}_{-24.1}$ au |
| | | | 8 mm | $53.8^{+13.2}_{-14.7}$ au |
| | | | 10 mm | $62.6^{+11.1}_{-12.4}$ au |
| HD 163296[b] | 36 $L_\odot$ | 2.3 $M_\odot$ | 0.85 mm | $121.7^{+15.2}_{-18}$ au |
| | | | 1.3 mm | $101.8^{+19.1}_{-24.4}$ au |
| | | | 9.8 mm | $22.9^{+15.6}_{-17}$ au |
| FT Tau[c] | 0.31 $L_\odot$ | 0.55 $M_\odot$ | 1.3 mm | $96.8^{+14.7}_{-20.5}$ au |
| | | | 2.6 mm | $60.1^{+11}_{-16.6}$ au |
| | | | 8.0 mm | $36.2^{+2.3}_{-1.9}$ au |
| | | | 9.83 mm | $30.6^{+2.2}_{-2.9}$ au |
| CY Tau[d] | 0.4 $L_\odot$ | 0.48 $M_\odot$ | 1.3 mm | $108.3^{+25.7}_{-7.6}$ au |
| | | | 2.8 mm | $115.9^{+10}_{-14.5}$ au |
| | | | 7.14 mm | $69.1^{+12.5}_{-11.5}$ au |
| DR Tau[c] | 1.09 $L_\odot$ | 0.8 $M_\odot$ | 1.3 mm | $62.8^{+13.2}_{-18.5}$ au |
| | | | 7.05 mm | $36.8^{+5.4}_{-6.7}$ au |
| | | | 7.22 mm | $43.9^{+12.3}_{-12.2}$ au |
| DoAr 25[f] | 1.3 $L_\odot$ | 1 $M_\odot$ | 0.88 mm | $215.1^{+16.7}_{-24.9}$ au |
| | | | 2.8 mm | $179.8^{+11.9}_{-47.5}$ au |
| | | | 8 mm | $101^{+20.7}_{-16.3}$ au |
| | | | 9.8 mm | $73.5^{+9.2}_{-7}$ au |

Table 5.3 (cont'd): Dust Lines

| Object | Stellar Lum. | Stellar Mass | Observed Wavelength | Outer Radius/Dust Line |
|---|---|---|---|---|
| TW Hya[g] | 0.28 $L_\odot$ | 0.8 $M_\odot$ | 0.87 mm | 60 ± 10 au |
| | | | 1.3 mm | 50 ± 10 au |
| | | | 9 mm | 25 ± 10 au |

References. — Dust lines are calculated from Archival data as detailed in Table 5.1. Dust lines for TW Hya are from Powell et al. (2017). Superscript letters denote references for stellar parameters and a discussion and references for stellar ages are given in the text. [a]Herbig & Bell (1988) [b]Natta et al. (2004) [c]Ricci et al. (2010) [d]Bertout et al. (2007) [f]Andrews et al. (2008) [g]Rhee et al. (2007); Qi et al. (2013)

Integrating the re-normalized surface density profiles allows us to solve for the total disk mass. The total disk masses are given in Table 5.5. The disk masses derived following the method described in this work are given in the first column. Previously published mass estimates using conventional tracer calculations are given in the third and fourth columns.

Several disks in our sample have age estimates that vary significantly across the literature. We choose a single age for our modeling purposes that is consistent with literature values for each disk as discussed below. The largest range we found in the literature for the stellar age is 7 Myr for TW Hya. We note that this is the most well-studied object in our sample, suggesting that other disks may also have large age uncertainties. We again note that the derived surface density values depend linearly on disk age as shown in Equation (5.1). The stellar age likely introduces the largest uncertainty in our modeling. In Table 5.5, we provide errors for our mass estimates resulting from the variation of stellar ages quoted in the literature.

*AS 209*

The most massive disk in our sample is AS 209 with a disk mass that is 27%

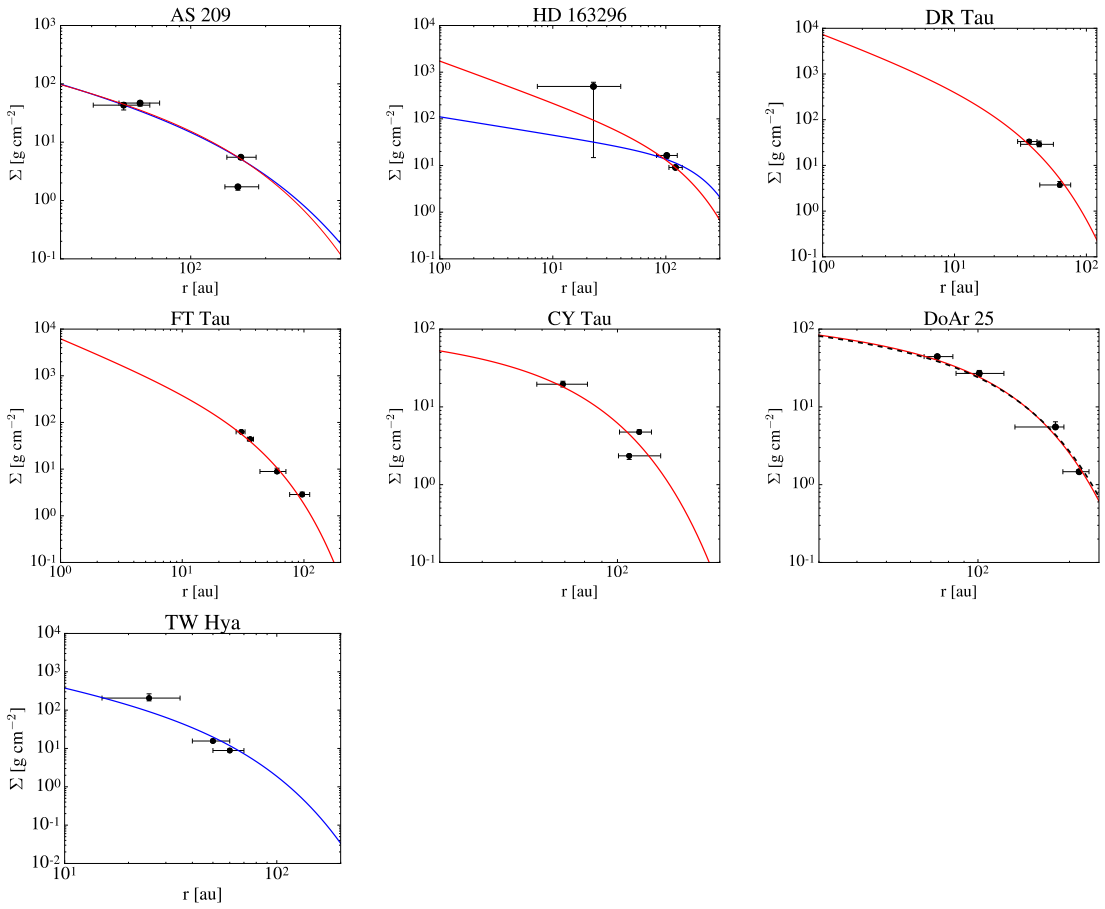


Figure 5.4: Our newly derived surface density values (black points) can be well matched by renormalized surface density profiles derived from either multiwavelength dust observations (red lines) or CO observations (blue lines). These plots are provided for a range larger than is probed by the observations to provide an idea of the general shape and scale of these systems. The plotted radii vary for each disk because the surface density profiles have different shapes and scales. The disk DoAr 25 does not have one single published surface density profile derived from multiwavelength millimeter observations or from CO emission. Instead, the best fit surface density profile for the newly derived surface densities (black, dashed line) is shown as well as the normalized dust surface density profile from observations of the disk at 2.8 mm (red line).

Table 5.4: Derived Disk Surface Density Profile Normalization and Temperature Constant

| Object | $T_0$ [K] | $\Sigma_0$ [g cm$^{-2}$] |
|---|---|---|
| AS 209 | 131 | 44[a] |
| | " " | 40[b] |
| HD 163296 | 284 | 29[a] |
| | " " | 14[b] |
| FT Tau | 89 | 183[a] |
| CY Tau | 98 | 55 [a] |
| DR Tau | 121 | 315[a] |
| DoAr 25 | 123 | 68[a] |
| TW Hya | 82 | 175[b] |

[a]For the normalized dust surface density profile.

[b]For the normalized CO surface density profile.

as massive as its host star. The newly derived disk mass is a factor ∼15 times larger than previous estimates based on dust observations. The new disk mass is a further 115 times larger than the mass derived from CO observations. While both masses are inconsistent with the newly measured mass, the CO derived mass is particularly small. This indicates that the disk AS 209 may be significantly depleted in CO compared to the ISM. AS 209 is a relatively young disk; we choose the commonly quoted age of 1.6 Myr (Andrews et al. 2009), however, age estimates for this system in the literature range as low as 0.5 Myr (Natta et al. 2006; Fedele et al. 2018) which would bring the disk mass estimate down by a factor of ∼3.

*DoAr 25*

The disk around DoAr 25 has a mass that is 23% the mass of its host star and is the second most massive disk in our sample. The newly derived mass is roughly a factor of 8 larger than the mass derived from dust observations. For DoAr 25 we choose

an age of 2 Myr as this is consistent with age estimates given for the Ophiuchus star forming region in Cox et al. (2017) though the age estimates in the literature are as high as 4 Myr (Andrews et al. 2009).

*CY Tau*

The disk around CY Tau has a mass that is 21% of its host's stellar mass. The newly derived mass is roughly a factor of 6 larger than the mass derived from dust observations. Age estimates for the disk CY Tau vary from 0.8 Myr to $\sim$ 3 Myr (Bertout et al. 2007; Isella et al. 2009; Andrews et al. 2013; Guilloteau et al. 2014). We choose an age of 1 Myr as this is consistent with the literature (e.g., Isella et al. 2009; Andrews et al. 2013) and is representative of disk ages in the Taurus star forming region.

*FT Tau*

The disk around FT Tau has a mass that is 18% of its host's stellar mass. The newly derived mass is roughly a factor of 7 larger than the mass derived from dust observations. For FT Tau we model using the only commonly quoted literature age of 1.6 Myr (Garufi et al. 2014).

*TW Hya*

The disk around TW Hya has a mass that is 14% as massive as its host star. The newly derived mass is roughly a factor of 6 larger than the mass derived from dust observations. The new disk mass is also a factor of 37 larger than the mass derived from CO observations. TW Hya therefore shows moderate depletion of CO at a lower level than for the disk AS 209 but significantly larger than the disk HD 163296. For TW Hya we choose an age of 5 Myr though the literature age estimates range from 3-10

Myr (Barrado Y Navascués 2006; Vacca & Sandell 2011).

*DR Tau*

Table 5.5: Total Gas Disk Mass

| Object | Age | Dust Line Derived Disk Mass[a] | Mass Uncertainty Based on Disk Age | Mass From Integrated Dust Emission | Mass From CO Line Emission | Mass From HD Line Emission |
|---|---|---|---|---|---|---|
| AS 209 | 1.6 Myr | 0.24 $M_\odot$[b] | $-0.165$ $M_\odot$ | 0.0149 $M_\odot$ | 0.002 $M_\odot$[a] | - - - |
| HD 163296 | 5 Myr | 0.21 $M_\odot$[b] | $-0.084$ $M_\odot$ | 0.12 $M_\odot$ | 0.048 $M_\odot$ | - - - |
| “ ” | “ ” | 0.16 $M_\odot$[c] | $-0.064$ $M_\odot$ | “ ” | “ ” | - - - |
| FT Tau | 1.6 Myr | 0.10 $M_\odot$[b] | - - - | 0.015 $M_\odot$ | - - - | - - - |
| CY Tau | 1 Myr | 0.10 $M_\odot$[b] | $-0.02/+0.2$ $M_\odot$ | 0.0165 $M_\odot$ | - - - | - - - |
| DR Tau | 1 Myr | 0.09 $M_\odot$[b] | $-0.081/+0.18$ $M_\odot$ | 0.014 $M_\odot$ | - - - | - - - |
| DoAr 25 | 2 Myr | 0.23 $M_\odot$[b] | $+0.23$ $M_\odot$ | 0.03 $M_\odot$ | - - - | - - - |
| TW Hya | 5 Myr | 0.11 $M_\odot$[c] | $-0.044/+0.11$ $M_\odot$ | 0.018 $M_\odot$ | 0.003 $M\odot$[a] | $> 0.05$ $M_\odot$ |

References. — Tazzari et al. (2016); Isella et al. (2007); Williams & McPartland (2016); Guilloteau et al. (2011); Huang et al. (2016);
Cox et al. (2017); Menu et al. (2014); Rosenfeld et al. (2012); Bergin et al. (2013).
Mass uncertainty based on disk age is quoted based on age ranges from the literature. A line divides TW Hya from
the rest of the objects in this sample as the dust lines used in this modeling are taken from Powell et al. (2017).

[a]Mass derived from integrating the observationally determined surface density profile.

[b]Mass derived from integrating the normalized dust surface density profile.

[c]Mass derived from integrating the normalized CO surface density profile.

The disk around DR Tau has a mass that is 11% as massive as its host star. The newly derived mass is roughly a factor of 6 larger than the mass derived from dust observations. For the disk DR Tau age estimates range from 0.1 Myr to $\sim$ 3 Myr (Isella et al. 2009; Andrews et al. 2013). We again choose an age of 1 Myr as this is consistent with many age estimates given in the literature.

*HD 163296*

The disk around HD 163296 has a mass that is 9% of its host's stellar mass and is the third most massive disk in our sample. This disk orbits a Herbig Ae star and is one of the two oldest disks in our sample. HD 163296 has similarity solutions derived using both integrated dust observations and CO emission. We quote newly derived masses considering each of these two profiles in Table 5.5. For the discussion in the text, however, we consider the mass derived via renormalizing the similarity solution profiled derived from integrated dust observations. The newly derived mass estimate is almost a factor of 2 larger than the mass derived from dust observations in Isella et al. (2007). We note, however, that integrating the surface density profile derived in Guidi et al. (2016) from optically thin millimeter dust emission derives a disk mass of $\sim$ 0.01 $M_\odot$ (c.f. Figure 5.6), which is more than an order of magnitude lower than our derived disk masses. The new disk mass is also a factor of 4.5 larger than the mass derived from CO observations. This indicates that HD 163296 may not exhibit as marked a depletion of CO as the other disks in our sample with CO mass estimates. While the disk HD 163296 has age estimates as low as 3 Myr (Péricaud et al. 2017), we choose the common literature age value of 5 Myr for our modeling (van den Ancker et al. 1998; Montesinos

et al. 2009). For HD 163296 we also re-derive the dust line locations with the updated Gaia DR2 distance of 100 pc. We find dust lines located at $94^{+29.7}_{-38.2}$ au, $84^{+7.1}_{-13.0}$ au, $23.2^{+9.7}_{-10.7}$ au corresponding to the observed wavelengths of 0.85 mm, 1.3 mm, 9.8 mm respectively. Using these dust lines to derive mass, without updating the inferred stellar parameters, results in a mass estimate of 0.27 $M_{\odot}$.

### 5.6.1 Trends

Given the derived disk masses found in this work, it is possible that all disks are more massive than was thought previously. All of the disks in this sample have a newly estimated disk mass that is larger than the mass derived from either integrated dust emission or CO observations. Furthermore, the disks in our sample have masses that range from 9 - 27 % of their host's mass. This may well be a selection effect as our sample is biased towards bright, massive disks that are most readily observed. However, this indicates that the typically assumed dust-to-gas ratio of $10^{-2}$ is likely incorrect. This conclusion lends weight to the idea that grain growth and drift should alter the dust-to-gas ratio throughout the disk (e.g., Birnstiel et al. 2012; Hughes & Armitage 2012). These results are also in agreement with the less-favored result in Brauer et al. (2007), where they found that high disk masses may bring the drift timescales of millimeter grains into agreement with disk lifetimes. Furthermore, the CO-to-$H_2$ ratio also seems to be altered in these disks from the typically assumed ISM value. This also supports the idea that CO chemistry or other physical processes in the disk are more complicated than was initially assumed such that disks can appear to be depleted of gaseous CO. Interestingly, while the factor needed to match integrated dust emission derived masses

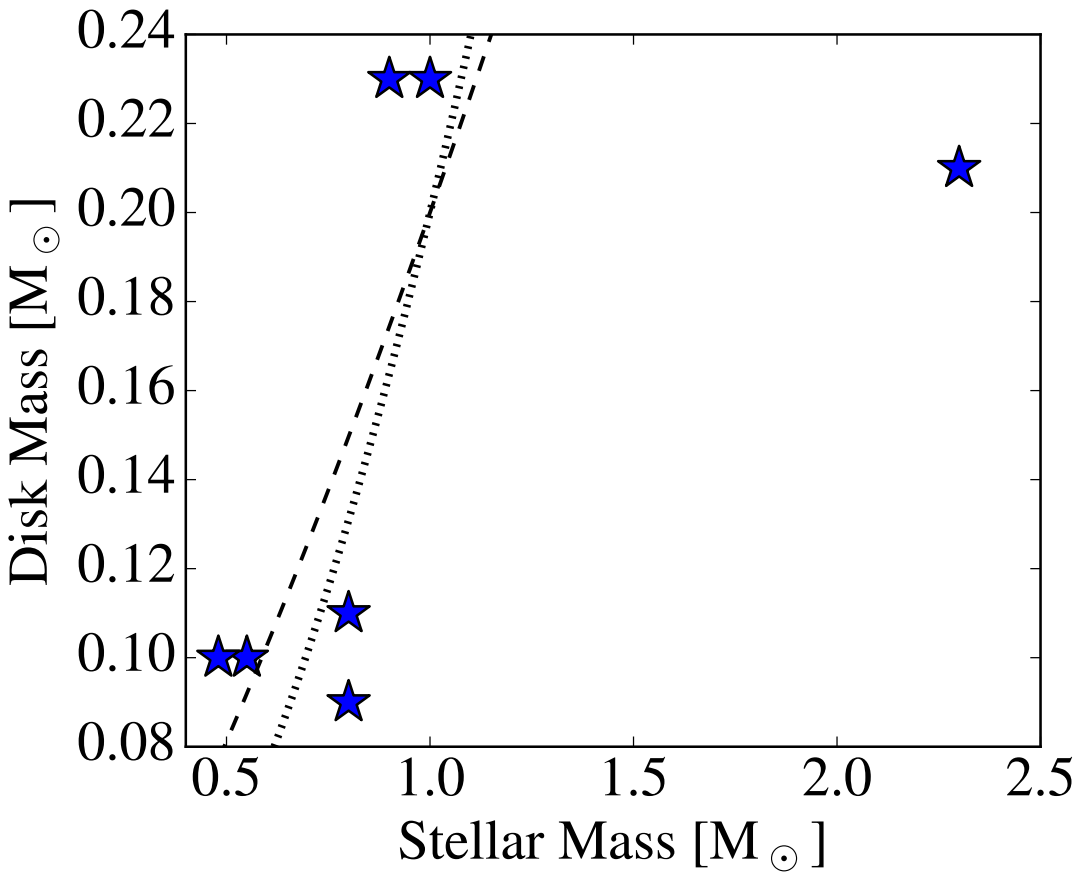


Figure 5.5: The derived disk masses in this sample (blue stars) are consistent with the Pascucci et al. (2016) steeper than linear scaling relationship between disk dust mass and stellar mass, except for the disk HD 163296 which orbits a massive Herbig Ae star. Our normalized relationship is a factor of 50 larger than the best-fit relationship derived assuming an ISM dust-to-gas ratio in Pascucci et al. (2016) such that $M_{disk} \sim 0.2 M_{\odot}$ $(M_{\star}/M_{\odot})^{1.3}$ (dashed line) and $M_{disk} \sim 0.2 M_{\odot}$ $(M_{\star}/M_{\odot})^{1.9}$ (dotted line)

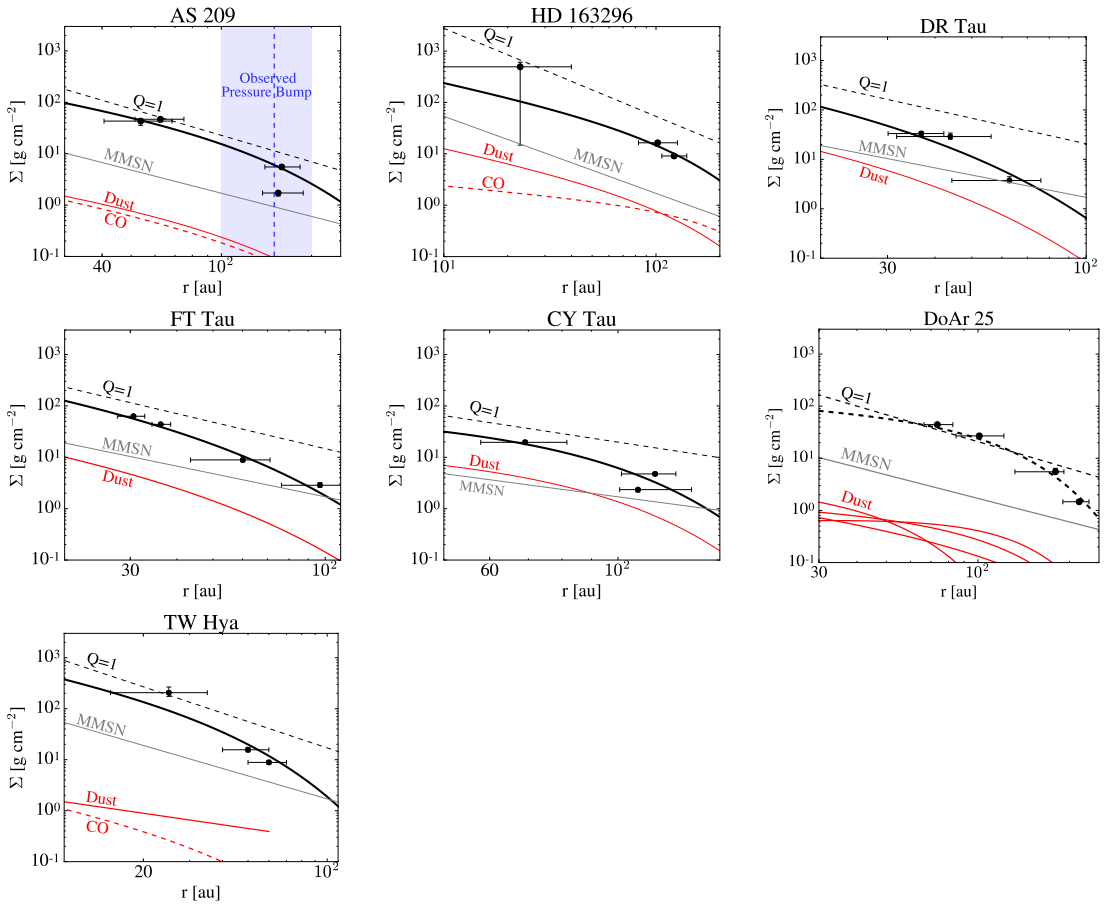


Figure 5.6: The renormalized total surface density profiles (black lines) as shown in Figure 5.4 are plotted for comparison with several other profiles: the total surface density profile derived from integrated dust emission (red lines) or CO emission (red, dashed lines), the minimum mass solar nebula (gray lines) and the gravitational stability limit (dashed, black lines) derived from Toomre-Q stability analysis. We show renormalized profiles derived from integrated dust emission except for the disks TW Hya and DoAr 25 (see text). We choose radius ranges probed by the resolved millimeter continuum observations. AS 209 has a ring of emission observed in both CO and dust observations (blue, dashed line) as discussed in Section 5.7.1.

(2-15) with the newly derived masses is similar across all of the disks in our sample, the factor needed to adjust the CO masses (5 - 115) seems to vary significantly across individual disks. It may therefore be likely that dust is a better tracer of the total mass inventory in disks than CO line emission, although the ratio of dust-to-gas should be carefully chosen. In Section 5.6.3, we find an average value of $\sim 10^{-3}$ for the dust-to-gas ratio of the disks in our sample.

While this is not a statistical sample of disks, in Figure 5.6 we compare our derived disk masses to their host stellar mass to see if we recover the steeper than linear scaling of disk dust mass with stellar mass from Pascucci et al. (2016). The disks in our sample follow a trend with a roughly consistent slope. The Pascucci et al. (2016) relations were derived using an ALMA survey at 887 $\mu$m for disks orbiting host stars with masses $\sim$ 0.03 to 2 $M_\odot$ in the Chamaeleon star forming region and comparing the mass in dust with the host's stellar mass. There is some expected scatter in this relationship which may be due to differences in disk age and accretion history. If the disk dust mass is directly proportional to the total mass, then we can naively expect this relation to hold for the disks in our sample. This is indeed what we find. A normalized scaling relation of $M_{disk} \sim 0.2 M_\odot \ (M_\star/M_\odot)^{1.3}$ or $M_{disk} \sim 0.2 M_\odot \ (M_\star/M_\odot)^{1.9}$, a factor of 50 larger than the best-fit relationship derived assuming a dust-to-gas ratio of $10^{-2}$ from Pascucci et al. (2016), match the derived data well. The disk HD 163296 is a significant outlier in this trend, which is not surprising as this scaling relation would predict a disk mass of 0.56-1 $M_\odot$, far exceeding the limit for gravitational stability (see Section 5.6.2). The scaling relation for more massive stars, therefore, likely has a

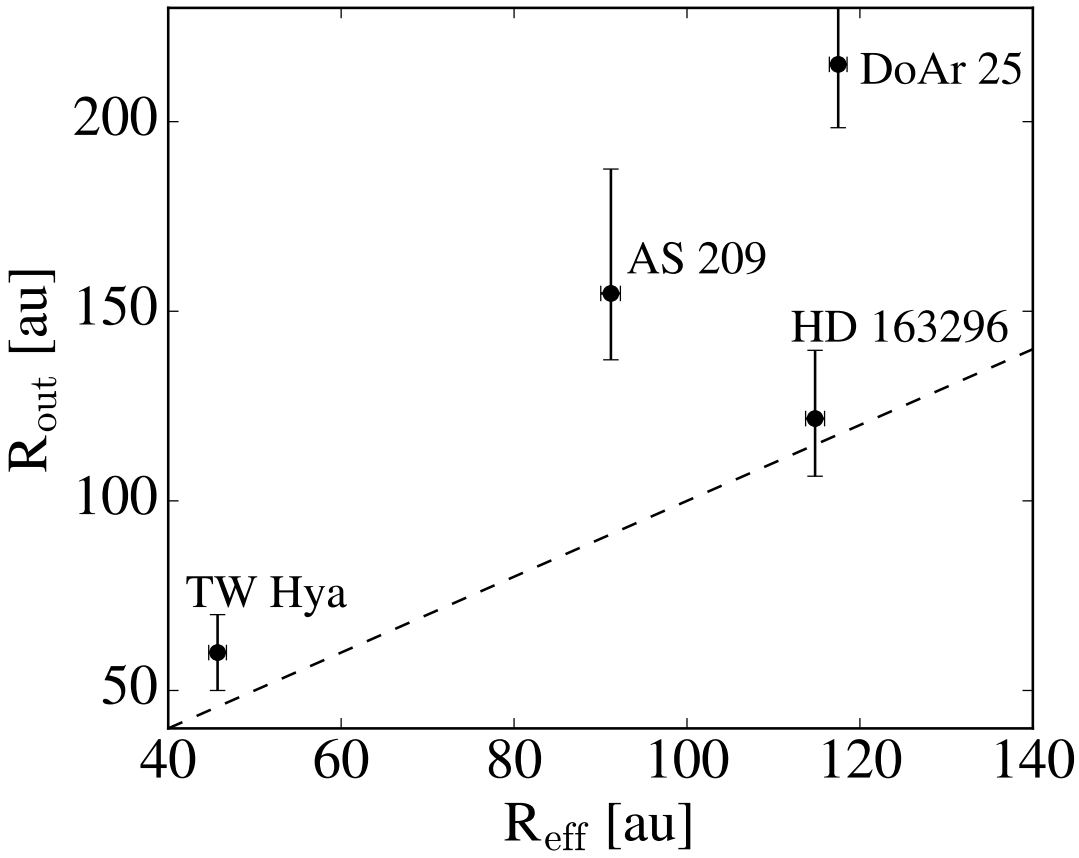


Figure 5.7: The calculated disk outer radius, $R_{out}$, which measures the location at which the flux falls off steeply, is larger for every disk in our sample than the effective radius, $R_{eff}$, which measures the radius that encompasses 68 % of the disk flux as calculated in Tripathi et al. (2017). The one-to-one line is also shown (dashed).

different scaling.

Interestingly, there does not seem to be a clear correlation between the stellar age and disk mass. We note that the disk masses in this sample are all the same to within a factor of 3, although there is a wide range in stellar ages. The lack of a clear trend between disk mass and stellar age is likely not apparent in this sample because older disks with lower masses may not be massive enough for current high resolution observations. Our sample does indicate, however, that some disks may not be able to

viscously evolve efficiently (see Section 5.6.2).

The newly determined total surface density profiles can also be placed in context of other typically assumed disk profiles such as the minimum mass solar nebula (MMSN). The new profiles for these disks can also be directly compared to their previously derived disk surface density profiles. This comparison is shown in Figure 5.6 for the regions of the outer disk where our modeling work is the most readily tied to empirical evidence. For the MMSN we use the following standard prescription (Weidenschilling 1977b; Hayashi 1981):

$$\Sigma_{\rm MMSN} = 1700 \text{ g cm}^{-2} \ r_{\rm au}^{-3/2} \tag{5.13}$$

For every disk in our sample the newly derived surface density profile and mass exceeds the MMSN ($\rm M_{MMSN} = 0.02 M\odot$) at most radii which itself exceeds the estimate derived from other observational tracers. While the disks in our sample are more massive than the MMSN, the disks DR Tau and FT Tau are comparable at large radii past the critical radius.

The four of the disks in our sample with disk radii measured at $\sim 0.9$ mm (340 Ghz) were also included in the analysis done by Tripathi et al. (2017). The outer radii measured in this work are indeed larger than the effective disk radii from Tripathi et al. (2017) as expected, although there is not a systematic offset as shown in Figure 5.6.1. However, this is to be expected as the effective disk radius depends on the inner disk index such that disks with more centrally concentrated intensity profiles have smaller effective radii (Tripathi et al. 2017). The outer radius in contrast is only determined by

the radius where disk emission approaches zero. For a discussion on the errors of these measurements see Section 5.4.

### 5.6.2 Gravitational Stability

We briefly analyze the stability against gravitational collapse of the newly derived disk surface densities through a Toomre-Q stability analysis. Following the Toomre-Q instability criterion, a disk is unstable to collapse if the local gravity in a region of any arbitrary size overcomes rotational and thermal support, which requires

$$Q \equiv \frac{c_s \Omega}{\pi G \Sigma} \lesssim 1 \quad , \tag{5.14}$$

where $c_s$ is the sound speed, $\Omega$ is the orbital frequency, and $\Sigma$ is the disk surface density (Toomre 1964).

The surface density that corresponds to a Toomre-Q parameter of unity (roughly the first point in which a profile becomes unstable to collapse) is shown for each disk in Figure 5.6. The Toomre-Q parameter varies throughout the disks and reaches a minimum at a particular semi major axis. The value of the Toomre-Q parameter for the full disk sample as a function of radius is shown in Figure 5.6.2. All of the disks in our sample, except for the disk DoAr 25, respect the Toomre-Q stability criterion as expected by their smooth morphologies. The disk DoAr 25 has a derived surface density profile that just reaches this limit at roughly 100 au. This disk was previously thought to be massive based on classical dust emission observations which also indicate that this object may be approaching gravitational instability (Andrews et al. 2009),

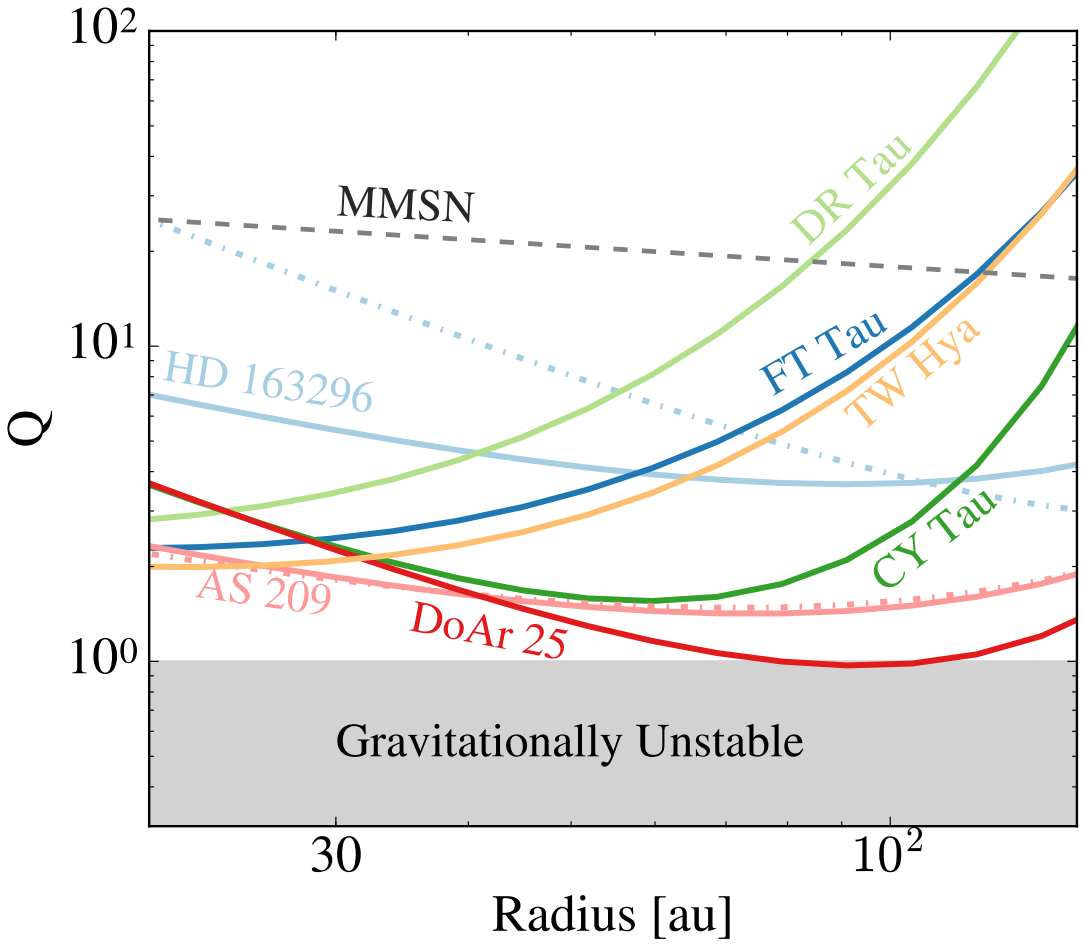


Figure 5.8: All of the disks in our sample are stable against gravitational collapse. The Toomre-Q parameters as a function of radius are shown for the renormalized dust surface density profiles (solid lines) and renormalized CO surface density profiles (dot dashed lines). The disk DoAr 25 is close to exceeding the limit for stability as its Toomre-Q parameter approaches 1 near its critical radius. The Toomre-Q parameter for the MMSN is provided for comparison.

although high resolution imaging at 1.3 mm shows three bright rings located at 86, 111, and 137au instead of spiral arms (Huang et al. 2018b). Furthermore, while our newly derived estimates of disk surface density for the other 6 disks in our sample do respect the gravitational stability limit, they all reach Q values less than 10.

We conclude that at least among the brightest sample of disks in the sky, low Toomre-Q values are not uncommon. This idea is supported by recent ALMA observations in which 4 disks have so far been shown to have spiral arm structures that suggest instability to collapse (Huang et al. 2018b; Pérez et al. 2016).

We note that it is seemingly easier theoretically to produce massive disks that approach gravitational instability as disks may form near the limit of stability (e.g., Williams & Cieza 2011) and it is non-trivial to trigger viscous evolution in disks via the magneto-rotational instability (e.g., Chiang & Murray-Clay 2007; Bai & Goodman 2009; Marcus et al. 2015; Cleeves et al. 2015). Understanding why some disks have been able to accrete efficiently while others have not may shine a light on how non-ideal magnetohydrodynamics (MHD) operates in protoplanetary disks.

### 5.6.3 Derived Dust Surface Densities and Numerical Validation

Following the method described in Section 5.3.1, we now derive the dust surface density for our modeled disks through a consideration of a particle coagulation. We derive the dust-to-gas ratio and hence the disk surface density using Equation (5.8) and multiply this by our total gas surface density profile to derive a dust surface density profile. An example of our derived dust surface densities is shown in Figure 5.6.3 for the disk FT Tau which is representative of the other disks in our sample. Using our

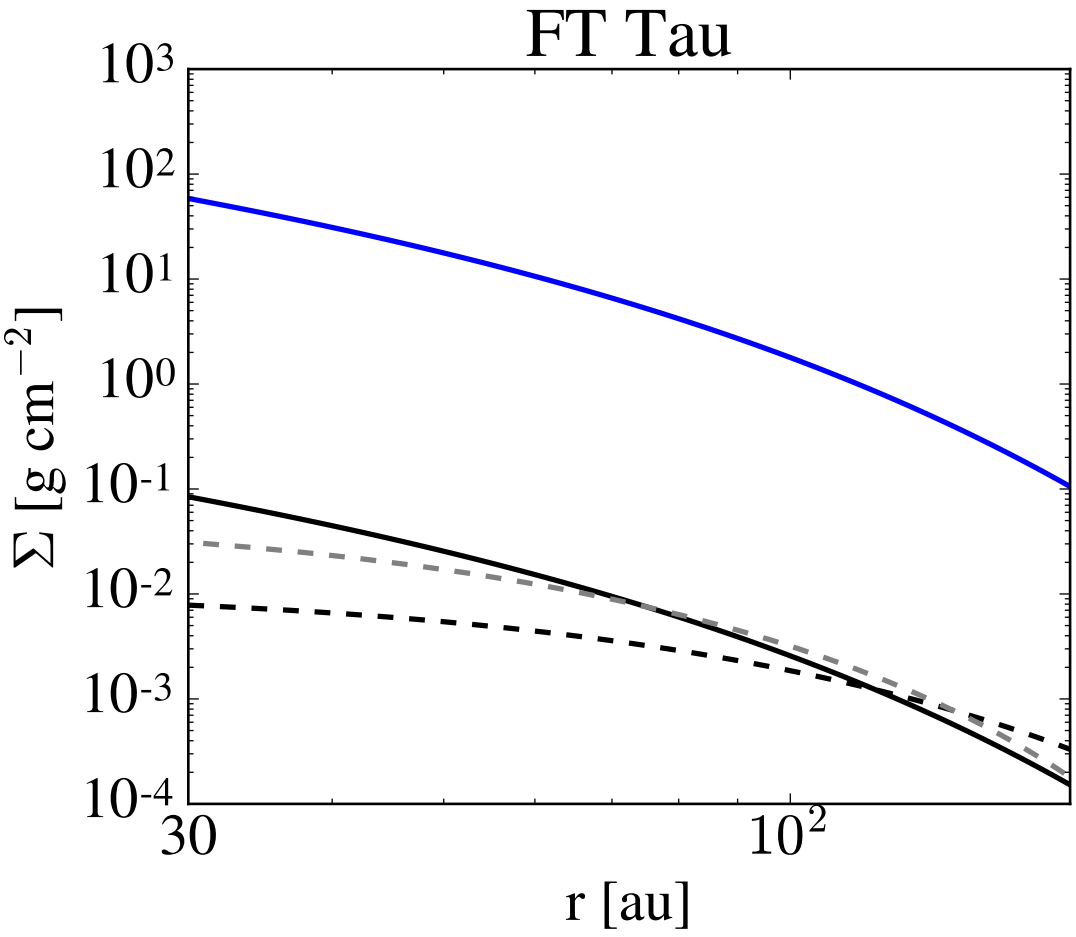


Figure 5.9: Our model for dust surface density for the disk FT Tau (black dashed line) is roughly consistent with the observationally derived dust surface density profile (black solid line, Tazzari et al. 2016). The newly derived dust surface density profile is also fairly consistent with the dust surface density derived when we input our derived disk parameters into the Birnstiel et al. (2012) dust evolution code (gray dashed line). The newly derived gas surface density profile using our model (blue line) is also shown.

order-of-magnitude derivation we find rough agreement with observations. We find this level of agreement particularly encouraging as there are many unaccounted for sources of error in both dust observations (i.e. the dust grain opacity) and our model (see Section 5.3.2).

Every disk in our sample has a derived dust-to-gas ratio of approximately $10^{-3}$ in the outer disk with the exception of the disks TW Hya and HD 163296 which have an average dust-to-gas ratio of $10^{-4}$ in the outer disk, in good agreement with the dust surface density profiles derived from integrated dust emission.

While we derive lower present day dust-to-gas ratios than the typically assumed ISM value of $10^{-2}$, the implication is that at earlier times the dust mass was much higher. The larger disk masses in both gas and dust (at earlier times) may help resolve problems in planet formation theory as applied to extrasolar system formation as presented in Manara et al. (2018).

While we do not use a dust opacity model to calculate a dust-to-gas ratio, we can use our results to roughly derive an opacity model. The derived dust opacity in our modeling is only different than typically assumed values for each disk due to the difference in dust-to-gas ratio. As our calculated dust surface density profiles are in rough agreement with those inferred from integrated dust emission, the total dust opacity is in agreement with the dust opacity assumed in the literature (see Table 5.1) when relating dust emission to total mass for each object with a modifying constant due to the decreased dust-to-gas ratio. The assumed literature dust opacities vary for the objects in our sample from $\sim$0.01 - 8 cm$^2$ g$^{-1}$ at $\sim$1.3 mm (Isella et al. 2007; Guilloteau

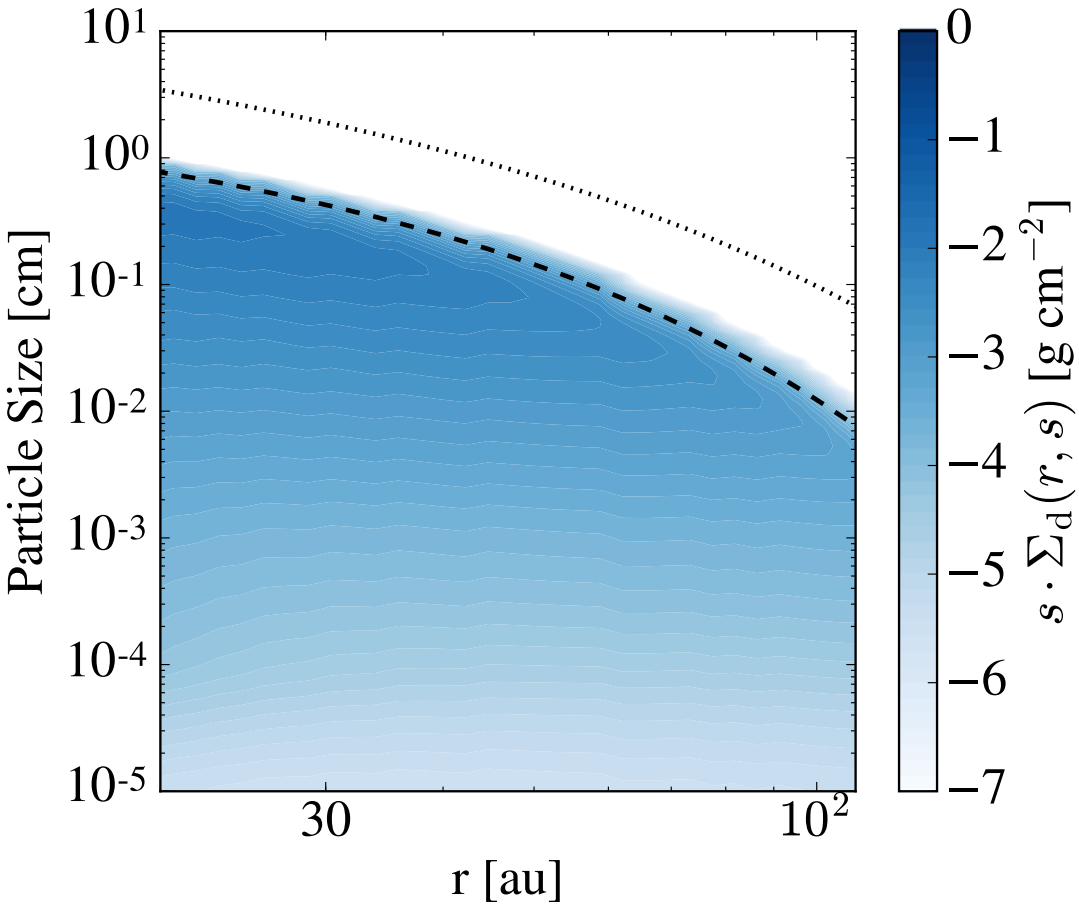


Figure 5.10: There is good agreement between the location of the millimeter particles found numerically when we input our derived disk parameters into the Birnstiel et al. (2012, 2015) dust evolution code and the location of the particles in the observations. Shown are the location of particles at 1.6 Myr for the disk FT Tau as modeled using this numerical code. The contour lines represent the surface density of reconstructed particle size distribution as a function of radius. The dashed line represents the drift limit (the largest particles present) and the dotted line is the fragmentation limit. This simulation had an initial dust-to-gas ratio of $10^{-2}$, indicating that this disk formed with more solid material than is available at present.

et al. 2011; Menu et al. 2014; Tazzari et al. 2016; Cox et al. 2017). The average literature opacity value for objects in our sample at 1.3 mm, removing the high and low outliers, is $\sim$0.5 cm$^2$ g$^{-1}$ ($\sim$1.5 cm$^2$ g$^{-1}$ with outliers), which is lower than the $\sim$3 cm$^2$ g$^{-1}$ at the same wavelength adopted in the DHSARP survey (Birnstiel et al. 2018).

The total dust opacity used to derive dust masses from disk fluxes in the sub-mm could therefore be described simply as:

$$k_{\lambda}^{'} = f_d k_{\lambda}, \tag{5.15}$$

where $k_{\lambda}^{'}$ is the total dust opacity at a given wavelength in units of cm$^2$ g$^{-1}$, $f_d$ is the dust-to-gas ratio, which varies from $\sim 10^{-4} - 10^{-3}$ for objects in our sample, and $k_{\lambda}$ is the previously assumed dust absorption opacity at a given wavelength also in units of cm$^2$ g$^{-1}$ which can differ from disk to disk. Other than the change in the assumed dust-to-gas ratio, our inferred dust opacities are in rough agreement with those commonly assumed in the literature for the different objects in our sample (c.f. Figure 5.6.3).

We further verify our disk model using the publicly available dust evolution code from (Birnstiel et al. 2012, 2015). The model from Birnstiel et al. (2012, 2015) evolves the disk from early times and reconstructs a full particle size distribution. They find that this semi-analytic model matches well with more detailed numerical modeling in several tested regimes of interest. We input our derived disk parameters into the (Birnstiel et al. 2012) dust evolution code and find that we are able to reproduce the particle locations as a function of radius. This is shown in Figure 5.6.3 for the disk FT Tau where we assume $\alpha = 10^{-3}$, no viscous gas evolution, and an initial dust-to-gas

ratio of $10^{-2}$ and run the model to the current age of the system, 1.6 Myr. In this code we also derive a low dust-to-gas ratio that varies as a function of radius with an average value of $\sim 10^{-3}$ for the radii of interest in agreement with the results from our model. We therefore find our new disk model to be both numerically reproducible and in good agreement with observational work as shown in Figure 5.6.3.

In summary, an increase in the total gaseous surface density allows for larger particles to remain coupled to the gas for longer such that their drift is slowed. The increased gas mass derived in our modeling, therefore, readily explains the observed locations of differently sized dust particles.

## 5.7 Discussion

### 5.7.1 Disk Substructure

Recent observations of disks in the millimeter using ALMA have revealed the richness of disk substructure in the form of rings, gaps, spiral arms, vortices, and more (e.g., ALMA Partnership et al. 2015; Pérez et al. 2016; Huang et al. 2018b; Long et al. 2017; Andrews et al. 2018). In particular, the prevalence of ring structures suggest that these features may be fundamental to the majority of protoplanetary disks (e.g., Huang et al. 2018b; Long et al. 2017). Several theoretical models exist to explain the generation of disk rings such as: planet-disk interactions (e.g., Lin & Papaloizou 1986; Zhu et al. 2012), or disk specific mechanisms such as large scale instabilities causing pressure bumps (Lorén-Aguilar & Bate 2016), grain growth around ice lines (e.g., Zhang et al. 2015; **?**), and many more. While the cause of these rings is an active area of research,

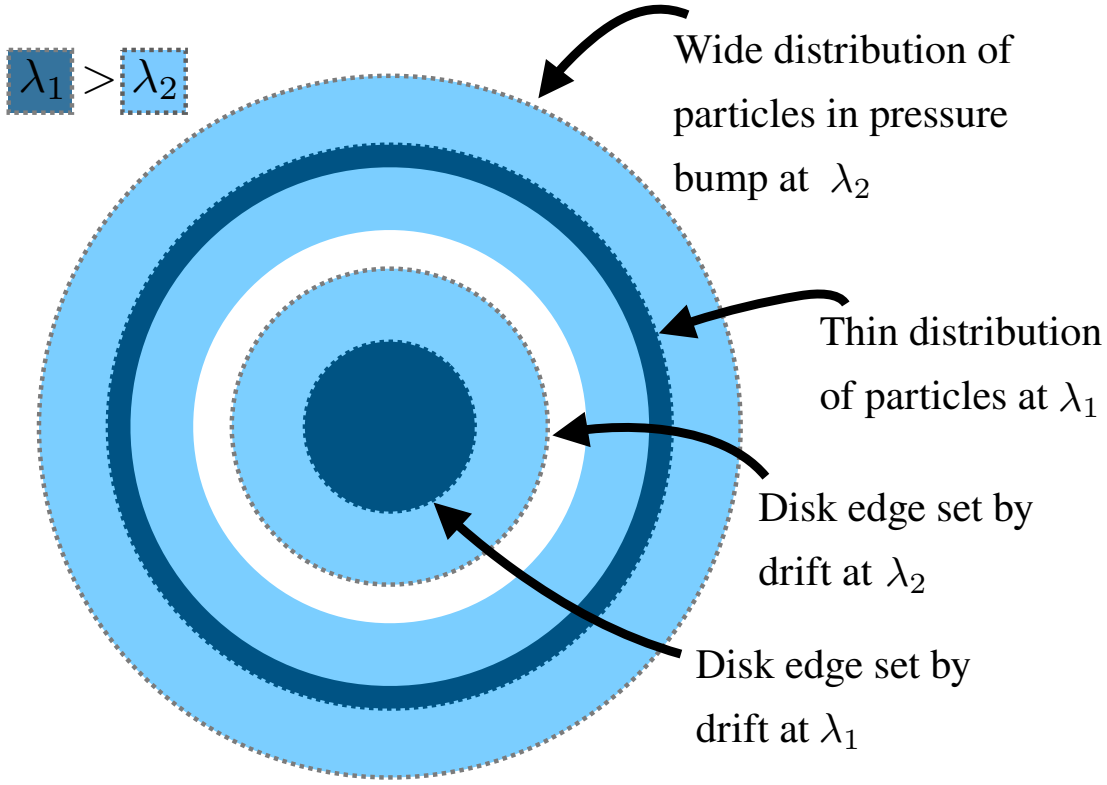


Figure 5.11: Cartoon of how the presence of a pressure trap in a disk will alter the signature of particle drift. Particles of size $2\pi/\lambda_1$, where $\lambda_1$ is the longer observational wavelength, will be strongly affected by the pressure trap and should exhibit a narrow ring of emission when viewed at $\lambda_{\rm obs} = \lambda_1$. Interior to the pressure trap there will be a large gap as these particles drift relatively quickly. Particles of size $2\pi/\lambda_2$, where $\lambda_2$ is the shorter observational wavelength, will be less strongly effected by the pressure trap and should generate a wider ring of emission when viewed at $\lambda_{\rm obs} = \lambda_2$. Interior to the pressure trap there will be a smaller gap as these smaller particles are slower drifters.

these models tend to create ring-like features through the presence of dust traps that can slow drift and cause particle pileups at particular radial locations. We provide a brief discussion of how dust traps may influence our method of determining total disk surface density and leave detailed modeling to future work.

**Dust Lines and Efficient Dust Traps**

If dust traps are indeed prevalent in disks they will have clear signatures depending on the efficiency of the trapping. If the dust trap is efficient in trapping particles then we should see a distinct increase in emission at the same dust trap radial location at each millimeter wavelength. The radial width of the dust trap may vary at different wavelengths, however, as larger particles that are more influenced by drift are trapped more strongly in the pressure bump than smaller particles (see Figure 5.7.1). If an efficient dust trap is present exterior to the maximum location that a particle could be present due to drift then it is possible that there will be an uptick in disk emission at the radial location of the dust trap. The dust line would therefore be set by dust trapping instead of particle drift. In this case, resolved disk images would show a ring of emission present across millimeter wavelengths with an interior gap in emission. At longer wavelengths that probe larger grains we would expect this gap to appear larger as the large grains interior to the dust trap would drift quickly. Correspondingly, at shorter wavelengths we would expect to see a smaller gap. This is summarized in Figure 5.7.1. In the case that multiwavelength high resolution images of disks show these signatures of a pressure bump, the disk edge set by drift can thus be disentangled from the empirical disk dust line which we have defined as the disk outer edge.

Alternatively if the dust trap is interior to the disk dust line but also strongly efficient then it could be possible that the drop off in emission is sufficiently sharp interior to the radial location set by drift such that modeling disk visibilities places the dust line location interior to the drift location. Given our modeling sensitivities (see Figure 5.4)

this outcome is not likely. Furthermore, in this scenario we would also expect an efficient dust trap to be present at the same location across different millimeter wavelengths.

**Evidence of Dust Traps in Our Sample**

In our multiwavelength modeling of dust lines, only two objects show strong evidence of efficient dust trapping for various particle sizes: AS 209 and CY Tau. Three of the other disks in our sample, HD 163296, FT Tau and DoAr 25, have recent high resolution ALMA observations that indicate ringed substructure in observations taken at 1.3 mm (Long et al. 2017; Huang et al. 2018b; Isella et al. 2018). However, as we do not derive the same dust line at different observed wavelengths, these substructures likely correspond to less efficient particle trapping. As these disks do not have published reduced visibility data suitable for our derivation of disk dust lines, we compare these disk outer radii based on the analysis of the new ALMA observations to our derived radii at the same or similar wavelengths. For HD 163296, our derived disk outer radius at 1.3 mm is consistent with the radius of the outermost disk ring as presented in Isella et al. (2018). We note that for this disk, the ring features seen in dust emission are not present at the same contrast in similarly resolved CO emission (Isella et al. 2016, 2018), indicating a weaker pressure bump than is viewed in AS 209 (see below). While we do not model DoAr 25 at 1.3 mm in this work, the derived location of the outermost ring in Huang et al. (2018b) is consistent with our disk dust line at 2.8 mm. For FT Tau, recent modeling work finds that 90% of the disk flux is contained within 42 au Long et al. (2017). This is somewhat different from the outer radius that we derive for this disk at 1.3 mm. However, the radius that encompasses 90% of the disk flux is different

from the dust line measurement presented in this work as we are interested in the radius at which disk emission goes to zero. This distinction is described in more detail in our discussion of the outer radius as defined in Tripathi et al. (2017) (see Section 5.4).

One of the key features of efficient dust trapping, as shown in Figure 5.7.1, is the presence of disk dust lines at the same location at different observed wavelengths. Our analysis of the disk AS 209 is consistent with such efficient trapping. Observations in CO find an increase in emission at roughly 150 AU (see Figure 5.6, Huang et al. 2016; Guzmán et al. 2018) and a ring of emission in millimeter dust observations at roughly the same radius (e.g., Fedele et al. 2018). We correspondingly find two dust lines located at the same radial distance and recent observations of AS 209 using ALMA at 1.3 mm find an outermost ring in emission consistent with the dust lines derived at 0.85 and 2.8 mm (Huang et al. 2018b; Guzmán et al. 2018). This may indicate the presence of a pressure bump creating a dust trap at 150 AU which may obscure the location of the outer edge caused by drift for these particle sizes. In the case of AS 209 the larger particles with dust lines interior to 150 au have seemingly drifted interior to this point and must not be efficiently trapped at 150 au. This may constrain the way in which dust traps affect particles of different sizes. Alternatively, the dust trap may have formed after these particles drifted inwards to their present location which could constrain the timescale over which the dust trap formed in the disk. Either way, the presence of dust lines interior to such a trap allows for accurate scaling of previously derived surface density profiles such that the method for deriving surface density profiles presented in this paper is still useful.

The disk CY Tau is also a candidate for having an outer ring due to an efficient particle trap. The dust lines at the shorter wavelengths (1.3 mm and 2.8 mm) for this disk are both located at roughly the same location. Again, the presence of dust lines interior to this particle trap help constrain our disk modeling work.

#### Dust Lines and Inefficient Dust Traps

For dust traps that do not efficiently trap grains, we may expect to see two different behaviors. For disks with closely spaced inefficient pressure traps, we would expect that they will slow particle drift and generate a multiplicative factor in the drift velocity that translates to a multiplicative factor for the disk surface density. This multiplicative factor would cause the derived disk surface density to decrease. If the drift efficiency is only moderately slowed, the effect on this modeling should be within the observational error. We comment as an aside that the derived dust line locations may look like a step function in this case because the particles will spend most of their time in the pressure traps. If the inefficient pressure traps are not close together then we would expect that, while particles may spend a longer time in the pressure trap, the disk outer edge caused by drift will be apparent in high resolution imaging interior to this location as described above.

### 5.7.2 Porous Aggregate Particles

Recent laboratory work and numerical simulations have indicated that particles in disks may form as porous aggregates with filling factors as low as $10^{-4}$ corresponding to particles with very low densities (e.g., Okuzumi et al. 2012; Kataoka et al. 2013b,a).

Using effective medium theory (EMT), Kataoka et al. (2014) show that the absorption mass opacity of aggregate particles can be characterized by the product of the particle radius ($s$) and the filling factor ($f$). This is because the absorption mass opacity depends directly on the imaginary refractive index, which is proportional to the filling factor, and the size parameter, which is proportional to the particle size. At certain wavelengths the absorption mass opacity of compact grains show distinct interference patterns that are not present in the absorption mass opacity of aggregates with the same value of $sf$. However, for the different values of $sf$ shown in Kataoka et al. (2014) that correspond to our observed wavelengths (see their Figure 3), the absorption opacity for compact grains differs by less than an order of magnitude for aggregates with the same characteristic parameter given our assumption that $\lambda_{\rm obs} = 2\pi s_{\rm obs}$. The observed particle size is therefore given by $s_{\rm obs} \approx sf$. Here $s_{\rm obs}$ refers to to the particle size we would expect to dominate the emission and to drift if the actual particles are of a the same effective size.

Therefore the true particle size, which sets the aerodynamic properties of the grains is given by $s = s_{\rm obs}/f$. The particle density is correspondingly different from the typically assumed internal density of compact grains such that $\rho_{\rm agg} = \rho_s f$. The equation for deriving surface density can therefore be rewritten for aggregate particles:

$$\Sigma_g(r) \approx \frac{t_{\rm disk} v_0 \rho_{\rm agg} s}{r} \approx \frac{t_{\rm disk} v_0 \rho_s f s_{\rm obs}}{fr} \approx \frac{t_{\rm disk} v_0 \rho_s s_{\rm obs}}{r} \tag{5.16}$$

which reduces such that it is equivalent to Equation (5.1).

This model for deriving gaseous disk surface densities is therefore robust for

both compact and aggregate dust grains as it is roughly independent of the particle filling factor.

While our derived gas disk surface densities do not depend on grain porosity, the coagulation process of porous grains may differ from compact grains. For porous particles with larger cross sections, particle growth may well be more efficient if their sticking efficiency and fragmentation threshold are otherwise similar to compact grains. Thus, if aggregates are an order of magnitude more efficient at particle growth then this would change our derived value of the dust-to-gas ratio and therefore our derived dust surface density profile.

### 5.7.3 Implications for Other Disks

There are several other disks in the literature with resolved multiwavength observations that may be well suited to this type of modeling work. However, as many of these disks have only been observed at two observational wavelengths and many others were not published with their complete reduced visibility profiles they are not included in this initial work.

We briefly model the disk UZ Tau E based off of the analysis from Tripathi et al. (2018) as shown in Figure 5.7.3. In their analysis they determine an effective disk radius ($R_{\rm eff}$) that corresponds to a fixed fraction (68 %) of the total luminosity as we discuss previously (see Section 5.6.1). As this is not the true dust line (outer radius) in the sense used in our modeling, this model for UZ Tau E is a rough approximation. We note, however, that this seems to be a good candidate disk for this modeling work in the future as the derived surface density points are stable against collapse and seem to

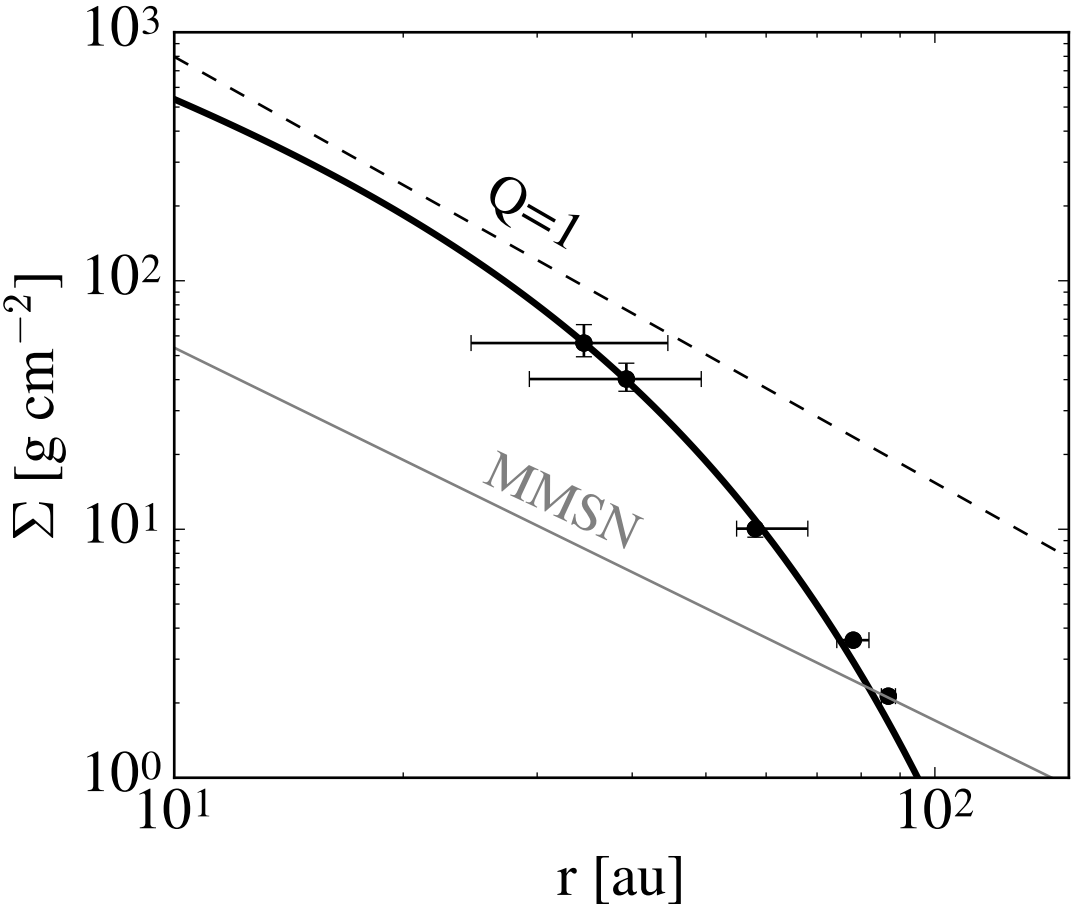


Figure 5.12: The disk UZ Tau E may also be well described following this method. We derived surface density points using the radii from Tripathi et al. (2018) in which they consider a disk radius that encompasses 68% of the total flux (black points). Because these radii are not the disk dust lines, this result is approximate. Nevertheless, a similarity solution fit to the derived surface density points (black line) is a good fit and is stable against collapse. The limit of gravitational stability (dashed, black line) and the surface density profile for the MMSN (gray line) are shown for reference.

follow a profile that is believable for the surface density of a protoplanetary disk. We us a $\chi^2$ minimization to fit the derived surface density points as a similarity solution profile (see Equation 5.12) and derive the following parameters: $r_{\rm crit} = 23$ au, $\gamma = 0.9$, $\Sigma_0 = 369$ g cm$^{-2}$.

This work is not the only evidence for disks being massive as discussed in Section 5.2. Four disks recently observed in high resolution using ALMA show evidence of spiral arms (Pérez et al. 2016; Huang et al. 2018b), indicating gravitational instability. Furthermore, in the survey by Pascucci et al. (2016), several disks in their sample are within a factor of 3 of being gravitationally unstable. If the dust-to-gas ratio for these objects is instead $10^{-3}$, then a significant fraction of their sample will be approaching the limit of gravitational instability. If future observations confirm the prevalence of disks that show features of gravitational instability, and massive masses in dust, it further indicates that many protoplanetary disks are likely more massive than previously assumed.

### 5.7.4 Further Observational Verification of the Dust Line Model

We briefly discuss two observational diagnostics as described in Powell et al. (2017) that may provide independent verification of the disk surface density model described in this work. For further details of these diagnostics and observational tools see Section 5 of Powell et al. (2017).

The first of these diagnostics is whether or not the surface density profile derived from a disk ice line matches the surface density profile derived from disk dust lines. As the location of a species's ice line depends on disk surface density, the surface

density can be derived from ice line locations if the radial location of the ice line in the disk midplane is well-constrained and if drift is important in influencing the dynamics of grains at this location or the species's abundance is well constrained.

The second of these diagnostics is whether or not the dust and ice lines scale oppositely with disk surface density. We expect that this will happen because disks with dust lines at larger radial scales should have ice lines located at smaller radii for a given disk temperature structure and molecular abundance. This diagnostic may be approachable with a large sample of well-observed disks.

## 5.8 Summary and Conclusions

We apply a novel method of determining the surface density of protoplanetary disks to a set of 7 diverse objects that does not rely on a tracer-to-$H_2$ ratio or an assumed dust opacity model. We use an MCMC method to model spatially resolved images of disks at multiple wavelengths and infer the location of the disk outer edge (i.e. a disk dust line). This measurement is then related to the maximal radial locations in which particles of size $2\pi/\lambda_{\rm obs}$ are observed. Then, through a consideration of the aerodynamic properties of these grains, the total gaseous disk surface density is derived at specific radial locations. These derived surface density values are then used as benchmarks to scale previously modeled surface density profiles derived either from combined multiwavelength dust or CO emission observations. This method may be particularly robust as it does not rely on an assumed dust-to-gas or CO-to-$H_2$ ratio to derive total gas surface densities. This new method is appropriate for disks that have evolved ages

($t_{\rm disk} \gtrapprox 1$ Myr) and have different radial extents at different observed wavelengths. For the 7 bright protoplanetary disks in our sample, we derive total gas disk masses and compare these masses to previous values determined from CO and dust emission. We further derive disk dust-to-gas ratios and dust surface density profiles.

Our new disk masses for objects in our sample are 9-27% as massive as their stellar hosts and have minimum Toomre-Q values below 10 even for the disks in our sample that are relatively old. Our sample is biased towards the brightest and most massive disks in the sky as they are the most readily observed. However, understanding why some disks may be able to efficiently viscously evolve away from the limit of gravitational instability with time while others do not may shed light on the mechanisms that govern magnetohydrodynamics in protoplanetary disks.

Most of our newly derived masses are larger than the total mass obtained by dust observations by a factor of ∼6-8. The disk HD 163296 has a new mass that is roughly consistent with the previous dust emission mass measurement and AS 209 has a new mass that is a factor of 15 larger than measured from integrated dust emission. The three disks with resolved CO observations have new constraints on disk mass that exceed the mass derived from CO emission alone. The amount of observed depletion of CO varies significantly for the three disks in our sample and ranges from a factor of 3-115. This supports the popular idea that CO may be depleted or missing in protoplanetary disks. Though more massive, our new total gas masses scale more consistently with masses inferred from integrated dust emission than from CO emission, indicating that dust is a more robust tracer of total gas mass.

We further consider the growth of the observed particles to infer the disk dust-to-gas ratio and thus the disk surface density profile. Our model dust surface density profiles match the surface density profiles derived via millimeter observations well. The dust surface densities and locations of the particles in this model can also be reproduced with semi-analytic simulations when our new disk parameters are used as input initial conditions.

The derived dust-to-gas ratio is typically $\sim 10^{-3}$ for the disks in our sample in the outer disk. It is perhaps more appropriate to use this value when calculating total disk mass from integrated dust observations that probe the outer disk. The exceptions in this sample are the disks HD 163296 and TW Hya which have a dust-to-gas ratio of $10^{-4}$. These low dust-to-gas ratios suggest that there was significantly more dust mass available earlier in the lifetime of these disks before particles begin to drift rapidly. The larger disk dust mass at earlier times may help resolve problems in the application of planet formation theory to extrasolar planetary systems.

Some of the disks in our sample appear to have dust lines set by dust traps as their outer radius is at roughly the same location at multiple wavelengths. In particular, two disks in our sample show evidence of an outer ring that may efficiently trap particles that are relatively small in size. For one disk this ring is also present in CO observations. We provide a method of qualitatively determining the location of the disk outer edge set by drift in the case where there is an efficient particle trap present in the disk. We further show that this method of determining surface density is roughly independent of particle porosity. This method could be applied to many disks that are currently observed and

may be observed in the future with ALMA at multiple millimeter wavelengths. To continue to validate (or invalidate) this method we stress the importance of having a large sample of objects in which to perform this analysis.

# Chapter 6

# Non-Equilibrium Ice Formation Controls the Distribution of CO in Protoplanetary Disks

Empirical constraints on the fundamental properties of protoplanetary disks—such as the disk mass, composition, and turbulent transport properties—are essential for understanding planet formation and the properties of planetary systems such as planet masses, the composition of planetary cores, and the composition of atmospheres (Pollack et al. 1994; Öberg et al. 2011). However, observations of protoplanetary disks using different tracers are inconsistent (Ansdell et al. 2016; Bergin et al. 2013; Schwarz et al. 2016; Zhang et al. 2019) and both the composition and diffusive properties of protoplanetary disks are almost exclusively determined from observations of trace gas species in the upper warm molecular layers (Andrews 2020) that do not trace the bulk

disk properties. Here we show that non-equilibrium ice formation in protoplanetary disks is key to understanding observations of disks using different tracers and can be used to derive an appropriate initial condition for planet formation models. Our model successfully explains the observed severe carbon monoxide (CO) gas depletion and the radial distribution of CO gas in the upper layers of the four most well-studied protoplanetary disks(Zhang et al. 2019). We constrain the solid and gaseous CO inventory at the midplane and disk diffusivities and resolve inconsistencies in estimates of the disk mass—three crucial parameters that control planetary formation.

There are three key processes in protoplanetary disks that can affect the observed abundance of gaseous CO: chemistry, ice formation, and transport (Fig. 6.4). Previous modeling of chemical processing and ice formation could not explain the observed distribution of CO gas. The chemical processing of CO and previous theories of condensation and particle transport overpredict the abundance of CO gas (Dodson-Robinson et al. 2018; Schwarz et al. 2018; Krijt et al. 2016). Even when combined, previous models of these two processes could not explain the CO gas abundance in observed disk lifetimes (Zhang et al. 2020b; Krijt et al. 2020). Importantly, previous models of ice formation form small ice particles that are readily lofted to a warm molecular layer several scale heights above the midplane where disks are heated by high energy photons. There these small ice grains release CO gas, altering the abundance of CO to levels inconsistent with many observations.

Here we show that the observed distribution and abundance of CO gas in protoplanetary disks can be explained by using a non-equilibrium ice formation model

that takes into account the Kelvin effect, a critical component of ice formation that was not included in previous theories. The Kelvin effect considers the increase in the saturation vapor pressure of a gas over a curved surface, which is important in evaluating rates of condensation (Zhang et al. 2012), including in meteorological processes on Earth (Bogdan 2018), and is given by:

$$P_{\mathrm{sat,eq}}(a,T) = \exp\left(\frac{2\sigma v}{aRT}\right) P_{\mathrm{sat}}(T) \tag{6.1}$$

where $P_{\mathrm{sat,eq}}(a,T)$ is the saturation vapor pressure over a curved surface, $P_{\mathrm{sat}}(T)$ is the saturation vapor pressure over a flat surface, $\sigma$ is the surface energy of the condensible species, $v$ is the volume per mole of the species in the condensible phase, $R$ is the universal gas constant, $a$ is the radius of the particle facilitating the phase transition, and $T$ is the temperature of the particle. Given a surface energy of CO ice of 24.84 erg cm$^{-2}$ (see methods), the saturation vapor pressure over a large grain of 20 $\mu$m in radius is 88% smaller than the saturation vapor pressure over a small grain of 0.1 $\mu$m. Including the Kelvin effect thus causes large grains ($> \sim 20$ $\mu$m) to nucleate ice more efficiently than small grains. We find that, due to the Kelvin effect, very small particles do not form a stable coating of CO ice (Figure 6.1a). Small grains thus have to undergo growth via coagulation until they are large enough for ice formation to occur.

The ice particles that do form grow to relatively large sizes via the processes of condensation and coagulation before they drift radially inwards towards the host star. The majority of the solid CO mass is located in the largest ice-coated particles. These large ice particles settle below the warm molecular layer to a region of the disk that is too

cold for evaporation and is optically thick to UV photons, such that ice photodissociation does not occur (Figure 6.1a). This settling of large grains is prevalent throughout the ice forming regions of the disk (Figure 6.2a), leading to a large sequestration of volatile material in the disk midplane. The continuous ice formation in the disk midplane causes CO gas to be depleted rapidly in the regions where it is initially supersaturated. Once CO gas from the warm molecular layer is diffusively mixed downwards to the cool regions of the disk, more ice formation and gas depletion occurs. Depletion of CO gas from the higher layers occurs over a vertical diffusion timescale because the ice formation timescale is fast once gas diffuses to the disk midplane. Unless there is a local resupply of CO gas due to radial diffusion, the CO gas mole fraction will be constant with height and fixed to the midplane CO saturation mole fraction (Figure 6.2b) once a vertical diffusion time has elapsed. On the other hand, if the Kelvin effect is neglected, ice forms on particles of all sizes, including small grains that can be lofted efficiently into the warm molecular layer, where they release CO ice back into the gas phase. This lofting limits the maximum amount of gaseous CO depletion (Figure 6.1b). In other words, by considering the Kelvin effect that largely prevents small grains from bearing CO ice, we circumvent the problem of CO resupply to the warm molecular layer through lofting and evaporation of small CO ice grains (Figure 6.1b).

The amount of observed CO gas in protoplanetary disks also varies with semi-major axis and the disk age. Depletion occurs quickly immediately exterior to the midplane CO ice line because gas is able to quickly diffuse to the disk midplane and form ice. The vertical diffusion timescale increases in the outer disk where the scale

heights are large due to disk flaring. As a result, while the depletion of CO at the midplane in the outer disk is large due to the low midplane temperature, the observed depletion in the upper warmer layer will be minimal if the vertical diffusion timescale is longer than the current age of the system. At ages younger than a million years, a typical disk may exhibit only a slight depletion of CO gas just exterior to the midplane ice line (Figure 6.2b). In the outer disk, the amount of observed depletion varies with semi-major axis and increases with time such that the disk will become more depleted in gaseous CO as it evolves (Figure 6.2b). In other words, the amount of CO gas depletion in the outer disk is simply a function of the fraction of the disk diffusion timescale that has elapsed since the system's birth (Figure 6.3a). This is in agreement with recent observations of gaseous CO where very young disks (<1 Myr) do not appear to be depleted in CO gas while older systems (>1 Myr) can be depleted significantly (Zhang et al. 2020b). Depending on the speed of particle growth and drift, there can also be a local enhancement of CO gas around the ice line at intermediate and late times once solid CO ice particles have drifted inwards and released their volatile material. This feature is initially very narrow in radial extent and is diffusively broadened with time (Figure 6.2b). The CO-enriched gas interior to the disk critical semi-major axis is then accreted onto the host star.

We model four systems and compare to observations in Figure 6.3b-e. Using this modeling, we constrain the bulk diffusive properties in disks and the composition of solid and gaseous material in the planet forming regions of the disk as a function of both disk semi-major axis and time. Diffusion in disks can be driven by several different

physical processes—such as the magneto-rotational instability, hydrodynamic instabilities, and gravitational instabilities—however, the properties of turbulence generated in disks remain poorly understood. The amount of observed depletion is not always directly correlated with disk age in the observed sample, as some young disks are very depleted in CO gas while some older disks are not (Zhang et al. 2020a). The amount of depletion from initial values depends sensitively on the diffusion present in the system. Thus, in addition to the system age, the primary factor that controls the distribution of gaseous CO is the level of diffusion in the disk. We thus optimize the fit of our model to the data by varying the level of diffusion present in the system (see methods). Our empirical constraints of the diffusion parameter (Table 6.2) all fall within a range of plausible values (Andrews 2020).

While the relative CO abundance depends sensitively on the diffusion present in the system, the total CO mass present in the system depends on the total disk mass. This modeling demonstrates that CO gas is indeed depleted in systems such that a simple conversion from CO gas emission to other fundamental properties such as the total disk mass is not appropriate without modeling non-equilibrium ice formation. With the modeling presented in this work, disk masses estimated from CO are in agreement with those estimated from dust line modeling, HD observations (when relevant), and dust emission (with a dust-to-gas ratio of $\sim 10^{-3}$ appropriate when considering grain growth and particle drift, Powell et al. (2017, 2019b)).

We constrain the inventory of CO in gas and solids in these protoplanetary disks (Table 6.2). Our results are consistent with an initial CO abundance in these

systems that is similar to the interstellar ratio (which we take to be $10^{-4}$ by number, Lacy et al. (1994)). The partitioning of the CO mass inventory depends on the disk diffusion parameter, $t_{\rm age}/t_{\rm diff}$, where $t_{\rm age}$ is the age of the system and $t_{\rm diff}$ is the diffusion timescale (see methods). When the diffusive parameter is very small, as is the case for the disk around HD 163296, the majority of the initial CO mass remains in the gas phase in the outer disk where it is being converted to CO ice as described in the first step in Figure 6.4. As the diffusive parameter increases relative to the disk age, the ice formation process continues and the majority of the initial CO mass will be located in solid ice in the outer disk, as is the case for the disk around DM Tau. At larger diffusive parameters, the ice particles that have depleted the outer disk CO have drifted inwards past the CO ice line where they desorb their volatile materials (steps 2-4 in Figure 6.4). Thus, disks with larger diffusive parameters have either a roughly equal amount of their initial CO mass located in gas in the inner disk and lost to accretion, like the disk around TW Hya, or have lost a majority of their initial CO mass to accretion, like the disk around IM Lup.

Our results demonstrate that the abundance of the gaseous and solid material in protoplanetary disks in the planet forming regions changes as a function of time and disk semi-major axis. For the solid material, the fraction of ice relative to refractory solids in the outer disk is a function of time and particle size. At late times probed by observations, the total mass of CO ice-free grains is roughly an order of magnitude larger than the total mass of CO ice particles. At early times, however, the bulk ice to refractory ratio is larger due to an ice fraction on large particles that is much higher than

the bulk ice to refractory ratio. Large bodies that form in protoplanetary disks at early times via the processes of streaming instability or pebble accretion, which preferentially accrete relatively large particles, are likely to have compositions with significant volatile components. Once particle drift becomes prevalent at later times, icy particles are removed from the outer disk more efficiently than ice-free grains. The population of small CO ice-free grains that is abundant throughout the vertical and radial extent of the disk is likely to dominate the reflected light flux and possess scattering properties different from those of larger CO-rich particles. Future observational studies of the reflective properties of these small grains could validate this prediction.

A similar process of depletion should occur for the other volatile species in disks, such as $H_2O$ and $CO_2$—meaning that future modeling can constrain the abundance ratios in disks. The abundance ratios of different elements, such as the C/O ratio, are the only currently known way to determine a planet's formation region via comparing the abundances of a planet to the abundance ratios as a function of radius in protoplanetary disks. Exterior to the CO ice line, we expect that the bulk composition of the ice particles at the midplane will be a stellar abundance and similarly, the bulk composition of the ice particles between the $CO_2$ and CO ice lines should be sub-stellar as predicted in Öberg et al. (2011). This is because our modeling indicates that the ice formation of volatile species in these regions is regulated by the same vertical diffusion timescale, even though these species have different ice formation efficiencies. Because giant planets that form via core-accretion are thought to obtain the majority of their metallicity primarily from solid material, the compositions of young, giant planets that

span this region should see a corresponding change in C/O ratios. Indications of this trend is emerging for the planets in the HR8799 planetary system where the two planets in the outer solar system (b and c) likely have stellar C/O ratios (Konopacky et al. 2013; Barman et al. 2015; Lavie et al. 2017; Wang et al. 2020). While the C/O ratios of the two inner planets are not as well constrained, there have been some indications of substellar C/O ratios (Lavie et al. 2017) which agrees with these predictions. The C/O ratios should deviate from those predicted in Öberg et al. (2011) interior to the $CO_2$ ice line. Qualitatively, this will occur because the radial transport rates of solid $CO_2$ and gaseous CO will differ though further work is needed to robustly constrain abundance ratios in the inner disk.

We note that the Kelvin effect will be important for understanding the composition of solids of different sizes, particularly at later times once particle drift is efficient. This is because species with larger surface energies will be more likely to form on larger particles which are more susceptible to drift and vice versa which could lead to a solid abundance that varies with particle size and disk semi-major axis. Once gas has been depleted on a vertical diffusion timescale, the gas composition will be set by the saturation vapor pressures of the various gas species and should differ significantly from stellar abundance ratios though the overall gas metallicity will be greatly reduced. Our work provides new constraints on the environment of planet formation and sheds light on the variation of the bulk composition of planetary bodies and their building blocks with orbital distance and formation timescale.

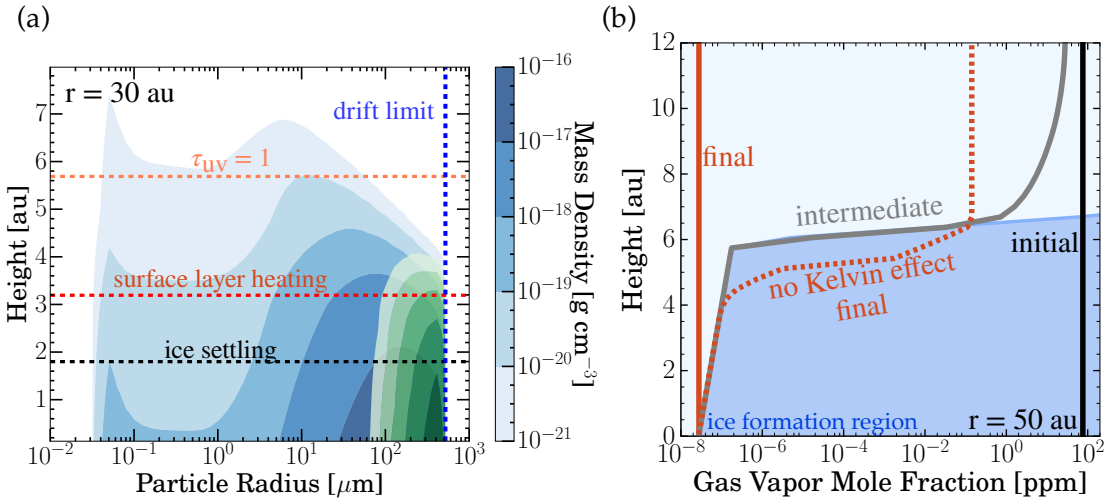


Figure 6.1: The distribution of gaseous CO is regulated by preferential condensation of CO onto large particles. (a) A fiducial distribution of ice coated particles (green) and ice-free grains (blue) at a given disk semi-major axis (r = 30 au, here for TW Hya at 5 Myr). The growth of the large particles is limited by particle drift (blue dashed line). The remaining CO ice-coated particles settle to the disk midplane (black dashed line) and are not readily lofted to the upper regions of the disk where surface layer heating occurs (red dashed line) or where the disk becomes optically thin to UV-photons (the UV optical depth, $\tau_{\rm UV} = 1$, dashed orange line). The ice particles are thus unable to release their volatile material due to either evaporation or photodissociation. (b) The initial CO abundance (black line) is first depleted (gray line) in the regions where it is supersaturated (dark blue shaded region). CO from the upper layers is then mixed downwards and depleted on a vertical diffusion timescale. Without radial resupply, the final CO gas mole fraction will be constant with height and fixed to the midplane CO saturation mole fraction (solid coral line). If the Kelvin effect is not included, then CO would condense on small grains as well. These small grains can be lofted and will release their volatile components in the warm upper layers, thus limiting the maximum amount of depletion possible at a given semi-major axis (dashed coral line).

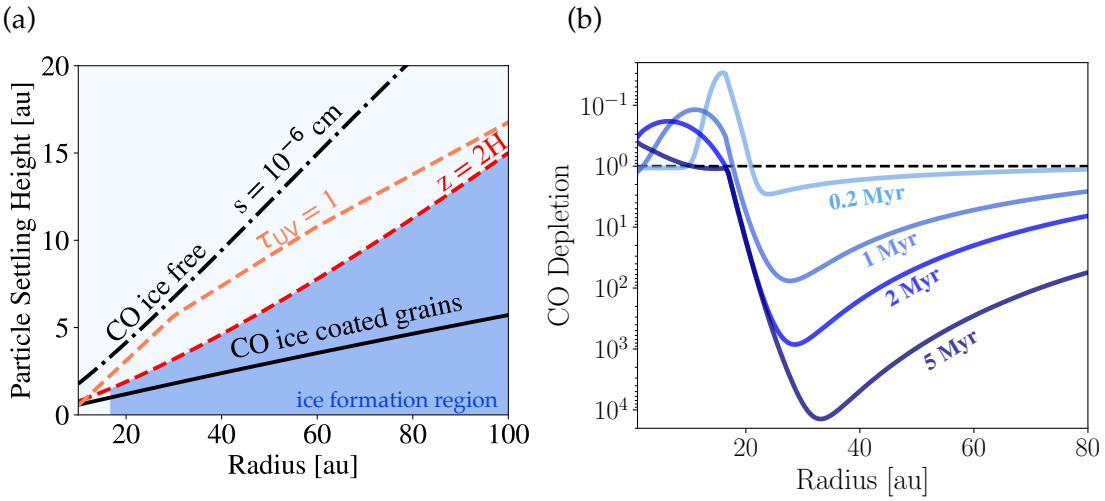


Figure 6.2: The radial evolution of CO gas in the disk around TW Hya: (a) Ice-coated particles settle radially throughout the disk below the surface layer heated region which we approximate as beginning at an altitude, z, that is two scale heights, H, above the midplane (red dashed line) based on more detailed modeling. The ice-coated particles also remain below the region that is optically thin (with a UV optical depth, $\tau_{\rm UV} < 1$) to UV photons (orange dashed line), allowing CO to be sequestered in solids. (b) The amount of CO gas depletion defined as the initial (interstellar) CO-to-H2 ratio divided by the final ratio (blue lines) in protoplanetary disks varies with semi-major axis and increases with time such that the disk will become more depleted in gaseous CO in the outer disk as it evolves. The results were calculated using disk parameters for the disk around TW Hya (see methods).

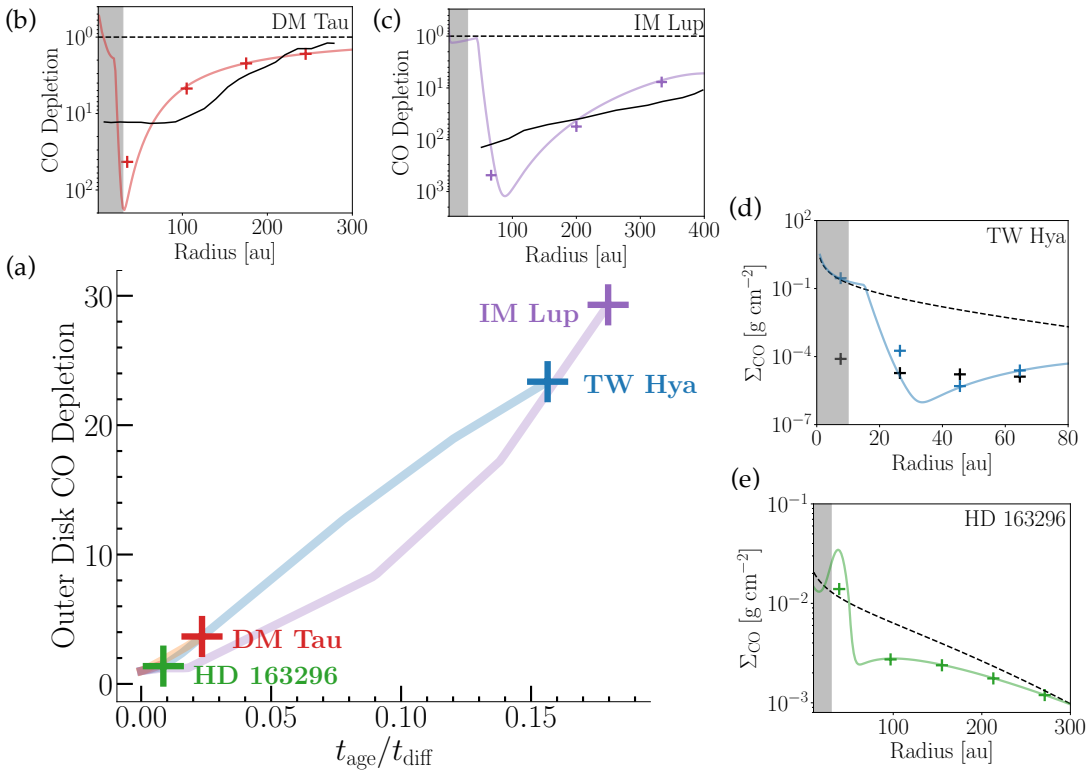


Figure 6.3: The amount of CO gas depletion depends on the disk diffusion timescale: (a) The average CO depletion (see Figure 6.2) exterior to the midplane ice line is a function of the current disk age divided by the disk diffusion timescale. The amount of gaseous CO depletion increases with time (colored lines). For each system we compare our model results (colored lines and crosses indicating the beam-size-convolved value) to the quantity reported in the observational literature (black solid lines or crosses indicating the half-beam separation). The literature reported quantity is either CO surface density or CO depletion (see Figure 6.2). The initial CO gas distribution is also shown (black dashed lines). CO is likely optically thick throughout the vertical extent of the disk for all commonly observed CO isotopologues in the gray shaded region. For a detailed discussion of our model-data comparisons see methods. (b) DM Tau (Zhang et al. 2019; McClure et al. 2016) (c) IM Lup (Zhang et al. 2019) (d) TW Hya (Schwarz et al. 2016), (e) HD 163296: disk-averaged values indicate a lack of CO depletion while higher spatial resolution data show some features(Zhang et al. 2019, 2020a; Williams & McPartland 2016; Booth et al. 2019).

| Disk | Disk Mass [$M_\odot$] | $\alpha$ | Accreted Mass [%] | Inner Gas Mass [%] | Outer Gas Mass [%] | Ice Mass (outer disk) [%] |
|---|---|---|---|---|---|---|
| TW Hya | 0.11 | $8 \times 10^{-4}$ | 51 | 47 | 2 | <1 |
| HD 163296 | 0.21 | $10^{-4}$ | 4 | 16 | 62 | 18 |
| DM Tau | 0.05 | $3 \times 1-^{-3}$ | 14 | 12 | 24 | 50 |
| IM Lup | 0.10 | $1.5 \times 1-^{-2}$ | 69 | 17 | 2 | 12 |

Table 6.1: The bulk disk properties: the total disk mass, turbulent viscosity parameter, and the percentage of Initial CO Mass Located in Solids in the Outer Disk, Gas in the Inner and Outer Disk, and Lost due to Accretion.

## 6.1 Methods

We model the formation of CO ice in a series of vertical one-dimensional (1D) columns for a discrete set of disk semi-major axes. Each vertical disk model starts with an initial population of small grains that are allowed to grow via coagulation and the nucleation and condensation of CO ice. The model is then coupled with a global model of gaseous diffusion and radial dust grain aerodynamics. In particular, we account for accretion onto the star from the disk as well as the release of gaseous CO due to the influx of icy pebbles from the disk's outer regions into its hotter, inner regions.

The primary inputs to our modeling are the total gaseous surface density of the protoplanetary disk, the midplane temperature structure, the age of the system, and the diffusion coefficient that describes the mixing in the system. The diffusion coefficient is treated as a free parameter, as it is not significantly constrained from observations.

### 6.1.1 Non-Equilibrium Ice Formation and Particle Evolution

We model a series of 1D vertical columns separated by 10 au exterior to the midplane CO ice-line with an additional vertical column immediately radially exterior to the midplane ice-line. The results presented in this work do not change when the radial resolution of the models is doubled. At each vertical column we sample the disk density and midplane temperature (for values see the Disk Parameters section) at that location and use these values as inputs in our modeling of vertical particle evolution.

The primary quantities of interest from the modeling of CO ice formation are the extent to which gas can be vertically depleted in the column at a given semi-major

axis, the solid ice to gas ratio, and the resulting size distribution of the particles at that location. To derive these quantities, it is essential to treat ice formation as a non-equilibrium process and to fully resolve the size distribution of particles.

We modify the 1D Community Aerosol and Radiation Model for Atmospheres (CARMA) to simulate the formation of CO ice in the diffuse outer regions of protoplanetary disks. CARMA computes the vertical and size distributions of ice particles by solving the discretized aerosol continuity equation, taking into account particle nucleation (homogeneous and heterogeneous), condensation, evaporation, and coagulation. CARMA uses bins to resolve the particle size distribution, allowing for multiple particle modes to be simulated simultaneously and avoiding the need to parameterize the size distribution using an analytical function. We refer the reader to Powell et al. (2018) and the appendix of Gao et al. (2018) for an additional detailed description of CARMA and its history. We do not consider particle fragmentation or the photodissociation of CO ice. For the regions of the disk where the formation of CO ice occurs (typically beyond ∼10 au), the process of fragmentation is not likely to contribute to the shaping of the particle size distribution assuming reasonable levels of disk turbulence and particle compositions Booth et al. (2019). We do not include the photodissociation of CO ice as all of the ice covered particles in our modeling evaporate quickly once they reach the heated surface layers, which is often several au deeper in the disk than the region that is optically thin to UV photons (see Figure 6.2a). We approximate the UV optical depth using the method described in Krijt et al. (2016) (see their Equation 7).

For each column, we begin with an initial interstellar medium (ISM) abundance

(dust-to-gas mass ratio of $10^{-2}$) of small, $10^{-6}$ cm, grains. This initial grain size is smaller than the $\sim 0.1\mu$m size of a typical ISM grain though this assumption does not affect the resulting particle size distribution. These particles are allowed to coagulate and grow to larger sizes (see appendix section A.3 of Gao et al. (2018) for details of the coagulation scheme) as well as grow via the nucleation and condensation of CO ice. The particle size grid in our modeling is discretized into 72 bins with a mass ratio between successive bins equal to two.

The total solid surface density in a vertical column decreases with time because particles drift radially inwards due to gas drag. Because we do not have a two-dimensional (2D) microphysical model we approximate the time evolution of the column's solid surface density analytically. At early times, the huge influx of particles from the outer disk may lead to a particle surface density given by Lambrechts & Johansen (2014). However, at late times relevant to current observations of disks, we are in a regime where particle growth is limited by drift throughout the radial extent of the disk such that the maximum particle size present at each radial location is given by Powell et al. (2019b):

$$a_{\text{max, drift}}\left(r, t_{\text{disk}}\right) = \frac{\Sigma_g r}{2.5 t_{\text{disk}} \nu_0 \rho_s} \tag{6.2}$$

where $\Sigma_g$ is the disk surface density which varies with semimajor axis, $t_{disk}$ is the current age of the system, $\nu_0$ approximately corresponds to the maximum drift velocity and is defined as $\nu_0 \equiv c_s^2/2v_k$ where $v_k$ is the local Keplerian velocity and $c_s$ is the local gas sound speed, $\rho_s$ is the internal particle density, and $r$ is the orbital distance

in the disk. When particles grow larger than the size in Equation 6.2, we remove them from the column, reflecting the fact that they have drifted inwards.

In addition to removing particles due to drift, we also account for the influx of smaller particles due to particle drift from larger orbital distances at each time-step ($\Delta t$). After particles have grown large enough to experience drift, we calculate the flux of particles into a bin as $F_{\text{drift}} = 2\pi r v_{\text{drift}} \Sigma_g f_d$, where $v_{\text{drift}} = \Sigma_g / \nu_0 \rho_s a_{\text{max, drift}}$ is the particle drift velocity (in the relevant Epstein drag regime) that was used to derive Equation 6.2, and $f_d$ is the solid-to-gas mass ratio (including both refractories and ice) defined just exterior to the radius of interest (r+1 au) and is calculated analytically based on a treatment of particle growth following Powell et al. (2019b) equation 8. We have validated that this approximation for $f_d$ is appropriate because the dust-to-gas ratio calculated using CARMA at each orbital distance closely matches the analytic expression for dust-to-gas ratio described in Powell et al. (2019b) as coagulation is the dominant mode of large particle growth in all of our models. The mass of particles that drift inwards due to drift is calculated as $F_{\text{drift}} \Delta t$. This additional mass is added to the particle bin that is smaller than the maximum particle size bin at that time. We assume that the composition of the drifting particles is equivalent to particles of that size at the given radius.

In each column, the nucleation and condensation of CO are calculated. To adapt CARMA to the diffuse outer regions of protoplanetary disks, we make several common choices for nucleation and condensation following classical nucleation theory. The heterogeneous nucleation process is the dominant formation pathway for CO ice

formation as CO cannot undergo efficient homogeneous nucleation at the low pressures found in the outer regions of protoplanetary disks. Thus, once the initial population of CO ice-free small grains grows to sizes large enough such that nucleation is stable and ice formation can occur, CO nucleates heterogeneously. We treat a particle that has accreted CO as an ice particle unless it evaporates and releases the CO ice back to the gas phase. CARMA tracks the ice fraction of each particle throughout its evolution which enables us to self-consistently calculate mass conservation in our coupled model.

We follow Nachbar et al. (2016) (see their Appendix Section A.1) to calculate the heterogeneous nucleation of CO ice on seed grains using classical nucleation theory, which has been shown to be useful in understanding experiments of the nucleation of $CO_2$ ice in the diffuse regions of Mars's atmosphere and elsewhere. We assume that seed grains are coated by water ice though we note that this assumption primarily determines the density of the seed particles and does not have a significant effect on the formation of CO ice. In this formulation, which includes the Kelvin effect, CO molecules diffuse over a seed particle's surface after impinging upon it until a sufficiently large number of molecules can congregate into a critical cluster, resulting in nucleation. We make the assumption that the nonisothermal coefficient that accounts for the released heat of sublimation during ice growth is unity as the close contact of the forming ice and the seed particle increases the efficiency of heat dissipation for particle seeds larger than a critical cluster size 34. Due to a lack of experiments, we assume that the contact angle between the seed particle and the forming ice is $\sim 90°$. We also assume that the mean jumping distance of a CO molecule is 0.4 (due to a lack of experimental measurements

we take the value for $CO_2$ Wood (1999)).

Once CO has heterogeneously nucleated onto a seed grain, the ice particle can grow by coagulation and/or condensation. The ice particle can also evaporate, be lofted, and/or settle to the midplane. In the scheme treated in this work, once particles coagulate, they are treated as compact grains. While the aggregate or compact nature of grains is unknown, this assumption is reasonable, particularly if condensation processes increase the compactification of particles that form as aggregates. During coagulation, when an ice particle coagulates with a seed grain, the resultant particle is treated as an icy particle. We use a formulation of particle condensation that is applicable in the diffuse outer regions of protoplanetary disks where molecules do not diffuse along a path but instead interact collisionally, such that the change in mass of a particle with time is given by:

$$\frac{dm_p}{dt} = \pi a^2 n m v_{\rm th} \left(1 - \frac{1}{S_{\rm eq}}\right) \tag{6.3}$$

where $m_p$ is the mass of the ice particle, a is the radius of the ice particle, n is the number density of condensible molecules, $m$ is the mass of a vapor molecule, and $v_{\rm th} = (8/\pi)^{1/2} c_s$ is the thermal velocity, and $S_{\rm eq}$ is the saturation ratio over a curved particle surface given by:

$$S_{\rm eq} = \frac{P_{\rm CO}}{P_{\rm sat,eq}\left(a, T\right)}. \tag{6.4}$$

The partial pressure of the CO gas, $P_{\rm CO}$, changes with time and altitude as the system

evolves.

The equilibrium condensate saturation vapor pressure depends on the size of the grain facilitating the phase change as given in Equation 1 in the main text. The saturation vapor pressure for CO is taken from Wylie (1958),

$$P_{\rm sat}\left(T\right) = 1333.2239 \times 10^{(2.4482 - 418.44/T + 4.134\log_{10}\left(T\right) - 0.02599T)} \text{ dynes/cm}^2 \tag{6.5}$$

The growth processes in Equation 6.3 thus include the Kelvin effect through the supersaturation term $S_{\rm eq}$. This formulation is adapted from the Hertz-Knudsen model for particle growth Hill (1966) with a few standard simplifying assumptions. In particular, we set the condensation and evaporation constants to be unity such that all molecules impinging on the ice particle are incorporated into the ice and evaporation is set purely by theoretical arguments and not explicitly benchmarked to laboratory data. We further assume that the ice temperature and background disk temperature are in equilibrium. For a discussion of this formulation and the simplifying assumptions we make see Pathak et al. (2013).

### 6.1.2 Radial Diffusion and Accretion

We couple our microphysical model of non-equilibrium ice formation to a global model of gaseous diffusion. We make several simplifying assumptions in the absence of a spatially 2D microphysical model which is the subject of future work. We assume that the vertical and radial diffusion coefficients are the same at each location in the disk.

The diffusion coefficient, $D$, is set by $D = \alpha c_s H$. The parameter $\alpha$ is a parameter of ignorance (see Shakura & Sunyaev (1973)). The sound speed and disk scale height, $H$, are defined locally at the disk midplane. We divide the disks into two hundred radial bins with an even linear spacing. We note that simulations with double the number of radial bins produce the same results.

As can be seen in Figure 6.1b, CO gas is only abundant in the warm upper layers of the disk which are also the regions accessible to observations (Schwarz et al. 2016). We thus model the radial diffusion of CO gas in the warm molecular layer using the 1D diffusion equation in cylindrical coordinates including radial transport due to accretion. We use a modified forward Euler scheme such that at each grid cell the volume mixing ratio of CO is set by:

$$u_i^{n+1} = g \times [\left(\frac{1}{r_i}\frac{1}{\Delta r^2}\left(r_{i+1/2}D_{i+1/2}\left(u_{i+1}^n - u_i^n\right) - r_{i-1/2}D_{i-1/2}\left(u_i^n - u_{i-1}^n\right)\right)\right) dt + u_i^n + u_{\text{acc, in}} - u_{\text{acc, out}}] \tag{6.6}$$

where $u$ is the volume mixing ratio of CO gas at a given point in our time grid n and radial distance grid $i$. The loss of CO gas due to ice formation outside of the midplane CO ice line is taken into account through the term $g = 1 - (\Delta t/\tau_{\text{vert, diff}})$, which is the fraction of the local vertical diffusion timescale that has occurred over a given time-step. The vertical diffusion timescale is calculated as $\tau_{\text{vert, diff}} = 3H^2/D$ where $H$ is defined at the disk midplane. This treatment of vertical diffusion is validated using our vertical column microphysical modeling.

While both diffusion and accretion are viscous processes that are dictated by the amount of diffusion in the system, we treat them separately because CO gas is diffusively mixed to reduce concentration gradients while also accreting following the accretion flux of the background $H_2$ gas. To calculate the terms $u_{\mathrm{acc,\ in}}$ and $u_{\mathrm{acc,\ out}}$, we thus determine the local accretion fluxes of $H_2$ gas and then multiply these fluxes by the local CO abundance to determine the flux in and out of the radial grid cell. Each of our $H_2$ gaseous surface density profiles are similarity solutions such that we can calculate the flux from accretion through each orbital distance grid cell using the analytic prescription described in Hartmann et al. (1998) (see their Equation 21) which is appropriate for disk surface density profiles of this form. The outer disk boundary condition is set to be a zero radial concentration gradient while the inner disk boundary condition is set to be a zero disk surface density. We note that the boundary condition in the diffusion equation at the inner edge of the disk does not have an effect on our results. To accurately account for the reservoir of solid CO as a function of time we determine the dust-to-gas ratio and ice-to-dust ratio ($f_{\mathrm{i}}$) as a function of time from our microphysical modeling of ice formation and linearly interpolate these values along our radial grid.

Around the midplane CO ice line, we must additionally treat the formation and drift of ice as we radially evolve the gas present in the system because there is significant cycling of particles and gas around this region 41-45. We calculate the location of the midplane ice line as the hottest radial location in the disk where the nominal saturation ratio over a flat surface is equal to unity, i.e. the radius where $P_{\mathrm{CO}}/P_{\mathrm{sat}}\,(T) = 1$ in

the midplane. Particles that drift across the midplane CO ice line quickly lose their ice mantles at a radial region just interior to the midplane ice line due to their small particle sizes (Powell et al. 2017). Cycling occurs because some of the increased abundance of CO gas interior to the ice line will diffuse back outwards across the ice line, due to the steep radial concentration gradient. After gas diffuses across the midplane ice line, it is rapidly incorporated into solid ice due to the relatively short vertical diffusion timescale near the CO ice lines. Once more ice forms, there is again an increase in particle drift and the cycle repeats.

We model the surface density of CO ice immediately exterior to the midplane CO ice line following:

$$f_{\rm ice} = f_{\rm d} f_{\rm i} + f_{\rm accum} \tag{6.7}$$

where $f_{\rm d}$ is the analytic dust-to-gas mass ratio as a function of time described above and $f_i$ is the solid ice fraction from the microphysical modeling also described above. The term $f_{\rm accum}$ accounts for the accumulation of CO ice due to the radial cycling of solids and gas around the ice line. It is calculated as $f_{\rm accum}^{n+1} = f_{\rm accum}^{n} + \Sigma_i/\Sigma_g - \Sigma_l/\Sigma_g$ where $\Sigma_i = (1-g)\, u_i^{n+1} \Sigma_g / g$ is the surface density in ice that has condensed in the last time step, $\Sigma_g$ is the surface density of the background hydrogen gas that evolves with time due to accretion, and $\Sigma_l = 2\pi r_{\rm iceline} v_{\rm drift} \Sigma_i^n$ is the amount of the accumulated ice surface density that has been lost to drift in the last time step. We assume that the majority of the total solid mass is located in the largest particles in the size distribution which is well supported by the results from our microphysical

modeling and from previous works of drift limited particle growth Birnstiel et al. (2012). We calculate the inward flux of icy pebbles at the iceline as:

$$F_{\rm ice} = 2\pi r_{\rm iceline} v_{\rm drift} \Sigma_g f_{\rm ice} \ . \tag{6.8}$$

We add the CO gas mass that drifts through the midplane ice line in a given timestep, $F_{\rm ice}\Delta t$, to the radial bin just interior to the midplane CO ice line. In our models, the cycling of material around the ice line leads to an ice-to-gas ratio immediately exterior to the ice-line that is enhanced with time and a corresponding enhanced abundance of CO gas interior to the CO ice line as found in previous works (Stevenson & Lunine 1988; Cuzzi & Zahnle 2004; Ciesla & Cuzzi 2006; Schoonenberg & Ormel 2017; Booth et al. 2017).

Our simulations differ from those presented in Krijt et al. (2016) and Krijt et al. (2020) as we include the accretion of gaseous CO onto the host star and allow the amount of diffusion present in the system to be a free parameter. We do not include chemical processing of CO as we find that we are able to reproduce observed levels of depletion with CO ice formation alone.

### 6.1.3 Disk Parameters

We derive the total gaseous surface densities for the disks around TW Hya and HD 163296 from previous modeling Powell et al. (2019b) using observations of dust lines. For the disk around HD 163296, we use the surface density shape derived from CO observations. For the disk around DM Tau, which has a mass estimate from HD

observations of warm molecular hydrogen which is one of the relatively direct indicators of disk mass, we normalize the surface density profile from Zhang et al. (2019) (see their Table 4 and Equation 1) such that the total disk gas mass is equal to $4.7 \times 10^{-2}$ $M_{\odot}$ McClure et al. (2016) (the surface density normalization, $\Sigma_c = 0.94$ g cm$^{-2}$). For the disk around IM Lup, which does not yet have observations of a robust tracer of total disk mass, we use the gas surface density profile parameters, namely the surface density index of the gas and the gas critical radius, from Zhang et al. (2019) (see their Table 4 and Equation 1). We then choose a surface density profile normalization ($\Sigma_c = 15$ g cm$^{-2}$) such that the total disk mass falls in the range of masses described in Powell et al. (2019b) though we note that while this choice changes the derived CO mass, it has a minimal effect on the amount of depletion from the original CO abundance which is primarily controlled by diffusion.

We assume our fiducial disk temperature structures, particularly in the outer disk, are controlled by irradiation Chiang & Goldreich (1997) (see Powell et al. (2019b) for more details). Several scale heights above the midplane, the disk is heated by high-energy photons Chiang & Goldreich (1997). We allow surface heating to occur in the disk two scale heights above the midplane such that the disk is isothermal within the first two scale heights $T = T_{\rm mid}\,(r)$. The temperature increases linearly within the third scale height of the disk until $T = 3T_{\rm mid}\,(r)$ and remains at this value beyond this height. This temperature structure is thus comparable to that used in Xu et al. (2017). We note that the exact location of surface layer heating does not impact our results as long as the first scale height remains cool enough for ice formation to occur. This is because

the level of depletion in the disk is sensitive to the saturation vapor pressure at the disk midplane, and thus the temperature at the disk midplane. The vertical density profile is in hydrostatic equilibrium calculated using these temperature profiles. The parameters used for all of the disks modeled in this work are given in the Supplementary information (see Table 6.2).

### 6.1.4 Comparison to Observations

For DM Tau, we compare our beam-convolved model results (red crosses) to the shape of the depletion profile from Zhang et al. (2019) (black line) as shown in Figure 6.3b. We also find agreement with the total level of CO depletion in our models, a factor of 3.7, and the level of depletion reported in McClure et al. (2016) of a factor $\lesssim$5. For IM Lup, we compare our beam-convolved model results (purple crosses) to the shape of the depletion profiles from Zhang et al. (2019) (black line) as shown in Figure 6.3c.

For TW Hya, shown in 3d, we compare our beam-convolved model results (blue crosses) to observations from Schwarz et al. (2016) who report the observed CO surface density (black crosses). Our results also agree with the similar CO column density profile presented in Huang et al. (2018a). In addition, we also compare the shape of the CO depletion profile to the shape of the gaseous CO depletion profile presented in Zhang et al. (2019) (see their figure 8). We derive a similar profile shape with a dramatic increase in CO depletion at $\sim$20 au and a slightly reduced level of depletion exterior to this radius until the background gas disk itself becomes diffuse and truncated.

For HD 163296, shown in Figure 6.3e, we compare our beam-convolved model-

ing results (green crosses) to observations from Williams & McPartland (2016) (equivalent to the dashed black line). Our results show an overall lack of significant gas phase CO depletion though we do derive structures in the CO surface density profile. This is in agreement with the lack of disk integrated gaseous CO depletion derived in Booth et al. (2019) using $^{13}C^{17}O$, a rare, optically thin CO isotopologue. Both Booth et al. (2019) and Zhang et al. (2019) show a drop off in CO abundance at either ∼150 au or ∼70 au. Using our fiducial disk temperature profile, we find a drop off in CO abundance at ∼ 80 au, although the exact location is sensitive to the assumed disk midplane temperature structure. Our modeling for this disk is in agreement with results presented in Zhang et al. (2020a) which show an enhancement in CO abundance interior to the midplane ice line.

HD 163296, DM Tau, and IM Lup are likely to have optically thick CO emission out to at least ∼30 au for all commonly observed isotopologues of CO such that the observed abundance or depletion factor in this region is uncertain Zhang et al. (2019). For TW Hya, gaseous CO becomes optically thick interior to 10 au, even for rare isotopologues like $C^{18}O$ (Aikawa et al. 1996). In this region, the temperature structure is also uncertain Schwarz et al. (2016), which causes the observed amount of CO in this region to be uncertain. We mark these uncertain regions in Figure 6.3b-e in gray.

## 6.2 Supplementary Materials

In Figure 6.4 we describe the processes that shape the observed abundance of CO in protoplanetary disks. In Table 6.2 we describe the model parameters used to

model the four disks in our sample. In Table 6.3 we describe the material properties of CO used in our microphysical ice formation modeling.

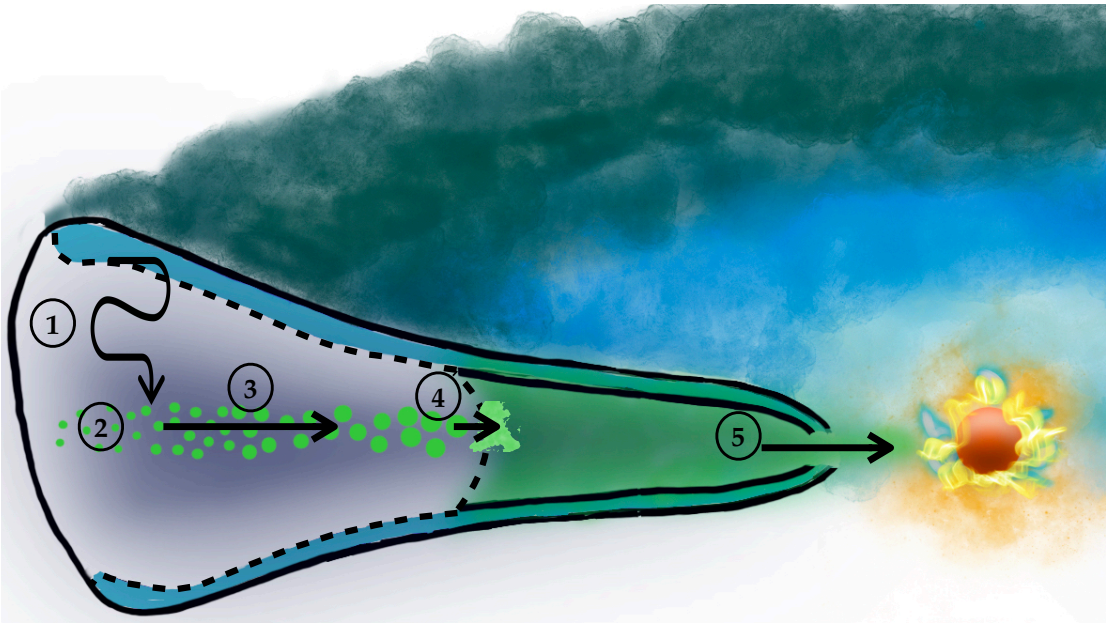


Figure 6.4: The evolution of CO in protoplanetary disks: 1. CO gas is mixed down to the disk midplane and depleted in the warm molecular layer (turquoise shaded region) above the surface ice line (black dashed line); 2. efficient ice formation sequesters CO in solids (green circles); 3. large ice coated particles drift inwards towards the host star; 4. particles lose their volatile ice content (light green shaded region) once they drift past the midplane CO ice line (black dashed line); 5. an enhanced abundance of gaseous CO (green shaded region) is accreted onto the host star.

| Disk | $T_0$ [at 1 au] | Midplane Ice Line | Disk outer radius | System Age | Stellar Mass |
|---|---|---|---|---|---|
| TW Hya | 82 K | 16 au | 80 au | 5 Myr | 0.8 $M_\odot$ |
| HD 163296 | 120 K | 44 au | 350 au | 5 Myr | 2.3 $M_\odot$ |
| DM Tau | 70 K | 19 au | 310 au | 1 Myr | 0.7 $M_\odot$ |
| IM Lup | 116 K | 45 au | 390 au | 1 Myr | 0.9 $M_\odot$ |

Table 6.2: Disk Model Parameters

| Property | Value |
|---|---|
| Surface energy | $27.77(1 - T[K]/132.92)^{1.126}$ Sprow & Prausnitz (1966) |
| Desorption energy ($F_{\text{des}}$) | 850 K Aikawa et al. (1996) |
| Condensed Density | 0.789 g/cm$^3$ (liquid) |
| Vibrational Frequency | $1.6 \times 10^{11} \sqrt{F_{\text{des}}/m_{\text{molecular, CO}}}$ |

Table 6.3: CO Material Properties

# Bibliography


Ackerman, A. S., & Marley, M. S. 2001, ApJ, 556, 872

Aikawa, Y., Miyama, S. M., Nakano, T., & Umebayashi, T. 1996, ApJ, 467, 684

Alexander, R. D., Clarke, C. J., & Pringle, J. E. 2006, MNRAS, 369, 216

ALMA Partnership, Brogan, C. L., Pérez, L. M., et al. 2015, ApJ, 808, L3

Andrews, S. M. 2020, Annual Review of Astronomy and Astrophysics, 58, null

Andrews, S. M., Hughes, A. M., Wilner, D. J., & Qi, C. 2008, ApJ, 678, L133

Andrews, S. M., Rosenfeld, K. A., Kraus, A. L., & Wilner, D. J. 2013, ApJ, 771, 129

Andrews, S. M., Rosenfeld, K. A., Wilner, D. J., & Bremer, M. 2011, ApJ, 742, L5

Andrews, S. M., & Williams, J. P. 2005, ApJ, 631, 1134

Andrews, S. M., Wilner, D. J., Hughes, A. M., Qi, C., & Dullemond, C. P. 2009, ApJ, 700, 1502

—. 2010, ApJ, 723, 1241

Andrews, S. M., Wilner, D. J., Hughes, A. M., et al. 2012, ApJ, 744, 162

Andrews, S. M., Wilner, D. J., Zhu, Z., et al. 2016, ApJ, 820, L40

Andrews, S. M., Huang, J., Pérez, L. M., et al. 2018, The Astrophysical Journal Letters, 869, L41

Ansdell, M., Williams, J. P., van der Marel, N., et al. 2016, ApJ, 828, 46

Apai, D., Rackham, B. V., Giampapa, M. S., et al. 2018, arXiv e-prints, arXiv:1803.08708

Armitage, P. J., Livio, M., & Pringle, J. E. 2001, MNRAS, 324, 705

Arras, P., & Socrates, A. 2010, ApJ, 714, 1

Bai, X.-N., & Goodman, J. 2009, ApJ, 701, 737

Banzatti, A., Testi, L., Isella, A., et al. 2011, A&A, 525, A12

Bardeen, C. G., Toon, O. B., Jensen, E. J., et al. 2010, Journal of Geophysical Research: Atmospheres, 115, n/a, d10204

Bardeen, C. G., Toon, O. B., Jensen, E. J., Marsh, D. R., & Harvey, V. L. 2008, Journal of Geophysical Research: Atmospheres, 113, n/a, d17202

Barman, T. S., Konopacky, Q. M., Macintosh, B., & Marois, C. 2015, ApJ, 804, 61

Barrado Y Navascués, D. 2006, A&A, 459, 511

Barstow, J. K., Aigrain, S., Irwin, P. G. J., & Sing, D. K. 2017, ApJ, 834, 50

Barth, E. L., & Toon, O. B. 2003, Icarus, 162, 94

—. 2004, Geophys. Res. Lett., 31, L17S07

—. 2006, Icarus, 182, 230

Batalha, N. E., Mandell, A., Pontoppidan, K., et al. 2017, PASP, 129, 064501

Batygin, K., & Stevenson, D. J. 2010, ApJ, 714, L238

Beckwith, S. V. W., Henning, T., & Nakagawa, Y. 2000, Protostars and Planets IV, 533

Beckwith, S. V. W., & Sargent, A. I. 1991, ApJ, 381, 250

Benneke, B. 2015, ArXiv e-prints, arXiv:1504.07655

Benneke, B., Knutson, H. A., Lothringer, J., et al. 2019, Nature Astronomy, 377

Bergin, E. A., Cleeves, L. I., Gorti, U., et al. 2013, Nature, 493, 644

Bertout, C., Siess, L., & Cabrit, S. 2007, A&A, 473, L21

Birnstiel, T., & Andrews, S. M. 2014, ApJ, 780, 153

Birnstiel, T., Andrews, S. M., Pinilla, P., & Kama, M. 2015, ApJ, 813, L14

Birnstiel, T., Klahr, H., & Ercolano, B. 2012, A&A, 539, A148

Birnstiel, T., Dullemond, C. P., Zhu, Z., et al. 2018, ApJ, 869, L45

Bixel, A., Rackham, B. V., Apai, D., et al. 2019, AJ, 157, 68

Blecic, J., Harrington, J., Madhusudhan, N., et al. 2014, ApJ, 781, 116

Blevins, S. M., Pontoppidan, K. M., Banzatti, A., et al. 2016, ApJ, 818, 22

Bogdan, A. 2018, The Journal of Physical Chemistry A, 122, 7777

Bohren, C. F., & Huffman, D. R. 1983, Absorption and scattering of light by small particles,

Bolis, V. 2013, Fundamentals in Adsorption at the Solid-Gas Interface. Concepts and Thermodynamics, 3

Booth, A. S., Walsh, C., Ilee, J. D., et al. 2019, ApJL, 882, L31

Booth, R. A., Clarke, C. J., Madhusudhan, N., & Ilee, J. D. 2017, MNRAS, 469, 3994

Brauer, F., Dullemond, C. P., Johansen, A., et al. 2007, A&A, 469, 1169

Brickhouse, N. S., Cranmer, S. R., Dupree, A. K., et al. 2012, ApJ, 760, L21

Brown, T. M., Charbonneau, D., Gilliland, R. L., Noyes, R. W., & Burrows, A. 2001, ApJ, 552, 699

Bruderer, S., van Dishoeck, E. F., Doty, S. D., & Herczeg, G. J. 2012, A&A, 541, A91

Buchner, J. 2016, PyMultiNest: Python interface for MultiNest, Astrophysics Source Code Library, ascl:1606.005

Burgasser, A. J., Vrba, F. J., Lépine, S., et al. 2008, ApJ, 672, 1159

Burrows, A., Hubeny, I., Budaj, J., & Hubbard, W. B. 2007a, ApJ, 661, 502

Burrows, A., Hubeny, I., Budaj, J., Knutson, H. A., & Charbonneau, D. 2007b, ApJ, 668, L171

Burrows, A., & Sharp, C. M. 1999, ApJ, 512, 843

Caldas, A., Leconte, J., Selsis, F., et al. 2019, A&A, 623, A161

Calvet, N., D'Alessio, P., Hartmann, L., et al. 2002, ApJ, 568, 1008

Carbary, J. F., Morrison, D., & Romick, G. J. 2004, Geophys. Res. Lett., 31, L13108

Carney, M. T., Fedele, D., Hogerheijde, M. R., et al. 2018, A&A, 614, A106

Chabrier, G., & Baraffe, I. 2007, ApJ, 661, L81

Chapillon, E., Guilloteau, S., Dutrey, A., & Piétu, V. 2008, A&A, 488, 565

Chapillon, E., Parise, B., Guilloteau, S., Dutrey, A., & Wakelam, V. 2010, A&A, 520, A61

Charnay, B., Meadows, V., & Leconte, J. 2015, ApJ, 813, 15

Chiang, E., & Laughlin, G. 2013, MNRAS, 431, 3444

Chiang, E., & Murray-Clay, R. 2007, Nature Physics, 3, 604

Chiang, E., & Youdin, A. N. 2010, Annual Review of Earth and Planetary Sciences, 38, 493

Chiang, E. I., & Goldreich, P. 1997, ApJ, 490, 368

Ciesla, F. J., & Cuzzi, J. N. 2006, Icarus, 181, 178

Cleeves, L. I., Bergin, E. A., Qi, C., Adams, F. C., & Öberg, K. I. 2015, ApJ, 799, 204

Colaprete, A., Toon, O. B., & Magalhães, J. A. 1999, J. Geophys. Res., 104, 9043

Cox, E. G., Harris, R. J., Looney, L. W., et al. 2017, ApJ, 851, 83

Crossfield, I. J. M., Barman, T., Hansen, B. M. S., & Howard, A. W. 2013, A&A, 559, A33

Crossfield, I. J. M., & Kreidberg, L. 2017, AJ, 154, 261

Cushing, M. C., Roellig, T. L., Marley, M. S., et al. 2006, ApJ, 648, 614

Cuzzi, J. N., & Zahnle, K. J. 2004, ApJ, 614, 490

D'Alessio, P., Calvet, N., & Hartmann, L. 2001, ApJ, 553, 321

D'Alessio, P., Calvet, N., Hartmann, L., Franco-Hernández, R., & Servín, H. 2006, ApJ, 638, 314

Dang, L., Cowan, N. B., Schwartz, J. C., et al. 2018, Nature Astronomy, 2, 220

D'Angelo, G., Weidenschilling, S. J., Lissauer, J. J., & Bodenheimer, P. 2014, Icarus, 241, 298

Dartois, E., Dutrey, A., & Guilloteau, S. 2003, A&A, 399, 773

de Gregorio-Monsalvo, I., Ménard, F., Dent, W., et al. 2013, A&A, 557, A133

de Leeuw, N. H., Parker, S. C., Catlow, C. R. A., & Price, G. D. 2000, Physics and Chemistry of Minerals, 27, 332

Debes, J. H., Jang-Condell, H., Weinberger, A. J., Roberge, A., & Schneider, G. 2013, ApJ, 771, 45

Deming, D., Wilkins, A., McCullough, P., et al. 2013, ApJ, 774, 95

Demory, B.-O., de Wit, J., Lewis, N., et al. 2013, ApJ, 776, L25

Dobbs-Dixon, I., Agol, E., & Burrows, A. 2012, ApJ, 751, 87

Dodson-Robinson, S. E., & Bodenheimer, P. 2010, Icarus, 207, 491

Dodson-Robinson, S. E., Evans, II, N. J., Ramos, A., Yu, M., & Willacy, K. 2018, ApJ, 868, L37

Dohnanyi, J. S. 1969, J. Geophys. Res., 74, 2531

Dorschner, J., Begemann, B., Henning, T., Jaeger, C., & Mutschke, H. 1995, A&A, 300, 503

Du, F., Bergin, E. A., & Hogerheijde, M. R. 2015, ApJ, 807, L32

Duan, Y., Petters, M. D., & Barros, A. P. 2019, Atmospheric Chemistry and Physics, 19, 1413

Dullemond, C. P., Henning, T., Visser, R., et al. 2007, A&A, 473, 457

Dutrey, A., Guilloteau, S., & Simon, M. 2003, A&A, 402, 1003

Ebert, E. E., & Curry, J. A. 1992, Journal of Geophysical Research: Atmospheres, 97, 3831

Egan, W. G., & Hilgeman, T. 1975, AJ, 80, 587

Eisner, J. A. 2015, ApJ, 803, L4

Evans, T. M., Sing, D. K., Wakeford, H. R., et al. 2016, ApJ, 822, L4

Fan, J., Zhang, R., Li, G., Tao, W.-K., & Li, X. 2007, Journal of Geophysical Research: Atmospheres, 112

Favre, C., Cleeves, L. I., Bergin, E. A., Qi, C., & Blake, G. A. 2013, ApJ, 776, L38

Fedele, D., Tazzari, M., Booth, R., et al. 2018, A&A, 610, A24

Feng, Y. K., Line, M. R., Fortney, J. J., et al. 2016, ApJ, 829, 52

Foreman-Mackey, D., Hogg, D. W., Lang, D., & Goodman, J. 2013, PASP, 125, 306

Fortney, J. J. 2005a, MNRAS, 364, 649

—. 2005b, MNRAS, 910

Fortney, J. J., Lodders, K., Marley, M. S., & Freedman, R. S. 2008, ApJ, 678, 1419

Fraine, J. D., Deming, D., Gillon, M., et al. 2013, ApJ, 765, 127

Fu, G., Deming, D., Knutson, H., et al. 2017, ApJ, 847, L22

Fukui, A., Kawashima, Y., Ikoma, M., et al. 2014, ApJ, 790, 108

Gaia Collaboration, Brown, A. G. A., Vallenari, A., et al. 2018, A&A, 616, A1

Gao, P., & Benneke, B. 2018, ApJ, 863, 165

Gao, P., Marley, M. S., & Ackerman, A. S. 2018, The Astrophysical Journal, 855, 86

Gao, P., & Powell, D. 2021, submitted to ApJ

Gao, P., Zhang, X., Crisp, D., Bardeen, C. G., & Yung, Y. L. 2014, Icarus, 231, 83

Gao, P., Fan, S., Wong, M. L., et al. 2017, Icarus, 287, 116

Gao, P., Thorngren, D. P., Lee, G. K. H., et al. 2020, Nature Astronomy, 4, 951

Garufi, A., Podio, L., Kamp, I., et al. 2014, A&A, 567, A141

Gibson, N. P., Aigrain, S., Barstow, J. K., et al. 2013, MNRAS, 436, 2974

Gibson, N. P., Aigrain, S., Pont, F., et al. 2012, MNRAS, 422, 753

Ginzburg, S., & Sari, R. 2015, ApJ, 803, 111

Ginzburg, S., Schlichting, H. E., & Sari, R. 2016, ApJ, 825, 29

Goodman, A. A., Pineda, J. E., & Schnee, S. L. 2009, ApJ, 692, 91

Goodman, J., & Weare, J. 2010, Communications in Applied Mathematics and Computational Science, Vol. 5, No. 1, p. 65-80, 2010, 5, 65

Greene, T. P., Chu, L., Egami, E., et al. 2016, in Proc. SPIE, Vol. 9904, Space Telescopes and Instrumentation 2016: Optical, Infrared, and Millimeter Wave, 99040E

Greenwood, G. W., Greer, A. L., Herlach, D. M., Kelton, K. F., & Cantor, B. 2003, Philosophical Transactions of the Royal Society of London. Series A: Mathematical, Physical and Engineering Sciences, 361, 409

Guidi, G., Tazzari, M., Testi, L., et al. 2016, A&A, 588, A112

Guillot, T., & Gautier, D. 2014, ArXiv e-prints, arXiv:1405.3752

Guillot, T., & Showman, A. P. 2002, A&A, 385, 156

Guilloteau, S., Dutrey, A., Piétu, V., & Boehler, Y. 2011, A&A, 529, A105

Guilloteau, S., Simon, M., Piétu, V., et al. 2014, A&A, 567, A117

Guzmán, V. V., Huang, J., Andrews, S. M., et al. 2018, ApJ, 869, L48

Han, Q., Zeng, J., Kuo, K.-S., Chen, H., & Smith, E. 2005, Geophysical Research Letters, 32, n/a, l13818

Hartmann, L., Calvet, N., Gullbring, E., & D'Alessio, P. 1998, ApJ, 495, 385

Hayashi, C. 1981, Progress of Theoretical Physics Supplement, 70, 35

Haynes, K., Mandell, A. M., Madhusudhan, N., Deming, D., & Knutson, H. 2015, ApJ, 806, 146

Hein Bertelsen, R. P., Kamp, I., van der Plas, G., et al. 2016, MNRAS, 458, 1466

Helling, C., Dehn, M., Woitke, P., & Hauschildt, P. H. 2008a, ApJ, 675, L105

Helling, C., Gourbin, P., Woitke, P., & Parmentier, V. 2019a, A&A, 626, A133

Helling, C., Klein, R., Woitke, P., Nowak, U., & Sedlmayr, E. 2004, A&A, 423, 657

Helling, C., Oevermann, M., Lüttke, M. J. H., Klein, R., & Sedlmayr, E. 2001, A&A,

376, 194

Helling, C., & Woitke, P. 2006, A&A, 455, 325

Helling, C., Woitke, P., & Thi, W.-F. 2008b, A&A, 485, 547

Helling, C., , G., Dobbs-Dixon, I., et al. 2016, MNRAS, 460, 855

Helling, C., Iro, N., Corrales, L., et al. 2019b, arXiv e-prints, arXiv:1906.08127

Heng, K. 2016, ApJ, 826, L16

Heng, K., Hayek, W., Pont, F., & Sing, D. K. 2012, MNRAS, 420, 20

Henning, T., & Stognienko, R. 1996, A&A, 311, 291

Herbig, G. H., & Bell, K. R. 1988,

Hildebrand, R. H. 1983, QJRAS, 24, 267

Hill, R. 1966, Nature, 210, 512

Hogerheijde, M. R., Bekkers, D., Pinilla, P., et al. 2016, A&A, 586, A99

Hollenbach, D., Kaufman, M. J., Bergin, E. A., & Melnick, G. J. 2009, ApJ, 690, 1497

Hu, R., Demory, B.-O., Seager, S., Lewis, N., & Showman, A. P. 2015, ApJ, 802, 51

Huang, J., Öberg, K. I., & Andrews, S. M. 2016, ApJ, 823, L18

Huang, J., Andrews, S. M., Cleeves, L. I., et al. 2018a, ApJj, 852, 122

Huang, J., Andrews, S. M., Pérez, L. M., et al. 2018b, arXiv e-prints, arXiv:1812.04193

Hubbard, W. B., Fortney, J. J., Lunine, J. I., et al. 2001, ApJ, 560, 413

Hubickyj, O., Bodenheimer, P., & Lissauer, J. J. 2005, Icarus, 179, 415

Hughes, A. L. H., & Armitage, P. J. 2012, MNRAS, 423, 389

Hughes, A. M., Wilner, D. J., Andrews, S. M., Qi, C., & Hogerheijde, M. R. 2011a, ApJ, 727, 85

Hughes, A. M., Wilner, D. J., Andrews, S. M., et al. 2011b, ApJ, 740, 38

Hughes, A. M., Wilner, D. J., Qi, C., & Hogerheijde, M. R. 2008, ApJ, 678, 1119

Hughes, A. M., Andrews, S. M., Wilner, D. J., et al. 2010, AJ, 140, 887

Imara, N. 2015, ApJ, 803, 38

Inamdar, N. K., & Schlichting, H. E. 2015, MNRAS, 448, 1751

—. 2016, ApJ, 817, L13

Isella, A., Carpenter, J. M., & Sargent, A. I. 2009, ApJ, 701, 260

—. 2010, ApJ, 714, 1746

Isella, A., Testi, L., Natta, A., et al. 2007, A&A, 469, 213

Isella, A., Guidi, G., Testi, L., et al. 2016, Physical Review Letters, 117, 251101

Isella, A., Huang, J., Andrews, S. M., et al. 2018, The Astrophysical Journal Letters, 869, L49

Isella, A., Huang, J., Andrews, S. M., et al. 2018, arXiv e-prints, arXiv:1812.04047

Iyer, A. R., Swain, M. R., Zellem, R. T., et al. 2016, ApJ, 823, 109

Jacobson, M. Z., Turco, R. P., Jensen, E. J., & Toon, O. B. 1994, Atmospheric Environment, 28, 1327

Jensen, E. J., & Ackerman, A. S. 2006, Geophysical Research Letters, 33, n/a, l08802

Jones, E., Oliphant, T., Peterson, P., et al. 2001, [Online; accessed ¡today¿]

Jones, M. G., Pringle, J. E., & Alexander, R. D. 2012, MNRAS, 419, 925

Jordán, A., Espinoza, N., Rabus, M., et al. 2013, ApJ, 778, 184

Kama, M., Bruderer, S., Carney, M., et al. 2016a, A&A, 588, A108

Kama, M., Bruderer, S., van Dishoeck, E. F., et al. 2016b, A&A, 592, A83

Kamp, I., Thi, W.-F., Meeus, G., et al. 2013, A&A, 559, A24

Kangarloo, H. 2010a, ICMEE2010, 2nd Int. Conf.

—. 2010b, ICMEE2010, 2nd Int. Conf.

Kataoka, A., Okuzumi, S., Tanaka, H., & Nomura, H. 2014, A&A, 568, A42

Kataoka, A., Tanaka, H., Okuzumi, S., & Wada, K. 2013a, A&A, 557, L4

—. 2013b, A&A, 554, A4

Kempton, E. M. R., Bean, J. L., & Parmentier, V. 2017a, ApJ, 845, L20

Kempton, E. M. R., Lupu, R., Owusu-Asare, A., Slough, P., & Cale, B. 2017b, PASP, 129, 044402

Kim, H., Jeremy Cho, H.-J., Narayanan, S., et al. 2016, Scientific Reports, 6, 19097

Kipping, D. M. 2013, MNRAS, 435, 2152

Kirk, J., Wheatley, P. J., Louden, T., et al. 2017, MNRAS, 468, 3907

Knutson, H. A., Benneke, B., Deming, D., & Homeier, D. 2014a, Nature, 505, 66

Knutson, H. A., Dragomir, D., Kreidberg, L., et al. 2014b, ApJ, 794, 155

Koll, D. D. B., & Komacek, T. D. 2018, The Astrophysical Journal, 853, 133

Komacek, T. D., & Showman, A. P. 2016, ApJ, 821, 16

Komacek, T. D., Showman, A. P., & Parmentier, V. 2019, The Astrophysical Journal, 881, 152

Komacek, T. D., & Youdin, A. N. 2017, ApJ, 844, 94

Konopacky, Q. M., Barman, T. S., Macintosh, B. A., & Marois, C. 2013, Science, 339, 1398

Korolev, A. V. 1994, Atmospheric Research, 32, 143

Kratter, K. M., Matzner, C. D., Krumholz, M. R., & Klein, R. I. 2010, ApJ, 708, 1585

Kreidberg, L., Bean, J. L., Désert, J.-M., et al. 2014a, ApJ, 793, L27

—. 2014b, Nature, 505, 69

Krijt, S., Bosman, A. D., Zhang, K., et al. 2020, arXiv e-prints, arXiv:2007.09517

Krijt, S., Ciesla, F. J., & Bergin, E. A. 2016, ApJ, 833, 285

Lacy, J. H., Knacke, R., Geballe, T. R., & Tokunaga, A. T. 1994, ApJ, 428, L69

Lambrechts, M., & Johansen, A. 2014, A&A, 572, A107

Lauer, T. R., Ajhar, E. A., Byun, Y.-I., et al. 1995, AJ, 110, 2622

Lavie, B., Mendonça, J. M., Mordasini, C., et al. 2017, AJ, 154, 91

Lavvas, P., Griffith, C. A., & Yelle, R. V. 2011, Icarus, 215, 732

Lavvas, P., & Koskinen, T. 2017, ApJ, 847, 32

Lavvas, P., Yelle, R. V., & Griffith, C. A. 2010, Icarus, 210, 832

Lecavelier Des Etangs, A., Pont, F., Vidal-Madjar, A., & Sing, D. 2008, A&A, 481, L83

Lee, G., Dobbs-Dixon, I., Helling, C., Bognar, K., & Woitke, P. 2016, A&A, 594, A48

Lee, G., Helling, C., Dobbs-Dixon, I., & Juncher, D. 2015a, A&A, 580, A12

Lee, G., Helling, C., Giles, H., & Bromley, S. T. 2015b, A&A, 575, A11

Lee, G. K. H., Blecic, J., & Helling, C. 2018, A&A, 614, A126

Lee, G. K. H., Taylor, J., Grimm, S. L., et al. 2019, MNRAS, 487, 2082

Lee, G. K. H., Wood, K., Dobbs-Dixon, I., Rice, A., & Helling, C. 2017, A&A, 601, A22

Lin, D. N. C., & Papaloizou, J. 1986, ApJ, 307, 395

Line, M. R., Knutson, H., Deming, D., Wilkins, A., & Desert, J.-M. 2013, ApJ, 778, 183

Line, M. R., & Parmentier, V. 2016, ApJ, 820, 78

Lines, S., Mayne, N. J., Manners, J., et al. 2019, Monthly Notices of the Royal Astronomical Society, 488, 1332

Lines, S., Mayne, N. J., Boutle, I. A., et al. 2018, A&A, 615, A97

Linsky, J. L. 1998, Space Sci. Rev., 84, 285

Lissauer, J. J., Hubickyj, O., D'Angelo, G., & Bodenheimer, P. 2009, Icarus, 199, 338

Lodders, K. 2002, ApJ, 577, 974

—. 2003, ApJ, 591, 1220

Long, F., Herczeg, G. J., Pascucci, I., et al. 2017, ApJ, 844, 99

Looper, D. L., Kirkpatrick, J. D., Cutri, R. M., et al. 2008, ApJ, 686, 528

Lorén-Aguilar, P., & Bate, M. R. 2016, MNRAS, 457, L54

Louden, T., & Kreidberg, L. 2018, MNRAS, 477, 2613

Louden, T., & Wheatley, P. 2019, in prep

Louden, T., & Wheatley, P. J. 2015, The Astrophysical Journal Letters, 814, L24

Louden, T., Wheatley, P. J., Irwin, P. G. J., Kirk, J., & Skillen, I. 2017, MNRAS, 470, 742

Lynden-Bell, D., & Pringle, J. E. 1974, MNRAS, 168, 603

MacDonald, R. J., & Madhusudhan, N. 2017, MNRAS, 469, 1979

MacGregor, M. A., Wilner, D. J., Andrews, S. M., & Hughes, A. M. 2015a, ApJ, 801, 59

MacGregor, M. A., Wilner, D. J., Andrews, S. M., Lestrade, J.-F., & Maddison, S. 2015b, ApJ, 809, 47

MacGregor, M. A., Wilner, D. J., Rosenfeld, K. A., et al. 2013, ApJ, 762, L21

Mackebrandt, F., Mallonn, M., Ohlert, J. M., et al. 2017, A&A, 608, A26

Mallonn, M., & Strassmeier, K. G. 2016, A&A, 590, A100

Mallonn, M., Bernt, I., Herrero, E., et al. 2016, MNRAS, 463, 604

Mamajek, E. E. 2005, ApJ, 634, 1385

Mamajek, E. E. 2009, in American Institute of Physics Conference Series, Vol. 1158, American Institute of Physics Conference Series, ed. T. Usuda, M. Tamura, & M. Ishii, 3–10

Manara, C. F., Morbidelli, A., & Guillot, T. 2018, A&A, 618, L3

Manara, C. F., Rosotti, G., Testi, L., et al. 2016, A&A, 591, L3

Mandell, A. M., Haynes, K., Sinukoff, E., et al. 2013, ApJ, 779, 128

Marcus, P. S., Pei, S., Jiang, C.-H., et al. 2015, ApJ, 808, 87

Marley, M. S., & McKay, C. P. 1999, Icarus, 138, 268

Marley, M. S., Saumon, D., Cushing, M., et al. 2012, ApJ, 754, 135

Matsumura, S., Pudritz, R. E., & Thommes, E. W. 2009, ApJ, 691, 1764

Mauney, C., & Lazzati, D. 2018, ArXiv e-prints, arXiv:1803.04323

May, E. M., Zhao, M., Haidar, M., Rauscher, E., & Monnier, J. D. 2018, AJ, 156, 122

McClure, M. K., Bergin, E. A., Cleeves, L. I., et al. 2016, ApJ, 831, 167

McCullough, P. R., Crouzet, N., Deming, D., & Madhusudhan, N. 2014, ApJ, 791, 55

McMullin, J. P., Waters, B., Schiebel, D., Young, W., & Golap, K. 2007, in Astronomical Society of the Pacific Conference Series, Vol. 376, Astronomical Data Analysis Software and Systems XVI, ed. R. A. Shaw, F. Hill, & D. J. Bell, 127

Mendonça, J. M., Malik, M., Demory, B.-O., & Heng, K. 2018, AJ, 155, 150

Menu, J., van Boekel, R., Henning, T., et al. 2014, A&A, 564, A93

Michelangeli, D. V., Toon, O. B., Haberle, R. M., & Pollack, J. B. 1993, Icarus, 102, 261

Miller, N., Fortney, J. J., & Jackson, B. 2009, ApJ, 702, 1413

Miotello, A., van Dishoeck, E. F., Williams, J. P., et al. 2017, A&A, 599, A113

Montesinos, B., Eiroa, C., Mora, A., & Merín, B. 2009, A&A, 495, 901

Morley, C. V., Fortney, J. J., Kempton, E. M.-R., et al. 2013, ApJ, 775, 33

Morley, C. V., Fortney, J. J., Marley, M. S., et al. 2012, ApJ, 756, 172

—. 2015, ApJ, 815, 110

Morley, C. V., Kreidberg, L., Rustamkulov, Z., Robinson, T., & Fortney, J. J. 2017, ApJ, 850, 121

Mundy, L. G., Looney, L. W., Erickson, W., et al. 1996, ApJ, 464, L169

Nachbar, M., Duft, D., Mangan, T. P., et al. 2016, Journal of Geophysical Research: Planets, 121, 753

Najita, J. R., Strom, S. E., & Muzerolle, J. 2007, MNRAS, 378, 369

Natta, A., & Testi, L. 2004, in Astronomical Society of the Pacific Conference Series, Vol. 323, Star Formation in the Interstellar Medium: In Honor of David Hollenbach, ed. D. Johnstone, F. C. Adams, D. N. C. Lin, D. A. Neufeeld, & E. C. Ostriker, 279

Natta, A., Testi, L., Neri, R., Shepherd, D. S., & Wilner, D. J. 2004, A&A, 416, 179

Natta, A., Testi, L., & Randich, S. 2006, A&A, 452, 245

Nomura, H., Tsukagoshi, T., Kawabe, R., et al. 2016, ApJ, 819, L7

Öberg, K. I., Murray-Clay, R., & Bergin, E. A. 2011, ApJ, 743, L16

Okuzumi, S., Tanaka, H., Kobayashi, H., & Wada, K. 2012, ApJ, 752, 106

Ormel, C. W., & Cuzzi, J. N. 2007, A&A, 466, 413

Ormel, C. W., & Kobayashi, H. 2012, ApJ, 747, 115

Oshagh, M., Santos, N. C., Ehrenreich, D., et al. 2014, A&A, 568, A99

Owens, D. K. J., & Wendt, R. 1969, Journal of Applied Polymer Science, 13, 1741

Papaloizou, J. C. B., & Nelson, R. P. 2005, A&A, 433, 247

Parmentier, V., & Crossfield, I. J. M. 2018, Exoplanet Phase Curves: Observations and Theory, 116

Parmentier, V., Fortney, J. J., Showman, A. P., Morley, C., & Marley, M. S. 2016, ApJ, 828, 22

Parmentier, V., Fortney, J. J., Showman, A. P., Morley, C., & Marley, M. S. 2016, The Astrophysical Journal, 828, 22

Parmentier, V., Guillot, T., Fortney, J. J., & Marley, M. S. 2015, A&A, 574, A35

Parmentier, V., Powell, D., & Zhang, X. 2019, in prep

Parmentier, V., Showman, A. P., & Lian, Y. 2013, A&A, 558, A91

Parmentier, V., Showman, A. P., & Lian, Y. 2013, Astronomy & Astrophysics, 558, A91

Parviainen, H., & Aigrain, S. 2015, MNRAS, 453, 3821

Pascucci, I., Testi, L., Herczeg, G. J., et al. 2016, ApJ, 831, 125

Pathak, H., Mullick, K., Tanimura, S., & Wyslouzil, B. E. 2013, Aerosol Science and Technology, 47, 1310

Pecaut, M. J., Mamajek, E. E., & Bubar, E. J. 2012, ApJ, 746, 154

Pérez, L. M., Carpenter, J. M., Chandler, C. J., et al. 2012, ApJ, 760, L17

Pérez, L. M., Chandler, C. J., Isella, A., et al. 2015, ApJ, 813, 41

Pérez, L. M., Carpenter, J. M., Andrews, S. M., et al. 2016, Science, 353, 1519

Perez-Becker, D., & Showman, A. P. 2013, ApJ, 776, 134

Péricaud, J., Di Folco, E., Dutrey, A., Guilloteau, S., & Piétu, V. 2017, A&A, 600, A62

Pinilla, P., Pérez, L. M., Andrews, S., et al. 2017, ApJ, 839, 99

Piso, A.-M. A., Öberg, K. I., Birnstiel, T., & Murray-Clay, R. A. 2015, ApJ, 815, 109

Piso, A.-M. A., Pegues, J., & Öberg, K. I. 2016, ApJ, 833, 203

Pollack, J. B., Hollenbach, D., Beckwith, S., et al. 1994, ApJ, 421, 615

Pollack, J. B., Hubickyj, O., Bodenheimer, P., et al. 1996, Icarus, 124, 62

Pont, F., Sing, D. K., Gibson, N. P., et al. 2013, MNRAS, 432, 2917

Pontoppidan, K. M. 2006, A&A, 453, L47

Posch, T., Kerschbaum, F., Fabian, D., et al. 2003, ApJS, 149, 437

Powell, D., Louden, T., Kreidberg, L., et al. 2019a, ApJ, 887, 170

Powell, D., Murray-Clay, R., Pérez, L. M., Schlichting, H. E., & Rosenthal, M. 2019b, ApJ, 878, 116

Powell, D., Murray-Clay, R., & Schlichting, H. E. 2017, ApJ, 840, 93

Powell, D., Zhang, X., Gao, P., & Parmentier, V. 2018, ApJ, 860, 18

Pruppacher, H. R., & Klett, J. D. 1978, Microphysics of clouds and precipitation / by Hans R. Pruppacher and James D. Klett (D. Reidel Pub. Co Dordrecht, Holland ; Boston),

Qi, C., D'Alessio, P., Öberg, K. I., et al. 2011, ApJ, 740, 84

Qi, C., Öberg, K. I., Andrews, S. M., et al. 2015, ApJ, 813, 128

Qi, C., Ho, P. T. P., Wilner, D. J., et al. 2004, ApJ, 616, L11

Qi, C., Öberg, K. I., Wilner, D. J., et al. 2013, Science, 341, 630

Rafikov, R. R. 2017, ApJ, 837, 163

Ranjan, S., Charbonneau, D., Désert, J.-M., et al. 2014, ApJ, 785, 148

Raymond, S. N., & Cossou, C. 2014, MNRAS, 440, L11

Rhee, J. H., Song, I., Zuckerman, B., & McElwain, M. 2007, ApJ, 660, 1556

Ricci, L., Testi, L., Natta, A., et al. 2010, A&A, 512, A15

Robinson, T. D. 2017, ApJ, 836, 236

Rosenfeld, K. A., Andrews, S. M., Wilner, D. J., Kastner, J. H., & McClure, M. K. 2013, ApJ, 775, 136

Rosenfeld, K. A., Qi, C., Andrews, S. M., et al. 2012, ApJ, 757, 129

Rosenthal, M. M., Murray-Clay, R. A., Perets, H. B., & Wolansky, N. 2018, ApJ, 861, 74

Salyk, C., Herczeg, G. J., Brown, J. M., et al. 2013, ApJ, 769, 21

Saumon, D., Marley, M. S., Abel, M., Frommhold, L., & Freedman, R. S. 2012, ApJ, 750, 74

Schlawin, E., Zhao, M., Teske, J. K., & Herter, T. 2014, ApJ, 783, 5

Schlichting, H. E. 2014, ApJ, 795, L15

Schoonenberg, D., & Ormel, C. W. 2017, A&A, 602, A21

Schwarz, K. R., Bergin, E. A., Cleeves, L. I., et al. 2016, ApJ, 823, 91

—. 2018, ApJ, 856, 85

Seager, S., & Sasselov, D. D. 2000, ApJ, 537, 916

Sedaghati, E., Boffin, H. M. J., MacDonald, R. J., et al. 2017, Nature, 549, 238

Seinfeld, J., & Pandis, S. 2006, Atmospheric Chemistry and Physics: From Air Pollution to Climate Change, A Wiley-Interscience publication

Seki, J., & Hasegawa, H. 1983, Ap&SS, 94, 177

Shakura, N. I., & Sunyaev, R. A. 1973, A&A, 24, 337

Showman, A. P., Fortney, J. J., Lewis, N. K., & Shabram, M. 2013, ApJ, 762, 24

Showman, A. P., Fortney, J. J., Lian, Y., et al. 2009, ApJ, 699, 564

Shporer, A. 2017, PASP, 129, 072001

Shporer, A., & Hu, R. 2015, AJ, 150, 112

Sing, D. K., Pont, F., Aigrain, S., et al. 2011, MNRAS, 416, 1443

Sing, D. K., Lecavelier des Etangs, A., Fortney, J. J., et al. 2013, MNRAS, 436, 2956

Sing, D. K., Fortney, J. J., Nikolov, N., et al. 2016, Nature, 529, 59

Skemer, A. J., Marley, M. S., Hinz, P. M., et al. 2014, ApJ, 792, 17

Spiegel, D. S., Silverio, K., & Burrows, A. 2009, ApJ, 699, 1487

Sprow, F. B., & Prausnitz, J. M. 1966, AIChE Journal, 12, 780

Stark, C. R., & Diver, D. A. 2017, ArXiv e-prints, arXiv:1712.07866

Stevenson, D. J., & Lunine, J. I. 1988, Icarus, 75, 146

Stevenson, K. B. 2016, ApJ, 817, L16

Stevenson, K. B., Line, M. R., Bean, J. L., et al. 2017, AJ, 153, 68

Suhasaria, T., Thrower, J. D., & Zacharias, H. 2015, MNRAS, 454, 3317

—. 2017, MNRAS, 472, 389

Takeuchi, T., & Lin, D. N. C. 2002, ApJ, 581, 1344

Taylor, J., Parmentier, V., Irwin, P. G. J., et al. 2020, MNRAS, 493, 4342

Tazzari, M., Testi, L., Ercolano, B., et al. 2016, A&A, 588, A53

Teague, R., Guilloteau, S., Semenov, D., et al. 2016, A&A, 592, A49

Thi, W. F., van Dishoeck, E. F., Blake, G. A., et al. 2001, ApJ, 561, 1074

Thommes, E. W., Matsumura, S., & Rasio, F. A. 2008, Science, 321, 814

Thorngren, D. P., Gao, P., & Fortney, J. J. 2019, arXiv e-prints, arXiv:1907.07777

Tobin, J. J., Kratter, K. M., Persson, M. V., et al. 2016, Nature, 538, 483

Todini, P., & Ferrara, A. 2001, MNRAS, 325, 726

Toomre, A. 1964, ApJ, 139, 1217

Toon, O. B., Turco, R. P., Jordan, J., Goodman, J., & Ferry, G. 1989, Journal of Geophysical Research: Atmospheres, 94, 11359

Toon, O. B., Turco, R. P., Westphal, D., Malone, R., & Liu, M. S. 1988, Journal of Atmospheric Sciences, 45, 2123

Tremblin, P., Chabrier, G., Mayne, N. J., et al. 2017, ApJ, 841, 30

Tripathi, A., Andrews, S. M., Birnstiel, T., & Wilner, D. J. 2017, ApJ, 845, 44

Tripathi, A., Andrews, S. M., Birnstiel, T., et al. 2018, ApJ, 861, 64

Tsiaras, A., Waldmann, I. P., Zingales, T., et al. 2018, AJ, 155, 156

Turco, R., Hamill, P., Toon, O., Whitten, R., & Kiang, C. 1979a, Journal of the Atmospheric Sciences, 36, 699

Turco, R. P., Hamill, P., Toon, O. B., Whitten, R. C., & Kiang, C. S. 1979b, Journal of the Atmospheric Sciences, 36, 699

Turner, J. D., Leiter, R. M., Biddle, L. I., et al. 2017, MNRAS, 472, 3871

Vacca, W. D., & Sandell, G. 2011, ApJ, 732, 8

Vahidinia, S., Cuzzi, J. N., Marley, M., & Fortney, J. 2014, ApJ, 789, L11

Valenti, J. A., & Piskunov, N. 2012, SME: Spectroscopy Made Easy, Astrophysics Source Code Library, ascl:1202.013

van den Ancker, M. E., de Winter, D., & Tjin A Djie, H. R. E. 1998, A&A, 330, 145

van Leeuwen, F., ed. 2007, Astrophysics and Space Science Library, Vol. 350, Hipparcos, the New Reduction of the Raw Data

van Zadelhoff, G.-J., van Dishoeck, E. F., Thi, W.-F., & Blake, G. A. 2001, A&A, 377, 566

Venot, O., Parmentier, V., Blecic, J., et al. 2019, submitted to ApJ

Visscher, C., Lodders, K., & Fegley, Jr., B. 2010, ApJ, 716, 1060

von Paris, P., Gratier, P., Bordé, P., Leconte, J., & Selsis, F. 2016, A&A, 589, A52

von Paris, P., Gratier, P., Bordé, P., Leconte, J., & Selsis, F. 2016, A&A, 589, A52

Vorobyov, E. I. 2011, ApJ, 729, 146

Voshchinnikov, N. V. 2004, Astrophysics and Space Physics Reviews, 12, 1

Wakeford, H. R., & Sing, D. K. 2015, A&A, 573, A122

Wakeford, H. R., Visscher, C., Lewis, N. K., et al. 2017, MNRAS, 464, 4247

Wang, J., Wang, J. J., Ma, B., et al. 2020, AJ, 160, 150

Webber, M. W., Lewis, N. K., Marley, M., et al. 2015, ApJ, 804, 94

Weidenschilling, S. J. 1977a, MNRAS, 180, 57

—. 1977b, Ap&SS, 51, 153

Williams, J. P., & Best, W. M. J. 2014, ApJ, 788, 59

Williams, J. P., & Cieza, L. A. 2011, ARA&A, 49, 67

Williams, J. P., & McPartland, C. 2016, ApJ, 830, 32

Witte, S., Helling, C., Barman, T., Heidrich, N., & Hauschildt, P. H. 2011, A&A, 529, A44

Witte, S., Helling, C., & Hauschildt, P. H. 2009, in American Institute of Physics Conference Series, Vol. 1094, 15th Cambridge Workshop on Cool Stars, Stellar Systems, and the Sun, ed. E. Stempels, 572–575

Woitke, P., & Helling, C. 2003, A&A, 399, 297

—. 2004, A&A, 414, 335

Wong, I., Knutson, H. A., Lewis, N. K., et al. 2015, ApJ, 811, 122

Wong, I., Knutson, H. A., Kataria, T., et al. 2016, ApJ, 823, 122

Wood, S. E. 1999, PhD thesis, UNIVERSITY OF CALIFORNIA, LOS ANGELES

Wright, E. L. 1987, ApJ, 320, 818

Wylie, L. 1958, Thesis (Atlanta, GA: Georgia Institute of Technology)

Xu, R., Bai, X.-N., & Öberg, K. 2017, ApJ, 835, 162

Youdin, A. N., & Lithwick, Y. 2007, Icarus, 192, 588

Yu, M., Evans, II, N. J., Dodson-Robinson, S. E., Willacy, K., & Turner, N. J. 2017, ApJ, 841, 39

Yu, M., Willacy, K., Dodson-Robinson, S. E., Turner, N. J., & Evans, II, N. J. 2016, ApJ, 822, 53

Zeidler, S., Posch, T., Mutschke, H., Richter, H., & Wehrhan, O. 2011, A&A, 526, A68

Zhang, K., Bergin, E. A., Schwarz, K., Krijt, S., & Ciesla, F. 2019, ApJ, 883, 98

Zhang, K., Blake, G. A., & Bergin, E. A. 2015, The Astrophysical Journal Letters, 806, L7

Zhang, K., Bosman, A. D., & Bergin, E. A. 2020a, ApJL, 891, L16

Zhang, K., Schwarz, K. R., & Bergin, E. A. 2020b, ApJL, 891, L17

Zhang, M., Knutson, H. A., Kataria, T., et al. 2018, AJ, 155, 83

Zhang, X., Pandis, S. N., & Seinfeld, J. H. 2012, Aerosol Science and Technology, 46, 874

Zhang, X., & Showman, A. P. 2018a, The Astrophysical Journal, 866, 1

—. 2018b, The Astrophysical Journal, 866, 2

Zhang, Y., Macke, A., & Albers, F. 1999, Atmospheric Research, 52, 59

Zhu, Z. 2015, ApJ, 799, 16

Zhu, Z., Nelson, R. P., Dong, R., Espaillat, C., & Hartmann, L. 2012, ApJ, 755, 6

# Appendix A

# Cloud Compositions and Material Properties

## A.1 Condensible Species

As an update to the model presented in Powell et al. (2018), we consider a suite of six different condensible species: $TiO_2$, $Al_2O_3$, Fe, $Mg_2SiO_4$, Cr, and MnS. Three of these species, $TiO_2$, Fe, and Cr, are able to form through either homogeneous nucleation or heterogeneous nucleation due to the presence of these molecules in the gas phase. $TiO_2$ clouds homogeneously nucleate abundantly due to their very low surface energies, and $TiO_2$ can thus serve as cloud condensation nuclei for other cloud species (see Lee et al. 2018, for more details on cloud condensation nuclei at high temperatures). Since homogeneous nucleation is very efficient for this species, heterogeneous nucleation is not their favored pathway for formation. Thus, only Fe and Cr cloud particles can

form via homogeneous or heterogeneous nucleation pathways, though heterogeneous nucleation is typically favored if an abundance of cloud condensation nuclei are present due to their relatively high surface energies. $Al_2O_3$, $Mg_2SiO_4$, and MnS likely form via grain chemistry as they do not exist in this form as gases. We therefore model their formation as a parameterization of heterogeneous nucleation theory following Helling & Woitke (2006) and detailed in **?**. For all cloud species considered in this work we assume an initial solar concentration of gaseous species in an abundance given by equilibrium chemical modeling before rainout for that planetary temperature profile as described in **?**.

These cloud species will form when they reach a sufficient supersaturation in the atmosphere. This is defined as the point where a species' atmospheric partial pressure exceeds its saturation vapor pressure. This can be converted to a species' condensation curve as detailed in Morley et al. (2012) where we expect cloud particle growth to occur most rapidly at locations where the condensation curve intersects a planetary pressure temperature profile (Powell et al. 2018). The condensation curves for the species considered in this work are shown in Figure 3.3. However, these curves are approximations for the cloud formation process and should only be used as a rough guide. This is because cloud formation will be highly inefficient for cases where supersaturations are not sufficiently large. This is demonstrated in Powell et al. (2018) for planets with equilibrium temperatures of 1800 K and 1900 K. From a naive consideration of the condensation curve, one might expect these planets will form titanium clouds at their substellar points. However, in these cases titanium clouds do not form

significantly. This further highlights the importance of detailed microphysical cloud modeling.

## A.2 Material Properties Used in Microphysical Modeling

There are several material properties needed when modeling clouds from first principles with microphysics. In particular these are: latent heat of vaporization, desorption energy, the species' surface energy, and contact angle (for heterogeneous nucleation).

To derive a given species' latent heat, we use the Clausius-Clapyron relation in conjunction with the species' saturation vapor pressure (see **?**). We use this estimated latent heat of vaporization estimate to derive a species desorption energy (see Table A.1).

A species's desorption energy regulates the rate of heterogeneous nucleation such that higher desorption energies result in more nucleation (see **?**, Appendix A.1). This term is thus very important in regulating cloud formation processes. Based on experimental estimates for species not modeled in this work (such as $H_2O$), the desorption energy is typically on the same order, but less than, the latent heat of vaporization (Greenwood et al. 2003; Bolis 2013; Kim et al. 2016). In our modeling work we consider two different cases for the desorption energy as described in Section 3.4.4.

The species' surface energies used in our modeling are determined either through detailed modeling or laboratory experiements. The specific values are given in **?**.

Finally, the contact angle used in modeling heterogeneous nucleation is de-

Table A.1: Species Desorption Energies

| Species | Approximate Desorption Energy |
|---|---|
| $TiO_2$ | 3.22 eV |
| $Mg_2SiO_4$ | 3.223 eV |
| $Al_2O_3$ | 4.553 eV |
| Fe | 2.083 eV |
| Cr | 2.034 eV |
| MnS | 2.362 eV |
| $Na_2S$ | 1.378 eV |

termined through a consideration of the surface energy of the nucleating species and the cloud condensation nuclei ($TiO_2$ in this work). The contact angle regulates heterogeneous nucleation in a similar way to the desorption energy where larger contact angles lead to less nucleation. The maximum contact angle is $180^o$ which results in no heterogeneous nucleation. The contact angle can be defined as:

$$\cos\theta_c = \frac{\sigma_C - \sigma_{x,C}}{\sigma_x} \tag{A.1}$$

where $\theta_C$ is the contact angle between the cloud condensation nuclei and the condensing species, $\sigma_C$ is the surface energy of the cloud condensation nuclei, $\sigma_x$ is the surface energy of the condensing species, and $\sigma_{x,c}$ is the interfacial tension between the cloud condensation nuclei and the condensing species. The interfacial tension is given by: $\sigma_{x,c} = \sigma_C - \sigma_x - W_{C,x}$ where $W_{C,x}$ is the work of adhesion which can be estimated by various methods. In our modeling, we consider two different cases for the contact angle of a species as described in Section 3.4.4.

# Appendix B

# Particle Relative Velocities and Growth Timescales

## B.1 Order of Magnitude Derivations of Particle Relative Velocities

We provide a framework for understanding particle relevant velocities used in growth calculations in an order of magnitude sense. We consider the case when the relative velocity between two particles is determined by turbulence. This appendix is provided as a tool to increase intuition regarding particle growth in an order of magnitude sense. We did not find such a derivation in previously published work and this was greatly helpful in our understanding of this work and our derivation in Appendix B.2.

For a full discussion of the complete expression that we use to determine par-

ticle relative velocities in all regimes, see Equation 16 from Ormel & Cuzzi (2007).

### B.1.1 Kolmogorov Cascade

The Kolmogorov cascade describes how energy is transferred from large to small scales in a turbulent fluid. In a fluid that is in steady state we can use dimensional arguments to derive the following scalings:

$$E_k \propto k^{-5/3} \tag{B.1}$$

$$v_k \propto k^{-1/3} \tag{B.2}$$

where $k$ is the wavenumber with units of length$^{-1}$. These scalings follow directly from balancing the energy in and out of a particular eddy scale.

In the following discussion we take particle 1 to have a stopping time ($t_1$) and hence Stokes number, $St_1$ (see Equation B.9) that is larger than that for particle 2 ($t_2$), $St_2$.

### B.1.2 Tightly Coupled Regime – $t_1,\ t_2 < t_\eta$

For tightly coupled particles with stopping times less than the turnover time of the smallest scale eddies ($t_\eta = Re^{-1/2} t_L$ where $t_L$ is the turnover time of the largest eddies which we take to be the local orbital period and Re is the Reynold's number, defined as the ratio between the turbulent and molecular kinematic viscosities. In "$\alpha$ notation" this is: Re$= \alpha c_s H/\nu$ where $c_s$ is the sound speed, $H$ is the scale height, and $\nu$ is the kinematic viscosity of the gas), the particle will be able to reach an equilibrium

with eddies of every scale. This regime is valid if both particles have stopping times less than the turnover time of the smallest eddy such that $t_1, t_2 < t_\eta$. Therefore, when a particle enters any eddy it forgets its initial motion and aligns itself with the motion of the gas that comprises that eddy. In this regime, a particle's velocity relative to the gas can be described as the particle's settling terminal velocity.

These particles are continually accelerated by drag forces such that the particle's velocity relative to the gas can be thought of as the velocity where the acceleration from the eddies balances the acceleration from drag. An eddy of scale $k$ can accelerate a particle up to a velocity $v_k \propto k^{-1/3}$ on an eddy turnover timescale $t_k \propto (kv_k)^{-1} \propto k^{-2/3}$. This is the minimum acceleration needed to reach a velocity $v_k$ in a turnover time and is relevant because a particle can only couple to an eddy that can accelerate it to the eddy's velocity in less than or equal to a turnover time. Thus we have

$$a_k \propto v_k/t_k \propto k^{1/3} \tag{B.3}$$

which is the acceleration that an eddy of scale $k$ provides in a turnover time. Thus the acceleration is dominated by the smallest scale eddies (eddies with the largest $k$).

Equating the drag force with the acceleration from the smallest scale eddy

gives:

$$\frac{F_d}{m} \sim a_\eta \tag{B.4}$$

$$\frac{v_{pg}}{t_s} \sim \frac{v_\eta}{t_\eta} \tag{B.5}$$

$$v_{pg} \sim v_\eta \frac{t_s}{t_\eta} \tag{B.6}$$

where $F_d$ is the drag force, $a_\eta$ is the acceleration from the smallest eddy, $v_{pg}$ is the relative velocity between the particle and the gas, $v_\eta$ is the velocity of the smallest eddy and $t_s$ is the stopping time of the particle which is equal to the stokes number of the particle divided by $\Omega$.

Thus the relative velocity between two particles with stopping times $t_1$ and $t_2$ (assuming without loss of generality that $t_1 > t_2$) is:

$$v_{12} \sim \frac{v_\eta}{t_\eta} (t_1 - t_2) \tag{B.7}$$

We can put this equation into more familiar terms by using the following expressions: $v_L^2 \sim v_{gas}^2 \sim v_\eta^2 Re^{1/2} \sim v_\eta^2 t_L/t_\eta$ and $t_L \sim \Omega^{-1}$

$$v_{12}^2 \sim \frac{v_{gas}^2}{t_L t_\eta} (t_1 - t_2)^2 \sim v_{gas}^2 \frac{\Omega}{t_\eta} (t_1 - t_2)^2 \sim v_{gas}^2 \frac{\Omega^{-1}}{t_\eta} (St_1 - St_2)^2 \tag{B.8}$$

where $St$ is the Stokes number of a particle given by

$$St \approx \Omega t_s = \begin{cases} \Omega \rho_s s / \rho c_s & s < 9\lambda/4, \text{ Epstein drag,} \\ \Omega 4 \rho_s s^2 / 9 \rho c_s \lambda & s > 9\lambda/4, \mathrm{Re} \lesssim 1 \text{ Stokes drag} \end{cases} \tag{B.9}$$

(summarized in Chiang & Youdin 2010). Here $t_s$ is the particle's stopping time, $\rho$ is the gas midplane density, $\rho_s = 2$ g cm$^{-3}$ is the density of a solid particle, $s$ is the particle size, and $\lambda = \mu / \rho \sigma_{\rm coll}$ is the gas mean free path where $\sigma_{\rm coll} = 10^{-15}$ cm$^2$. Now we can derive our full expression:

$$v_{12}^2 = v_{gas}^2 \frac{t_L}{t_\eta} \left( St_1 - St_2 \right)^2 \tag{B.10}$$

which is Equation (27) of Ormel & Cuzzi (2007).

In the tightly coupled regime both the small and large particles are relevant in determining the relative velocity between the two particles.

### B.1.3 Intermediately Coupled Regime – $t_\eta \leq t_1 \leq t_L$ or $\mathrm{St}_1 < 1$

In this regime the larger particle ($t_1$) becomes decoupled from some but not all eddies. A particle is coupled to all eddies with turnover times longer than the particle's stopping time.[5] Smaller eddies have shorter turnover times and smaller velocities. Both particles are well-coupled to large scale eddies; the velocities of the particles are correlated and their relative velocities are low. On the scale at which one particle decouples,

[5]Note that in the above discussion we have also assumed that the time for a particle to cross over an eddy due to laminar drift, $t_{cross}$, is long. This is because, for $t_s \ll t_L$, we expect $v_{rel}(k)$, the relative velocity between the particle and the eddy with scale $k$, to be small, i.e. $\eta v_k St_1 / l < t_{cross}$, such that the particle will not drift over an eddy. See Youdin & Lithwick (2007) for further discussion.

the relative velocity is of order the total eddy velocity. We are thus interested in the eddy scale for which the eddy turnover time is $t_1$ because that is the decoupled eddy with the largest velocity. We refer to the eddy turnover time at this scale as $t^*$.

The eddy length scale is $l = 1/k$ and $v_k \sim l/t$ is the eddy velocity. We can derive the following scalings: $t_k = 1/(kv_k) \propto l^{2/3}$, $v_k \propto l^{1/3}$. This gives us $v_k \propto t_k^{1/2}$. Decoupling eddies are eddies such that $t < t^*$, the eddy fluctuation time is smaller than the particle's stopping time and the particle is not well-coupled to the eddy. We can therefore say that the relative velocities should roughly be: $v_k \propto \sqrt{t^*}$. We now have $t_* \sim t_s$ (c.f. Equation (3) of Ormel & Cuzzi 2007). As shown in Ormel & Cuzzi (2007), this is indeed the case – for small particles a good approximation for $t^*$ is $t^* = y_a^* t_s$ where $y_a^*$ is roughly 1.6. This gives $v_k \propto \sqrt{1.6 t_s}$.

Thus, relative velocities in this regime should be proportional to the square root of the Stokes number of the particle. From examination of Equation (28) of Ormel & Cuzzi (2007) this is indeed the case. A more detailed calculation yields the following expression:

$$v_{12}^2 = v_{gas}^2 \left[ 2y_a - (1+\epsilon) + \frac{2}{1+\epsilon} \left( \frac{1}{1+y_a} + \frac{\epsilon^3}{y_a + \epsilon} \right) \right] St_1 \tag{B.11}$$

where $\epsilon = St_1/St_2$. When particles grow from collisions with like-sized grains, their relative velocity can be approximated as $v_{12} \sim \sqrt{2 v_{\rm gas}^2 St_1}$.

In the intermediately coupled regime the large particle dominates the relative velocity between the two particles.

### B.1.4 Heavy Particle Regime – $St \gg 1$

A well known expression for the RMS velocity (relative to inertial space) of a particle with $St \gg 1$ is

$$v_p = \frac{v_{gas}}{\sqrt{1+St}} \tag{B.12}$$

This is derived in Youdin & Lithwick (2007) and Rosenthal et al. (2018). In this regime particles receive many uncorrelated "kicks" from the largest scale eddies over a single stopping time, causing the particle to random walk in velocity. These random walk kicks are balanced by settling. In general, we can write the RMS particle-particle relative velocity $\langle \delta v_{12}^2 \rangle$ as

$$\langle \delta v_{12}^2 \rangle = \langle \delta v_1^2 \rangle + \langle \delta v_2^2 \rangle - 2 \langle \delta v_1 \delta v_2 \rangle \tag{B.13}$$

Smaller particles can couple strongly to the same eddy, which will cause correlations in their velocity and lead to a non-zero value of $\langle \delta v_1 \delta v_2 \rangle$. For $St_1 \gg 1$ however, the large particle does not couple strongly to any eddy size, so we expect no correlation between the two particles' velocities, i.e. $\langle \delta v_1 \delta v_2 \rangle = 0$. In that case using Equation (B.12) in Equation (B.13) gives

$$\langle \delta v_{12}^2 \rangle = \langle \delta v_1^2 \rangle + \langle \delta v_2^2 \rangle \tag{B.14}$$

$$= v_{gas}^2 \left( \frac{1}{1+St_1} + \frac{1}{1+St_2} \right) \tag{B.15}$$

which is Equation (29) of Ormel & Cuzzi (2007).

We note here that the smaller particle dominates the relative velocity between the two particles.

## B.2 Early Stage Particle Growth

At early times particles must grow by several orders of magnitude in size from small submicron grains inherited from the ISM to large grains affected by particle drift or fragmentation. To approximate the time that a disk is in this regime we consider growth by particle collisions such that $\tau_{\rm grow} = m/\dot{m}$ where $\dot{m}$ is given in Equation (5.6).

For this broad range of particle sizes there are two relevant particle relative velocity regimes: the tightly coupled and intermediately coupled regimes (see Section B.1.1). In both regimes, particle growth is dominated by collisions with similarly sized grains when considering a Dohnanyi (or similar) size distribution. This is because for such a size distribution most of the mass is in the largest sizes which thus dominate the overall growth rate in spite of their slower relative velocities.

Very small tightly coupled particles have relative velocities, and thus growth rates, that depend on $\alpha$ though they are roughly independent of particle size (see Figure B.2). The growth of the tightly coupled particles is generally slower than the growth of intermediately coupled particles for values of $\alpha \lesssim 10^{-1}$.

Once particles grow to a large enough size that they begin to decouple from the gas, their growth rate increases. In the intermediate regime, the relative velocity between similarly sized particles can be approximated as $\Delta v \sim \sqrt{\alpha {\rm St}} c_s$ (see Section

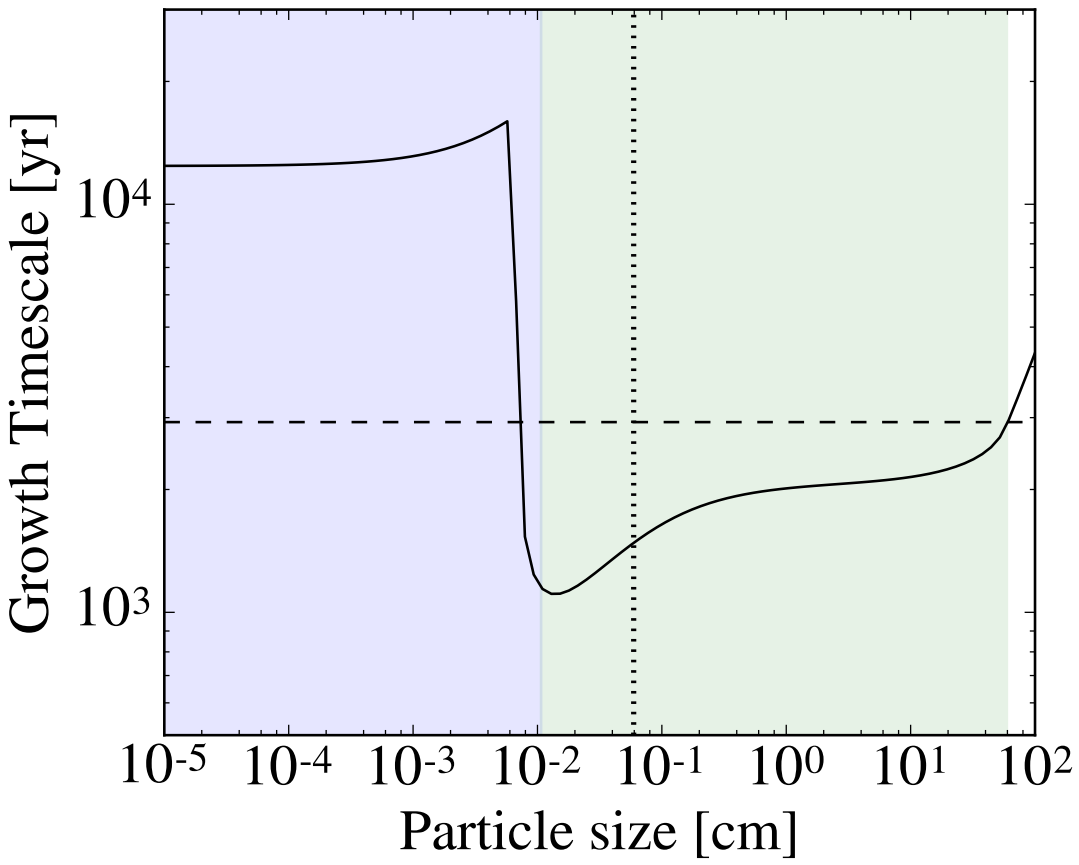


Figure B.1: The growth timescale as a function of particle size for a fiducial disk with a particle size distribution having most of the mass in the largest sizes. The horizontal dashed line is the growth timescale calculated by Birnstiel et al. (2012) ($1/(\Omega f_d)$ see Equation B.16), which is intended to approximate the growth timescale for intermediately sized grains. The dotted vertical line is the point at which the particle's stopping time is equal to $\alpha$; to the right of this line the dust scale height has settled to a value smaller than the gas scale height. The blue shaded region represents the small particle growth regime while the green shaded region represents the intermediately sized particle growth regime.

B.1.1). In the Epstein drag regime, the Stokes number is given by $St = \Omega \rho_s s / \rho_g c_s$. The scale height for these particles can be approximated as $H_d = H\sqrt{\alpha/St}$. For these particles the growth timescale can therefore be approximated as $\tau_{\rm grow} \sim 1/(\Omega f_d)$ (Birnstiel et al. 2012) which is independent of both size and $\alpha$. Following Birnstiel et al. (2012), because the growth timescale is roughly independent of particle size, the timescale that it takes to grow several orders of magnitude acts like a Coulomb logarithm and can be roughly approximated as

$$t_{\rm early\ grow} = \tau_{\rm grow} \ln\left(\frac{a_{\rm max}}{a_0}\right) \sim 1/(\Omega f_d) \ln\left(\frac{a_{\rm max}}{a_0}\right). \tag{B.16}$$

where $a_{\rm max}$ is the maximum particle size at a given location and $a_0$ is the size of the smallest particles inherited from the ISM.

We repeat this derivation replacing $\Delta v$ with the full particle relative velocity expression from Ormel & Cuzzi (2007) (see their Equation 16) and $H_d = H\sqrt{\alpha/(\alpha + St)}$ (Ormel & Kobayashi 2012) such that particles with St $\lesssim \alpha$ have a scale height equal to the gas scale height. We also assume $St_1 = 0.9St_2$, roughly the size difference that produces the maximum growth rate in a Dohnanyi size distribution as particles closer in size have relative velocities that approach zero. The growth timescale for particles over a range of sizes is shown in Figure B.2 for an $\alpha$ of $10^{-3}$ assuming a dust-to-gas ratio of $10^{-2}$.

The particle growth timescale is roughly independent of size for both very small and intermediately sized particles. However, the absolute scale between these regimes differs. The average growth timescale considering the growth of very small

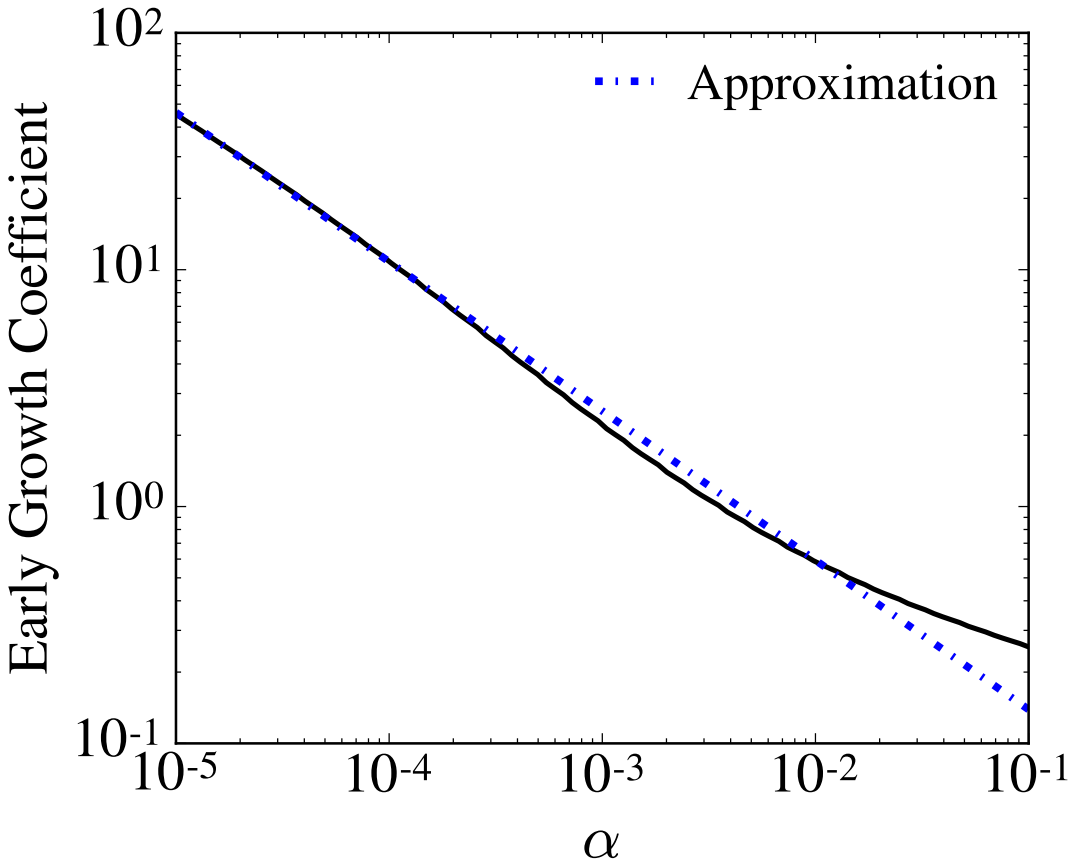


Figure B.2: The coefficient that determines the magnitude of the early growth timescale (black line) as a function of alpha. An approximation (blue, dashed line) of this relationship is added as a coefficient in Equation (B.17). This approximation is appropriate for $\alpha \lesssim 10^{-2}$.

grains differs from the timescale given in Equation (B.16) by a factor that is a function of $\alpha$ as shown in Figure B.2. For $\alpha$ values roughly less than or equal to $10^{-2}$, the early growth coefficient is inversely correlated with $\alpha$ such that the early particle growth rate can be well described as

$$t_{\text{early grow}} = \tau_{\text{grow}} \ln\left(\frac{a_{\max}}{a_0}\right) \sim \frac{0.033\alpha^{-0.63}}{\Omega f_d} \ln\left(\frac{a_{\max}}{a_0}\right). \tag{B.17}$$

In this work, we assume an $\alpha$ of $10^{-3}$. For this value of $\alpha$ it is appropriate to increase the early growth timescale in Equation (5.5) by a factor of 2. We find that the early growth timescale does not matter to our results unless $\alpha \lesssim 10^{-7}$.